NASA Technical Paper 1514

Wind-Tunnel/Flight Correlation Study of Aerodynamic Characteristics of a Large Flexible Supersonic Cruise Airplane (XB-70-1)

I - Wind-Tunnel Tests of a 0.03-Scale Model at Mach Numbers From 0.6 to 2.53

James C. Daugherty

NOVEMBER 1979

NASA

NASA Technical Paper 1514

Wind-Tunnel/Flight Correlation Study of Aerodynamic Characteristics of a Large Flexible Supersonic Cruise Airplane (XB-70-1)

I - Wind-Tunnel Tests of a 0.03-Scale Model at Mach Numbers From 0.6 to 2.53

James C. Daugherty
Ames Research Center
Moffett Field, California

NASA
National Aeronautics
and Space Administration

Scientific and Technical Information Branch

1979

NOTATION

The static-stability coefficients presented in this report were referenced to the systems of axes shown in figure 1. The longitudinal forces and moments were referred to the stability-axes system, and the lateral forces and moments were referred to the body-axes system. The origin of the axes systems was on the model centerline at the longitudinal station of the 25% of the reference chord. The vertical location of the axes origin was arbitrarily chosen in the fabrication reference plane (water plane 00.0) of the model.

All aerodynamic coefficients were based on the full-wing planform area, wing tips undeflected, and the corresponding span and mean aerodynamic chord.

The international system of units (SI) is used in this report. However, dimensional quantities are also indicated parenthetically in U.S. customary units, which are commonly used in engineering practices in the aircraft industry of the United States. Measurements were made in U.S. customary units and equivalent SI units were determined by using conversion factors given in reference 1.

Symbols

A_c inlet capture area, 18.46 cm^2 (2.86 $in.^2$)

A_o area of free-stream tube actually entering inlet, cm^2 ($in.^2$)

$\frac{A_o}{A_c}$ mass-flow ratio based on inlet capture area

b reference span, 96.01 cm (37.80 in.)

C_L lift coefficient, $\frac{\text{lift}}{q_\infty S}$

C_D drag coefficient, $\frac{\text{drag}}{q_\infty S}$

$C_{D_{BASE}}$ base-drag coefficient, $\frac{\text{base drag}}{q_\infty S}$

$C_{D_{INT}}$ duct internal drag coefficient

C_m pitching-moment coefficient, $\frac{\text{pitching moment}}{q_\infty S\bar{c}}$

C_ℓ rolling-moment coefficient, $\frac{\text{rolling moment}}{q_\infty Sb}$

C_n yawing-moment coefficient, $\frac{\text{yawing moment}}{q_\infty Sb}$

C_Y side-force coefficient, $\frac{\text{side force}}{q_\infty S}$

$\bar{c}$ reference chord, 71.81 cm (28.27 in.)

K_1 duct nozzle-calibration factor

K_2 total-head calibration constant, $\frac{P_{te}}{P_{t_1}}$

k nominal boundary-layer-trip particle size, cm (in.)

M Mach number

p_t total pressure, N/m^2 (psf)

q dynamic pressure, N/m^2 (psf)

Re unit Reynolds number, per m (per ft)

S reference area, 0.52685 m^2 (5.668 ft^2)

α angle of attack, deg

β angle of sideslip, deg

δ angle of control surface deflection (positive for positive force on the surface), deg

ϕ model and balance roll angle (relative to normal installation or orientation; positive clockwise, looking upstream), deg

In addition, the following symbols are used in appendix C in the development of the internal flow relations.

A flow area, (ft^2)

g acceleration due to gravity, 32.174 ft/sec^2

p static pressure, psf

R gas constant, 53.35 ft-lbf/°R-lb

T static temperature, °R

T_t total temperature, °R

V velocity, ft/sec

w gravimetric rate of airflow, lb/sec

γ ratio of specific heats, 1.4

θ angular inclination of the duct axis relative to the free stream, deg

ρ specific weight of air (density), lb/ft^3

Subscripts:

c canard

e elevon (used to designate deflection angle)

e duct-exit station (used to designate duct flow properties)

i configuration component index (used to designate specified component variations)

i duct-inlet station (used in development of internal flow relations)

L left-hand side

R right-hand side

r rudder

y wing tip

∞ free-stream condition

o duct free-stream station (used to designate duct flow properties)

1 duct station upstream of the metering nozzle restriction

2 duct station at the metering nozzle restriction

WIND-TUNNEL/FLIGHT CORRELATION STUDY OF AERODYNAMIC CHARACTERISTICS OF A LARGE FLEXIBLE SUPERSONIC CRUISE AIRPLANE (XB-70-1)

I - WIND-TUNNEL TESTS OF A 0.03-SCALE MODEL AT MACH NUMBERS FROM 0.6 TO 2.53

James C. Daugherty

Ames Research Center

SUMMARY

Wind-tunnel studies were made to determine the longitudinal and lateral forces and moments for a 0.03-scale deformed-rigid, static-force model of the XB-70-1 airplane. The model external shape was designed and fabricated to represent the airplane at specific speed-power-stabilized conditions corresponding to flight test at a Mach number of 2.53. Wind-tunnel Mach numbers ranged from 0.6 to 2.53 at a unit Reynolds number of 13.12×10^6/m (4×10^6/ft). Control effectiveness was determined for the elevon in pitch and roll, for the canard, and for the rudders. Component effects of the canard, deflected wing tips, variable-position canopy, bypass doors, and bleed-dump fairing were measured. Data were obtained to assess the effects of small variations in inlet mass-flow ratio and small amounts of asymmetric deflection of the wing tips. To permit the experimental determination of turbulent drag levels, studies were made using boundary-layer transition strips consisting of various sizes of distributed roughness particles to induce turbulent flow near the leading edges of the model surfaces.

INTRODUCTION

Evaluation of aircraft performance and validation of preflight drag predictions is highly dependent on an accurate assessment of engine net thrust. During the XB-70 Flight Research Program, jet-engine net thrust was calculated by a "gas-generator method." Analysis of flight-thrust calculations based on the gas-generator method and comparisons of ground-based static-thrust-stand measurements with calculations based on this method predicate a high level of confidence in the calculation of engine thrust (ref. 2).

Because of the unique size, speed, and sophisticated instrumentation capabilities of the XB-70-1 airplane (refs. 2, 3), and in view of the high quality of the engine-thrust measurements for the airplane, the National Aeronautics and Space Administration has established a program to correlate flight-derived values of lift-drag ratio and longitudinal stability and control parameters with predictions based on wind-tunnel-test results and analytical procedures. The program is a cooperative effort of the Ames, Dryden Flight, and Langley Research Centers and, by contract, the aircraft developer, Rockwell International (formerly, North American Rockwell Corporation).

Toward this goal, Ames Research Center has conducted studies to determine the static-force and moment characteristics on a 0.03-scale model of the XB-70-1; the study data will serve as a base for the predictions of the full-scale aerodynamic characteristics. The rigid model was designed and fabricated by Rockwell (ref. 4) to be representative of the steady-state flexible-airplane shape at the highest Mach number (2.53) for which speed-power-stabilized performance flight-test data were available. The wind-tunnel tests were made at Mach numbers from 0.6 to 2.53 at a unit Reynolds number of 13.12×10^6/m (4×10^6/ft). Angle of attack varied from -5° to +10°. Angle of sideslip was varied from -5° to +5°. A number of configurations were tested to allow evaluation of elevon, canard, and rudder effectiveness. The model was constructed to permit the determination of aerodynamic effects associated with various component modifications, including:

1. Removal of the canard
2. Addition of the "shaker vane"
3. Canopy position
4. Wing-tip deflection
5. Bypass-door deflection (no bypass airflow)
6. Addition of the bleed-dump fairing to the lower surface of the propulsion system nacelle (no inlet bleed airflow)

To allow determination of the characteristics of the model with an all-turbulent boundary-layer flow, studies were made using various sizes of distributed-roughness boundary-layer-transition trips. As an aid in interpretation of these results, visual-flow studies were made using subliming solids to validate transition to turbulent flow at the trip.

MODEL DESCRIPTION

A 0.03-scale static-force model of the XB-70-1 airplane was constructed for these tests by North American Rockwell Corporation. The rigid model was fabricated to conform to the estimated shape of the flexible airplane for a specific speed-power-stabilized flight-test point at a Mach number of 2.53. The flight-test conditions defining this point were specified by the Dryden Flight Research Center and are indicated in appendix A. Details of the procedures used to estimate the airplane flexible shape are contained in reference 4.

The model was constructed mainly of steel, with certain structurally noncritical fairings made of aluminum. Nozzles, used to regulate and meter the flow through the nacelle ducts were made of brass.

Sketches of the model are presented in figure 2. Photographs of the model for various wind-tunnel installations are presented in figure 3. Nomenclature for designating individual model components and certain associated geometrical data are given in appendix B.

Prior to these wind-tunnel tests, detailed coordinate measurements of the model external surfaces were made by the NASA-Langley Research Center.

The model was sting-mounted from the rear. Model forces and moments were measured by means of a six-component internal strain-gage floating-frame balance mounted in the nacelle component of the model. Pressures on the model base and in the balance cavity and internal flow ducts were measured with a pressure-sampling valve-drive-transducer combination mounted in the forebody of the model. Ten static pressure orifices were located on the top right-hand wing surface along the wing chord corresponding to the spanwise location of the right-hand vertical tail. These pressures were also measured with the internally mounted valve-drive-transducer. The results of these measurements are not reported herein; however, some comparisons of these measurements with flight-test results are included in reference 5.

TESTS AND PROCEDURES

The tests were conducted in the 11- by 11-foot transonic test section and in the 9- by 7-foot supersonic test section of the Ames Unitary Plan Wind Tunnel facility. The nominal test Mach numbers in each facility were:

11- by 11-foot test section:	0.60, 0.75, 0.80, 0.95, 1.20, 1.40
9- by 7-foot test section:	1.60, 2.10, 2.53

The unit Reynolds number in both facilities was 13.12×10^6/m (4×10^6/ft) except for a series of runs made at a Mach number of 2.53 and at a unit Reynolds number of 6.56×10^6/m (2×10^6/ft) to assess the combined effects of Reynolds number and model aeroelasticity.

Static force and moment data were obtained to define the aerodynamic characteristics of the various model configurations at angles of attack from -5° to +10° and at angles of sideslip from -5° to +5°. To maximize sensitivity in data acquisition and maintain structural integrity under high-load conditions, internally mounted force balances of differing load capabilities were used for the tests in each facility.

Corrections to Data

Stream angle- The data presented herein include corrections to angle of attack to account for test-section flow angularity. These corrections were obtained by testing a complete configuration in normal and inverted roll orientations at each Mach number. The stream-angle correction was then interpreted to be that value that would result in identical values of zero-lift angle of attack for the model in both normal and inverted orientations. It was determined that operation of the boundary-layer removal system, operating through the plenum chamber on the slotted walls of the transonic test section, had negligible effects on the test-section flow angularity at Mach numbers of 1.2 and 1.4. The stream-angle corrections applied for each Mach number were:

Mach number	Stream-angle correction, deg
0.60	0.10
.75	.09
.80	.09
.95	0
1.20	0
1.40	0
1.60	-.05
2.10	-.05
2.53	-.05

Typically, wind tunnels exhibit stream-angle variations in the model sideslip plane as well as in the pitch plane. Extensive testing is required to experimentally separate the effects of model left-right asymmetry from the effects of lateral flow angle. In addition, the model support systems in the Ames Unitary Plan Wind Tunnels do not permit pitching the model at precisely zero sideslip. On the basis of these considerations, no corrections for lateral flow angle were applied to the data.

Additional corrections have been made to angles of attack and angles of sideslip to account for elastic deflection of the balance, sting, and model support due to aerodynamic and weight-tare loadings.

Drag corrections- The model was mounted, as shown in figure 3(c), through the model base. Balance-cavity pressure was determined as the average of two pressure measurements in the cavity — one forward of the balance and one aft of the balance — but approximately 20 cm (8 in.) forward of the model base. Base pressure was determined as the average of 12 pressure measurements distributed over the model base. The model base was divided arbitrarily into 12 approximately equal areas, and a pressure orifice was located near the center of each area. These measurements were made for each data point. On the basis of these measurements, the drag data have been adjusted to correspond to a condition of free-stream static pressure in the balance cavity and on the model base.

A single measurement for each data point was made to determine the pressure acting on the base of the no-flow bleed-dump fairing on the underside of the nacelle. The drag data, which include the effects of the bleed-dump fairing, have been adjusted to represent free-stream static pressure acting on the fairing base.

Drag data determined in the supersonic test section include corrections to account for buoyant effects (buoyancy) assumed to be induced by variations in test-section longitudinal static pressure. The buoyancy corrections to drag coefficient were:

M	Correction
1.60	-0.00030
2.10	.00012
2.53	-.00003

In the transonic test section, the effects of clear-tunnel pressure gradients were negligibly small due to longitudinal placement of the model and no buoyancy corrections were made to the data.

Internal drag, determined as the losses (in the free-stream direction) in momentum and pressure forces (referred to free-stream conditions) for the air flowing through each duct, was subtracted from the measured drag. The internal drag was computed for each duct for each data point. Duct mass flows were measured by means of convergent metering nozzles located at the duct exits. Duct mass flow was modulated by using several sets of metering nozzles with different throat areas, each of which provided choked flow at the duct exit.

Appendix C contains a detailed discussion of the procedure followed in determining the internal drag and associated duct mass-flow ratio. In addition to the internal-flow correction to drag, the pitching- and yawing-moment data included corrections to account for asymmetric effects, relative to the moment reference center, of the internal drag calculated for each duct.

A "bench-test" calibration against standard ASME thin-plate orifices in a 20.32 cm (8-in.) diameter pipe was performed for all model nozzles. In addition, selected nozzles were check-calibrated in the supersonic test section at normal operating conditions. The fixtures for these in-tunnel calibrations consisted of relatively large diameter pipes connected by air-tight transition sections, bellows, and sealing arrangements to the base region of each duct exit. Each pipe included a flow nozzle that had been bench-tested (calibrated against the 20.32-cm (8-in.) standard pipe orifices), a turbulence screen upstream of the nozzle, and a plug valve at the pipe exit to modulate the mass-flow and nozzle-pressure ratios. The results of these nozzle calibrations are presented in figures 4 and 5 as plots of K_1, the nozzle-calibration factor (see appendix C), versus nozzle pressure ratio. Figure 4 presents the results of the bench-test calibrations and figure 5 presents the results of the in-tunnel calibrations.

Duct-exit Mach number was determined for each duct at each test point. Each duct contained a total-head rake consisting of three tubes mounted approximately four equivalent duct diameters upstream of the flow nozzle. A turbulence screen, located approximately four diameters upstream of the rake, assured subsonic flow approaching the nozzle. The duct total-head rake was calibrated in both test sections against an area-weighted total-head rake of 19 tubes externally mounted at the model base to measure pressures in each duct exit (fig. 3(f)). The calibrations, which determined the total-head calibration constant K_2 (see appendix C), were performed for each nozzle. The results of these calibrations are summarized in figures 6 and 7. Figure 6 is a summary of values of K_2 for all the nozzles for angles of attack from -2° to 6° at a Mach number of 1.6. Figure 7 is a summary of values of K_2 for the N_2- and N_7-component nozzles for angles of attack from -4° to 8° at Mach numbers from 0.6 to 1.6. Duct-exit static pressure, determined as the average of eight nozzle-throat static pressures measured 1.75 cm (0.7 in.) forward of each duct exit, was used together with the calibrated-rake total pressure to determine duct-exit Mach number.

Model/balance alignment- A misalignment, measured to be 0.03°, between the centerline of the balance cavity and the fabrication reference plane (designated water plane 00.00 by the manufacturer (ref. 4)) was accounted for in reducing the force-balance data to body-axes aerodynamic coefficients.

Balance interactions- The six-component strain-gage balances were bench-test calibrated prior to the tests. Linearized load interactions and sensitivities were deduced from these calibrations and were accounted for in reducing the balance data to forces and moments. The effects of multiple-component loadings and nonlinear variations in gage sensitivities are not included. Single gage-check calibrations conducted at the test installation of each balance indicated sensitivity errors of less than 1% throughout the load ranges encountered during the model tests.

Precision of the Data

The large range in Mach number in each test facility introduced large variations in dynamic pressure which, together with the effects of varying angles of attack and sideslip, resulted in large variations in the force-balance gage loadings. Therefore, a meaningful statement regarding the precision of the data for all the various test conditions based on classical error analysis is probably not possible. Instead, it is suggested that a more significant understanding of the precision of these data can be obtained by comparing the results from repeat runs at nominally identical test conditions. Data presented in figures 8 through 11 provide an indication of the precision (i.e., repeatability) of these test results.

The longitudinal data for the basic configuration with wing tips deflected 65° in the 9- by 7-foot test section are presented in figure 8. In general, the precision of these data was excellent. Only the pitching-moment results for high values of lift showed any significant differences between the various runs. Since only the data for one sequence of runs showed this disparity, the problem was probably associated with the operation of the force balance during that particular sequence of runs. However, the data gave an indication of the difficulties involved in acquiring a consistent set of results to define the aerodynamic effects associated with systematic changes in component geometry.

Longitudinal data for the basic test configuration with wing tips deflected 25° in the 11- by 11-foot test section are presented in figure 9. Although the overall repeatability of these data was reasonably good, it was quite apparent that the precision of the data at Mach numbers of 1.2 and lower was not as good as the data for Mach numbers of 1.6 and higher (fig. 8).

Longitudinal data for the basic test configuration with undeflected wing tips at all test Mach numbers in the 11- by 11-foot test section are given in figure 10. At Mach numbers of 1.2 and 1.4, the effect of operation of the tunnel auxiliary-plenum-pumping system was assessed. No discernible effects could be attributed to the operation of this system. However, on the basis of observations by the tunnel-operations crew that the model dynamic behavior was

better (i.e., less bounce), the remainder of the data at Mach numbers of 1.2 and 1.4 were obtained with the system operating.

The results shown in figure 10 indicated small, but significant, differences with model roll-angle orientation at some of the test Mach numbers. The reason for these differences was not evident; similar data in figure 8 did not indicate such differences.

Lateral-directional results for repeated sideslip runs in the 9- by 7-foot test section are shown in figure 11. Good repeatability was shown for these data.

The following out-of-sequence citations of figures 25(d) and figures 28-33 are made to facilitate the discussion without disrupting the logical grouping of other figures.

Although no repeated sideslip runs were planned for the tests in the 11- by 11-foot test section, data for identical runs at a Mach number of 1.2 are shown in figure 25(d). Misinterpretation of the on-line results for the initial run led to repeating those data. Again, the precision of the data was excellent.

In addition, the incremental effects associated with -1° of rudder deflection were determined twice during the studies in the 9- by 7-foot test section. One set of data defining these effects is contained in figures 28-30; the other set, in figures 31-33. During the tunnel shut-down at the conclusion of the runs presented in figures 31 through 33, a malfunction of certain tunnel operating equipment caused a shutdown at high total pressure and resulted in failure of the internal force balance. Since it was felt that the results presented in figures 31 through 33 were inadequate to define the effects of rudder deflection, the rudder deflection data were completely redone with a replacement force balance. These results are presented in figures 28 through 30. Comparison of the two sets of results indicated good precision. Some differences in the drag results were noticeable near zero lift and at negative values of lift (figs. 28 and 31). However, even these differences would have minimal effect on the prediction of flight characteristics because the precision was very good at lift coefficients corresponding to actual flight conditions (i.e., positive lift).

EXPERIMENTAL DATA AND COMMENTS

The wind-tunnel study results that serve as the data base for the XB-70-1 wind-tunnel-to-flight correlation program are presented in figures 12 through 42. Unless otherwise specified, the results were for a unit Reynolds number of 13.12×10^6/m (4×10^6/ft).

Boundary-Layer Transition

Transition was induced near the leading edges of all external surfaces by boundary-layer transition strips of distributed roughness particles (glass

beads). To obtain uniformly sized particles, commercially available glass beads were screened through sieves calibrated in accordance with the specifications of the United States National Bureau of Standards Fine Sieve Series. The sieving screens were nested one above another; the screen with the largest mesh being on top. Thus, as the glass beads dropped through the screens they encountered screens with successively smaller meshes. The beads remaining on a given screen were assumed to be larger than the mesh of that screen and smaller than the mesh of the preceding screen. The indicated size of the screened beads, k, is the average of the two mesh sizes.

The subliming-solids technique was used to visually assess the effectiveness of the various boundary-layer transition strips. For this program, the material selected for the subliming solid was fluorene ($C_6H_4CH_2C_6H_4$). The model was sprayed with a mixture of fluorene and petroleum ether. During the run, sublimation of the residual fluorene after evaporation of the petroleum ether showed the position of transition.

The results from tests with variously-sized transition-strip particles are presented in figure 12. There were no significant, or consistent, effects on the lift and pitching-moment characteristics that were attributable to particle size. As expected, the transition-strip particle size affected the drag coefficient measurements. Because of the difficulty associated with determining small drag increments at lifting conditions from C_L versus C_D curves, these results have been replotted in figure 13 as C_L^2 versus C_D variations for the various particle sizes. The data of figure 13 indicated that, for each of the Mach numbers studied and for any specific lift coefficient:

1. The largest particle size resulted in the highest drag coefficient.

2. The smallest particle size resulted in the lowest drag coefficient.

3. All the intermediate particle sizes produced essentially the same value of drag coefficient.

These results were consistent with the discussion presented in reference 6. The drag variation with particle size exhibited the "desirable plateau region" (ref. 6) associated with the constant measured drag coefficient for the intermediate particle sizes. The lift-drag polars obtained for these particle sizes, then represented turbulent flow aft of the transition strip on all model surfaces with no incremental effects on the aerodynamic characteristics associated with the transition strips themselves. Furthermore, the visual flow studies corroborated these drag results. That is, the smallest particle size did not fix transition at the transition strip. In most cases, the visual observation was that the next to smallest particle size was only marginally effective in causing boundary-layer transition near the strip.

Sideslip Effects

Flight-test measurements indicated asymmetries in the settings for the various trim and control surfaces. Some discussion of this problem, as

related to the deflections of the elevon segments, is contained in reference 4; however, the problem also existed for the settings of the twin rudders and the wing tips. The asymmetries in the flight vehicle were indicative of the difficulty of achieving trimmed flight with precisely zero sideslip. Therefore, data were obtained to assess sideslip effects on lift and drag characteristics.

Angle-of-attack and lift and drag coefficient results from sideslip runs at attitudes approximating flight conditions are presented in figures 14 and 15. For small variations in sideslip angle, only small effects on aerodynamic parameters were noted.

Lateral-directional data from sideslip runs at various angles of attack are given in figure 16. The yawing-moment curves typically exhibited a change in directional stability at approximately 2° of sideslip. As pointed out in reference 7, this stability change was associated with the presence of the canard. Unpublished data obtained from wind-tunnel tests at Ames at Mach numbers of 0.95 to 1.2 showed that this directional change was due to interference between the canard and vertical tail components. This interference was undoubtedly associated with the action of the tip vortices, generated by the canard, impinging on the twin tails.

Configuration-Component Effects

Shaker vane- During the XB-70-1 Flight Test Research Program some data were obtained with the shaker vane in place (fig. 2(a)) and some flight tests were done with the vane removed. For the flight-test points in this program (ref. 3), the shaker vane, when present, was locked in an immovable reference position. The data in figure 17 allow assessment of the incremental effects on longitudinal aerodynamics due to addition of the shaker vane. No effect on lift or pitching moment was indicated for any of the test Mach numbers. For Mach numbers of 2.1 and 2.53, there were no effects on drag coefficient; for Mach numbers of 1.6 and less, the shaker vane increased measured drag coefficients.

Windshield position- The basic, or reference configurations for these wind-tunnel studies were selected arbitrarily to include the high-speed canopy (i.e., windshield raised). This position corresponded to the "design-point" flight-test conditions for which the model geometry was defined. However, portions of the flight-test program were flown with the low-speed canopy (i.e., windshield lowered). The data of figure 17 allow assessment of the incremental aerodynamics effects associated with this difference in windshield position. For supersonic Mach numbers, the low-speed canopy increased the drag coefficient. At subsonic Mach numbers, including 0.95, the canopy configuration did not affect the drag or other longitudinal characteristics.

Aft-fuselage cover plate- During detailed design of the model, calculations indicated that no physical interference between the fuselage base and sting would occur during testing in the 9- by 7-foot test section. For certain configurations and test conditions in the 11- by 11-foot test section, similar calculations indicated that interference between the model and sting probably would occur. To preclude fouling of the internal force balance, two

aft-fuselage cover plates were fabricated for the model fuselage. The basic cover plate (low-profile), designated the B_1-fuselage, was tested in both facilities. The alternative (high-profile) cover plate, designated B_2 (which provided an additional 1.8 mm (0.07 in.) of sting clearance) was tested only in the 11- by 11-foot test section. The data (fig. 17) indicated that the high-profile cover plate, which slightly decreased the boat-tailing in the region between the twin vertical tails, resulted in a decrease in measured drag coefficient together with a slight nose-up incremental change in the pitching-moment coefficients.

Canard- In performing the aeroelastic analysis presented in reference 4, a knowledge of the aerodynamic increments associated with the canard was required. Data for configurations with and without the canard and for several different wing-tip deflections are presented in figures 17 and 19.

Bleed-dump fairing- To aid in developing corrections to adjust the wind-tunnel results for the effects of the inlet-bleed airflow on external aerodynamic characteristics, a no-flow sugar-scoop-type bleed-dump-fairing was mounted on the bottom of the propulsion system nacelle and tested; these data are presented in figure 22. As stated previously, the drag data had been adjusted to a condition of free-stream static pressure acting on the base of the fairing. At all Mach numbers except 0.95, addition of the bleed-dump-fairing slightly increased the drag coefficient and produced a small nose-down incremental change in pitching moment. At a Mach number of 0.95 and for lift coefficients corresponding to flight, the measured drag coefficient was lower with the bleed-dump fairing in place than with the fairing removed. This phenomenon may be due to the effect of inlet spillage airflow on the bulbous forward portion of the bleed-dump fairing.

Propulsion-system bypass doors- The effects on longitudinal characteristics of various deflections of the propulsion-system bypass doors, which are located between the twin vertical tails, can be determined from the results presented in figure 38. As with the bleed-dump component, the bypass doors were no-flow components; that is, no air from the internal flow duct was actually dumped overboard through the bypass doors. Because the bypass doors are located between the twin vertical tails, these studies were done using the low-profile aft fuselage cover plate in both test facilities. During these runs at a Mach number of 1.2, the wing-tip elevon segments were inadvertently set to the "design-point" deflections (E_5-component, see appendix B) instead of the basic undeflected (E_1) settings. Instead of repeating the runs with deflected bypass doors on a configuration with the E_1-elevon settings, a reference run with the E_5-elevon deflections and no deflection of the bypass doors was done. The drag results in figure 38 indicated a small but fairly consistent increase in drag coefficient with increasing door deflection. At a Mach number of 1.2, there was a small difference in pitching moment. For comparison purposes, the data for the low-profile cover plate and undeflected elevons were included in figure 38(d). These data indicated that the pitching-moment input of the E_5-elevon settings was greater than those from any of the deflected bypass doors. However, it is reasonable to expect, for the flight vehicle, significant effects on external aerodynamics due to the high-pressure, propulsion-duct air exhausting through the deflected bypass doors.

Longitudinal Trim and Control

On the XB-70-1, longitudinal trim and control were provided by combined deflections of the canard and elevons. The canard and elevons were interconnected through the longitudinal control system so that the surface deflections were not independent of one another. As might be expected for any complex servo-mechanical system, there were differences between the actual surface deflections and the deflections predicted by the idealized linear design-gearing curve (i.e., $\delta_e = 20° - (20/3)\delta_c$). In fact, there were significant differences in indicated deflections for the 12 elevon segments. Reference 4 provides a complete discussion of this problem, including its cause and, to some degree, its effect on longitudinal trim. In view of the relationships between aircraft flexibility, control-surface deflection, and trimmed flight, it is clearly impractical to duplicate all flight-test conditions in the wind tunnel. Only data to define the individual effects of canard and elevon deflections were obtained during this wind-tunnel program. In carrying out these tests, all deflected-elevon segments were set to the same angle. The predictions in reference 4 of flexible-aircraft trim requirements and control characteristics are based largely on the results of these tests. Data for the individual effects of deflection of the canard and elevons were determined for wing-tip deflections of 0°, 25°, and 65°. For these studies, the range of test Mach numbers for each wing-tip deflection was consistent with both the flight-test program and the requirements for the contractor's flexibility analysis (ref. 4).

Canard- The effects of canard deflections on longitudinal characteristics can be determined from the data presented in figures 18 and 19.

Segmented elevons- Longitudinal trim and control data for the segmented elevon are presented in figure 20. The configurations represented by these data do not include the bleed-dump fairing (fig. 2(b)). Data for elevon deflections of 0° and 10° with the bleed-dump fairing are shown in figure 22. Comparisons of the data from figures 20 and 22 do not indicate any significant interference effects due to the addition of the no-flow bleed-dump fairing.

Slab elevons- To better understand the aerodynamics associated with segmentation of the elevons, tests were made with the segmentation gaps filled and covered with transparent tape to correspond to the slab-elevon of the developmental model. These results, for elevon deflections of 0° and 10°, are shown in figure 21. Comparisons of the segmented-elevon data (fig. 20) with the slab-elevon data (fig. 21) showed that significant differences in longitudinal characteristics are associated with segmentation of the elevons.

Prior to the present tests, the aerodynamics of the segmented elevon had not been studied extensively. Early termination of the XB-70 development program precluded complete wind-tunnel investigation and analysis of the aerodynamic characteristics of the segmented elevon that was used on the XB-70-1. Limited results for a segmented-elevon configuration were obtained on a development model of the XB-70 during a program conducted to study lateral-directional control problems that occurred during the XB-70 Flight Research Program (ref. 7). Although those results were neither substantial nor

conclusive, for the initial phase of the work reported in reference 4, the contractor modified the extensive slab-elevon results obtained during the development on the basis of the limited segmented-elevon data. The current test data for the two elevon configurations were used by the contractor in the final work reported in reference 4.

Lateral-Directional Trim and Control

While analyzing the flight-test results for reference 4, the contractor observed that indicated values for various surface deflections did not agree with the idealized, or nominal values. In fact, tolerances required for rigging and operating the various flight-control systems generally resulted in left-right asymmetry during flight test. The previously mentioned differences in canard-elevon deflection values from the nominal gearing curve were due, in part, to these mechanical differences. In studying the flight-test results, it was found that the left-right asymmetries of the elevon deflections were associated with asymmetric deflections of the wing tips; the elevon asymmetry tended to increase with wing-tip deflection and Mach number. As with the longitudinal trim and control data, however, the assessment of each elevon segment to the rolling moment was deemed impractical, if not invalid, due to the mutual interference between the segments. Furthermore, because rudder deflection was limited to ±3°, it was decided that asymmetric deflections of the rudders could not produce a significant effect on lift-drag performance and the deflections were, therefore, not tested.

Asymmetric tip deflection- Data for asymmetric deflections of the wing tips are presented in figures 23 through 25. The primary effects on longitudinal characteristics were on the pitching-moment characteristics. Because of the aft position of the deflected wing tips, small changes in tip deflection which resulted in small changes in lift coefficient, caused significant changes in pitching-moment coefficient. The rolling- and yawing-moment coefficient results were similar in that small changes in lift and side force were amplified by the position of the wing tips relative to the moment-reference-center. To permit determination of lateral-directional trim settings (and the associated trim drag), lateral-directional characteristics for various asymmetric deflections of the wing tips are presented in figure 25.

Elevon deflection- Effects of roll-control deflections of the elevons (i.e., asymmetric deflection of the left- and right-hand elevon segments) are presented in figures 26 and 27. The data in figure 26 indicated the effects on longitudinal characteristics and the data in figure 27 provided information for lateral-directional trim. Although this correlation program was not oriented toward studying the lateral-directional control problems of the XB-70-1 configuration, it is interesting to note that the yawing-moment coefficient results in figure 27 provided an indication of the "adverse" yaw due to roll control of the elevons for the configuration. In particular, referring to figure 27(e), a nonlinear variation of yawing-moment coefficient at lift conditions with deflection of the left-hand elevon was apparent. In fact, the incremental effect on yawing-moment coefficient due to changing the left-hand elevon from +10° to +20° was just the opposite of the effect indicated for a change from 0° to +10°. Hence, for longitudinal-trim settings

of the elevons of 10° or greater, these rigid-model results indicated adverse yaw due to roll control.

Rudder deflection- Effects of deflection of the twin rudders are presented in figures 28 through 33. The purpose of these studies was to provide data on which to base estimates of the drag penalties associated with lateral-directional trim. A complete set of results for rudder deflections of 0°, -1°, and -3° is provided in figures 28 through 30. It should be noted that these data, including the results obtained in the 11-foot test section, are for configurations with the low-profile cover-plate fuselage. As explained previously, figures 31 through 33 may be considered repeat data for the 0° and -1° rudder deflections in the 9- by 7-foot test section.

Inlet Spillage Effects

For the flight tests during which the data for this correlation program were obtained, the inlets of the XB-70-1 airplane were operated as a fixed-geometry, mixed-compression system. Therefore, it was unnecessary during these wind-tunnel investigations to study the effects of ramp geometry. Rather, the inlet mass-flow ratio (A_o/A_c) of both the airplane and model were varied by back-pressuring the duct downstream of the inlet. For these studies, the back-pressuring of the model ducts was accomplished by various sizes of calibrated convergent flow nozzles located at the duct exits.

The A_o/A_c results for various Mach numbers and lift coefficients that corresponded closely with the selected speed-power-stabilized flight-test points (tables 1 and 3 of ref. 4) are summarized in figure 34. The variation of mass-flow ratio due to change in angle of attack for the various exit nozzles is provided in figure 35. It should be expected that small changes in nozzle contraction-ratio would produce small changes in spillage relative to the basic nozzles (N_2-component) used in this program. This was borne out by the variations in A_o/A_c shown in figures 34 and 35. The effects of these small changes in spillage on the longitudinal aerodynamic characteristics are shown in figure 36. Only the drag results showed any significant and consistent effects of A_o/A_c variations.

The results of base- and internal-drag coefficient measurements made with the various nozzle components are given in figure 37. The internal drag results were very consistent. This was not the case with the base-drag coefficients which showed considerable scatter-like variation, especially at the subsonic Mach numbers. The variations in base-drag coefficient indicated the difficulties in obtaining repeatable drag results at high subsonic Mach numbers.

Miscellaneous Effects

Presented in figure 39 are longitudinal characteristics at a Mach number of 2.53 for configurations with two different elevon deflections at two values of unit Reynolds number — 13.12×10^6/m (4×10^6/ft) and 6.56×10^6/m (2×10^6/ft). The variation in Reynolds number was accomplished by changing the wind-tunnel

dynamic pressure and temperature. However, the temperature changes in the 9- by 7-foot test section are secondary compared to the pressure changes. For these test conditions, no effects arising from bending of the elevon mounting brackets were apparent from the data. There was a consistent difference in the pitching-moment results for the two Reynolds numbers for each configuration. Whether this increment is a true effect of Reynolds number, an effect arising from model flexibility (although this model was very stiff), or a result from the calibration of the internal force-and-moment balance (such as inadequate definition of multiple-load interactions) is not known.

Data for a wing-tip deflection of 65° at Mach numbers of 1.4 and 1.2 are shown in figure 40. These results were determined at the request of the contractor for the work reported in reference 4.

Figure 41 presents data for a Mach number of 2.53 for a systematic "configuration buildup" from the basic or reference condiguration to a configuration with surface deflections corresponding to the "design point" flight-test conditions. These results indicated a trimmed lift coefficient of 0.083 for a moment-reference point (about 0.217 to 0.218$\bar{c}$) corresponding to the flight-test center-of-gravity location. The trimmed lift coefficient at the flight-test "design point" (tables 1 and 3 of ref. 4) was about 0.100. It is emphasized that a number of unaccounted-for items (such as bleed and bypass airflows and excressence effects) could affect the trim estimate determined from these test results with the indicated method.

CONCLUDING REMARKS

A 0.03-scale model of the XB-70-1 airplane was constructed to determine static-force and moment characteristics for a wind-tunnel-to-flight correlation. Extreme care was exercised during the design, fabrication, and testing of the model to assure that the wind-tunnel test results would provide a reliable base for the correlation. Examination of the test results indicated that the data are of very high quality and precision, and, therefore, should satisfy this objective. Additional analysis of these wind-tunnel test results, including interpretation and extrapolation to flight-test conditions, is provided in reference 8. A comparison of the wind-tunnel-based predictions with flight-test derived values of aerodynamic parameters is presented in reference 9.

Ames Research Center
National Aeronautics and Space Administration
Moffett Field, California, August 13, 1979

APPENDIX A

XB-70-1 FLIGHT-TEST CONDITIONS FOR DEFINING THE EXTERNAL SHAPE OF THE WIND-TUNNEL MODEL

The following values were specified by the Dryden Flight Research Center and constitute the model "design-point" conditions:

Mach number	2.53
Altitude, m (ft)	19,198 (62,980)
Mass, kg (lb)	168,421 (371,300)
Center-of-gravity location, percent $\bar{c}$	21.7
Mass distribution	Compatible with fuel loading for specified mass and center-of-gravity location
Wing-tip deflection (nominal), deg	65
Elevon deflection (nominal), deg	3.2
Canard deflection, deg	2.8
Normal load factor, g's	1.0
Nose-ramp (windshield) position	Raised
Bypass-door deflection (nominal), deg	1.8

APPENDIX B

MODEL NOMENCLATURE AND GEOMETRIC DATA

W_1, Wing

Fabricated to aeroelastic shape estimated for "design-point" flight-test conditions.

Area (ref.), includes 2076.6 cm^2 (321.71 $in.^2$) covered by fuselage but not 28.1 cm^2 (4.35 $in.^2$) of the wing-ramp area, cm^2 ($in.^2$)	5265.8 (816.19)
Span (ref., clipped tips), cm (in.)	96.01 (37.80)
Aspect ratio	1.751
Taper ratio	0.019
Chords	
Root (wing station 0), cm (in.)	107.68 (42.39)
Tip (wing station 48.01 cm (18.90 in.)), cm (in.)	2.00 (0.78)
Mean aerodynamic chord (ref.), cm (in.)	71.81 (28.27)
Sweepback angle, deg:	
Leading edge	65.57
Trailing edge	0
Folding wing tip (data for one tip only):	
Area, cm^2 ($in.^2$)	435.5 (67.51)
Nominal downward deflections, deg	0,25,65
Airfoil section	Modified 0.30-0.70 hexagon
Thickness ratio	
Root-to-wing-station 14.17 cm (5.58 in.)	0.0195
Wing station 35.05 cm (13.80 in.) to tip	0.025

E_1, Elevon (data for one side only)

Elevon consists of six separate segments located on the wing trailing edge extending from 34.1 to 73.0% b/2 (including air gaps). All segments have a constant chord length of 8.84 cm (3.48 in.).

	Segment 1	Segment 2	Segment 3	Segment 4	Segment 5	Segment 6
Area (nominal, including air gap), cm^2 ($in.^2$)	27.9 (4.33)	27.9 (4.33)	27.9 (4.33)	26.0 (4.03)	32.7 (5.07)	20.4 (3.16)
Span (measured at hinge line), cm (in.)	3.16 (1.24)	3.16 (1.24)	3.16 (1.24)	2.94 (1.16)	3.70 (1.46)	2.31 (0.91)
Location at inboard hinge end, % b/2	34.2	40.8	47.5	54.1	60.4	68.2

E_2, Elevon

Same as E_1 except elevon segments outboard of tip-fold hinge (segments 5 and 6) are set to zero deflection.

E_3, Elevon

Same as E_2 except air gaps between segments 1, 2, 3, and 4, and between segments 5 and 6 are filled and taped to represent the elevon configuration used during B-70 development wind-tunnel tests.

E_4, Elevon

Same as E_1 except each elevon segment is set to "design-point" deflection (specified by Dryden Flight Research Center), as follows:

	Segment 1	Segment 2	Segment 3	Segment 4	Segment 5	Segment 6
Left-hand wing	3.5°	4.2°	4.9°	4.2°	1.3°	2.2°
Right-hand wing	0.9°	2.0°	2.2°	2.6°	1.5°	1.0°

E_5, Elevon

Same as E_1 except elevon segments outboard of tip-fold hinge (segments 5 and 6) are set to "design-point" deflections. (Configuration used only to assess effects of bypass-door deflections in transonic test section.)

B_1, Body

Fabricated to aeroelastic shape estimated for "design-point" flight-test conditions. Includes forebody, propulsion system nacelle (including inlets and internal ducting forward of duct flow nozzles) and basic (low profile) upper cover plate at model base. Does not include canopy, duct flow nozzles, bleed dump under nacelle, or deflected bypass doors.

Forebody:

Length, cm (in.)	161.47	(63.57)
Maximum width, cm (in.)	7.59	(2.99)
Maximum depth, cm (in.)	7.62	(3.00)
Maximum cross-sectional area, cm^2 ($in.^2$)	44.97	(6.97)
Fineness ratio (equivalent)		21.43

Propulsion system nacelle:

Length, cm (in.)	95.87	(37.74)
Maximum width, cm (in.)	27.48	(10.82)
Maximum depth, cm (in.)	6.90	(2.72)
Maximum cross-sectional area, cm^2 ($in.^2$)	180.52	(27.98)
Fineness ratio (equivalent)		6.32

Inlets and internal ducting:

Consist of twin, two-dimensional, vertical-ramp, mixed compression and fixed-geometry inlets. The vertical ramp consists of three external

ramps having fixed ramp angles of 7°, 12°, and 16°, respectively. Internal ramp angle is 5.5°. The duct downstream of the cowl lip has a divergence angle of 1.5°. Each duct has an inlet area of 18.46 cm^2 (2.86 $in.^2$) and a capture-area at zero angles of attack and sideslip of 32.52 cm^2 (5.04 $in.^2$). In each duct, a 79% porosity flow screen is installed in the maximum flow area (29.55 cm^2 (4.58 $in.^2$)) portion of the duct at a point 24.07 cm (9.48 in.) upstream of the duct flow nozzle.

B_2, Body

Same as B_1 except fuselage upper cover plate raised 0.18 cm (0.07 in.) over a width of 8.1 cm (3.2 in.) at model base to provide sting clearance at high-load test conditions. Modification to cover plate extends upstream of model base approximately 3 cm (1.25 in.).

K_1, Canopy

High-speed canopy, simulating windshield raised configuration; basic lines included in B_1 forebody.

K_2, Canopy

Low-speed canopy, simulating windshield lowered configuration.

N_1, Duct flow nozzles

Consist of one convergent flow nozzle per duct located so that nozzle throat is at model base. In each duct, the maximum flow area (29.55 cm^2 (4.58 $in.^2$)) portion of the duct forms the upstream area (A_1) for the flow nozzle. The nozzle throat area (A_2) is the duct-exit area; A_{exit} = 21.23 cm^2 (3.29 $in.^2$).

N_2, Duct flow nozzles

Same as N_1 except A_{exit} = 20.30 cm^2 (3.15 $in.^2$)

N_3, Duct flow nozzles

Same as N_1 except A_{exit} = 19.38 cm^2 (3.00 $in.^2$)

N_4, Duct flow nozzles

Same as N_1 except A_{exit} = 18.46 cm^2 (2.86 $in.^2$)

N_5, Duct flow nozzles

Same as N_1 except A_{exit} = 17.54 cm^2 (2.72 $in.^2$)

N_6, Duct flow nozzles

Same as N_1 except A_{exit} = 16.61 cm^2 (2.58 $in.^2$)

N_7, Duct flow nozzles

Same as N_1 except A_{exit} = 15.69 cm^2 (2.43 $in.^2$).

C_1, Canard

Fabricated to aeroelastic shape estimated for "design-point" flight-test conditions.

Area, includes 127.74 cm^2 (19.80 $in.^2$) covered by fuselage, cm^2 ($in.^2$)	347.43 (53.85)
Span, cm (in.)	26.34 (10.37)
Aspect ratio	1.997
Taper ratio	0.388
Chords:	
Root (canard station 0), cm (in.)	19.01 (7.49)
Tip (canard station 13.17 cm (5.19 in.), cm (in.)	7.37 (2.90)
Mean aerodynamic chord, cm (in.)	14.04 (5.53)
Sweepback angle of leading edge, deg	31.7
Airfoil section	Modified 0.34-0.66 hexagon
Thickness ratio	0.025

V_1, Vertical tails (twin) (data for one panel only)

Area (outboard of intersection of tail leading edge with fuselage upper surface), cm^2 ($in.^2$)	188.13 (29.16)
Span, cm (in.)	13.72 (5.40)
Aspect ratio	1.000
Taper ratio	0.300
Chords:	
Root (tail station 0), cm (in.)	21.10 (8.31)
Tip (tail station 13.72 cm (5.40 in.)), cm (in.)	6.33 (2.49)
Mean aerodynamic chord, cm (in.)	15.04 (5.92)
Sweepback angle of leading edge, deg	51.77
Airfoil section	Modified 0.30-0.70 hexagon
Thickness ratio	
Root	0.0375
Tip	0.025
Rudder (vertical tail movable portion)	
Area, cm^2 ($in.^2$)	53.03 (23.72)
Sweepback angle of hinge line, deg	-44.9

S_1, Shaker vane (nonmovable, data for one side only)

Area, exposed, cm^2 ($in.^2$)	1.76	(0.27)
Span, exposed, cm (in.)	1.85	(0.73)
Aspect ratio		1.995
Taper ratio		0.490
Chords:		
Root (at fuselage surface, shaker vane station 0), cm (in.)	1.24	(0.49)
Tip (shaker vane station 1.91 cm (0.75 in.)), cm (in.)	0.61	(0.24)
Mean aerodynamic chord, cm (in.)	0.96	(0.38)
Sweepback angle of leading edge, deg		6.7
Airfoil section — slab-sided hexagon; 21° (total) leading-edge angle and 11° (total) trailing-edge angle		
Thickness ratio		
Root		0.078
Tip		0.104

D_1, Bleed-dump fairing

Simulates "sugar-scoop" fairing, no airflow out the base.

Length (total) aft of inlet ramp leading edge, cm (in.)	23.29	(9.17)
Base		
Area, cm^2 ($in.^2$)	7.28	(1.13)
Depth, cm (in.)	1.30	(0.51)
Width, cm (in.)	5.75	(2.26)

b_1, Bypass-door configuration

Consists of two trimmer doors, two inboard bypass doors, and two outboard bypass doors, each set arranged in tandem on each side of the wing upper surface (over the nacelle). No airflow out of the doors. Hinge line of forward and aft doors is 141.92 cm (55.88 in.) and 143.39 cm (56.45 in.) aft of the fuselage nose, respectively. Chord of each door is 1.01 cm (0.47 in.) with inboard hinge point at body plane 2.84 (1.12 in.); span of each inboard bypass door in 3.18 cm (1.25 in.) with inboard hinge point at body plane 5.05 cm (1.99 in.); span of each outboard bypass door is 4.14 cm (1.63 in.) with inboard hinge point at body plane 9.37 cm (3.69 in.).

Deflection angle, deg	4.0

b_2, Bypass-door configuration

Same as b_1 except:

Deflection angle, deg	8.0

b_3, Bypass door configuration

Same as b_1 except each door is set to "design point" deflection (specified by Dryden Flight Research Center), as follows:

	Left-hand outer bypass door	Left-hand inner bypass door	Left-hand trimmer door	Right-hand trimmer door	Right-hand inner bypass door	Right-hand outer bypass door
Forward doors	1.9°	1.9°	1.7°	2.5°	2.0°	1.1°
Rear doors	1.2°	1.9°	2.0°	2.5°	1.6°	1.1°

G_1, Roughness-type boundary-layer-transition trip

Strip of roughness particles 3-mm (1/8-in.) wide, located 6 mm (1/4 in.) aft of sharp leading edges; 6-mm (1/4-in.) wide strip of roughness particles located 2-1/2 cm (1 in.) aft of nose apex. No roughness particles on inlet wedge or underside of wing apex. Nominal particle density is 20-30 particles per 2-1/2 cm (1 in.) of 3-mm (1/8-in.) wide strip. Roughness particles are sieved glass beads with k = 0.39-mm (0.0152-in.) screened-particle diameter.

G_2, Roughness-type boundary-layer-transition trip

Same as G_1 except k = 0.33 mm (0.0128 in.).

G_3, Roughness-type boundary-layer-transition trip

Same as G_1 except k = 0.27 mm (0.0108 in.).

G_4, Roughness-type boundary-layer-transition trip

Same as G_1 except k = 0.23 mm (0.0090 in.).

G_5, Roughness-type boundary-layer-transition trip

Same as G_1 except k = 0.19 mm (0.0076 in.).

G_6, Roughness-type boundary-layer-transition trip

Same as G_1 except k = 0.10 mm (0.0038 in.).

G_7, Roughness-type boundary-layer-transition trip

Same as G_1 except strip of roughness particles is located 2-1/2 cm (1 in.) aft of sharp leading edges and roughness particles are randomly sprinkled in the strip with greater density; k = 0.23 mm (0.0090 in.).

G_8, Roughness-type boundary-layer-transition trip

Same as G_7 except k = 0.19 mm (0.0076 in.).

G_9, Roughness-type boundary-layer-transition trip

Same as G_7 except $k = 0.14$ mm (0.0054 in.).

G_{10}, Roughness-type boundary-layer-transition trip

Same as G_7 except $k = 0.10$ mm (0.0038 in.).

G_{11}, Roughness-type boundary-layer-transition trip

Same as G_7 except $k = 0.07$ mm (0.0027 in.).

APPENDIX C

INTERNAL FLOW RELATIONS

U.S. customary units are used to develop these internal flow relations and were the basis for measuring quantities during these tests.

Part 1 — Internal Drag Coefficient

Consider a duct operating as shown in sketch (a) below where the indicated stations refer to

o free stream
i duct inlet
e duct exit

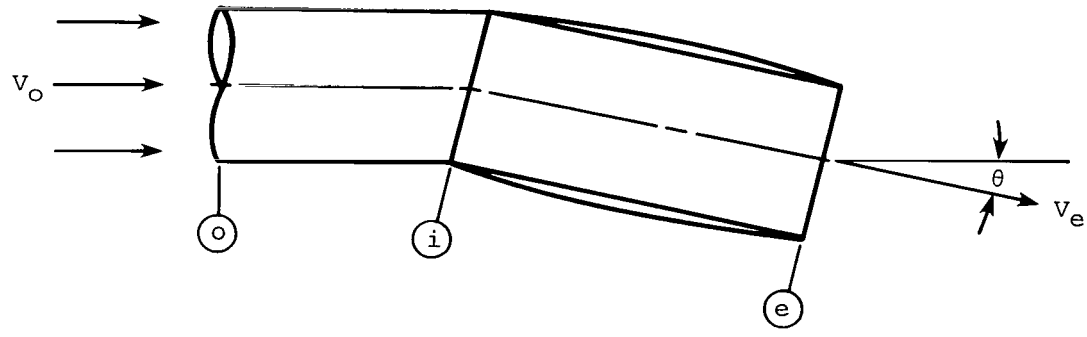

Sketch (a)

The "internal drag" is defined to be the losses — in the free-stream direction — in momentum and pressure forces (referred to free-stream pressure p_o) for the air flowing through the duct. Then, the equation describing the equilibrium of these forces is

$$\frac{w}{g} V_o + (p_o - p_o)A_o = \frac{w}{g} V_e \cos \theta + (p_e - p_o)A_e \cos \theta + D_{INT}$$

where

w gravimetric rate of airflow
g acceleration due to gravity
V velocity
p static pressure
A flow area
θ angular inclination of the duct relative to free stream
D_{INT} internal drag force

and the subscripts refer to the indicated stations. (Note: This development of "internal drag coefficient" from free stream, station o, and the duct exit, station e, includes the losses from free stream, station o, to duct inlet, station i, in the internal drag.)

Then,

$$D_{INT} = \frac{w}{g} V_o - \frac{w}{g} V_e \cos \theta - (p_e - p_o) A_e \cos \theta$$

Dividing by $q_o S$ and defining internal drag coefficient,

$$C_{D_{INT}} = \frac{wV_o}{gq_o S} - \frac{wV_e}{gq_o S} \cos \theta - \frac{(p_e - p_o) A_e}{q_o S} \cos \theta$$

where

q_o free-stream dynamic pressure
S reference area for aerodynamic coefficients

Additional relations are:

$$w = \rho_o V_o A_o = \rho_e V_e A_e$$

$$\rho_o = \frac{p_o}{RT_o}, \qquad \rho_e = \frac{p_e}{RT_e}$$

$$V_o = M_o \sqrt{g\gamma RT_o}, \qquad V_e = M_e \sqrt{g\gamma RT_e}$$

$$q_o = \frac{\gamma}{2} p_o M_o^2 \quad \text{or,} \quad p_o = \frac{2q_o}{\gamma M_o^2}$$

where

ρ density
R gas constant
T absolute temperature
γ ratio of specific heats
M Mach number

Substituting and algebraically manipulating,

$$C_{D_{int}} = \frac{\rho_o V_o^2 A_o}{q q_o S} - \left(\frac{\rho_e V_e^2 A_e}{q q_o S} + \frac{p_e A_e}{q_o S} - \frac{p_o A_e}{q_o S} \right) \cos \theta$$

$$= \frac{p_o M_o^2 g \gamma R T_o A_o}{R T_o g \frac{\gamma}{2} p_o M_o^2 S} - \left(\frac{p_e M_e^2 g \gamma R T_e A_e}{R T_e g \frac{\gamma}{2} p_o M_o^2 S} + \frac{p_e A_e}{\frac{\gamma}{2} p_o M_o^2 S} - \frac{p_o A_e}{\frac{\gamma}{2} p_o M_o^2 S} \right) \cos \theta$$

$$= 2 \frac{A_o}{S} - \left[\left(\frac{2}{\gamma} \frac{p_e}{p_o} \frac{\gamma M_e^2}{M_o^2} \frac{A_e}{S} \right) + \left(\frac{2}{\gamma} \frac{1}{M_o^2} \frac{p_e}{p_o} \frac{A_e}{S} \right) - \left(\frac{2}{\gamma} \frac{1}{M_o^2} \frac{A_e}{S} \right) \right] \cos \theta$$

but

$$\frac{A_o}{S} = \frac{A_o}{A_c} \frac{A_c}{S}$$

where A_c is the arbitrarily defined "capture area" of the duct. An expression for A_o/A_c is developed in the next subsection. Then,

$$C_{D_{INT}} = 2 \left(\frac{A_o}{A_c} \frac{A_c}{S} \right) + \frac{2}{\gamma} \frac{A_e}{S} \frac{1}{M_o^2} \left[1 - \left(\frac{p_e}{p_o} \right) (1 + \gamma M_e^2) \right] \cos \theta$$

Part 2 — Duct Mass-Flow Ratio

Consider a duct with an exit nozzle as shown in sketch (b).

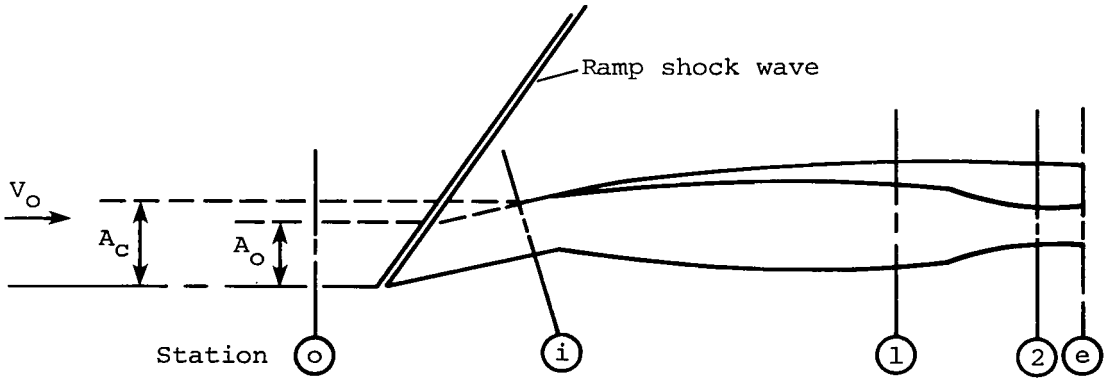

Sketch (b)

where the indicated stations are:

o free stream; i.e., a station free of disturbances generated by any part of the model, including those portions of the model (fuselage, canard, etc.) that extend forward of the inlet ramp

i duct inlet

1 duct maximum cross section

2 station at which nozzle-throat static pressure is measured

e duct exit (note: $A_2 = A_e$)

Then, by definition, the airflows through A_o and A_c are

$$w_o = \rho_o V_o A_o \quad \text{and} \quad w_c = \rho_o V_o A_c$$

But

$$w_o = w_i = w_1 = w_2 = w_e$$

So

$$\frac{w_i}{w_c} = \frac{w_o}{w_c} = \frac{\rho_o V_o A_o}{\rho_o V_o A_c}$$

where A_o/A_c is the capture-area ratio and is customarily referred to as the mass-flow ratio.

To compute airflow through the duct, the following equation is used:

$$w_h = 359CFd^2F_aY_a\sqrt{h_w\rho_1} \qquad \text{(ref. 10, p. 57, eq. 5)}$$

where

w_h weight rate of airflow, lb/hr

C coefficient of discharge, $\frac{\text{actual weight rate of flow}}{\text{theoretical weight rate of flow}}$

It is important to note the dependence of C on duct Reynolds number (ref. 10, pp. 11-17); but, for any specific operating condition, C is a specific value.

$$F = (1 - \beta^4)^{-1/2}$$

where

$$\beta = \frac{\bar{D}_2}{\bar{D}_1}$$

$\bar{D}_1$ and $\bar{D}_2$ are effective diameters at duct stations (1) and (2). And, by definitions (in ref. 10),

$$d = \bar{D}_2$$

and

$$F_a = 1.00 \quad \text{(ref. 10, p. 67, fig. 38).}$$

$$Y_A = \frac{\gamma}{\gamma - 1}\left(\frac{p_2}{p_1}\right)^{2/\gamma}\left[\frac{1 - (p_2/p_1)^{(\gamma-1)/\gamma}}{1 - (p_2/p_1)}\right]\left[\frac{1 - (\bar{D}_2/\bar{D}_1)^4}{1 - (\bar{D}_2/\bar{D}_1)^4 (P_2/P_1)^{2/\gamma}}\right]^{1/2}$$

(ref. 10, p. 74, fig. 43(a)).

So that, for any particular nozzle (i.e., a specific $\bar{D}_2/\bar{D}_1$), Y_a is a function of p_2/p_1, and

$$h_w = p_1 - p_2$$

measured in inches of water at 68° F, and

$$\rho_1 = \text{specific weight (lb/ft}^3\text{) at station (1)}$$

For any particular nozzle, define $K = CF$ and $\bar{D}_2 = (4/\pi)A_2$ where A_2 = nozzle-throat area in square feet.

Equation of state:

$$\rho_1 = \frac{p_1}{RT_1} \quad \text{(thermally perfect gas)}$$

And, $h_w = 0.19257\ (p_1 - p_2)$ where

p_1 = pressure at station (1), psf

p_2 = pressure at station (2), psf

T_1 = static temperature at station (1), °R

Assuming isentropic flow between stations 1 and 2

$$p_1 = p_{t_1}\left(1 + \frac{\gamma - 1}{2} M_1^2\right)^{-\gamma/(\gamma-1)}$$

$$T_1 = T_{t_1}\left(1 + \frac{\gamma - 1}{2} M_1^2\right)^{-1}$$

Since $p_{t_1} = p_{t_2}$, then

$$\frac{p_2}{p_{t_1}} = \left(1 - \frac{\gamma - 1}{2} M_1^2\right)^{-\gamma/(\gamma-1)}$$

So that the equation for airflow through the duct can be rewritten

$$w_s = (5.294\times10^{-5}) K Y_A A_2 \frac{p_{t_1}}{\sqrt{T_{t_1}}} \left(1 + \frac{\gamma - 1}{2} M_1^2\right)^{-(\gamma+1)/2(\gamma-1)}$$

$$\cdot \left[1 - \left(\frac{1 + \frac{\gamma - 1}{2} M_1^2}{1 + \frac{\gamma - 1}{2} M_2^2}\right)^{\gamma/(\gamma-1)}\right]^{1/2}$$

where w_s is gravimetric rate of flow, lb/sec. (Note: W_s and W_h are equivalent expressions for duct airflow.)

In a similar manner, the airflow through the capture area A_c at free-stream conditions can be determined. The result is

$$w_c = \left(\sqrt{\frac{g\gamma}{R}} A_c\right) \frac{p_{t_o} M_o}{\sqrt{T_{t_o}}} \left(1 + \frac{\gamma - 1}{2} M_o^2\right)^{-(\gamma+1)/2(\gamma-1)}$$

In addition to the assumption of isentropic flow between stations (1) and (2), assume adiabatic flow from station (0) to station (e). Since $w_s = w_o$,

$$\frac{w_o}{w_c} = \frac{A_o}{A_c} = (5.7652\times10^{-5}) K Y_A \frac{A_2}{A_c} \frac{p_{t_1}}{p_{t_o}} \frac{1}{M_o} \left[1 - \left(\frac{1 + \frac{\gamma - 1}{2} M_1^2}{1 + \frac{\gamma - 1}{2} M_2^2}\right)^{\gamma/(\gamma-1)}\right]^{1/2}$$

$$\cdot \left(\frac{1 + \frac{\gamma - 1}{2} M_o^2}{1 + \frac{\gamma - 1}{2} M_2^2}\right)^{(\gamma+1)/2(\gamma-1)}$$

For any specific nozzle, let

$$K_1 = (5.7652\times10^{-5}) K Y_A \frac{A_2}{A_c}$$

$$= (5.7652\times10^{-5}) K Y_A \frac{A_e}{A_c},$$

because $A_e = A_2$. Then by substitution

$$\frac{A_o}{A_c} = K_1 \left(\frac{p_{t_1}}{p_{t_o}} \frac{1}{M_o} \right) \left[1 - \left(\frac{1 + \frac{\gamma - 1}{2} M_1^2}{1 + \frac{\gamma - 1}{2} M_2^2} \right)^{\gamma/(\gamma-1)} \right]^{1/2} \left(\frac{1 + \frac{\gamma - 1}{2} M_o^2}{1 + \frac{\gamma - 1}{2} M_1^2} \right)^{(\gamma+1)/2(\gamma-1)}$$

This expression serves as the basis for determining duct mass-flow ratio. Since

$$KY_A A_2 = \frac{K_1 A_c}{(5.7652 \times 10^{-5})}$$

then, substituting this expression into the equation for ω_s gives

$$w_s = \frac{K_1 A_c}{1.0883} \frac{p_{t_1}}{\sqrt{T_{t_1}}} \left(1 + \frac{\gamma - 1}{2} M_1^2 \right)^{-(\gamma+1)/2(\gamma-1)} \left[1 - \left(\frac{1 + \frac{\gamma - 1}{2} M_1^2}{1 + \frac{\gamma - 1}{2} M_2^2} \right)^{\gamma/(\gamma-1)} \right]^{1/2}$$

Solving for K_1 gives

$$K_1 = \frac{1.0883}{A_c} \frac{\sqrt{T_{t_1}}}{p_{t_1}} \left(1 + \frac{\gamma - 1}{2} M_1^2 \right)^{(\gamma+1)/2(\gamma-1)} \left[1 - \left(\frac{1 + \frac{\gamma - 1}{2} M_1^2}{1 + \frac{\gamma - 1}{2} M_2^2} \right)^{\gamma/(\gamma-1)} \right]^{-1/2} w_s$$

This expression provides a means for determining the nozzle calibration factor K_1 by measuring the airflow w_s with a standard metering device. It is emphasized that the computation of duct mass-flow ratio and the subsequent determination of the nozzle-calibration factor has assumed isentropic flow from station 1 to e and adiabatic flow through the duct.

Mach number M_2 is determined from the measured values of p_2 and p_{t_1}; then, M_1 is determined from the Law of Continuity. However, to calculate the internal drag, the duct-exit Mach number M_e is determined from the measured value of p_{t_1} and the total-head calibration constant; that is,

$$p_{t_e} = K_2 p_{t_1}$$

and the measured value of p_2 with the assumption that $p_e = p_2$.

REFERENCES

1. Mechtly, E. A.: The International Systems of Units, Physical Constants and Conversion Factors (Revised). NASA SP-7012, 1973.

2. Arnaiz, Henry H.; and Schweikhard, William G.: Validation of the Gas Generator Method of Calculating Jet-Engine Thrust and Evaluation of XB-70-1 Airplane Engine Performance at Ground Static Conditions. NASA TN-D-7028, 1970.

3. Edwards, E. L.: An Airborne Data Acquisition System for Use in Flight Testing the XB-70 Airplane. Selected Instrumentation Application Papers from AGARD Flight Mechanics Panel, Twenty-Sixth Meeting, AGARD Rep. 507, Paris, June 9-10, 1965, pp. 23-48.

4. Wykes, John H.; and Lawrence, Robert E.: Estimated Performance and Stability and Control Data for Correlation with XB-70-1 Flight Test Data. NASA CR-114335, 1971.

5. Fisher, David F.; and Saltzman, Edwin J.: Local Skin-Friction Coefficients and Boundary Layer Profiles Obtained in Flight From the XB-70-1 Airplane at Mach Numbers up to 2.5. NASA TN D-7220, 1973.

6. Braslow, Albert L.; Hicks, Raymond M.; and Harris, Roy V., Jr.: Use of Grit-Type Boundary-Layer Transition Trips on Wind-Tunnel Models. NASA TN D-3579, 1966.

7. Wolowicz, Chester H.; Strutz, Larry W.; Gilyard, Glenn B.; and Matheny, Neil W.: Preliminary Flight Evaluation of the Stability and Control Derivatives and Dynamic Characteristics of the Unaugmented XB-70-1 Airplane Including Comparisons with Predictions. NASA TN D-4578, 1968.

8. Peterson, John B., Jr.; Mann, Michael J.; Sorrels, Russel B., III; Sawyer, Wallace C.; and Fuller, Dennis E.: Wind-Tunnel/Flight Correlation Study of Aerodynamic Characteristics of a Large Flexible Supersonic Cruise Airplane (XB-70-1), II - Extrapolation of Wind-Tunnel Data to Full-Scale Conditions. NASA TP-1515, 1979.

9. Arnaiz, Henry H.; Peterson, John B., Jr.; and Daugherty, James C.: Wind-Tunnel/Flight Correlation Study of Aerodynamic Characteristics of a Large Flexible Supersonic Cruise Airplane (XB-70-1), II - A Comparison Between Characteristics Predicted from Wind-Tunnel Measurements and Those Measured in Flight. NASA TP-1516, 1979.

10. Flow Measurement. Instruments and Apparatus Supplement to ASME Power Test Codes, pt. 5, ch. 4, second ed., 1959.

Note:
1. Positive values of force and moment coefficients and angles are indicated.
2. Origin of stability axes has been displaced from the moment reference for clarity.

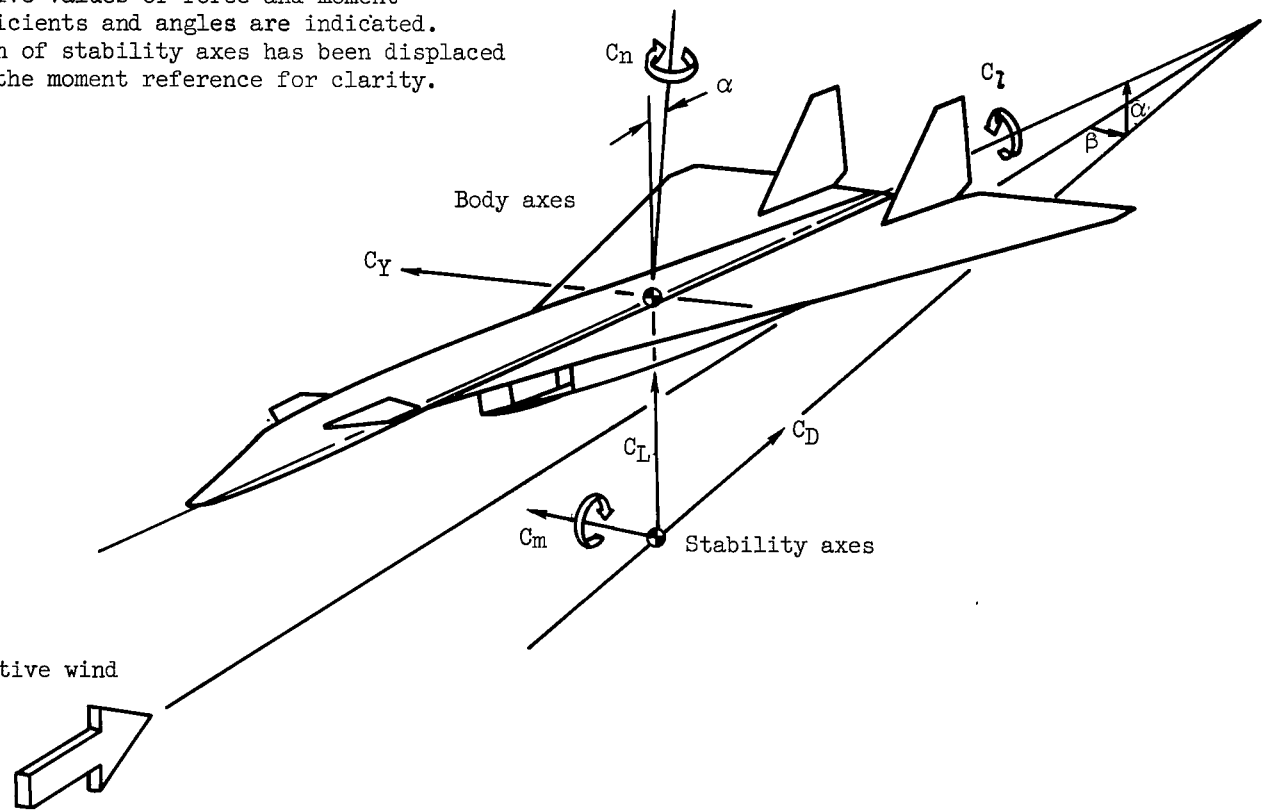

Figure 1.- Orientation of force and moment coefficients about body and stability axes.

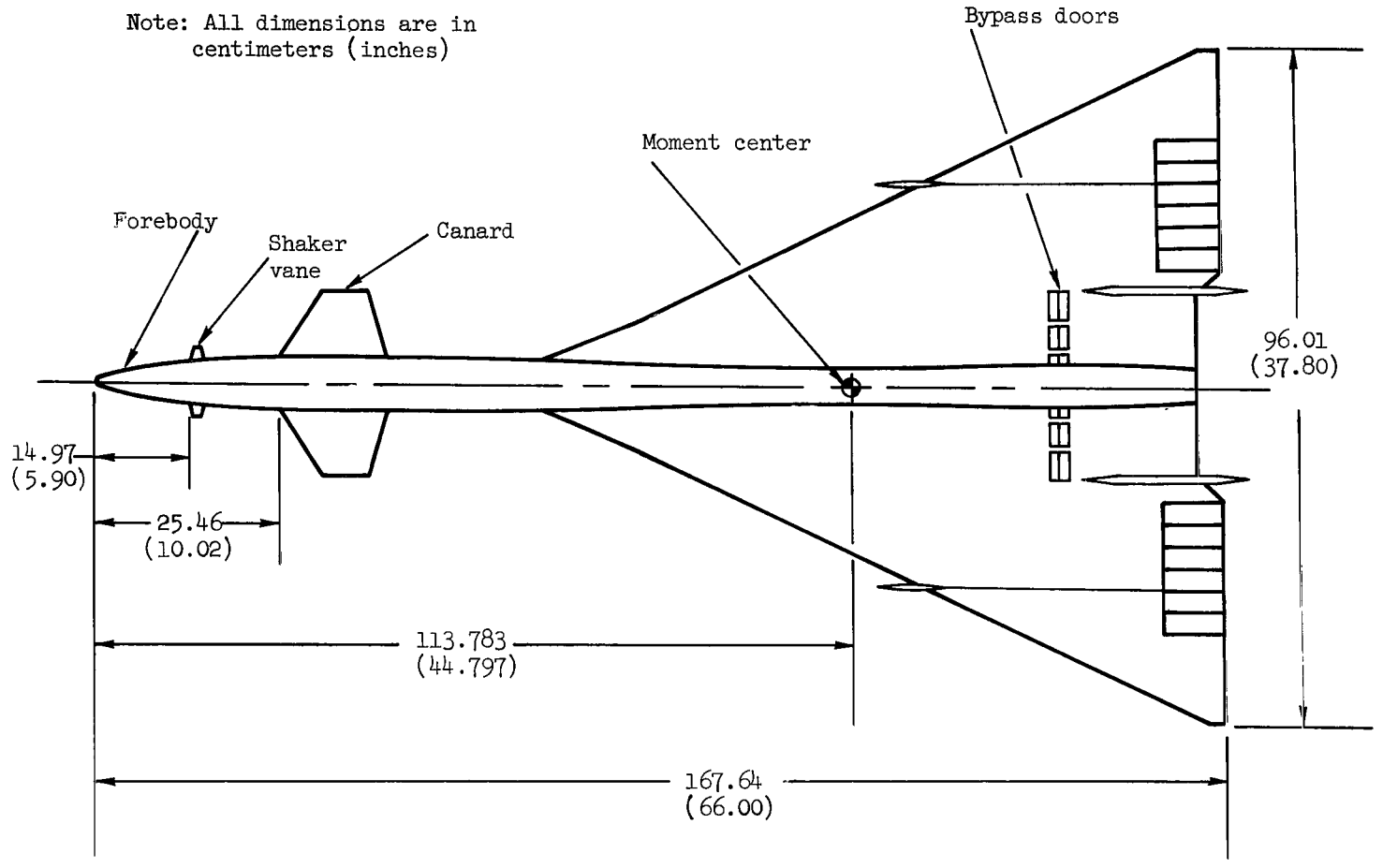

(a) Top view.

Figure 2.- Model drawing.

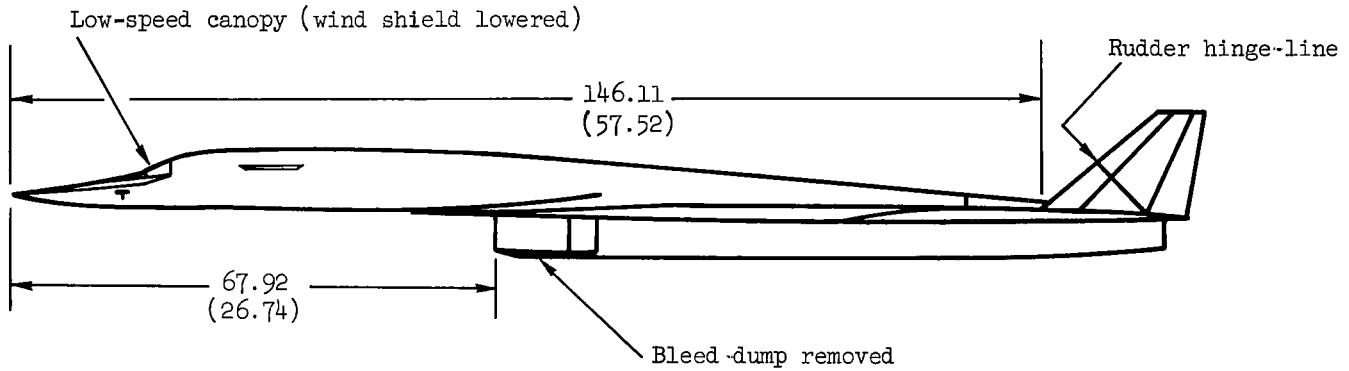

Note: All dimensions are in centimeters (inches)

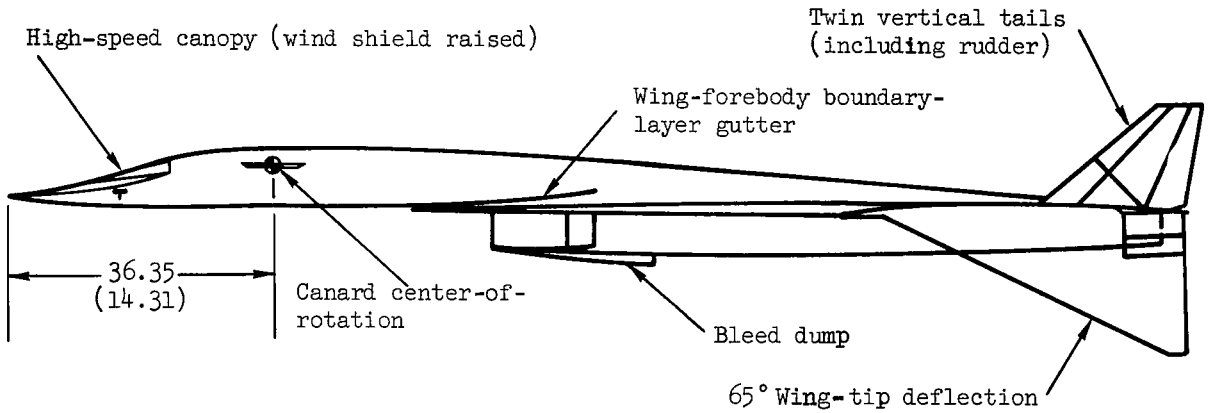

(b) Side views.

Figure 2.- Continued.

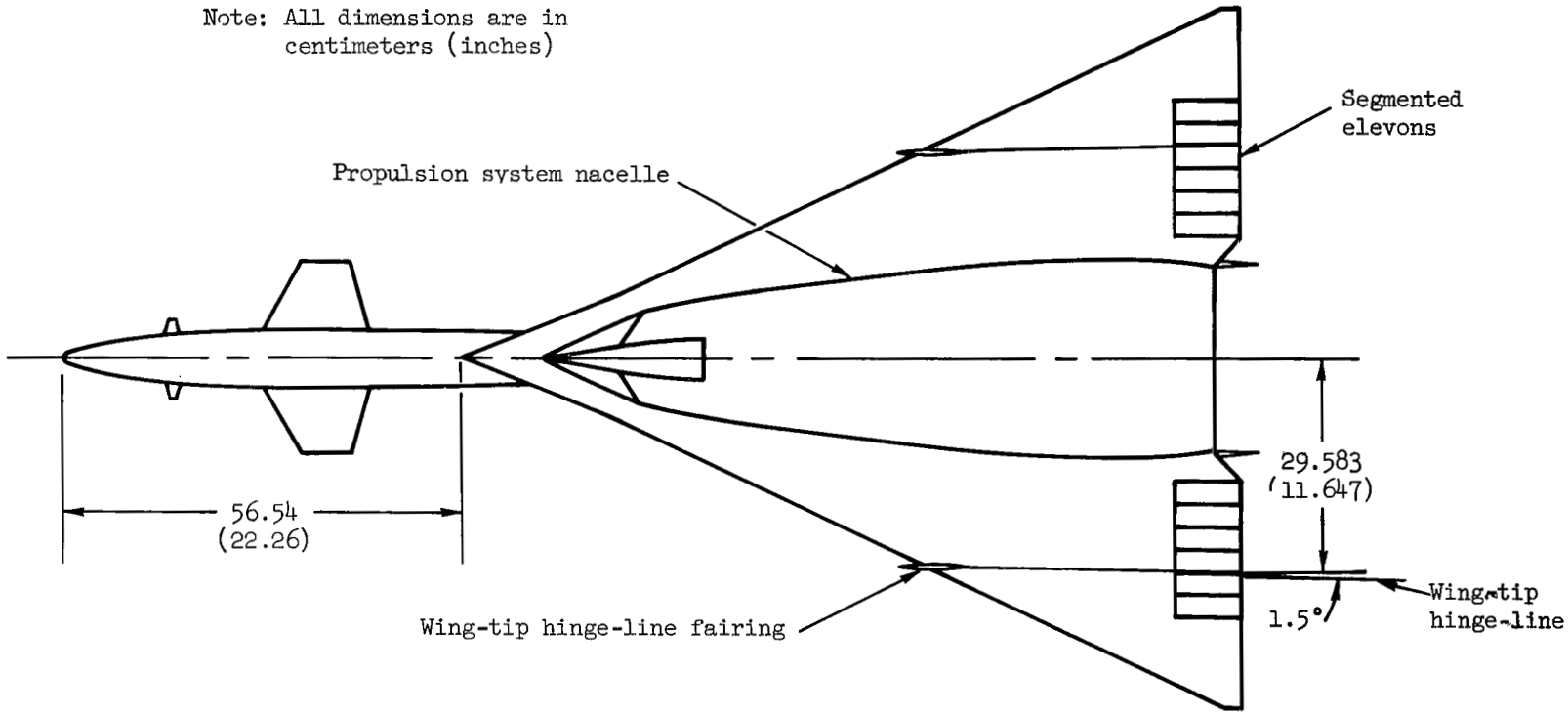

(c) Bottom view.

Figure 2.- Continued.

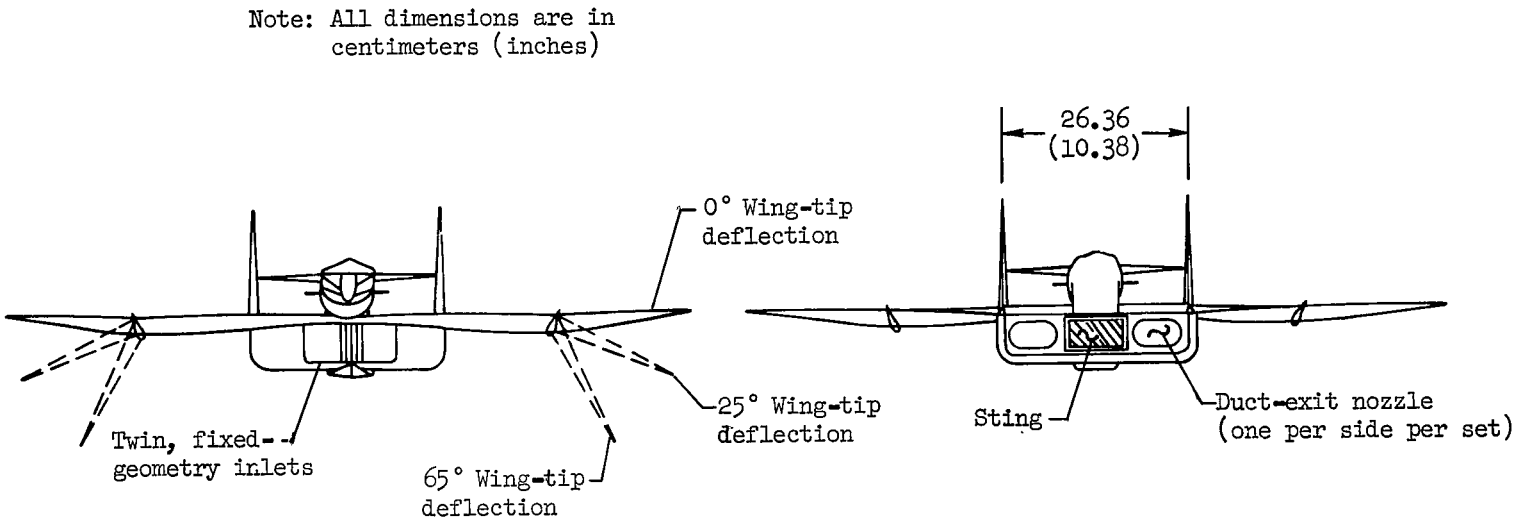

(d) Front view.

(e) Rear view.

Figure 2.- Continued.

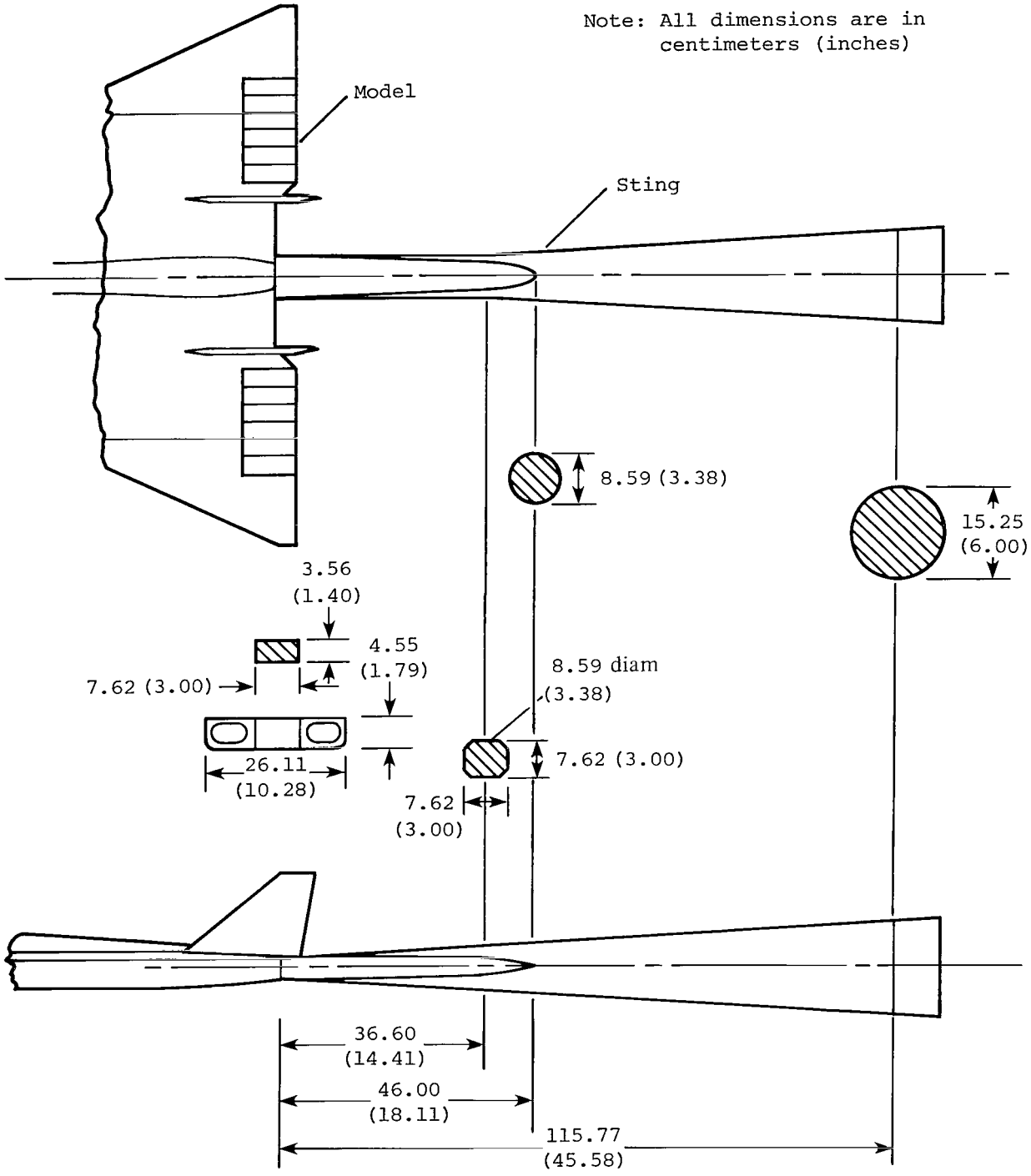

(f) Model base/sting geometry.

Figure 2.- Concluded.

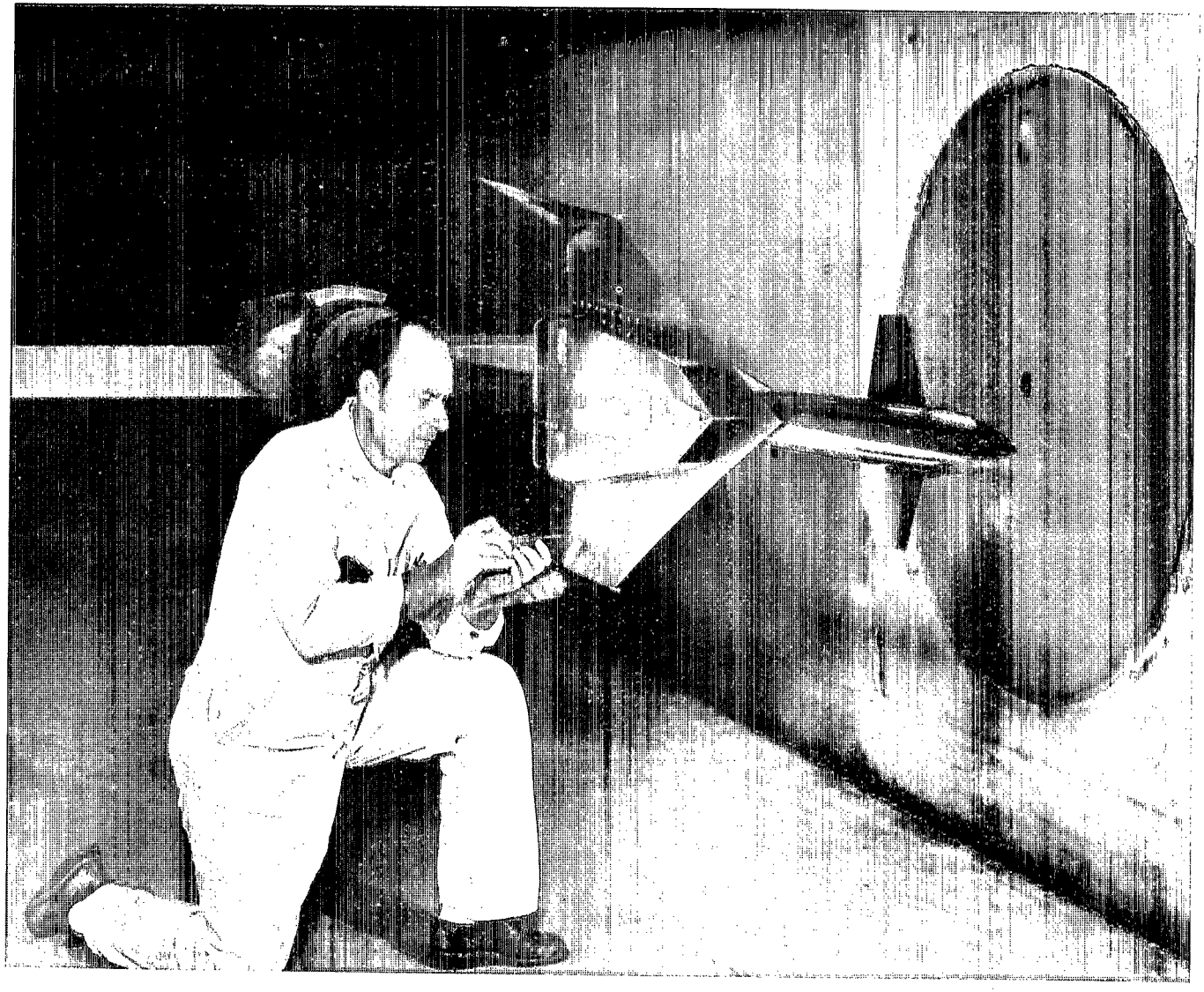

(a) Installation of model in 9- by 7-foot test section.

Figure 3.- XB-70-1 model.

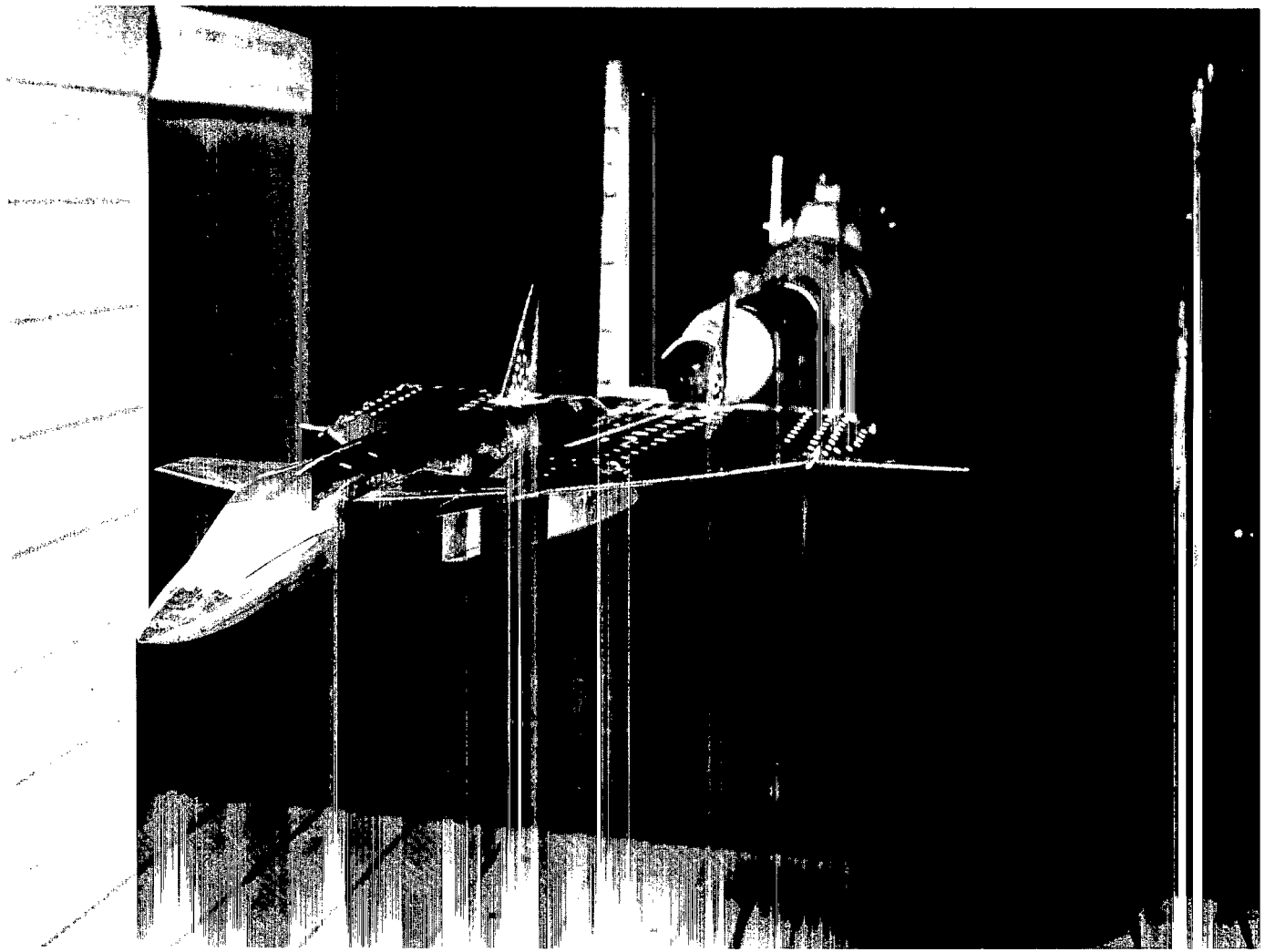

(b) Installation of model in 11- by 11-foot test section.

Figure 3.- Continued.

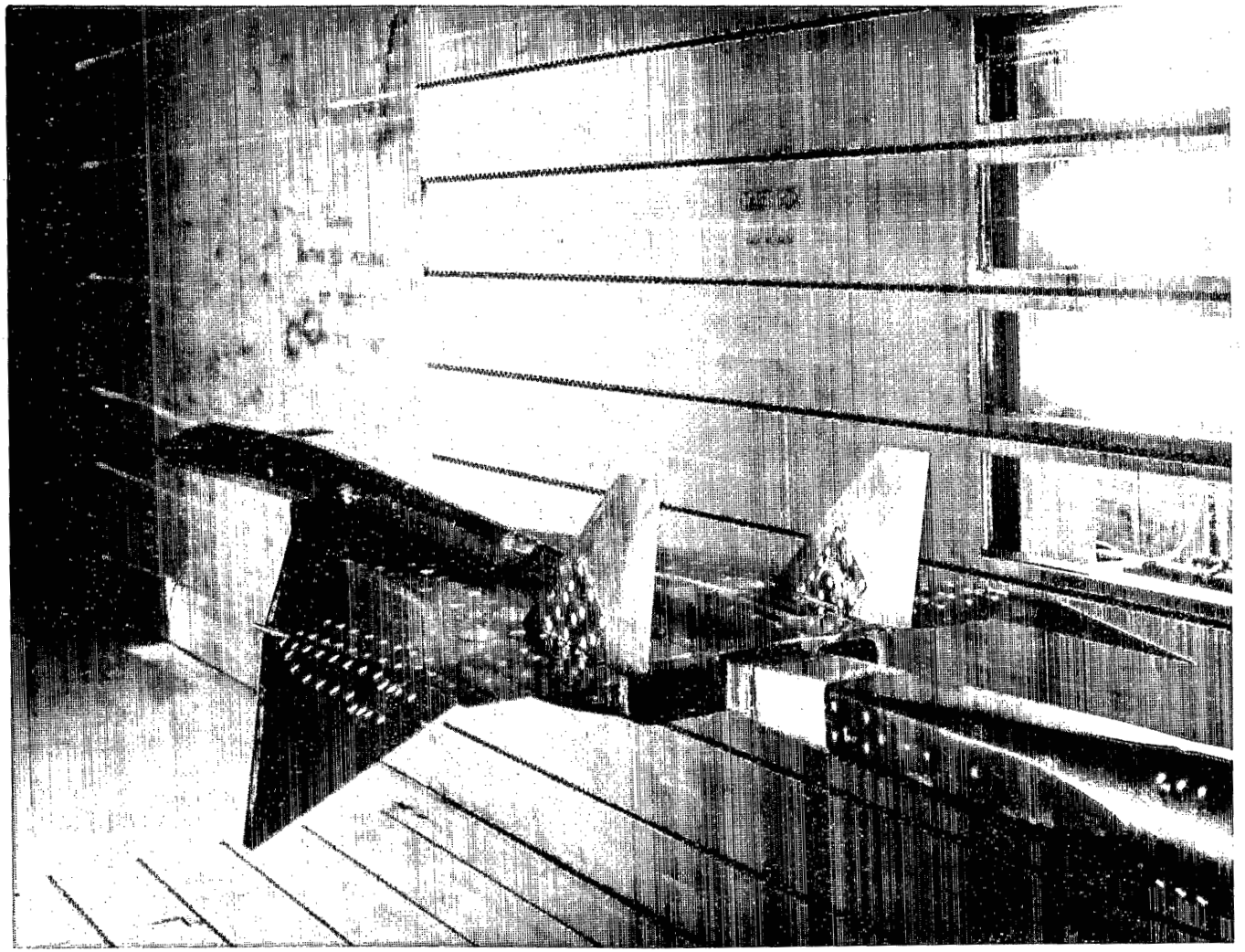

(c) Rear view showing model base and sting entry.

Figure 3.- Continued.

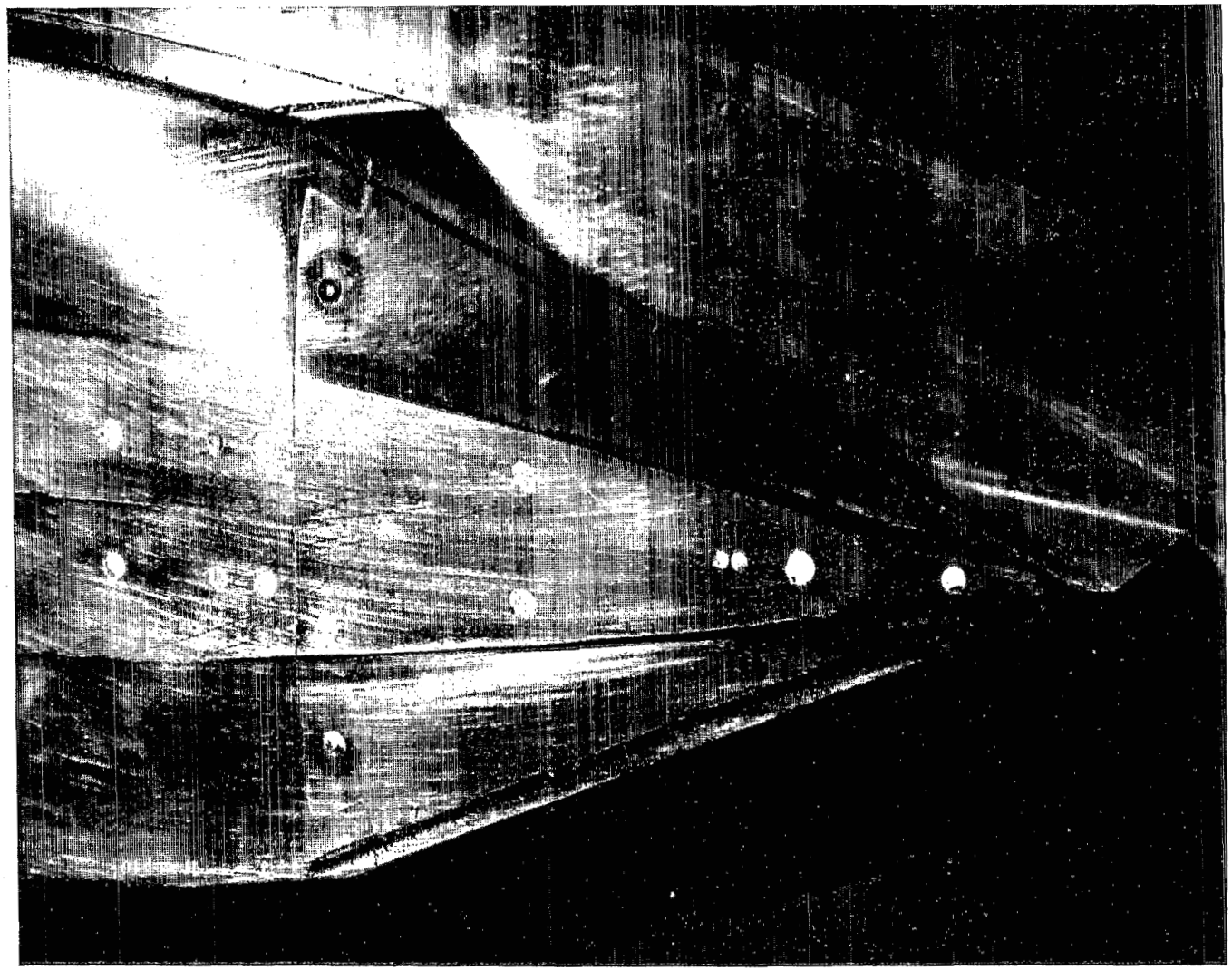

(d) Close-up of nacelle inlet with bleed dump removed.

Figure 3.- Continued.

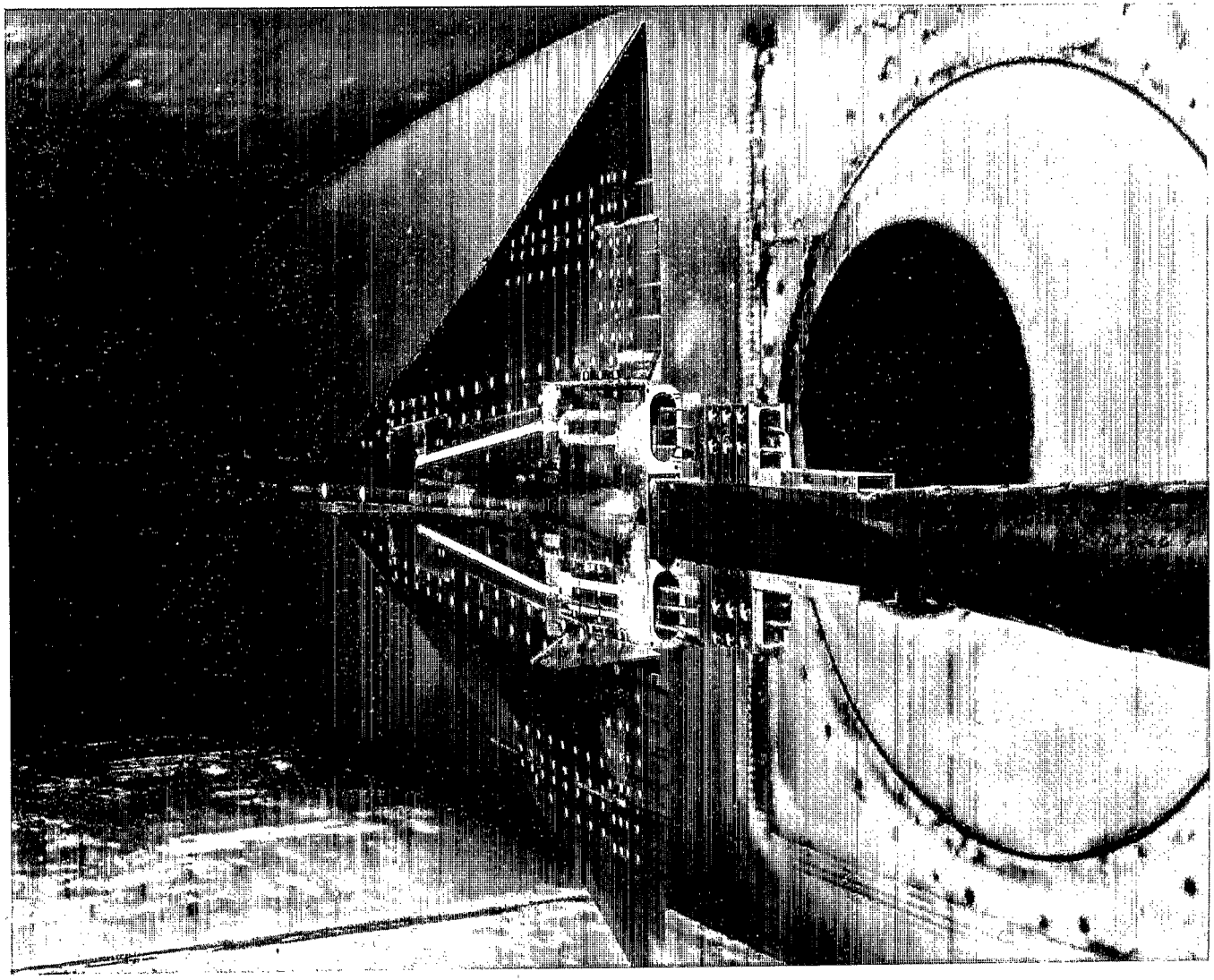

(e) Rear view with exit total-pressure calibration-rake installation.

Figure 3.- Continued.

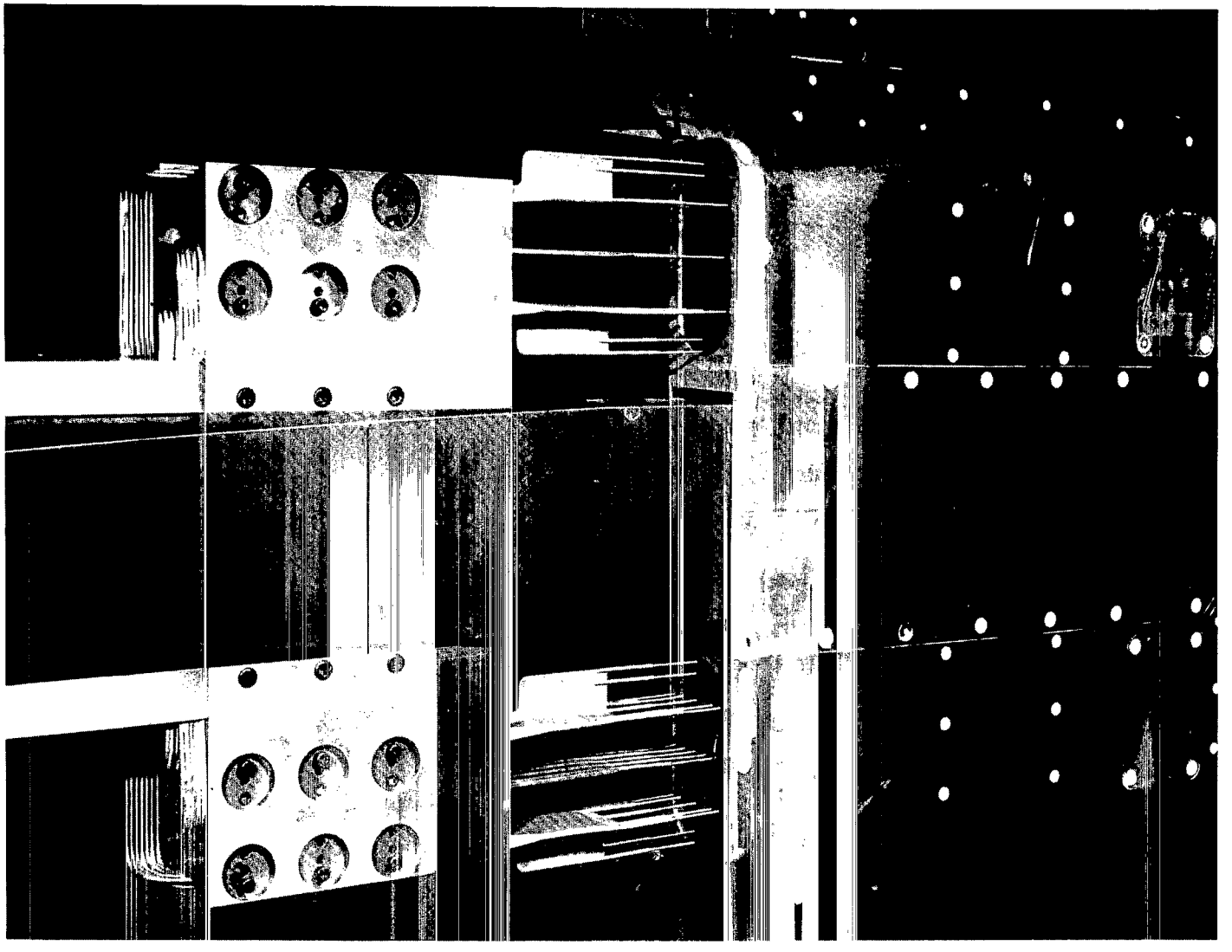

(f) Close-up of exit total-pressure calibration-rake installation.

Figure 3.- Continued.

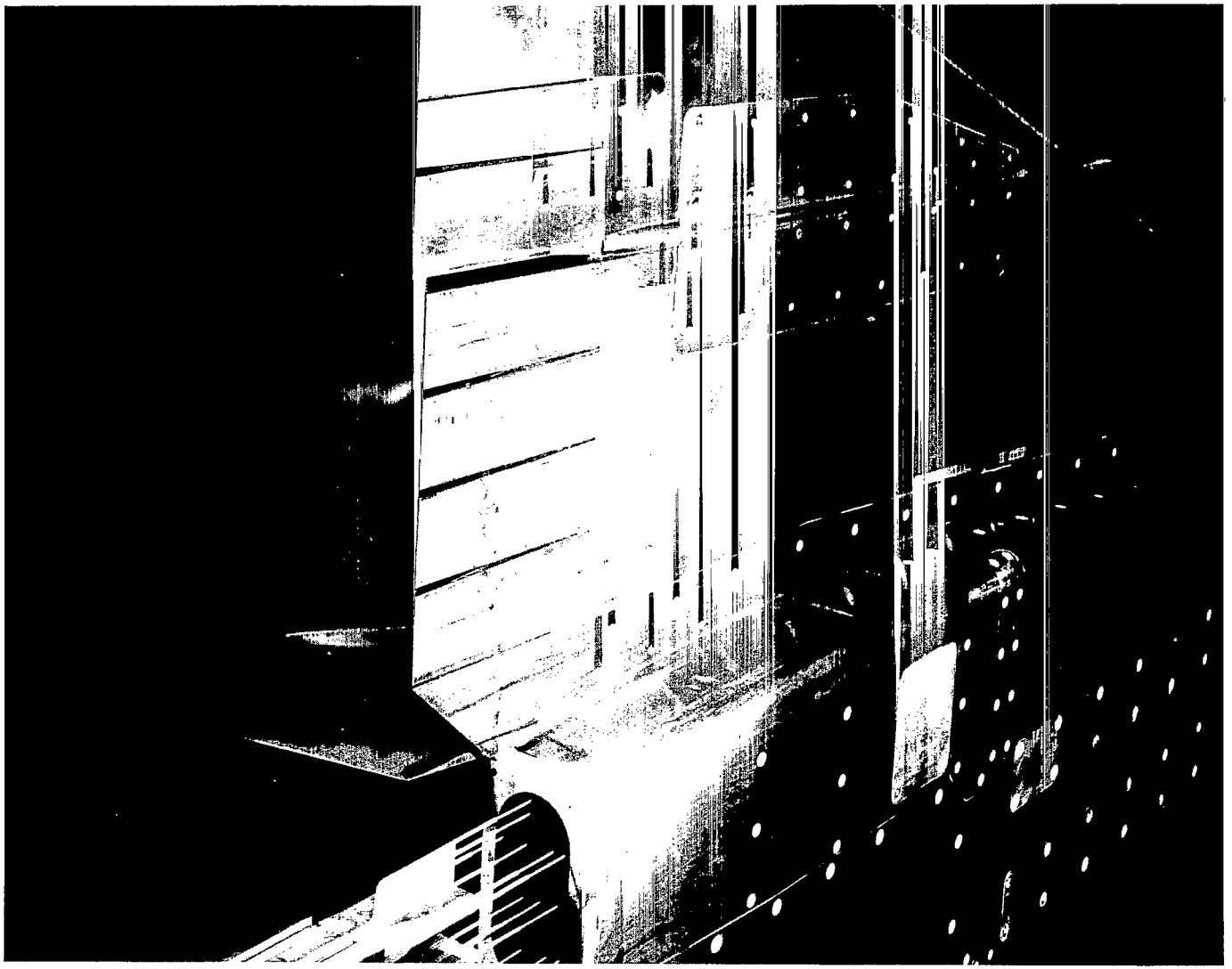

(g) Close-up of segmented elevons.

Figure 3.- Concluded.

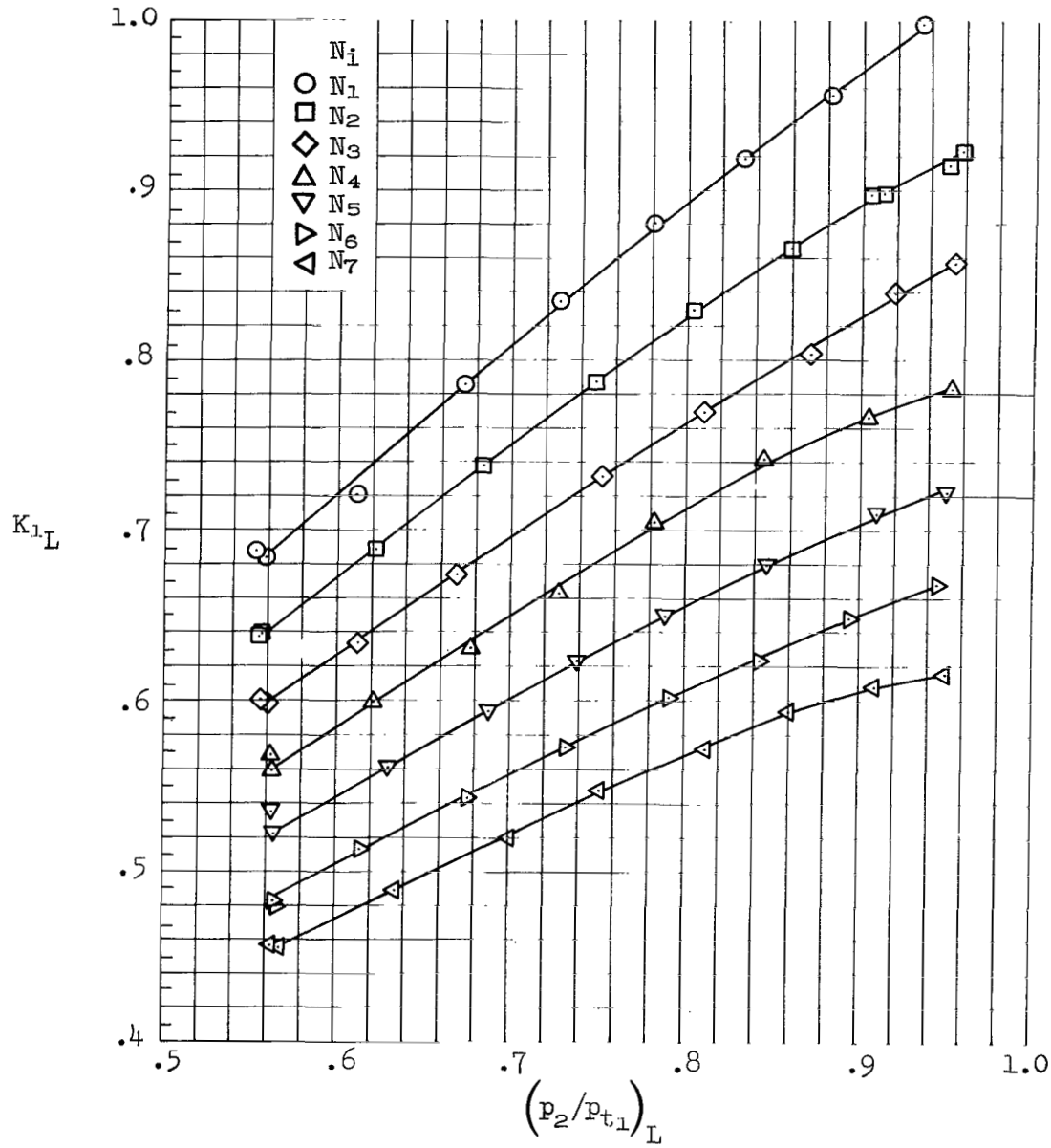

(a) Left-hand nozzles.

Figure 4.- Bench-test nozzle calibrations.

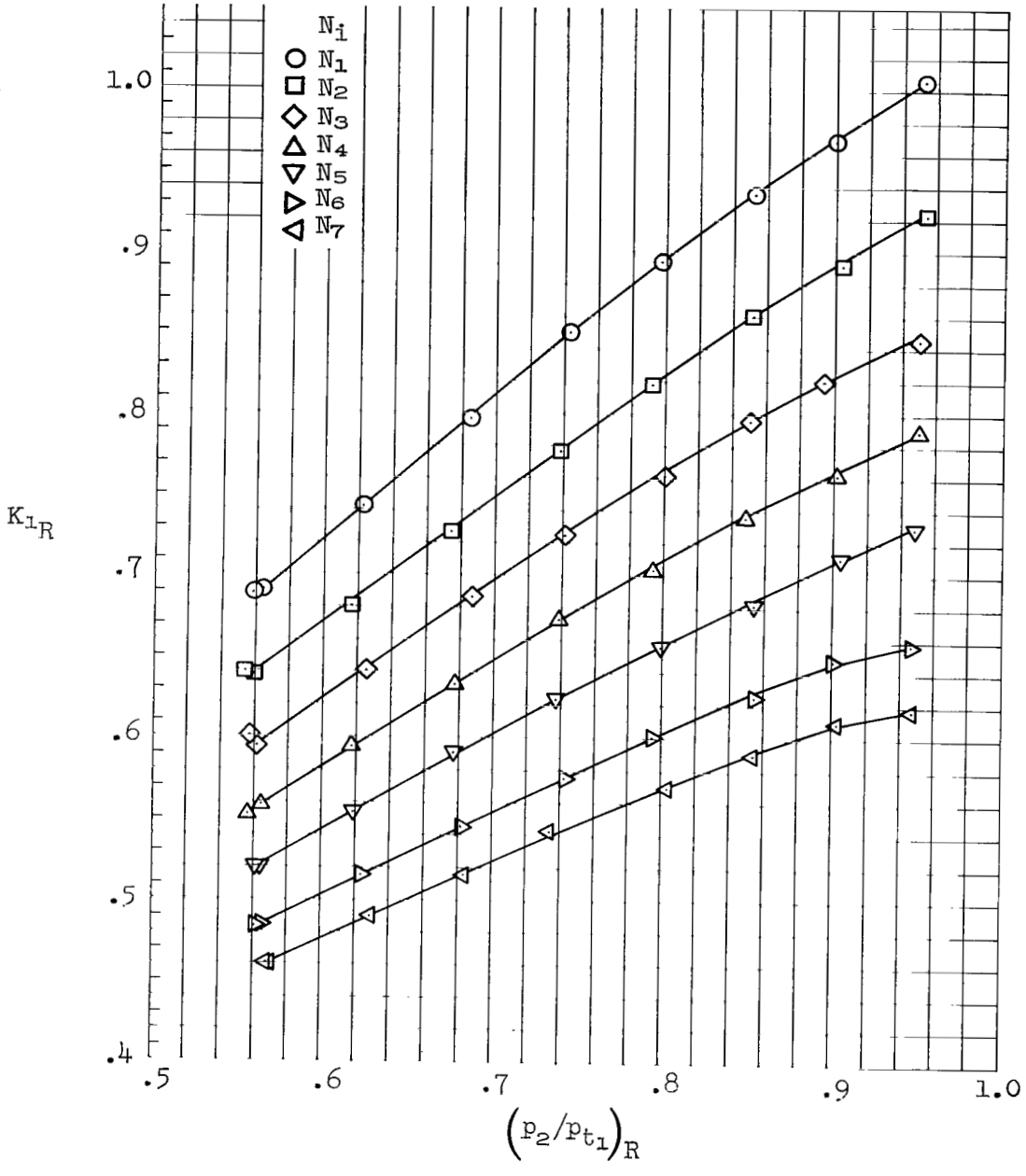

(b) Right-hand nozzles.

Figure 4.- Concluded.

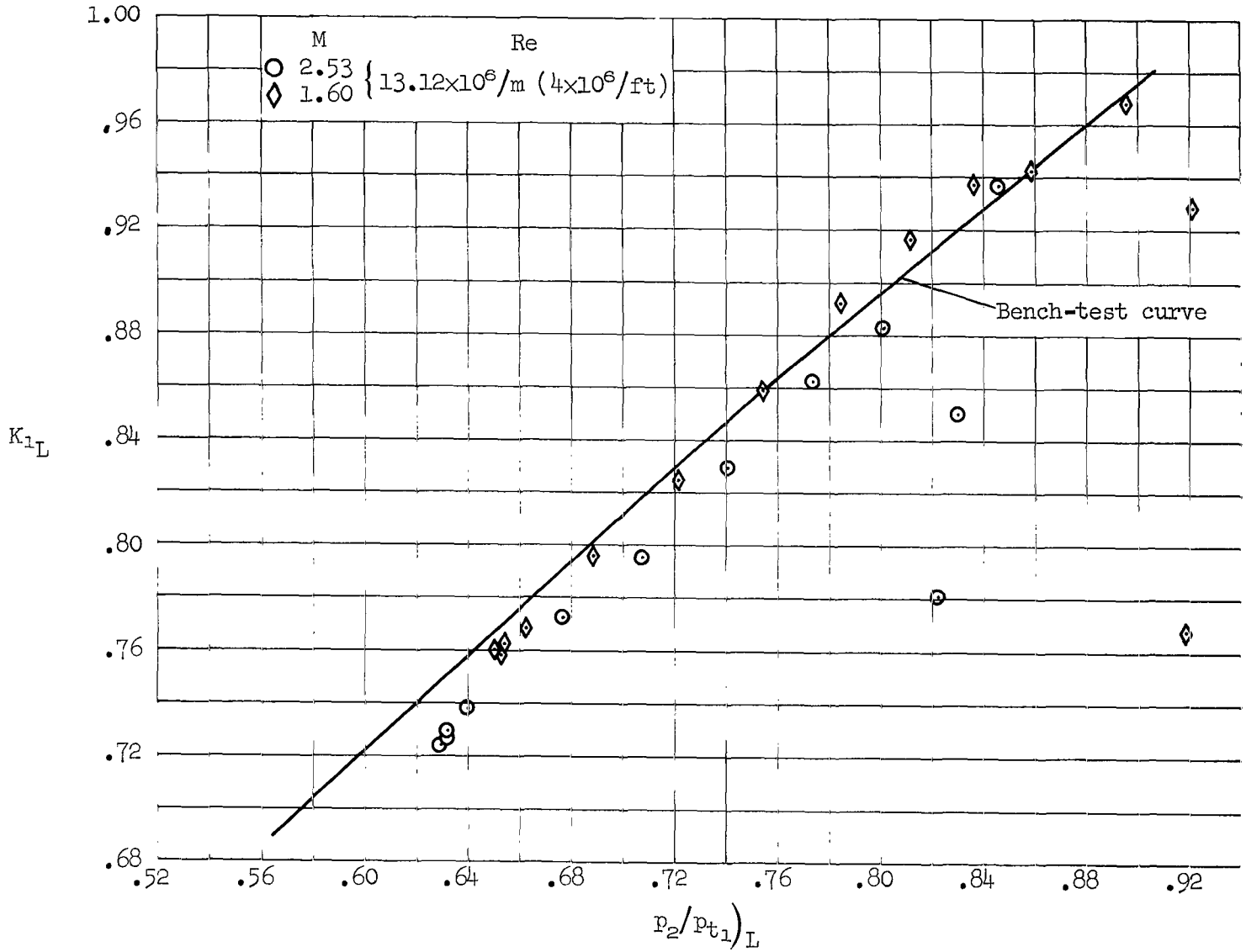

(a) Left-hand N_1 nozzle.

Figure 5.- Wind-tunnel nozzle calibrations.

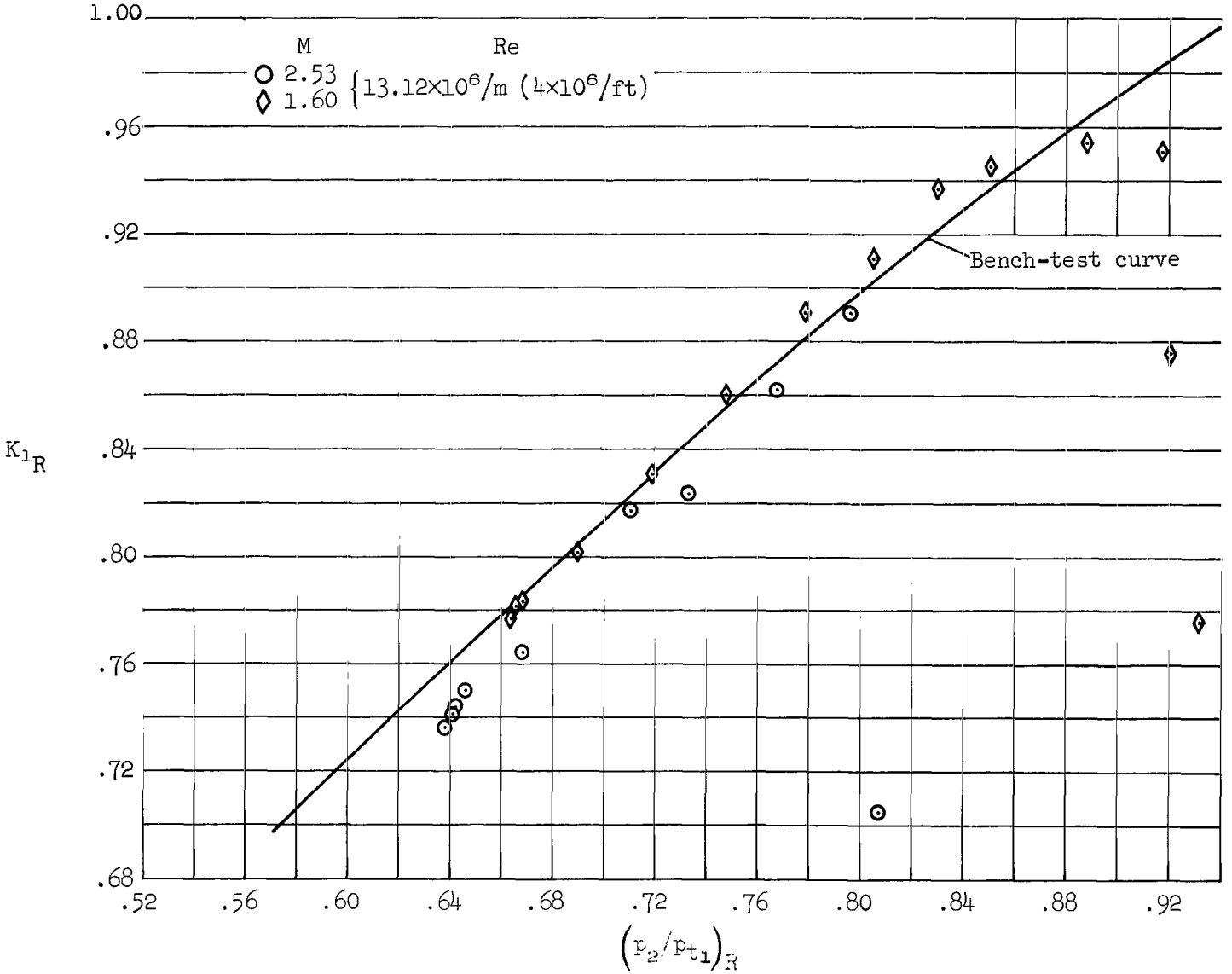

(b) Right-hand N_1 nozzle.

Figure 5.- Continued.

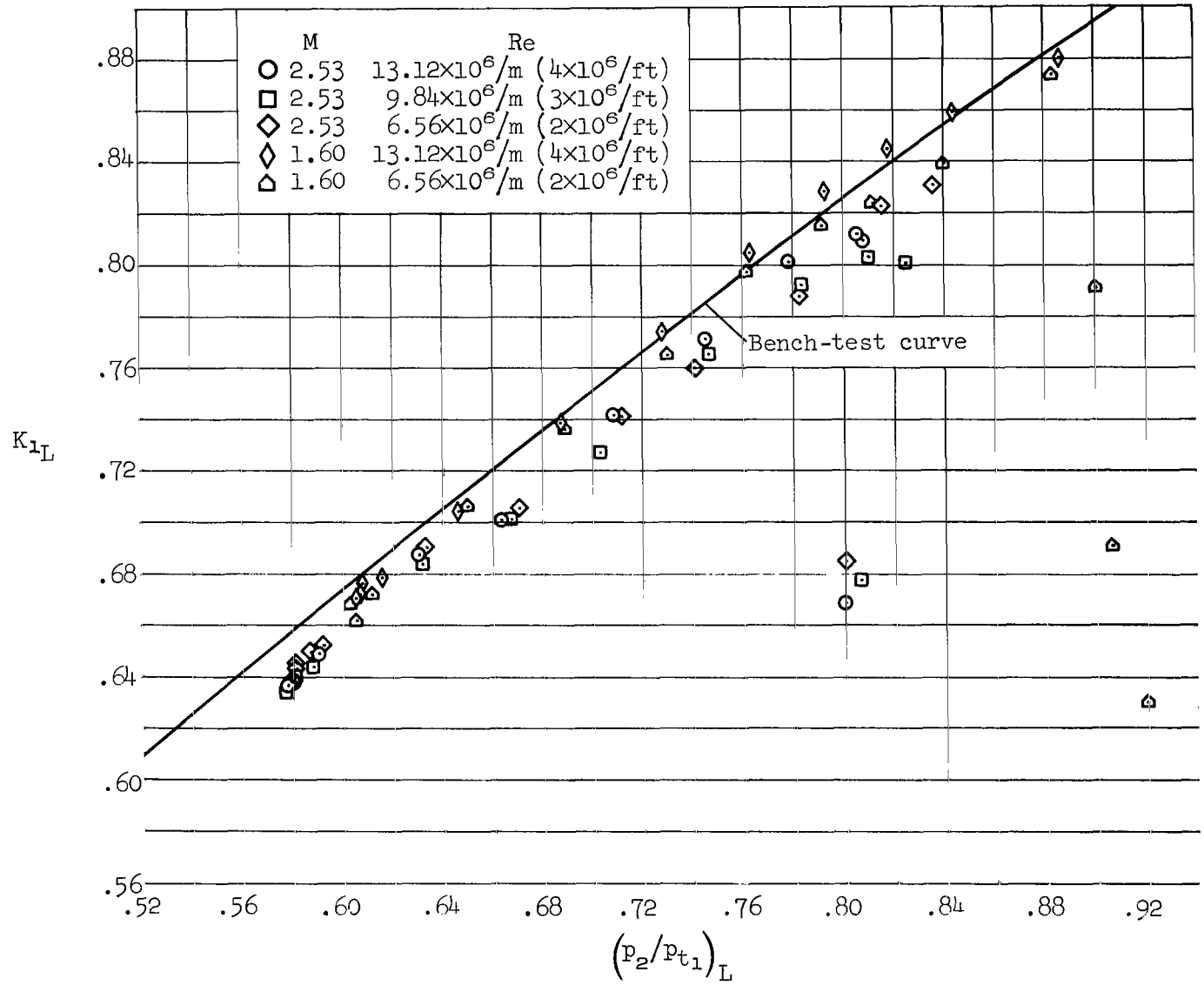

(c) Left-hand N_2 nozzle.

Figure 5.- Continued.

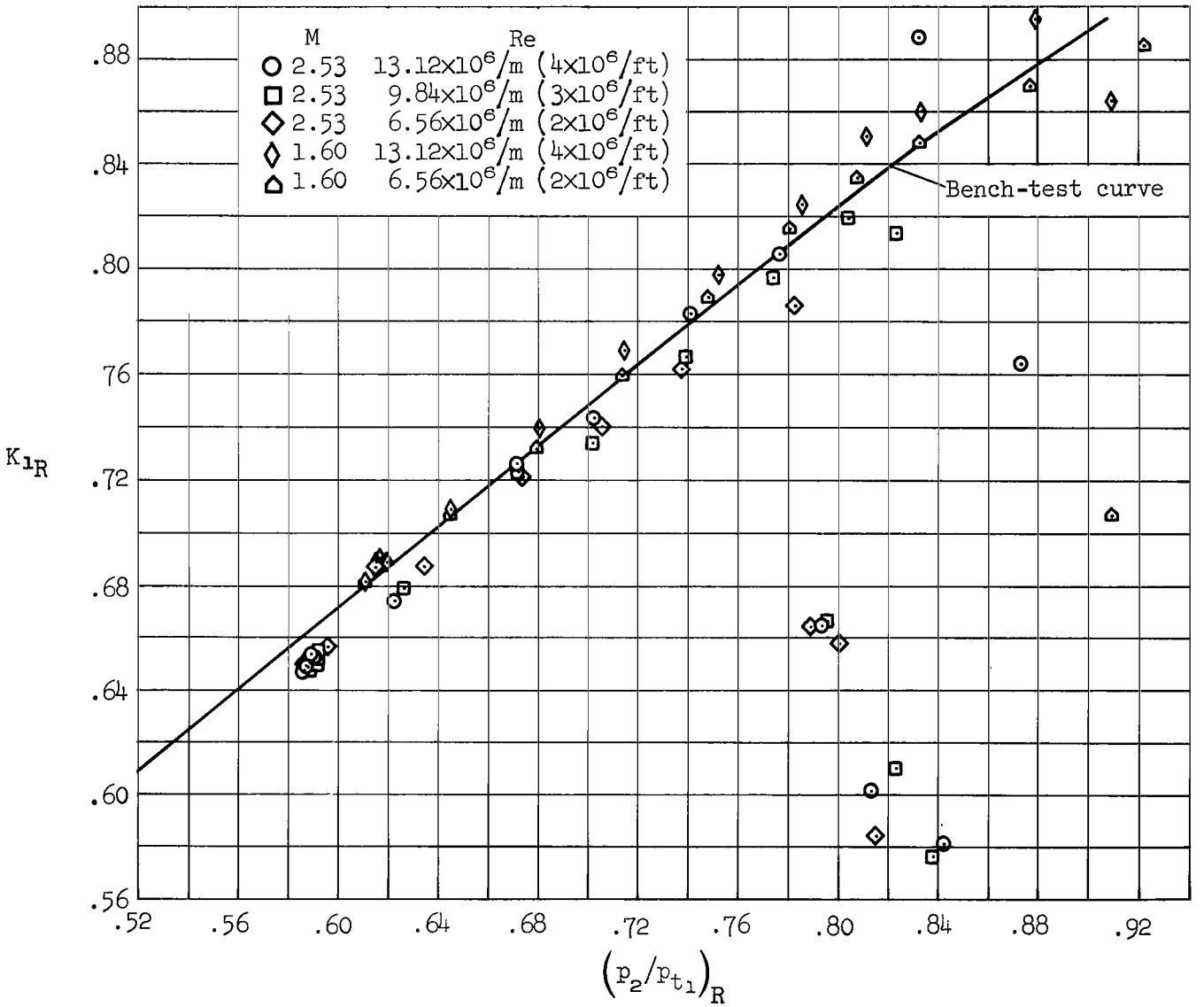

(d) Right-hand N_2 nozzle.

Figure 5.- Continued.

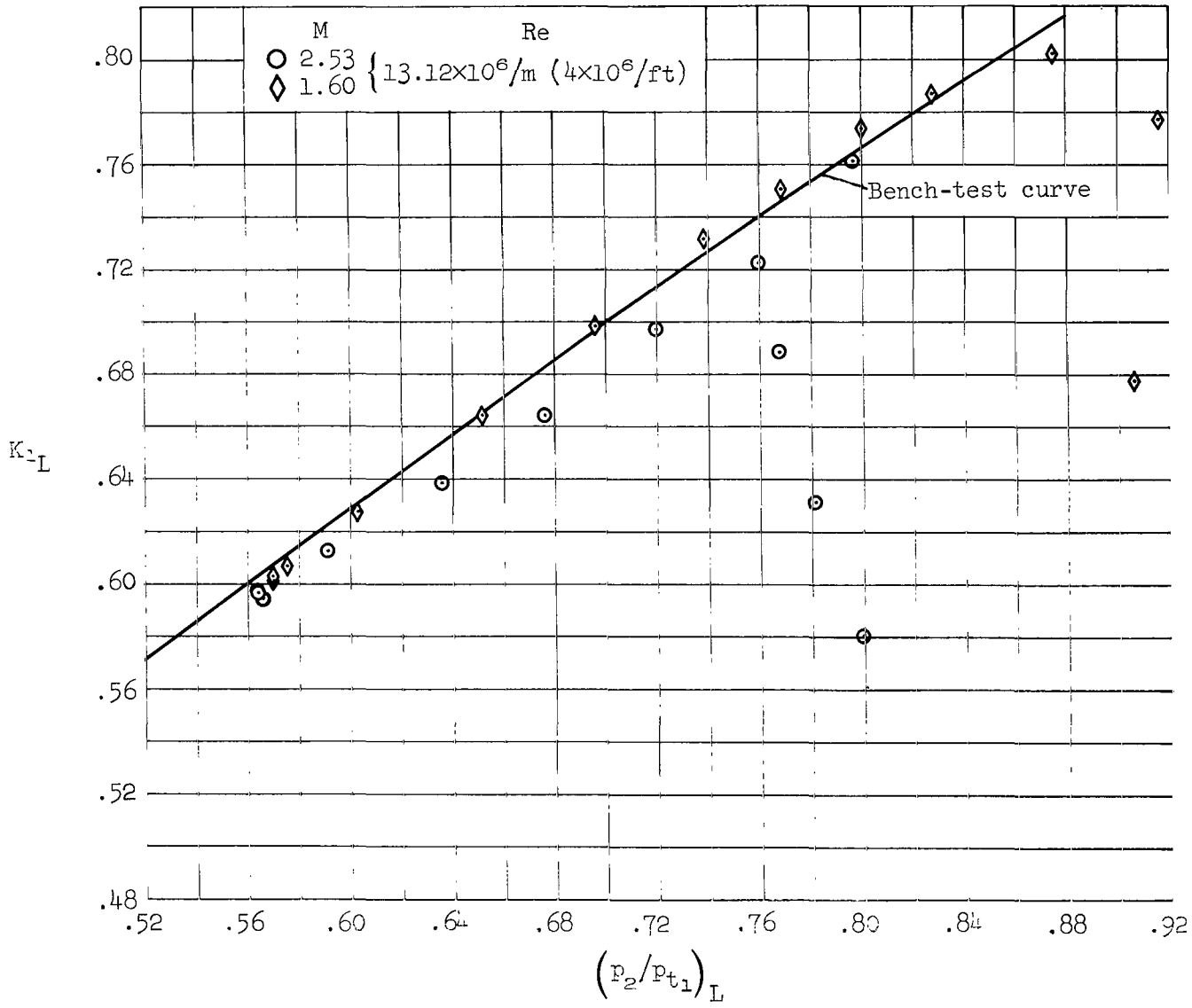

(e) Left-hand N_3 nozzle.

Figure 5.- Continued.

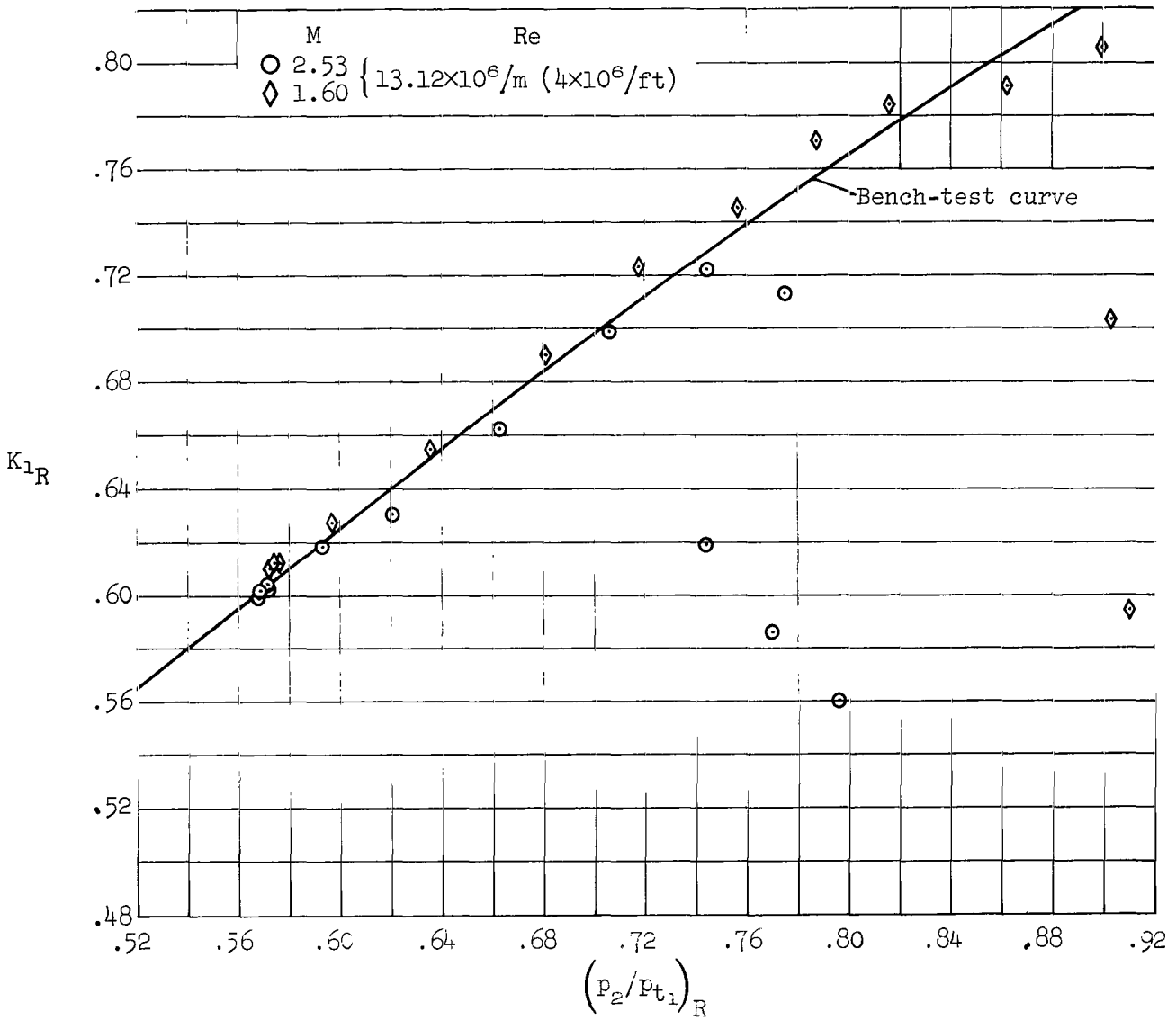

(f) Right-hand N_3 nozzle.

Figure 5.- Continued.

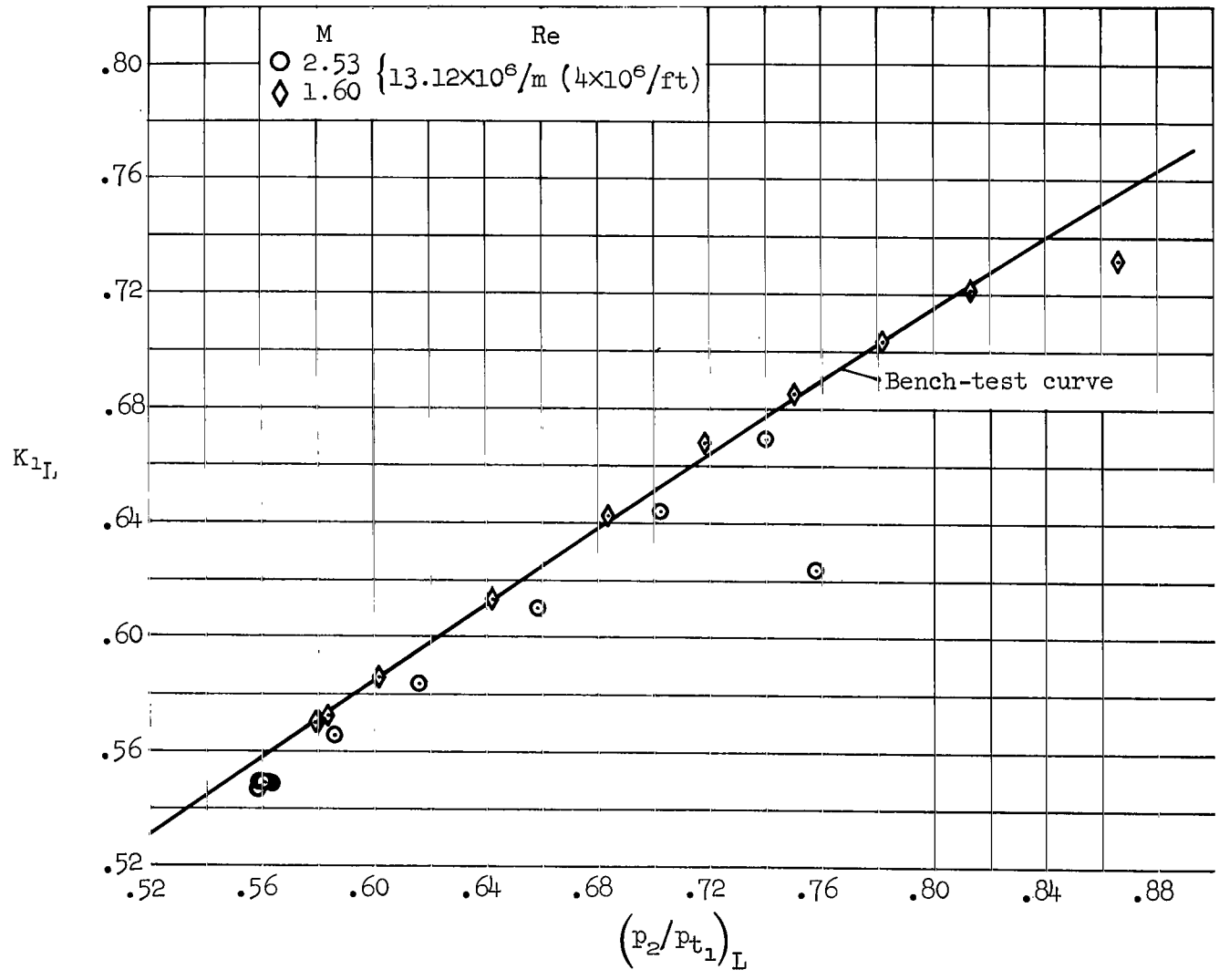

(g) Left-hand N_4 nozzle.

Figure 5.- Continued.

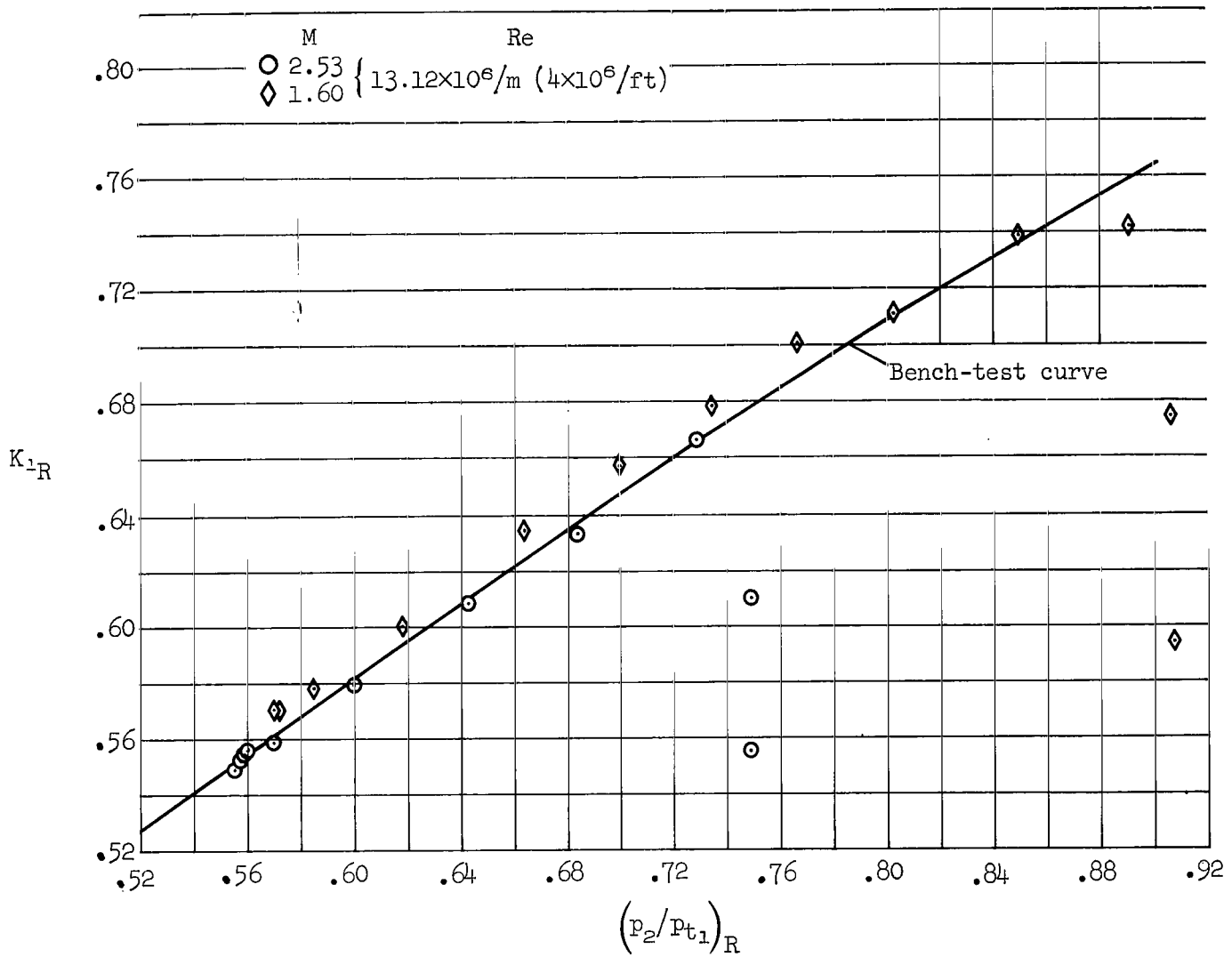

(h) Right-hand N_4 nozzle.

Figure 5.- Continued.

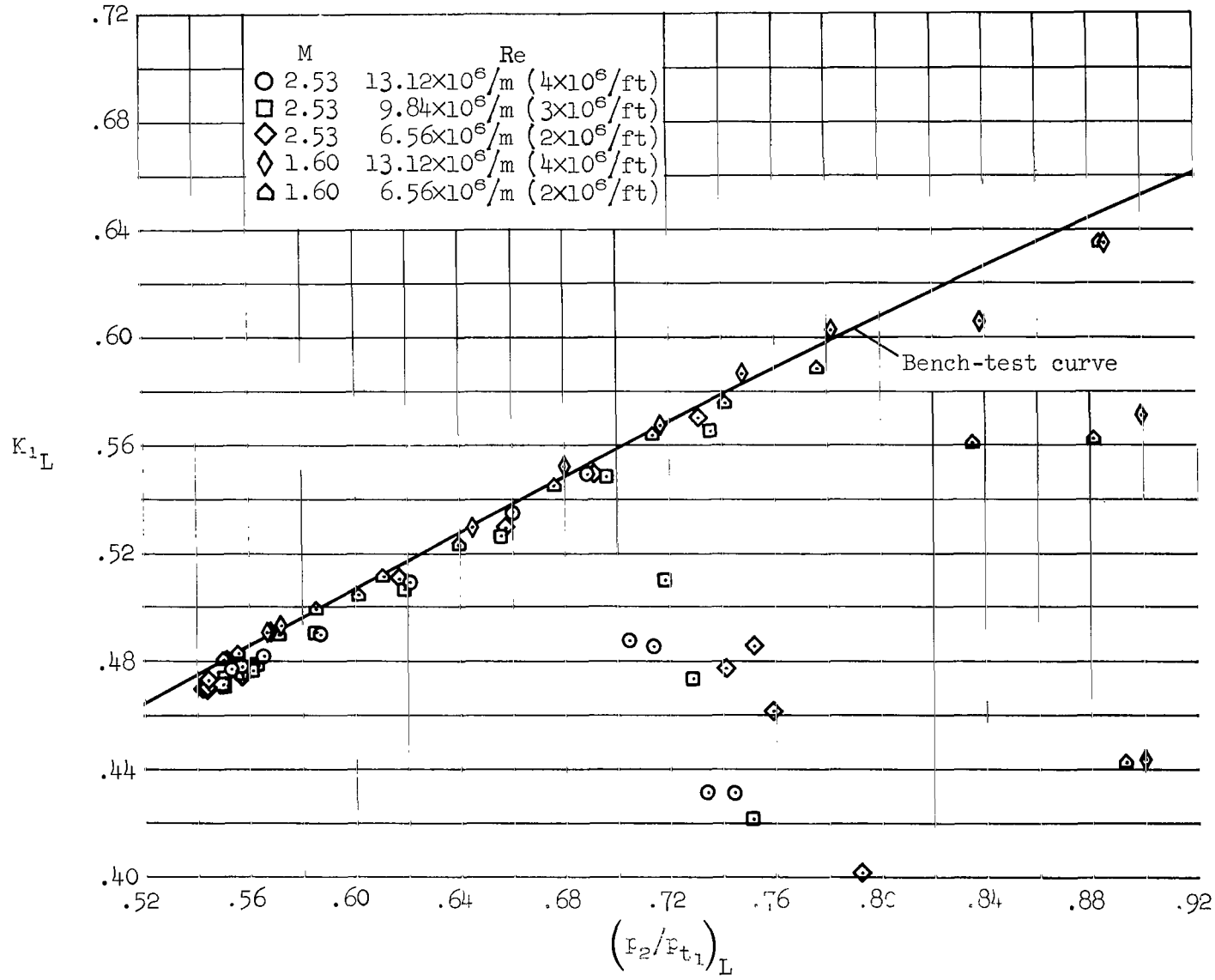

(i) Left-hand N_6 nozzle.

Figure 5.- Continued.

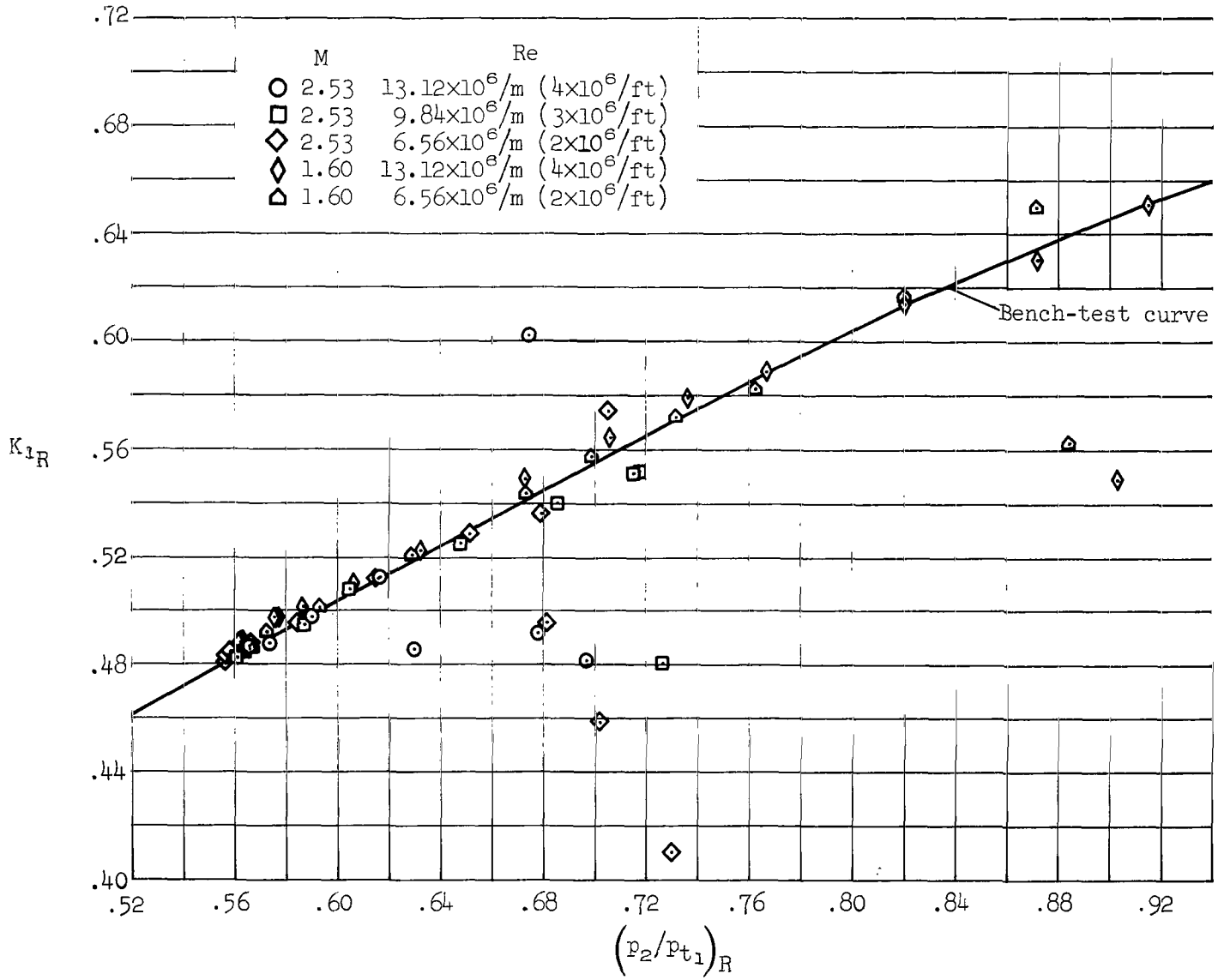

(j) Right-hand N_6 nozzle.

Figure 5.- Concluded.

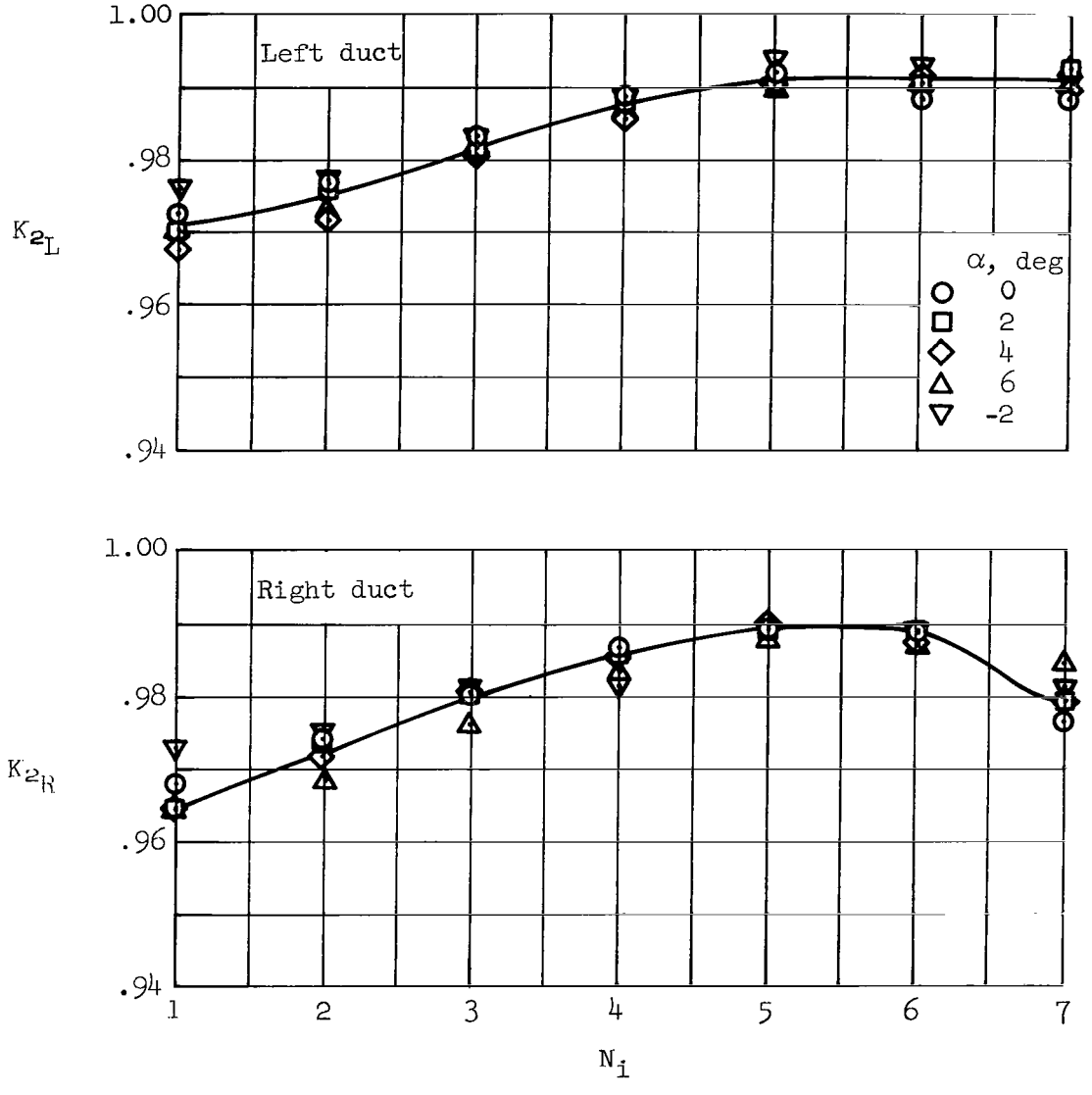

Figure 6.- Duct total-pressure-rake calibrations, M = 1.6.

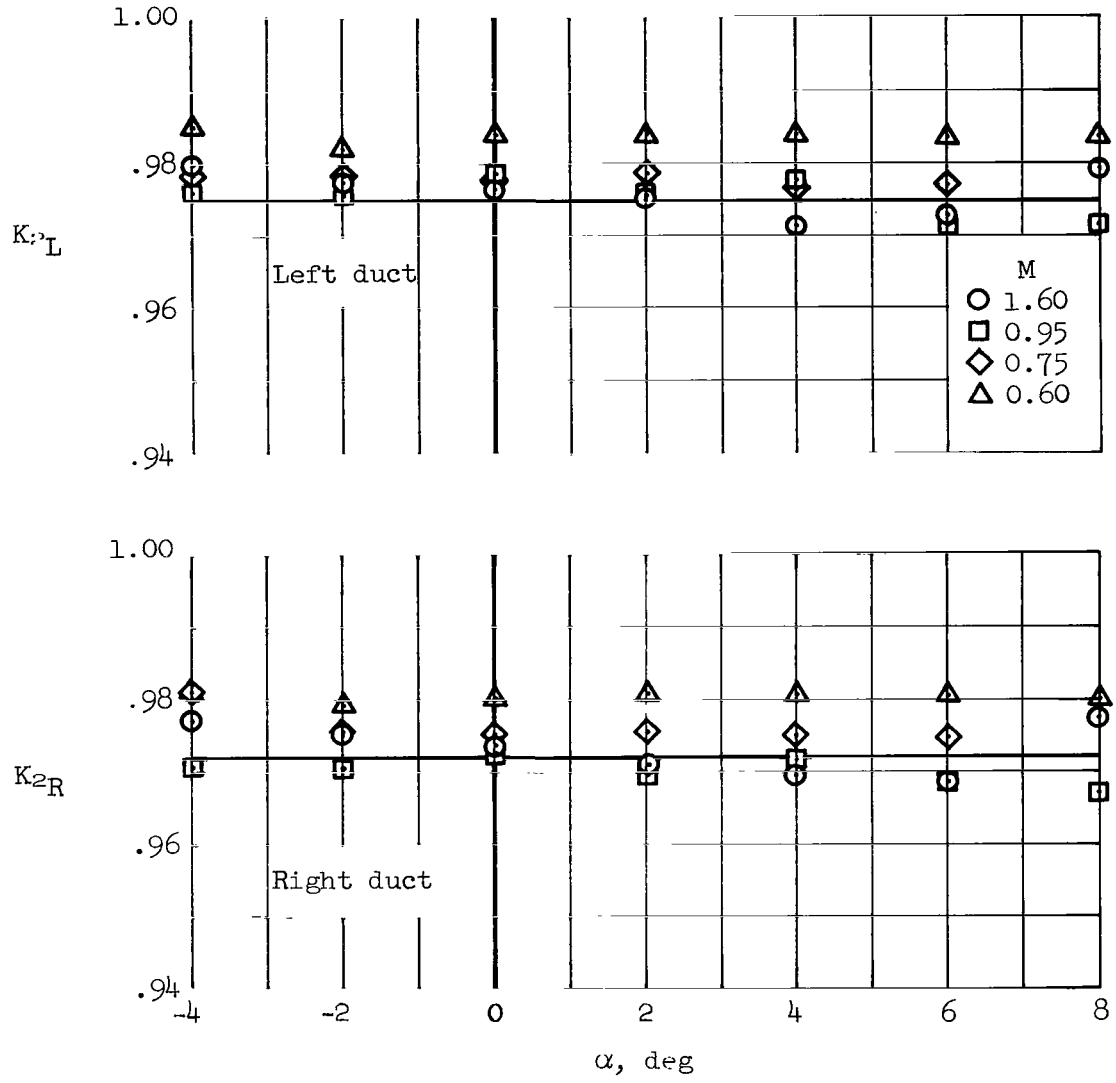

(a) N_2 nozzles.

Figure 7.- Duct total-pressure-rake calibrations at various Mach numbers.

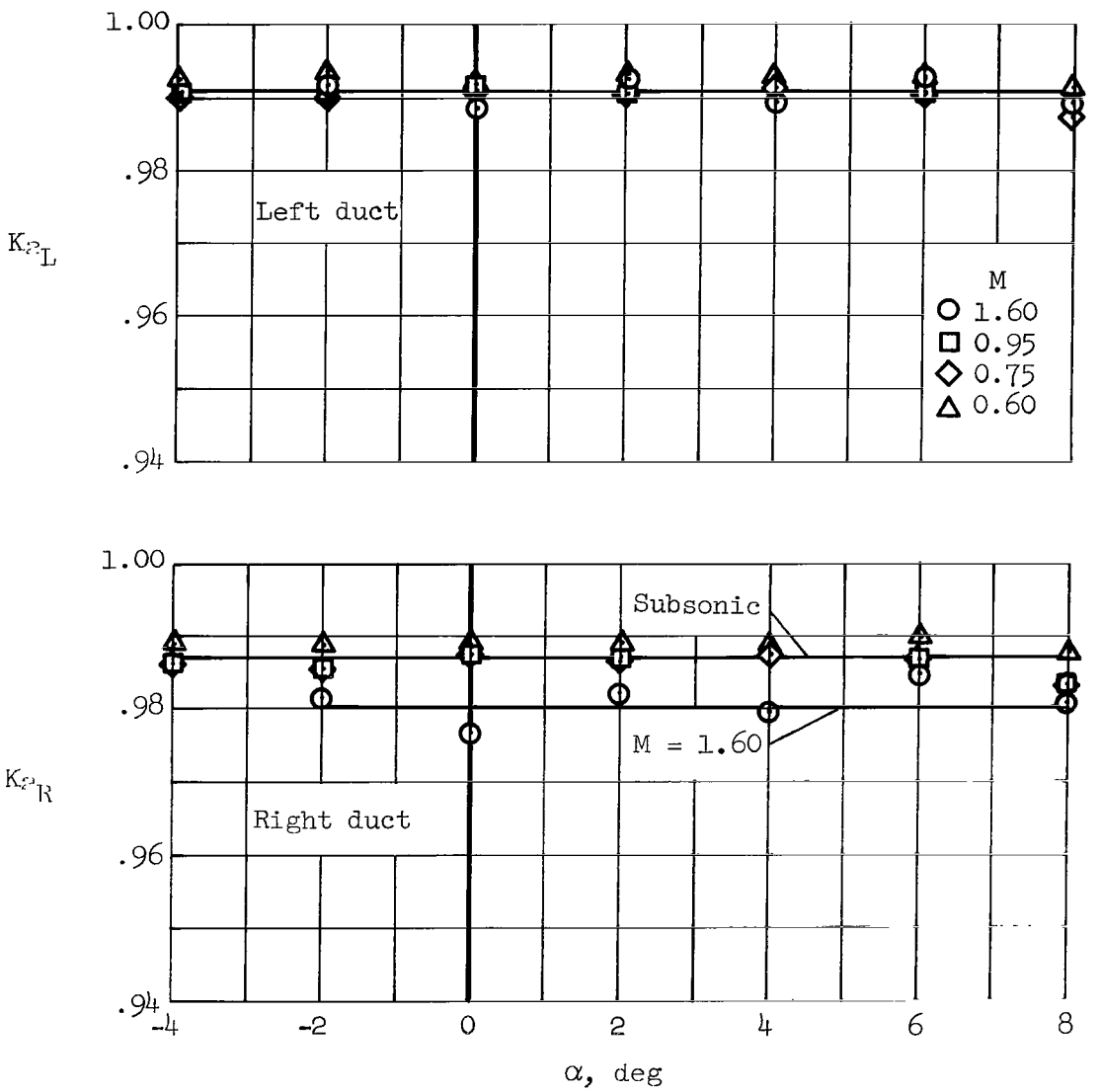

(b) N_7 nozzles.

Figure 7.- Concluded.

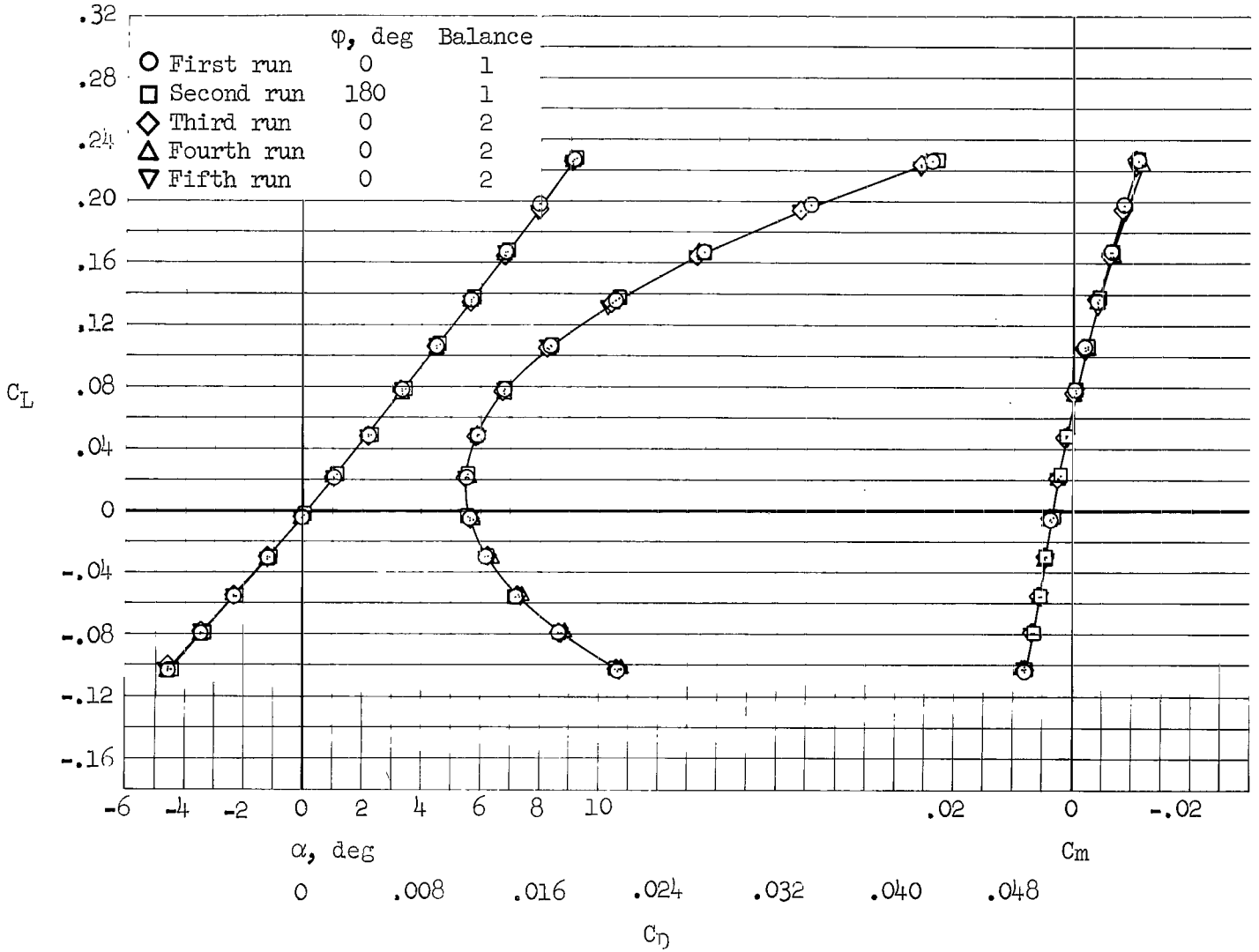

(a) M = 2.53

Figure 8.- Examples of repeatability of longitudinal data for configuration $W_1E_2B_1K_1N_2C_1V_1G_1$, $\delta_y = 65°$.

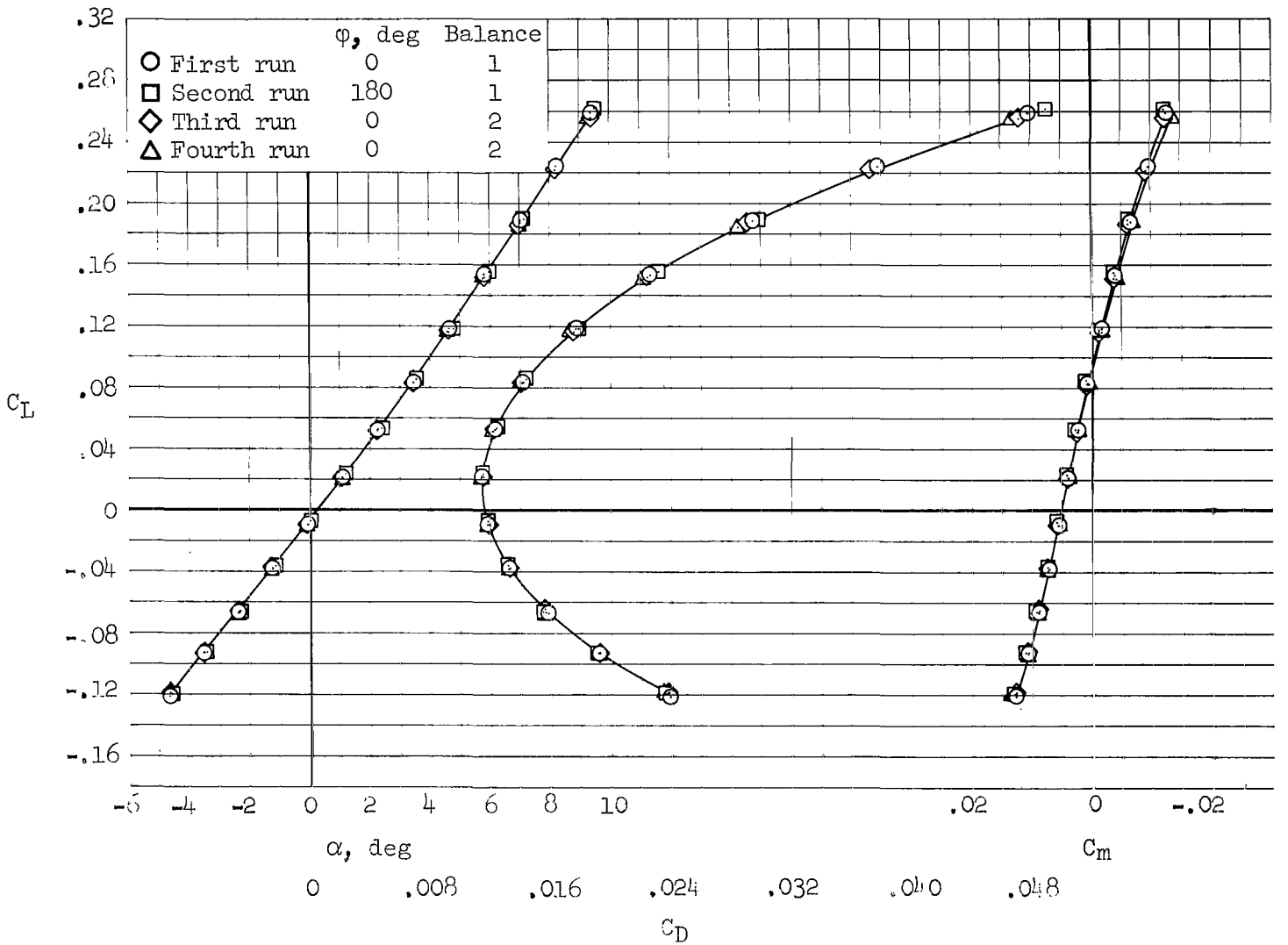

(b) M = 2.10

Figure 8.- Continued.

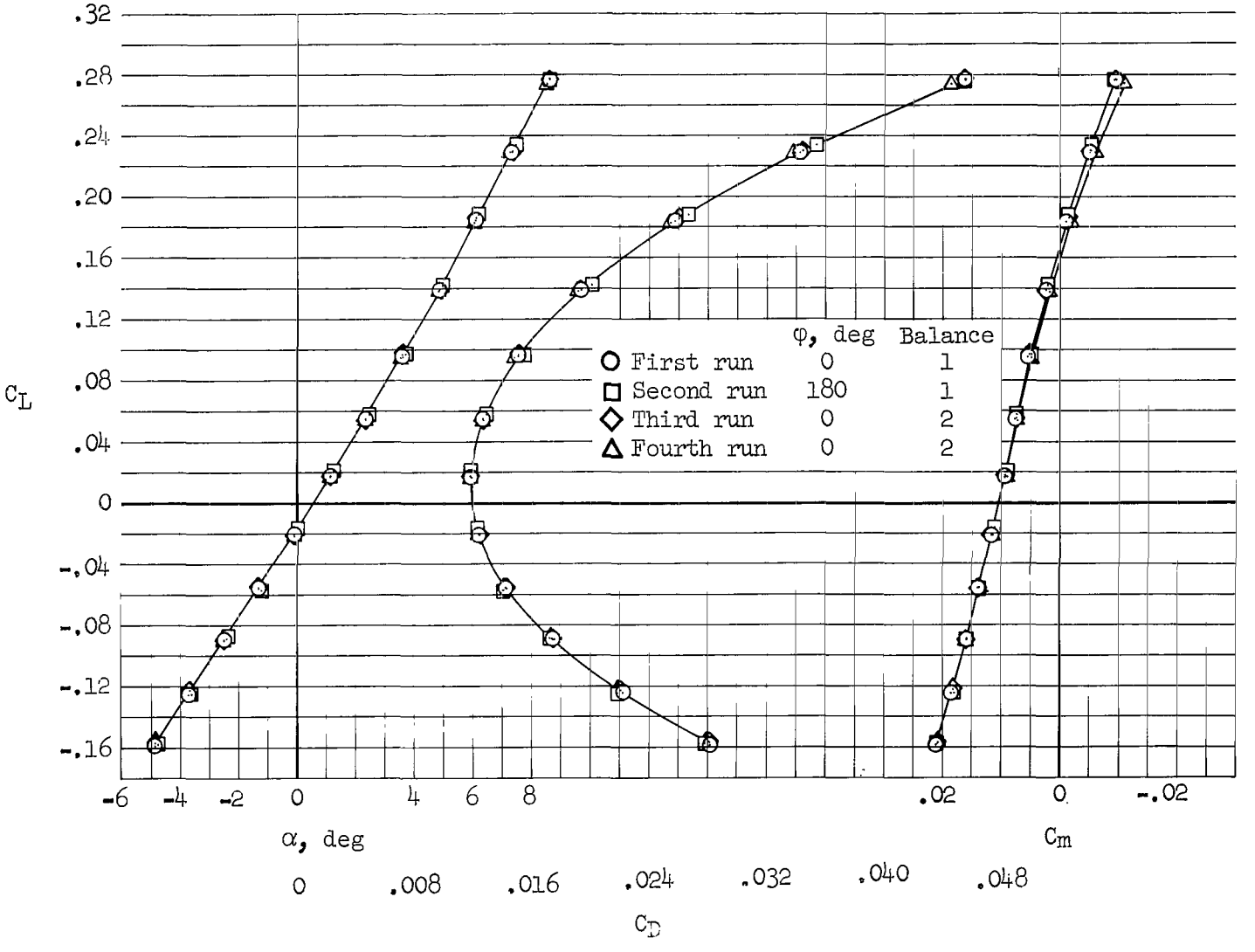

(c) M = 1.60

Figure 8.- Concluded.

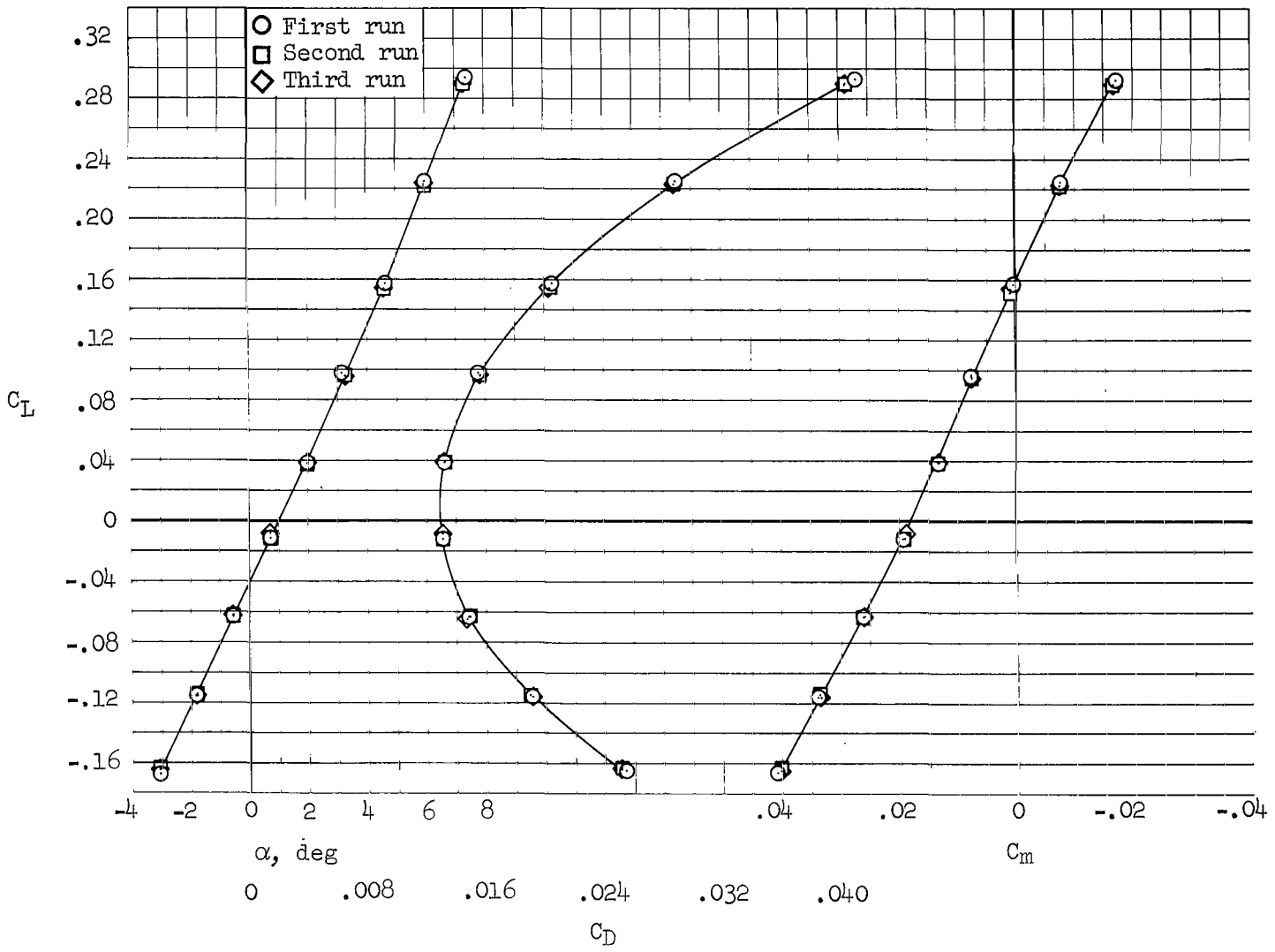

(a) M = 1.20

Figure 9.- Examples of repeatability of longitudinal data for configuration $W_1E_2B_2K_1N_2C_1V_1G_7$, $\delta_y = 25°$.

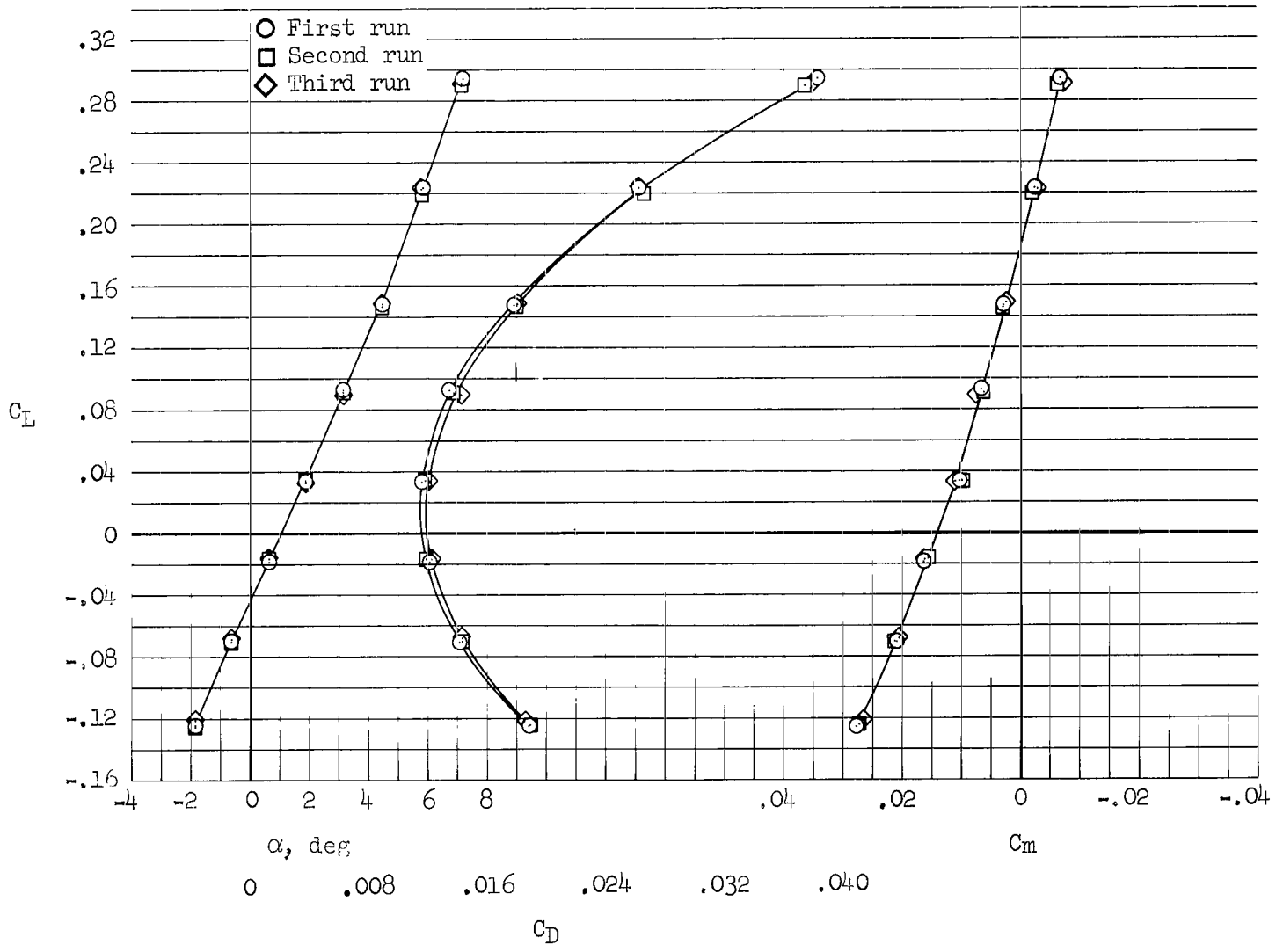

(b) M = 0.95

Figure 9.- Continued.

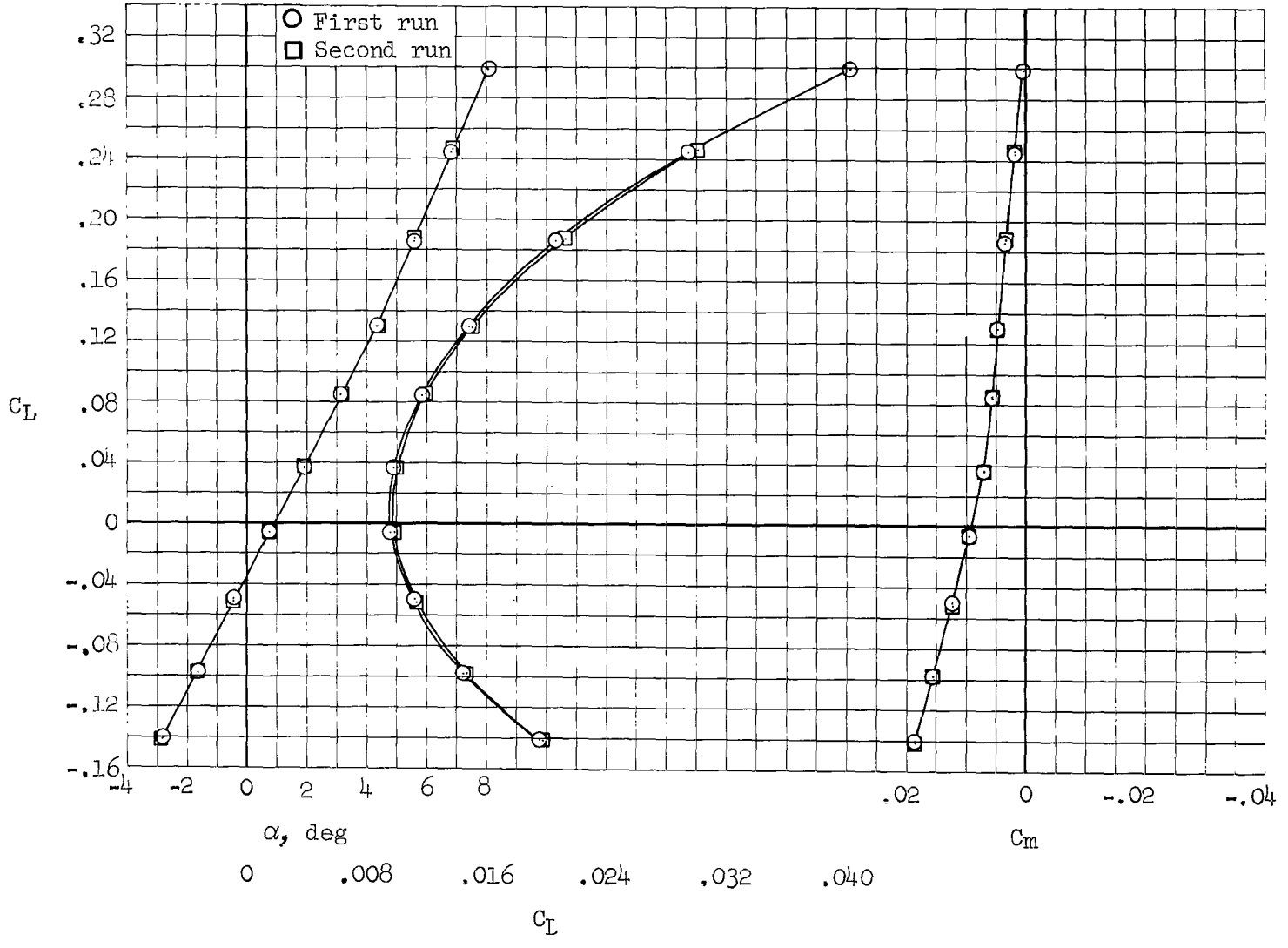

(c) M = 0.75

Figure 9.- Concluded.

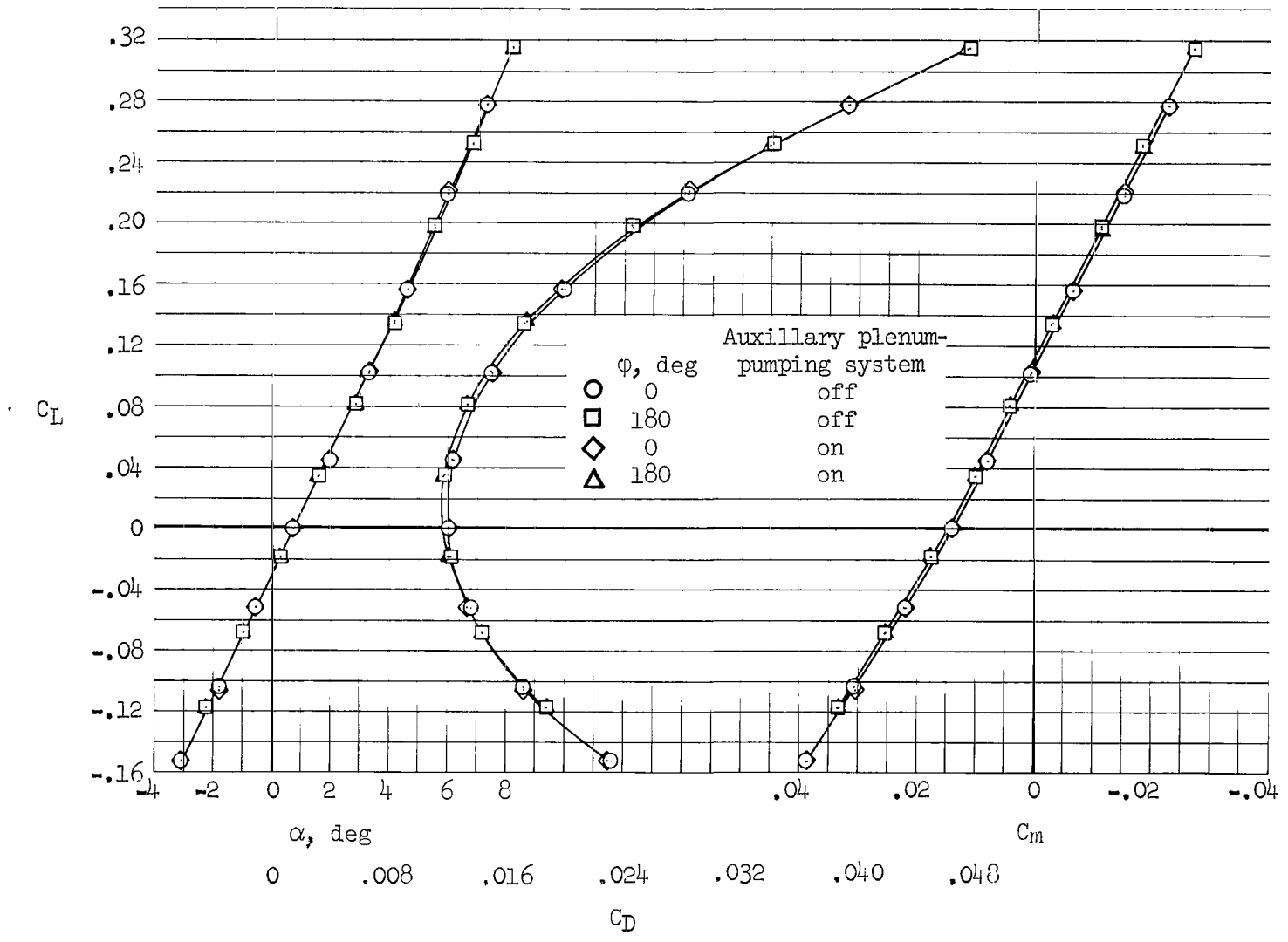

(a) M = 1.40

Figure 10.- Examples of repeatability of longitudinal data for configuration $W_1E_1B_2K_1N_2C_1V_1G_7$, $\delta_y = 0°$.

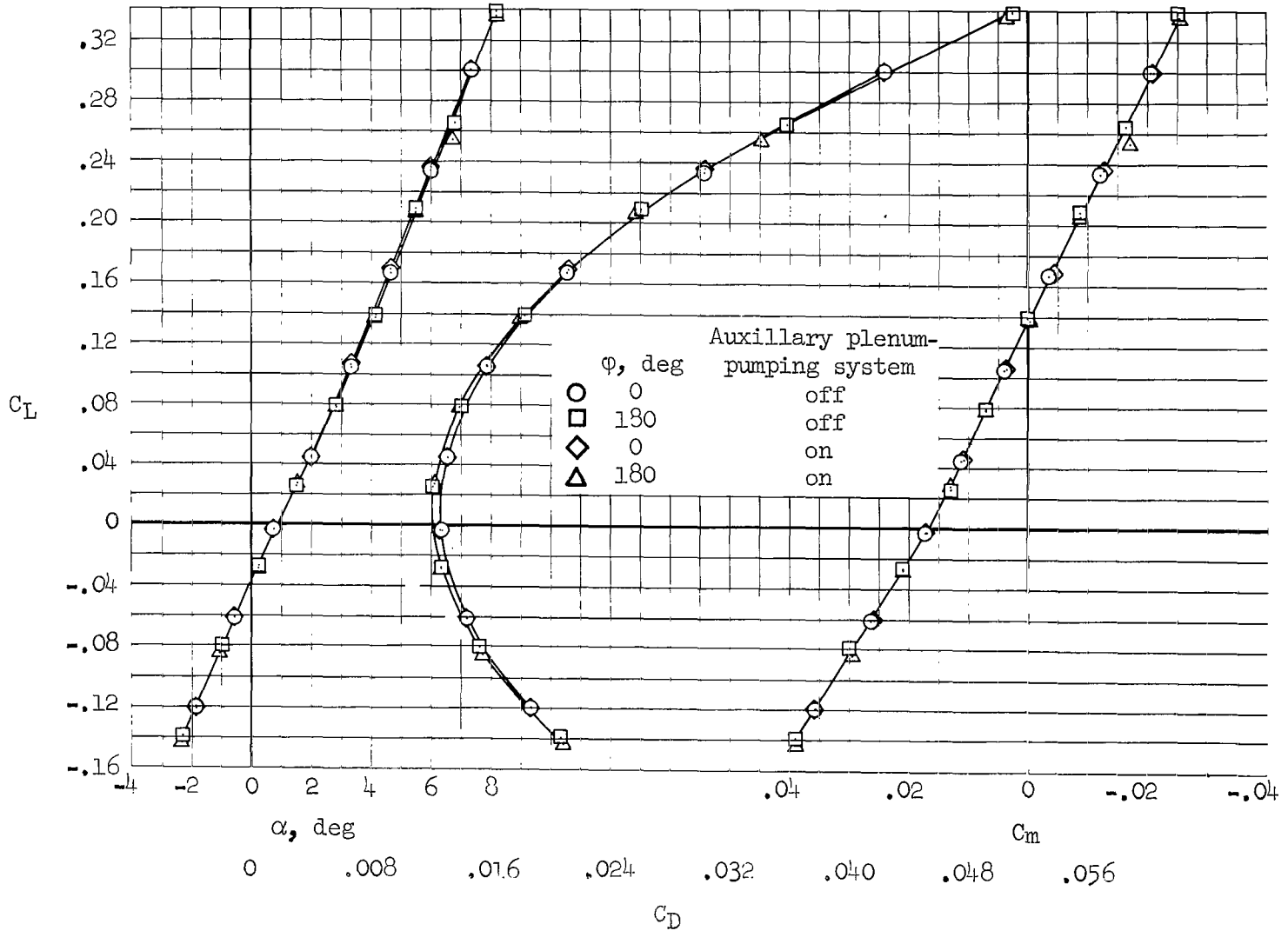

(b) M = 1.20

Figure 10.- Continued.

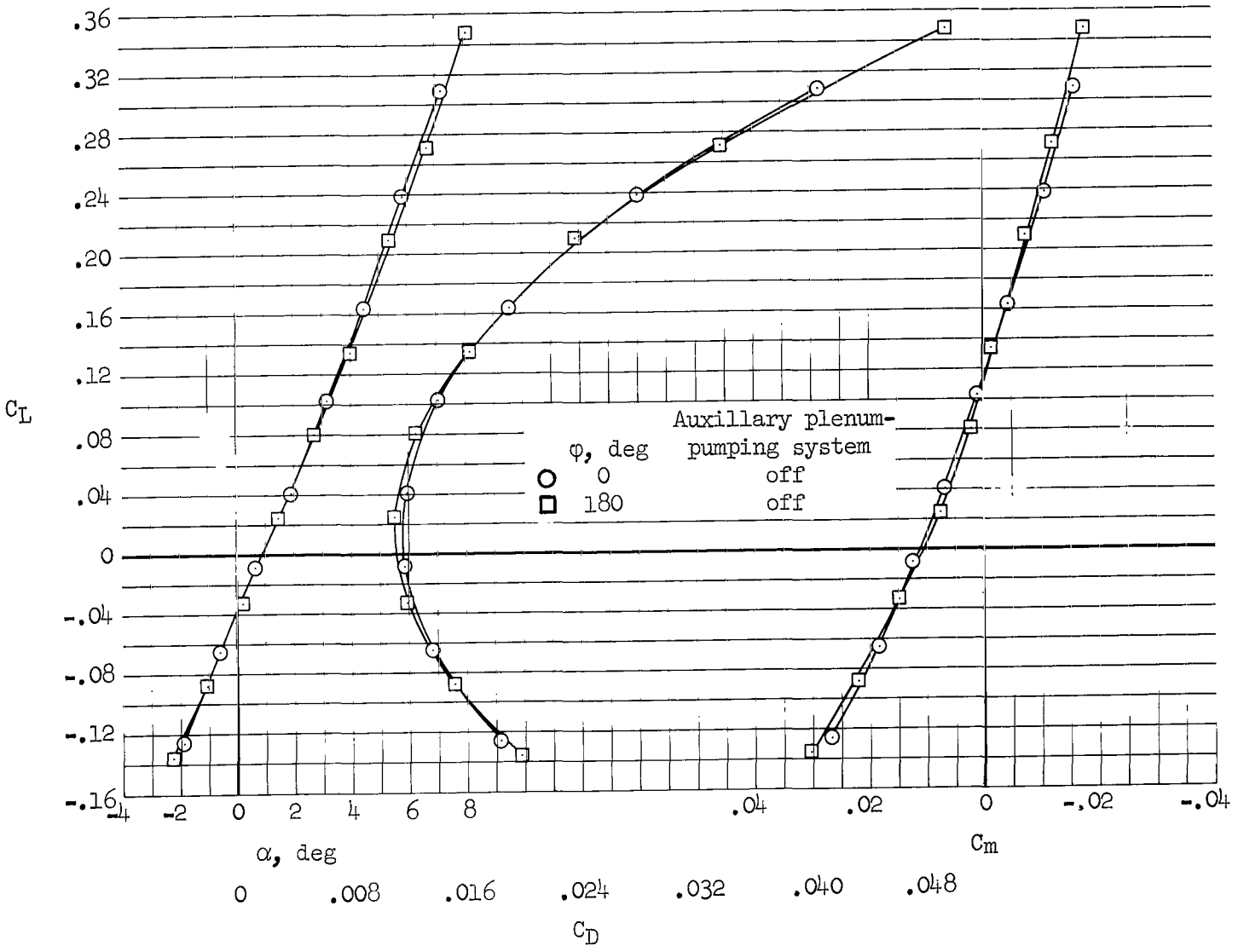

(c) M = 0.95

Figure 10.- Continued.

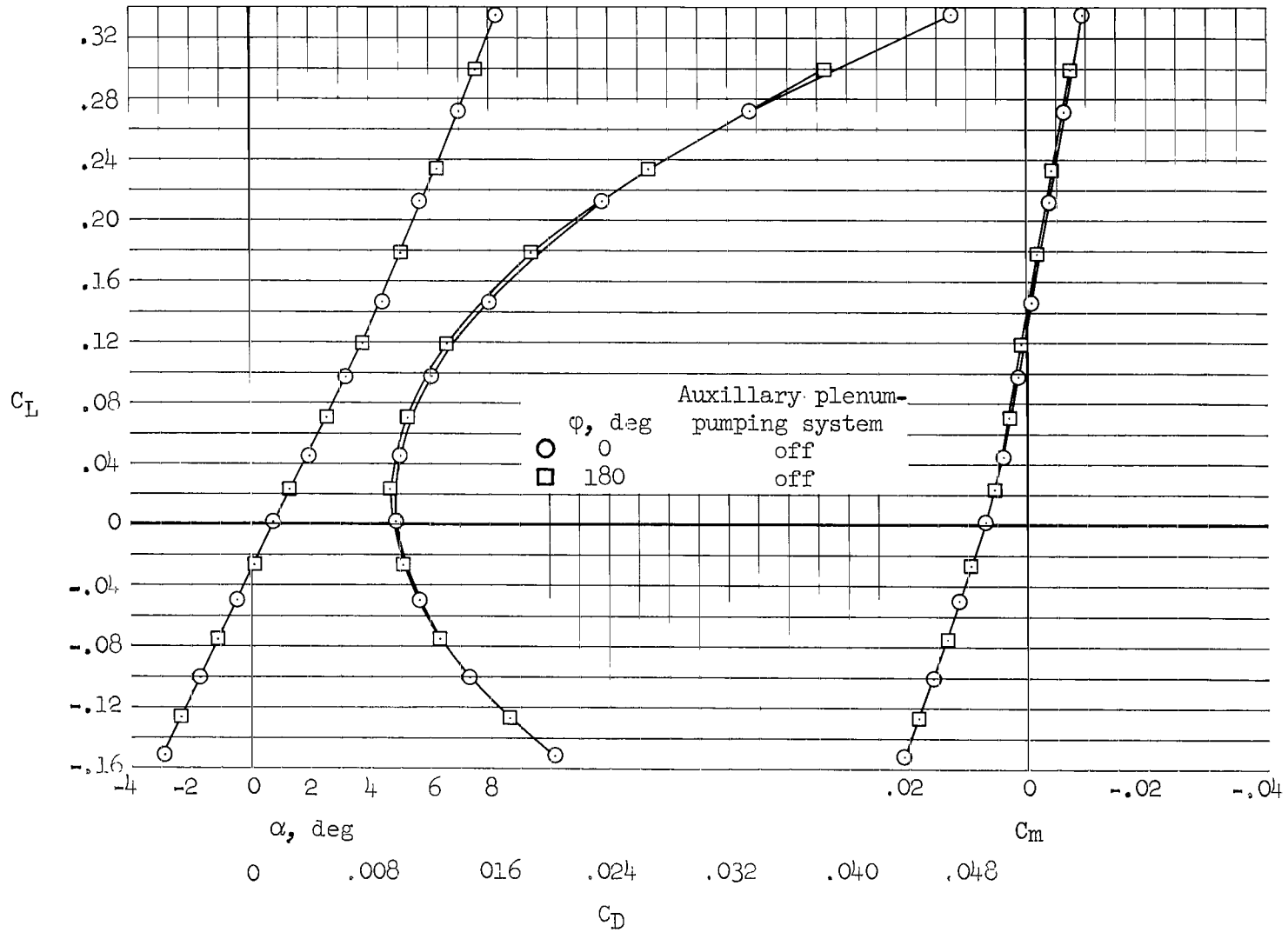

(d) M = 0.80

Figure 10.- Continued.

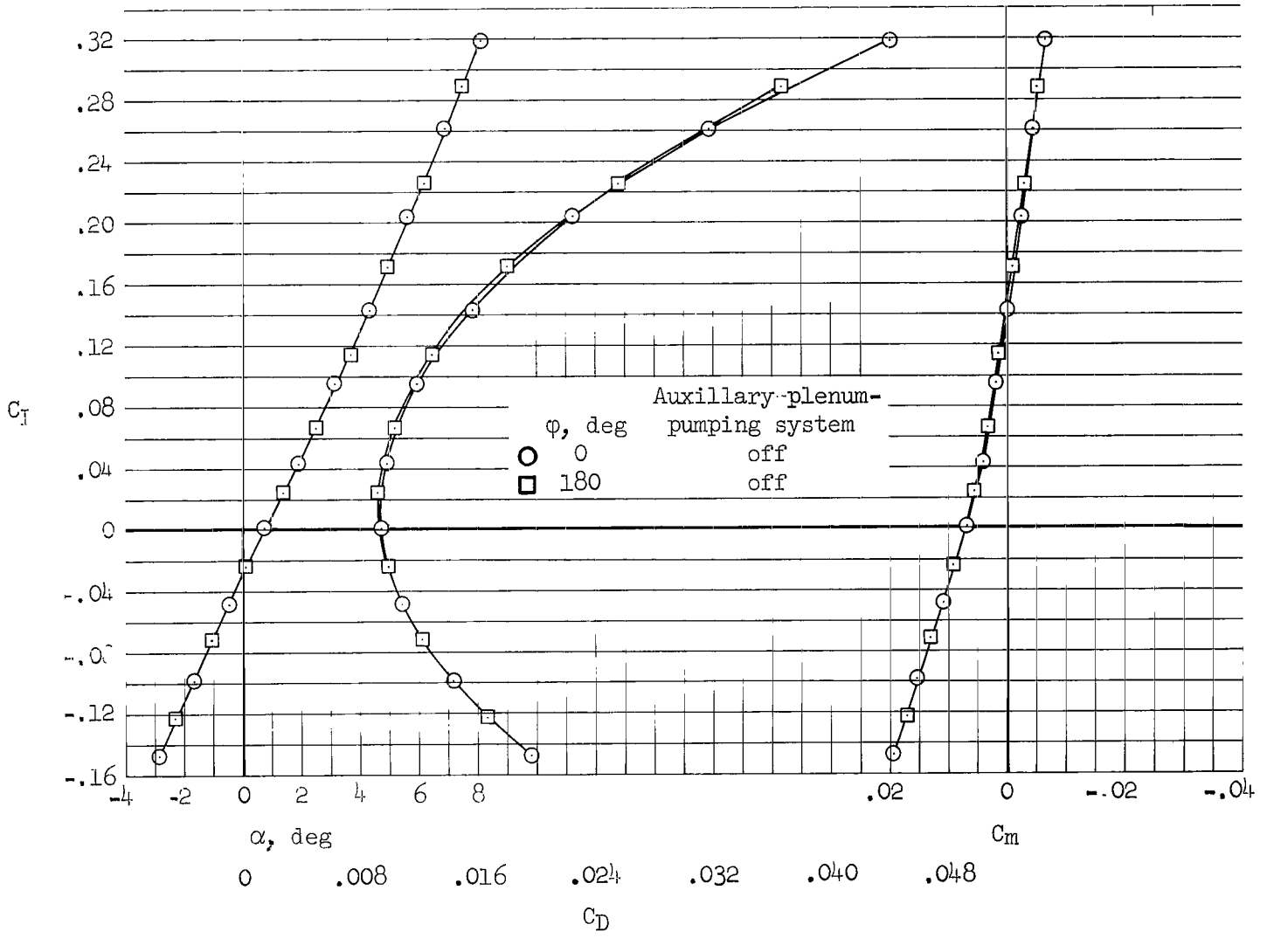

(e) M = 0.75

Figure 10.- Continued.

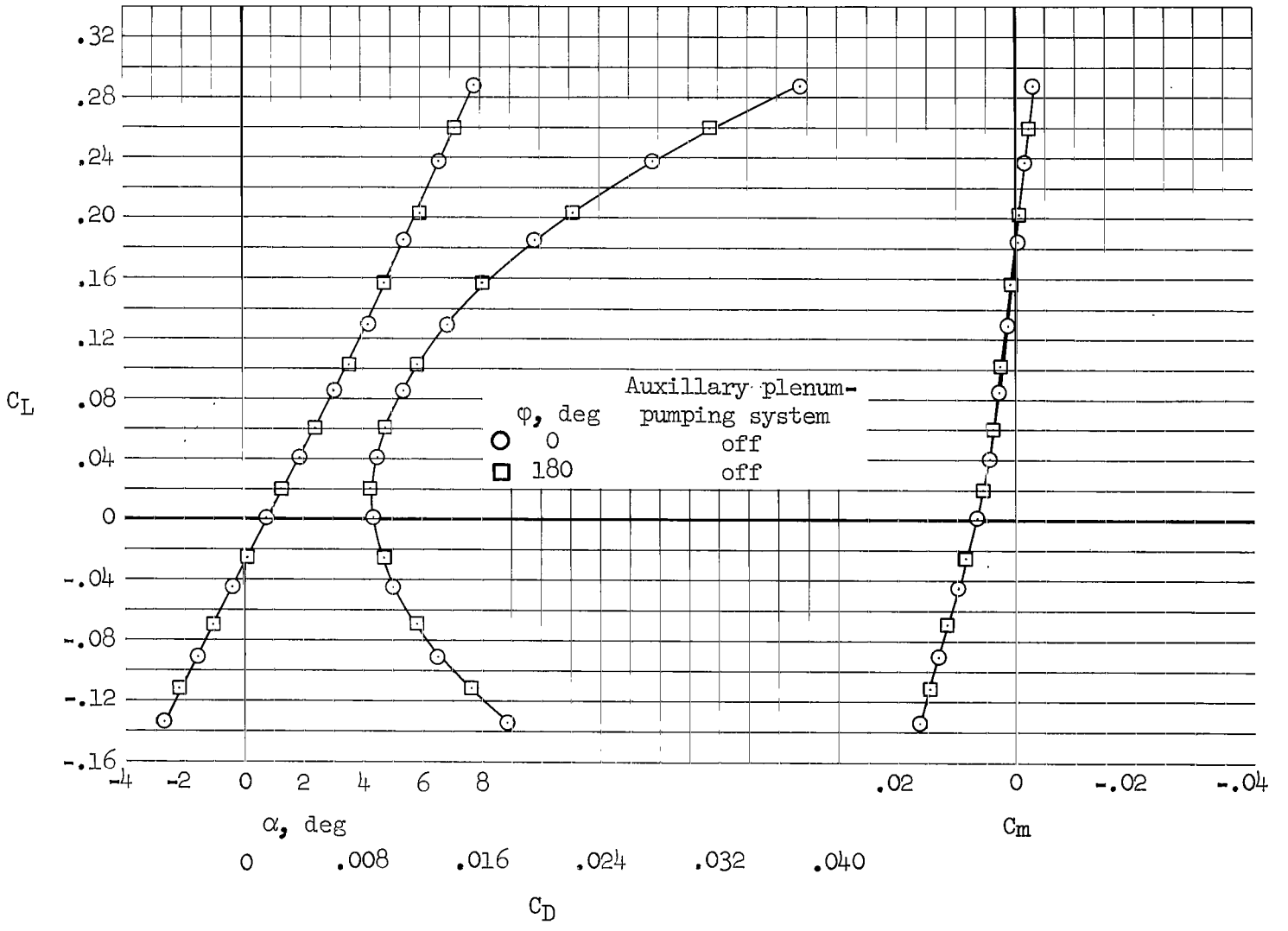

(f) M = 0.60

Figure 10.- Concluded.

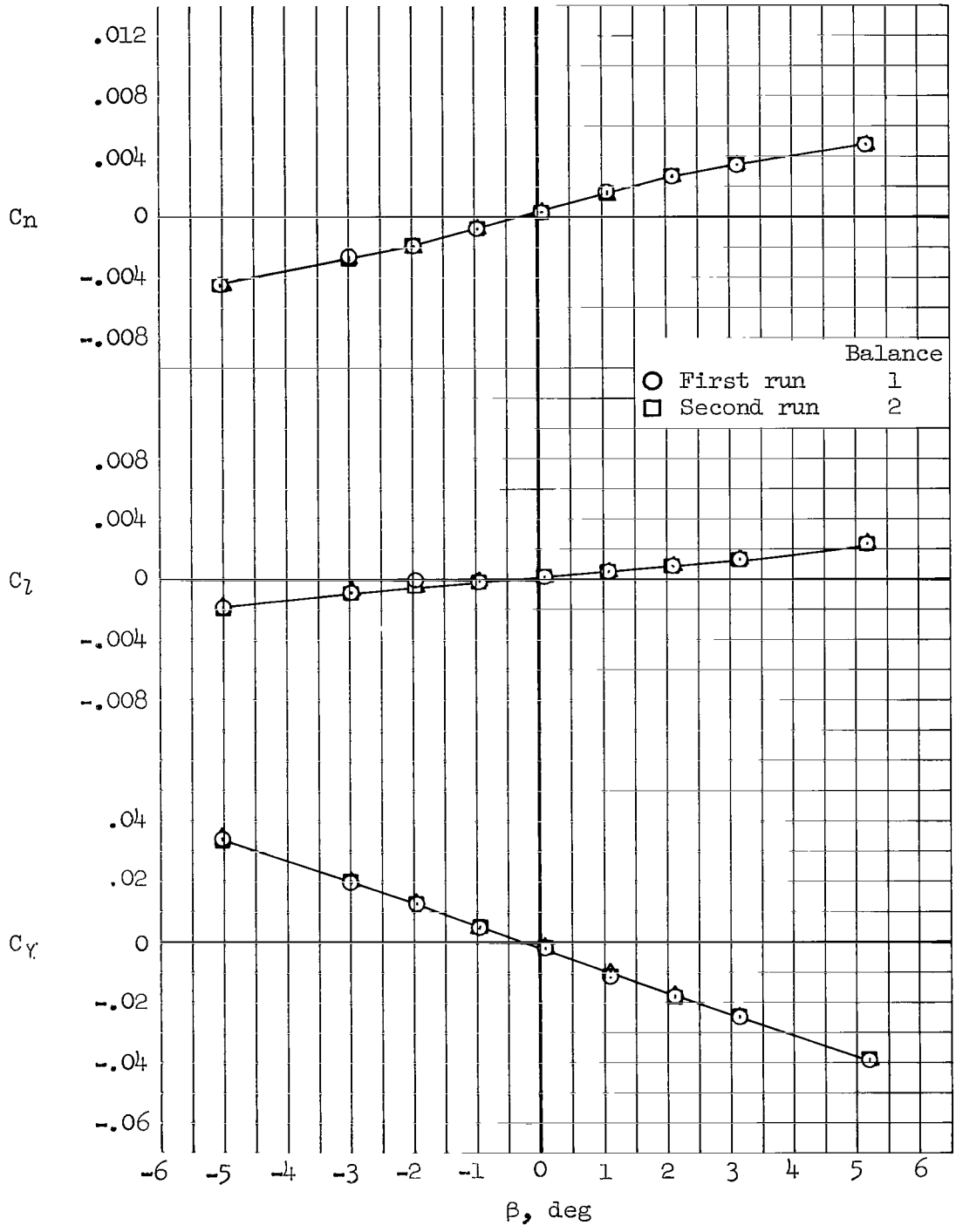

(a) M = 2.53, α = 4.5°

Figure 11.- Examples of repeatability of lateral-directional data for configuration $W_1E_2B_1K_1N_2C_1V_1G_1$, δ_y = 65°.

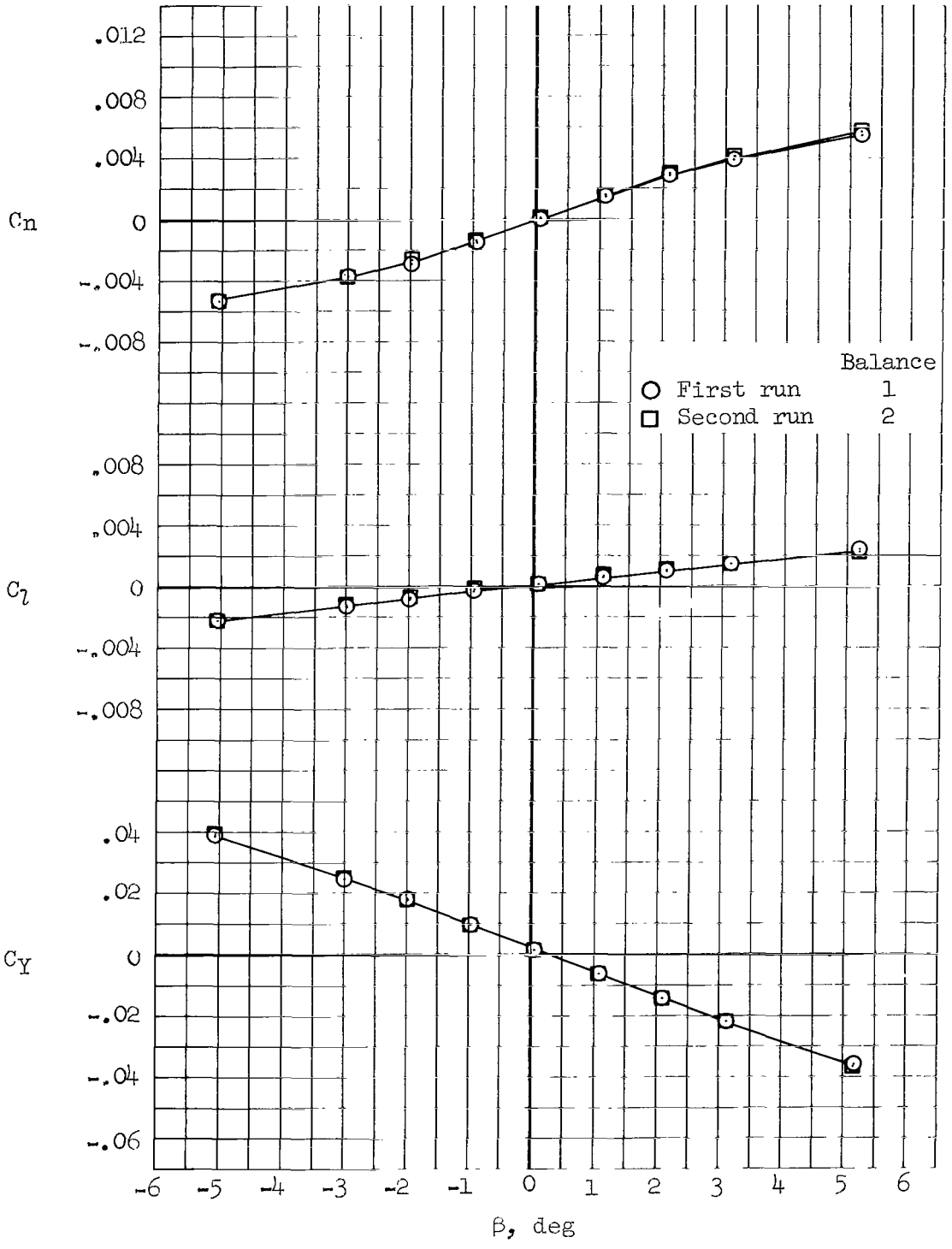

(b) M = 2.10, α = 4.6°

Figure 11.- Continued.

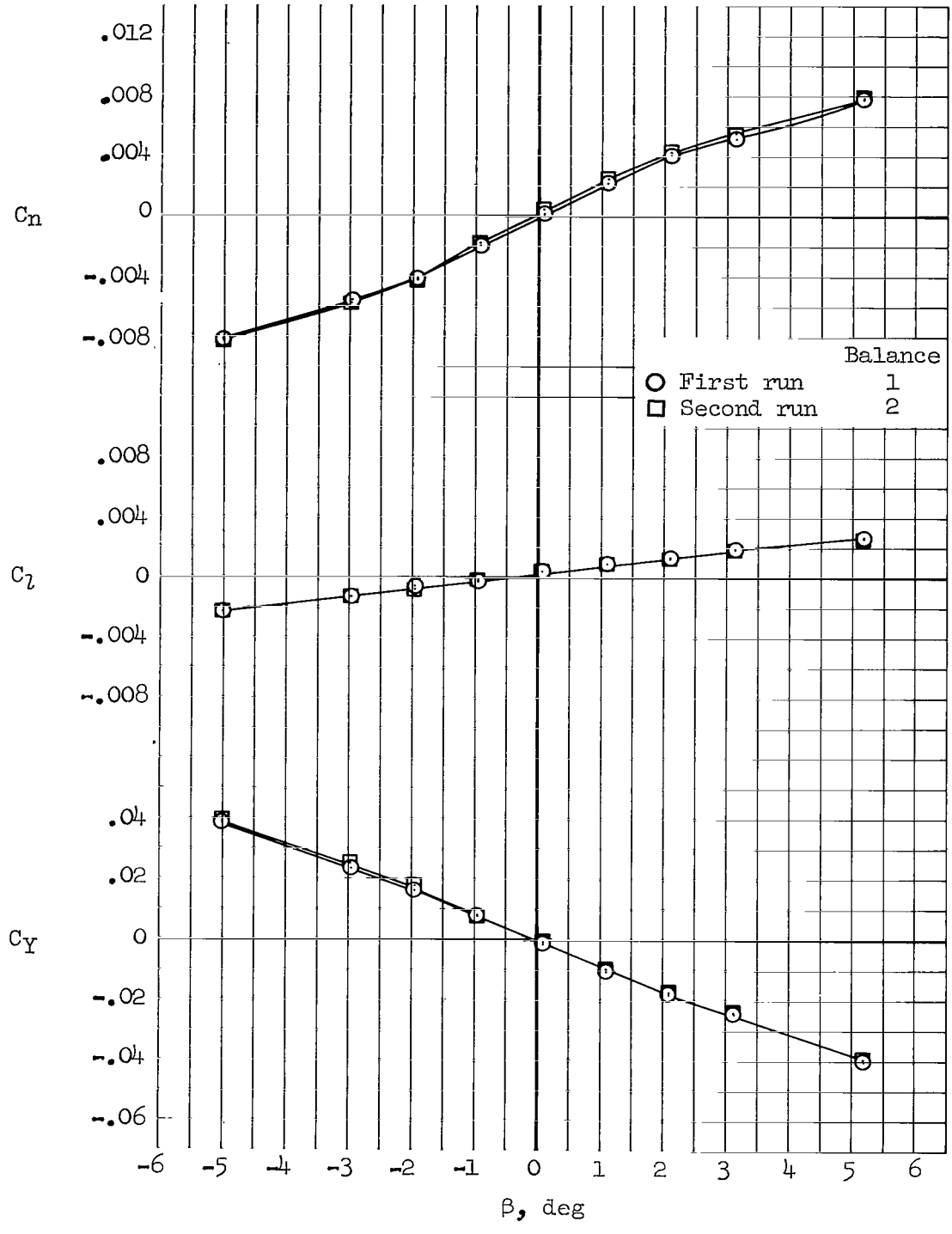

(c) M = 1.60, α = 4.8°

Figure 11.- Concluded.

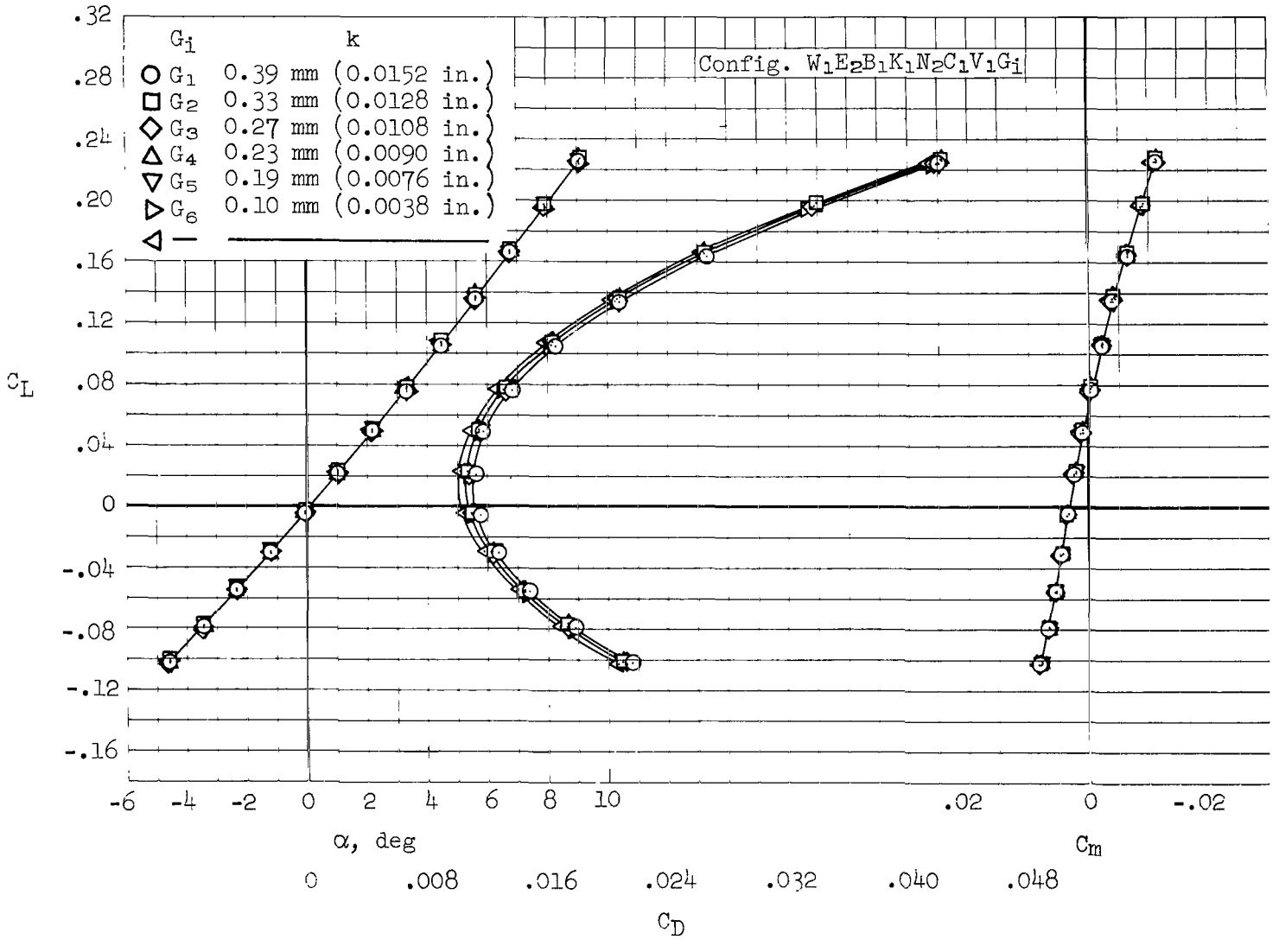

(a) M = 2.53, δ_y = 65°

Figure 12.- Effects of various sized transition-strip particles on longitudinal characteristics.

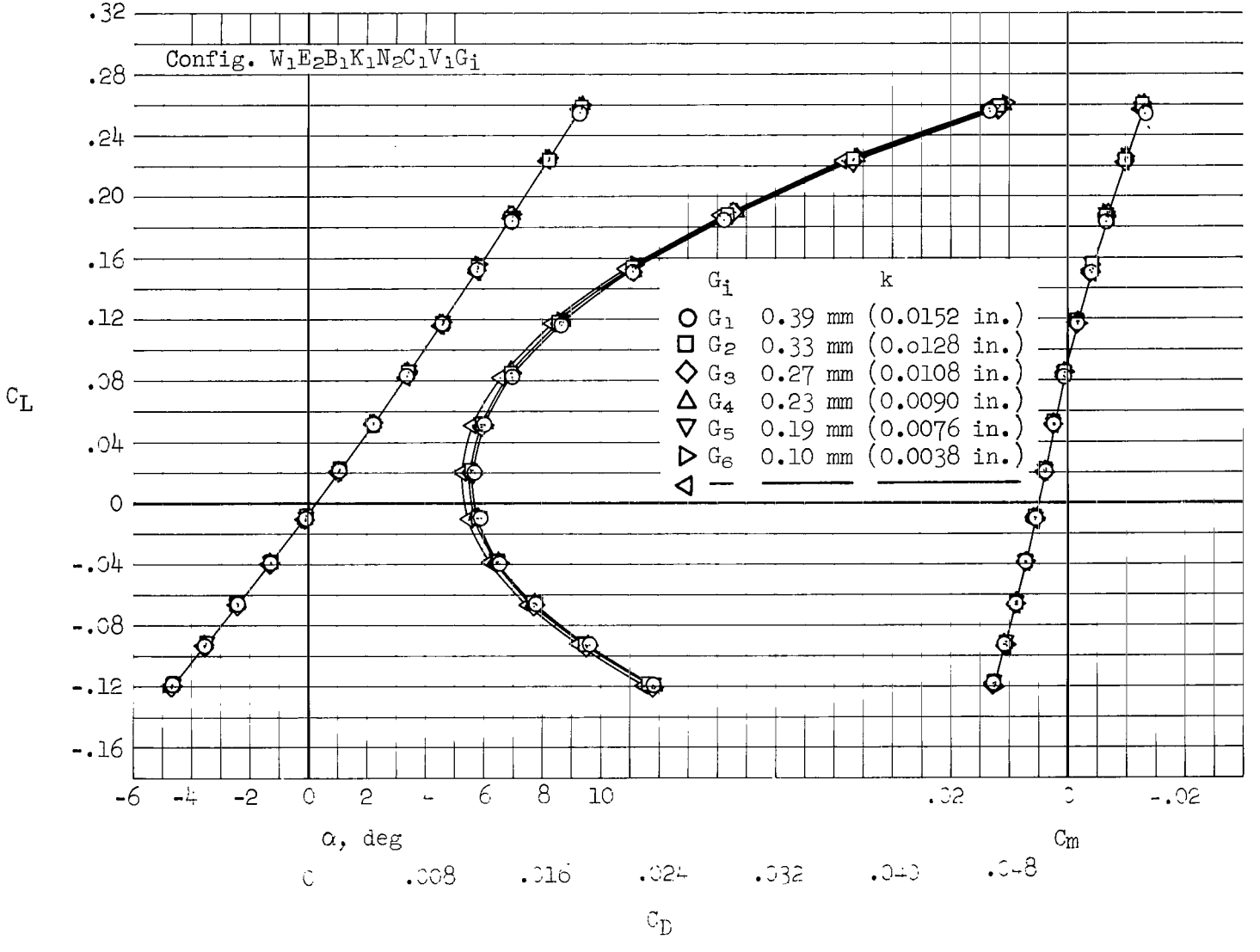

(b) M = 2.10, δ_y = 65°

Figure 12.- Continued.

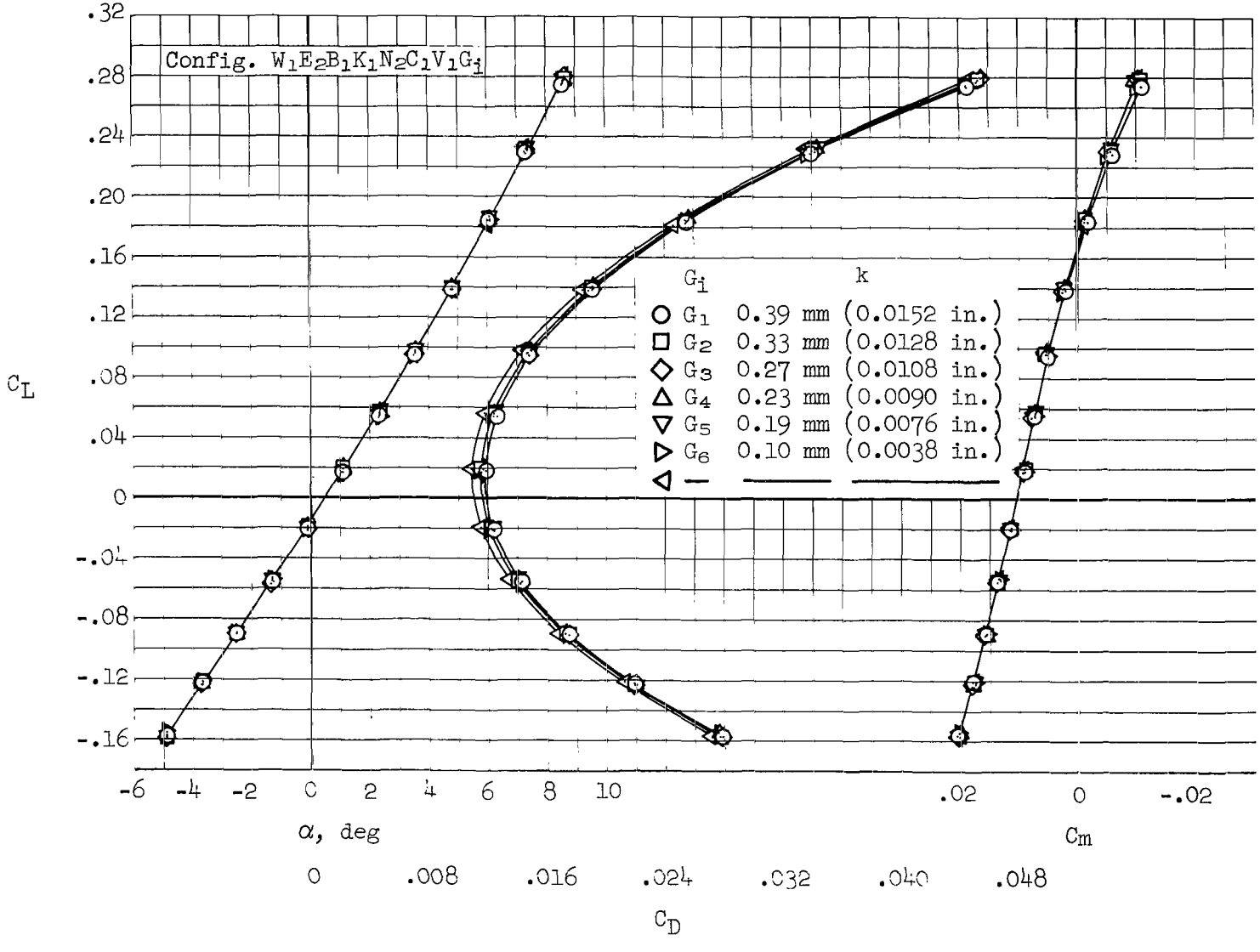

(c) M = 1.60, δ_y = 65°

Figure 12.- Continued.

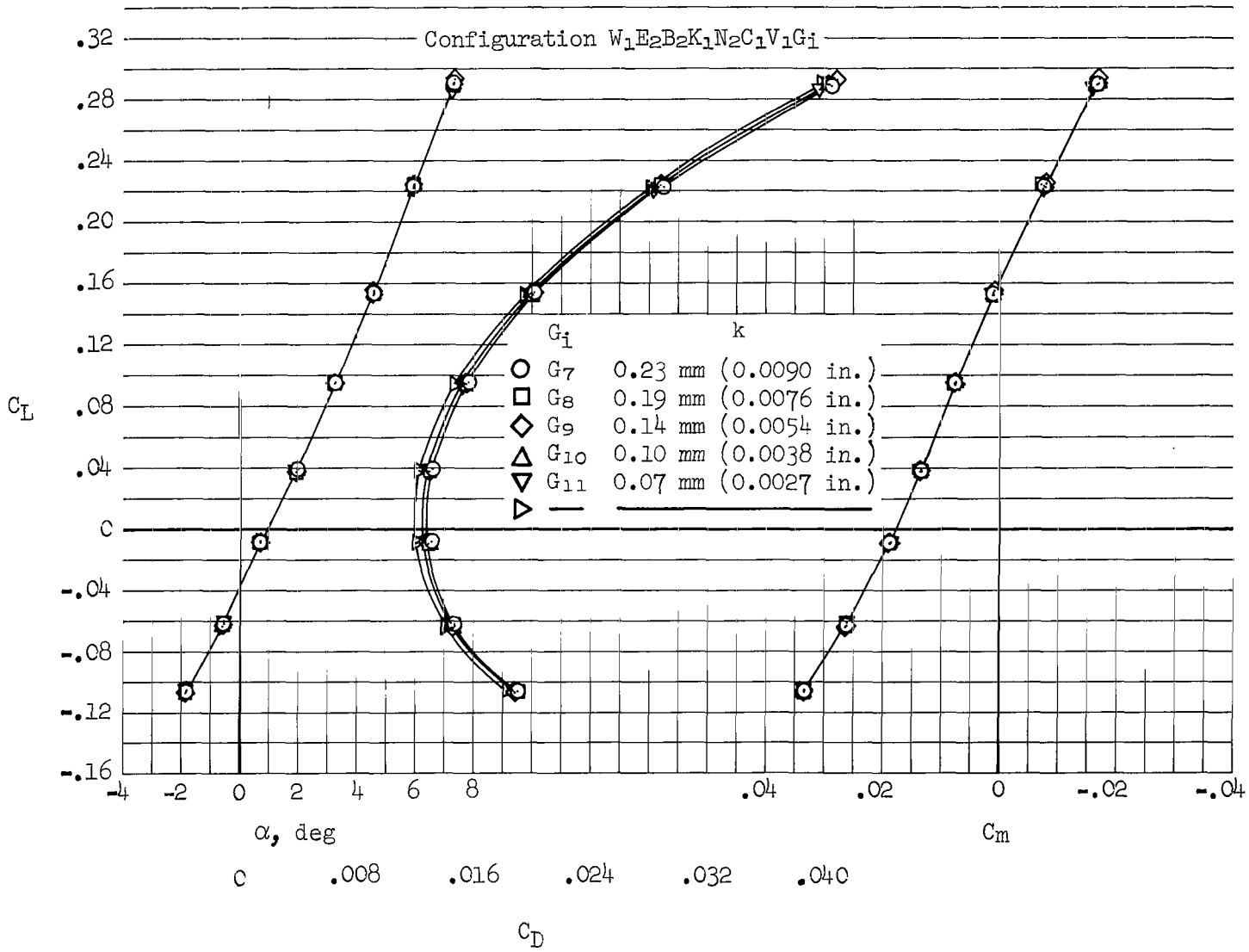

(d) M = 1.20, δ_y = 25°

Figure 12.- Continued.

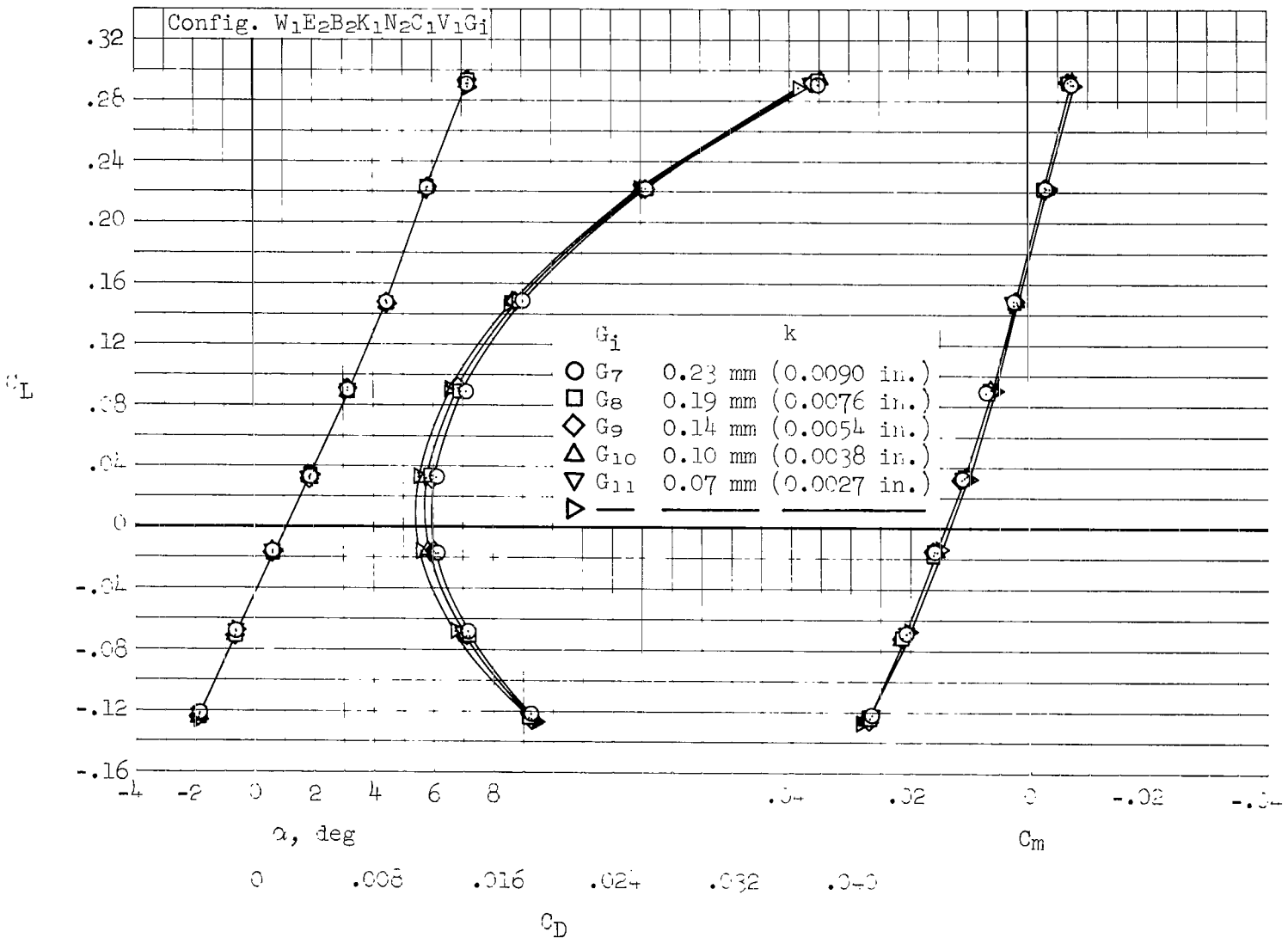

(e) M = 0.95, δ_y = 25°

Figure 12.- Continued.

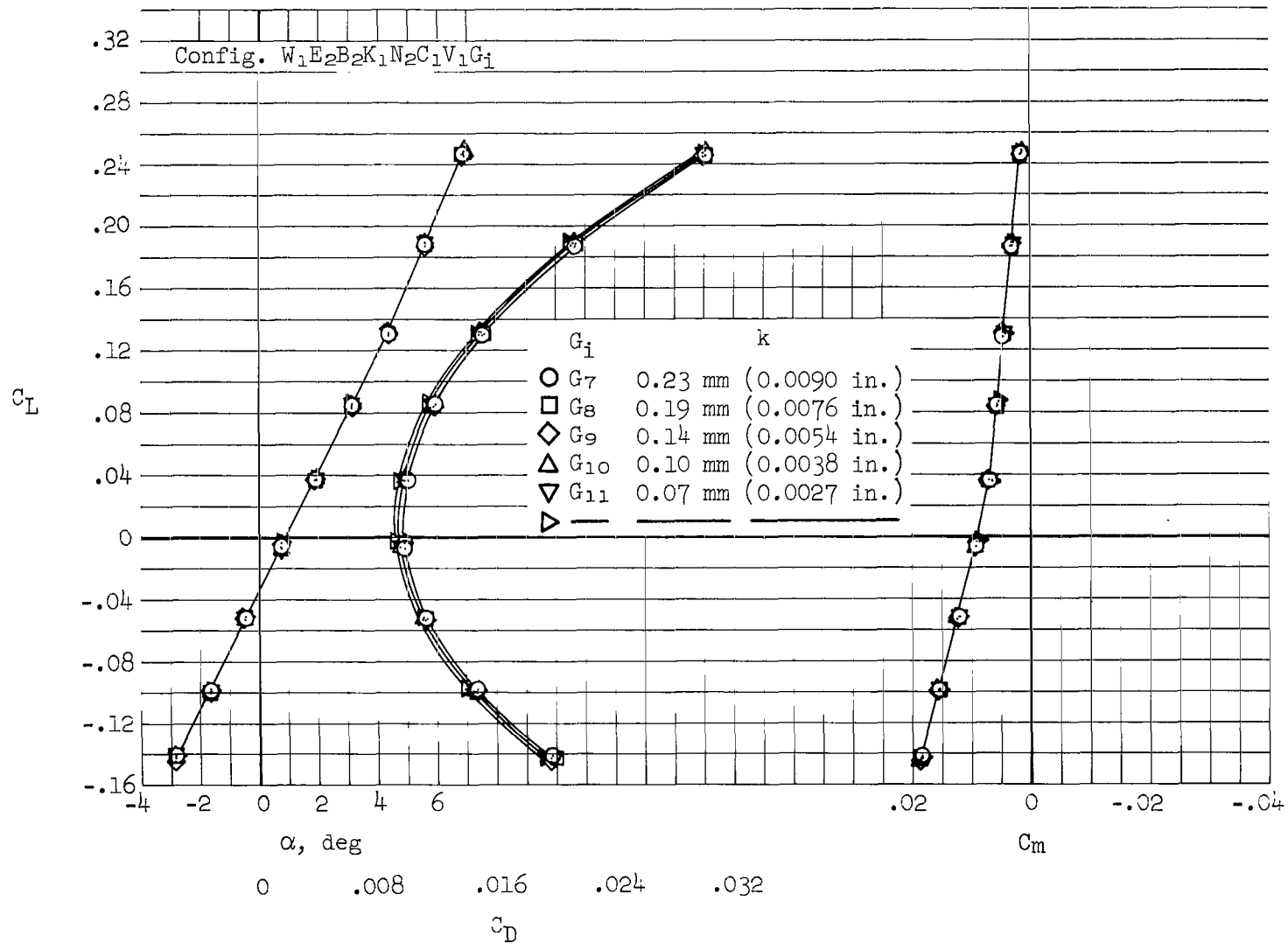

(f) M = 0.75, δ_y = 25°

Figure 12.- Concluded.

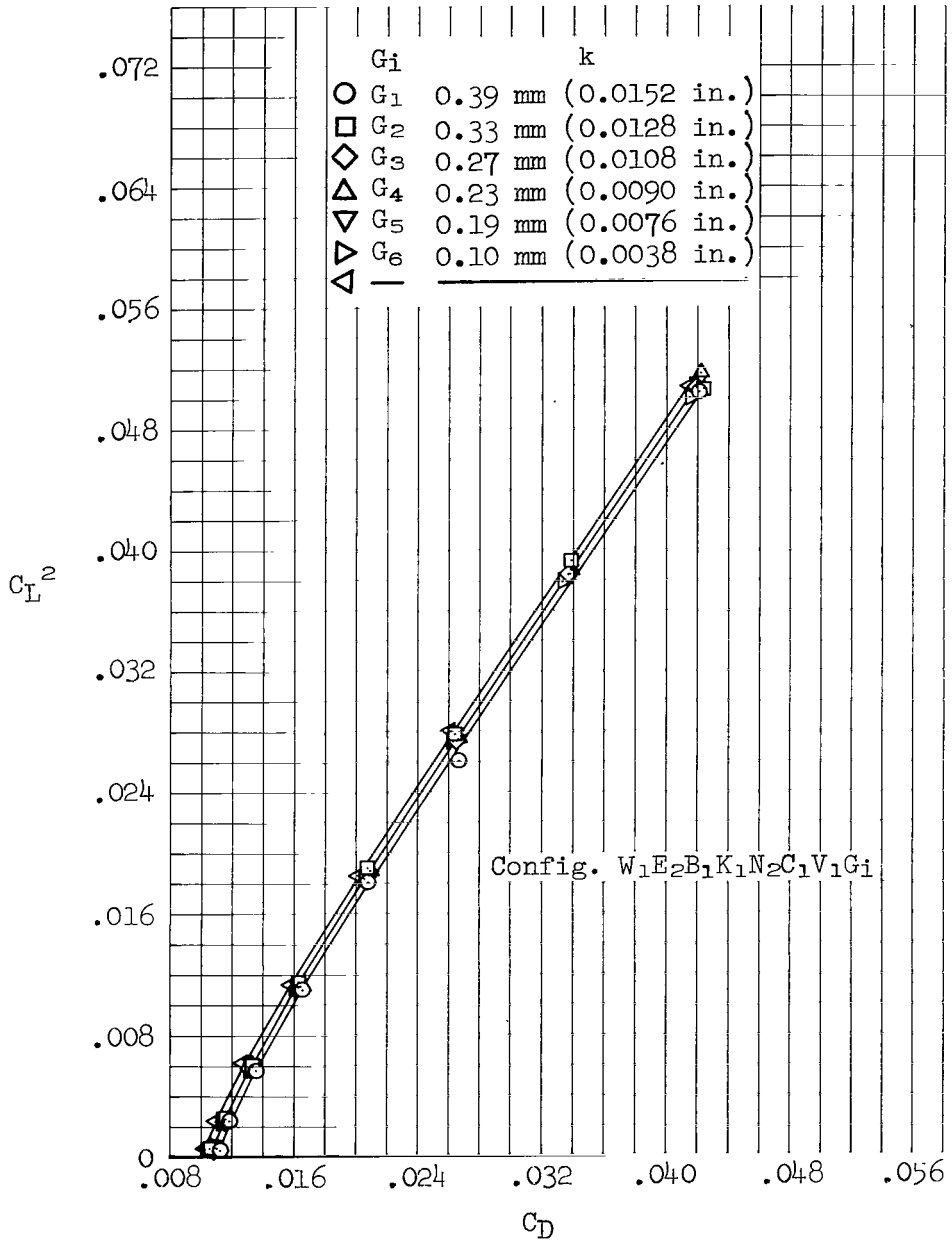

(a) M = 2.53, δ_y = 65°

Figure 13.- Effects of various sized transition-strip particles on drag characteristics.

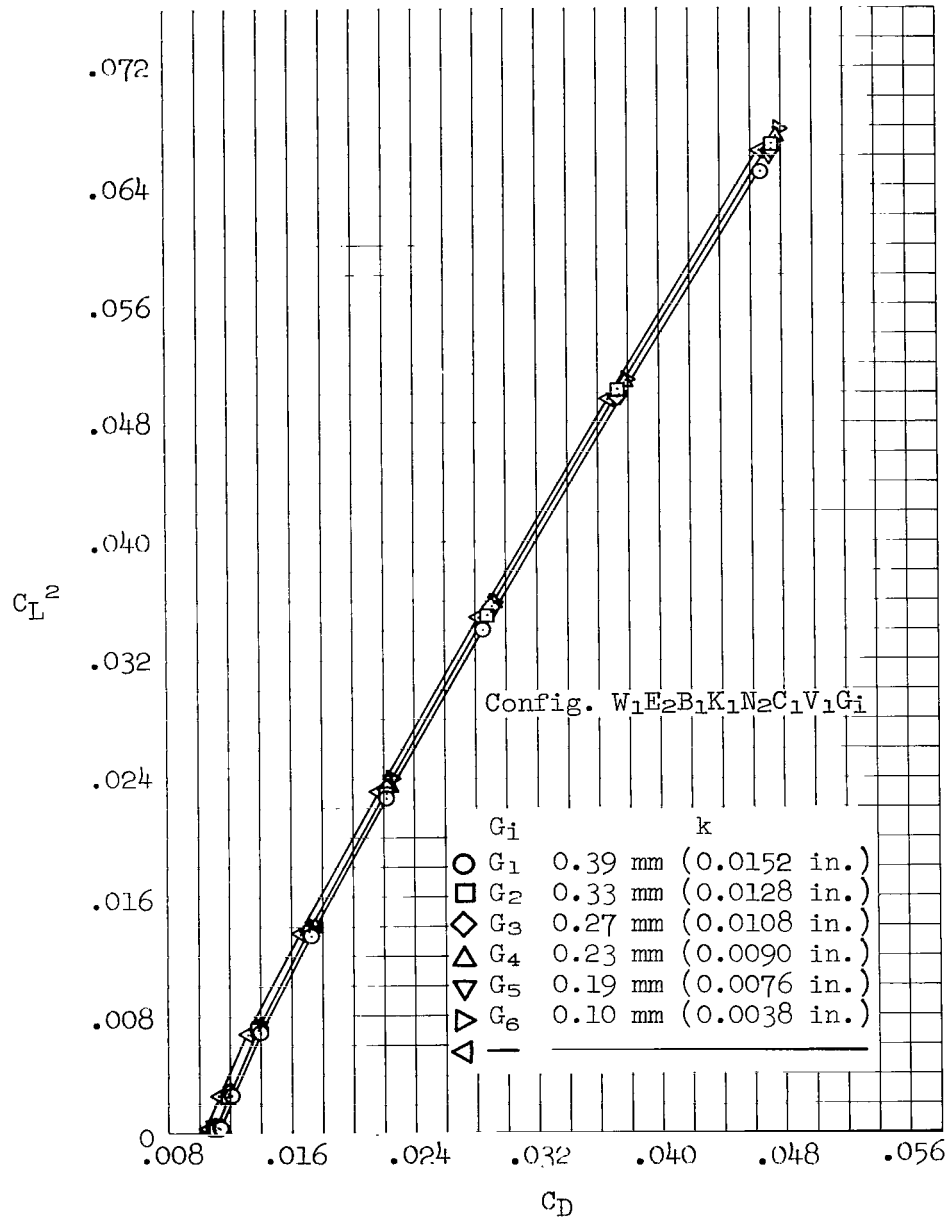

(b) M = 2.10, δ_y = 65°

Figure 13.- Continued.

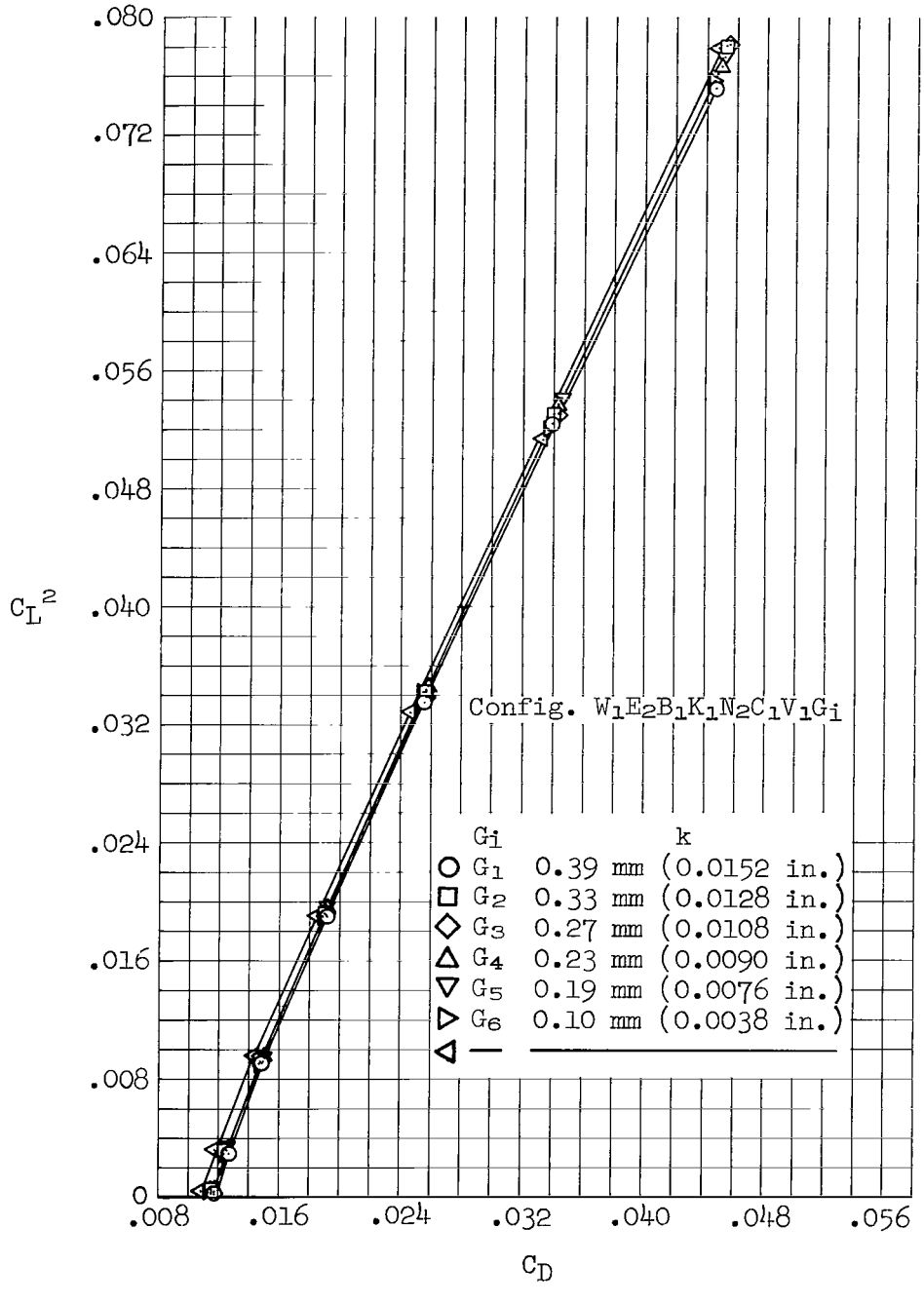

(c) M - 1.60, δ_y = 65°

Figure 13.- Continued.

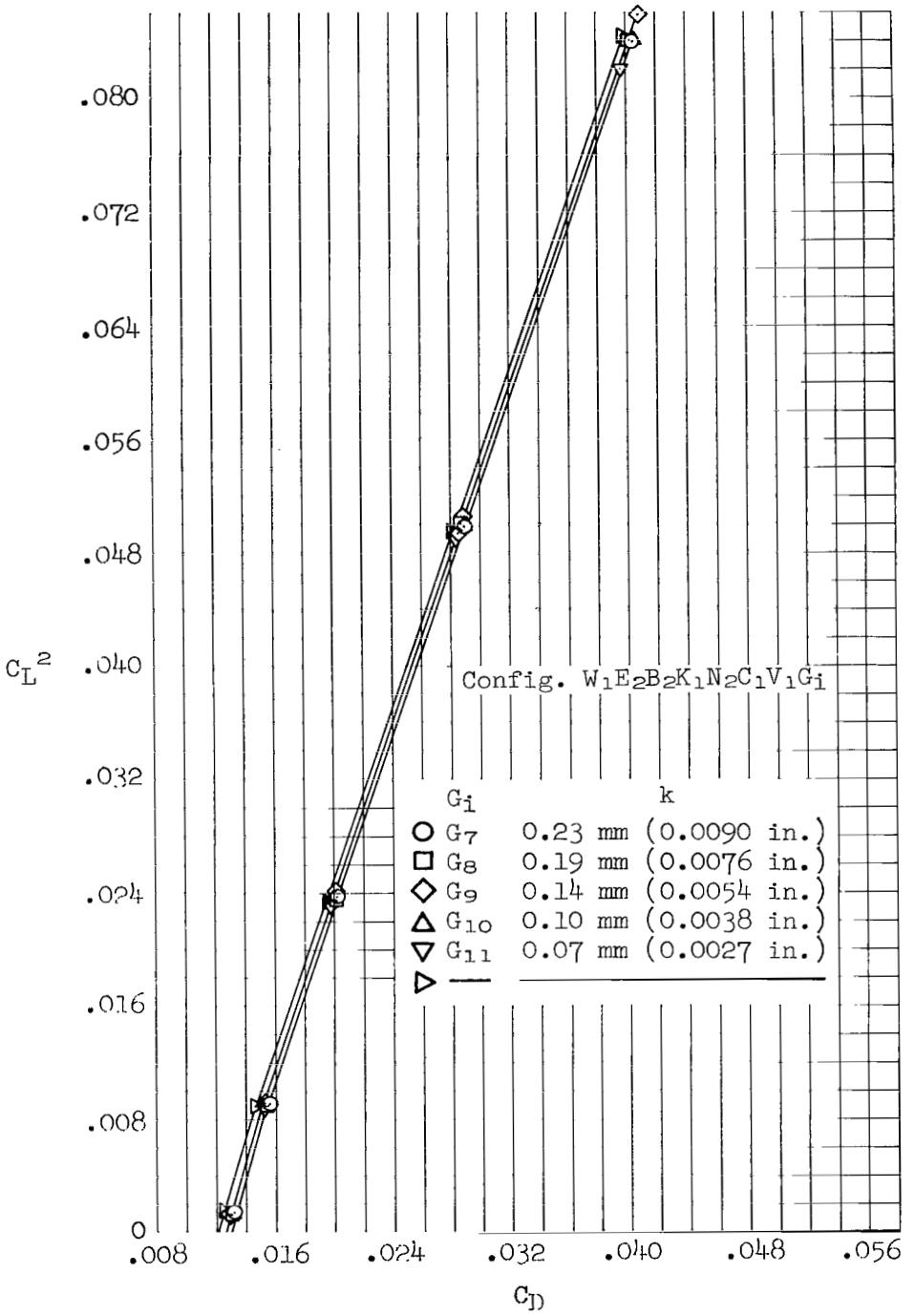

(d) M - 1.20, δ_y = 25°

Figure 13.- Continued.

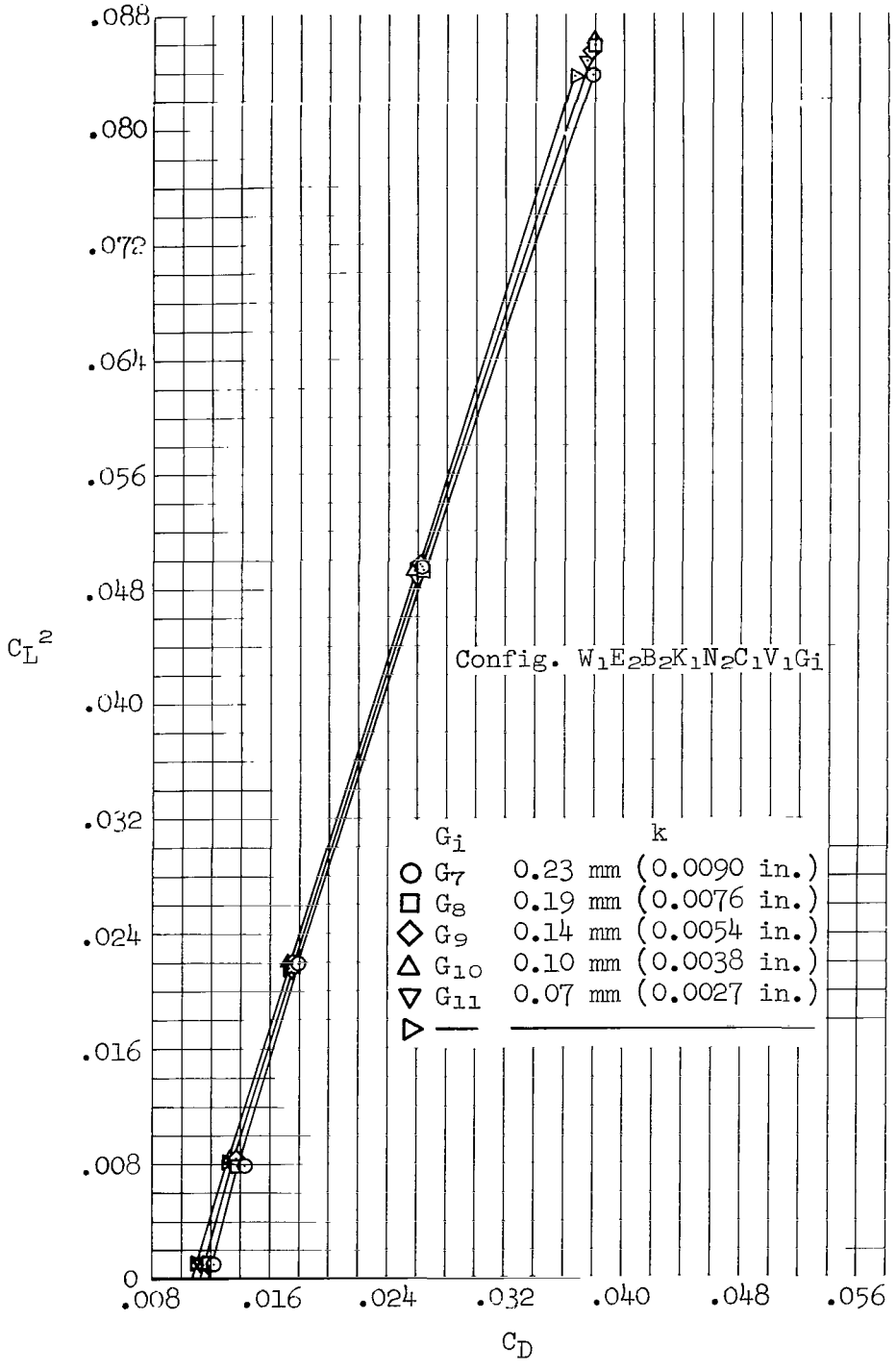

(e) M = 0.95, δ_y = 25°

Figure 13.- Continued.

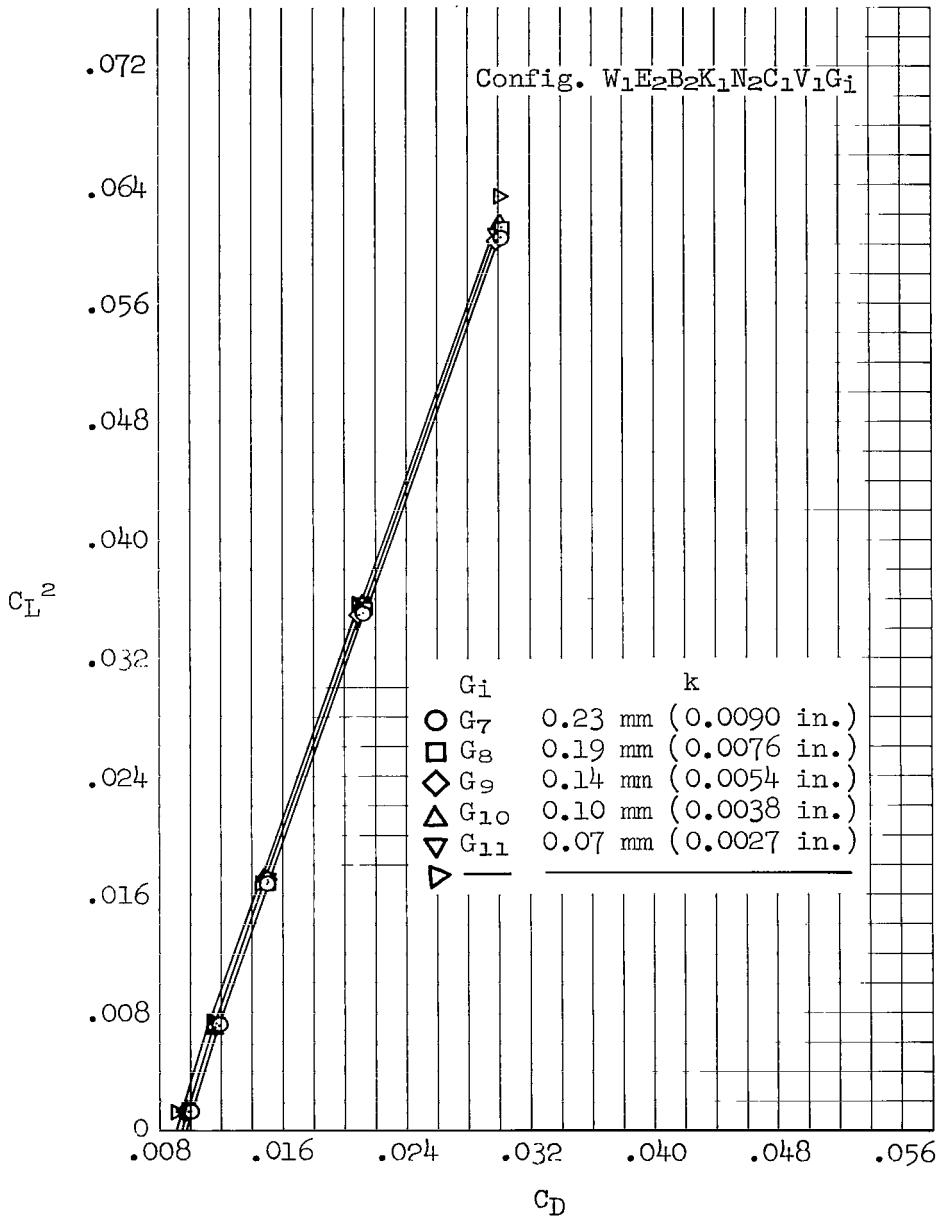

(f) M = 0.75, δ_y = 25°

Figure 13.- Concluded.

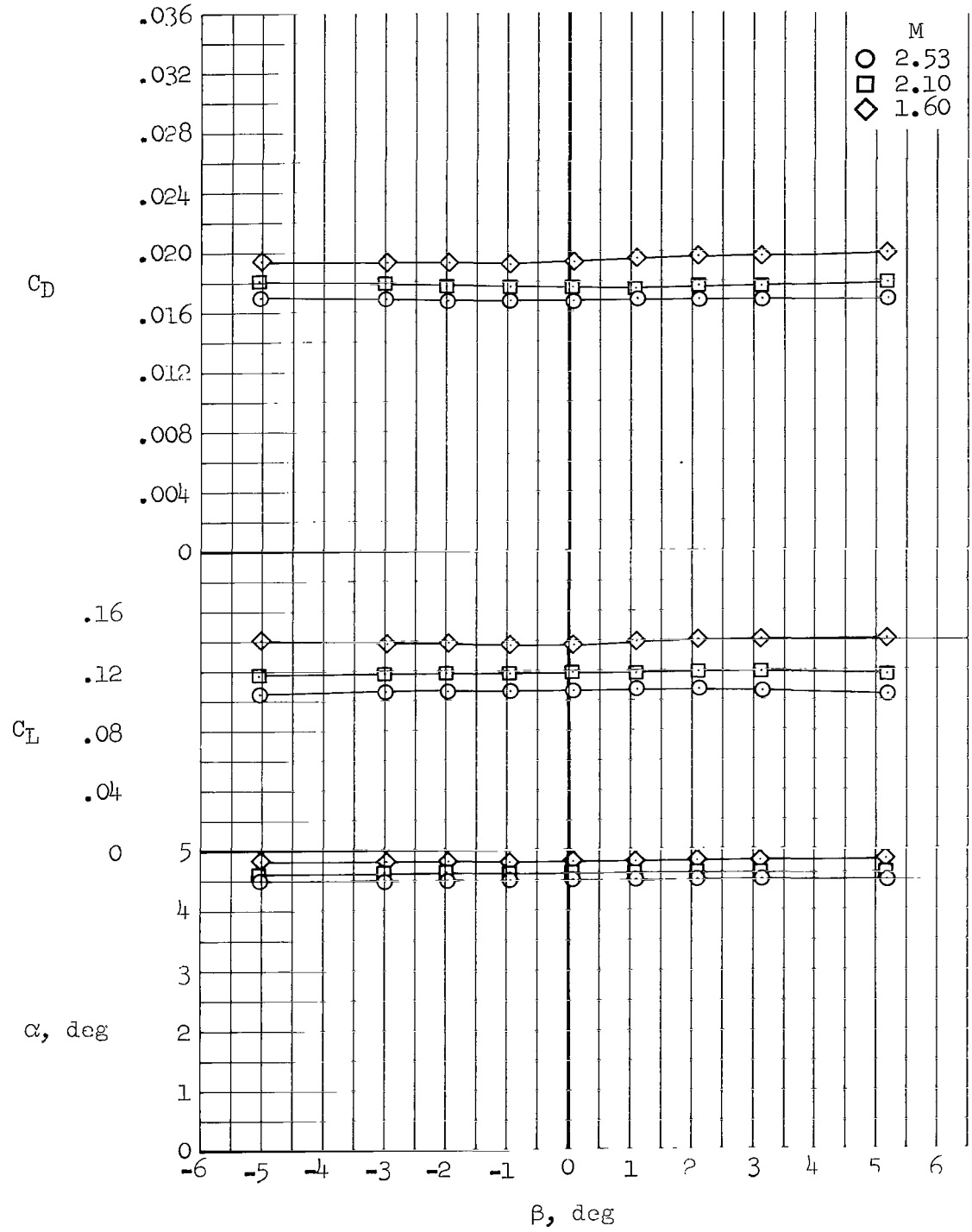

Figure 14.- Effects of sideslip angle on the lift and drag characteristics of configuration $W_1E_2B_1K_1N_2C_1V_1G_1$, $\delta_y = 65°$.

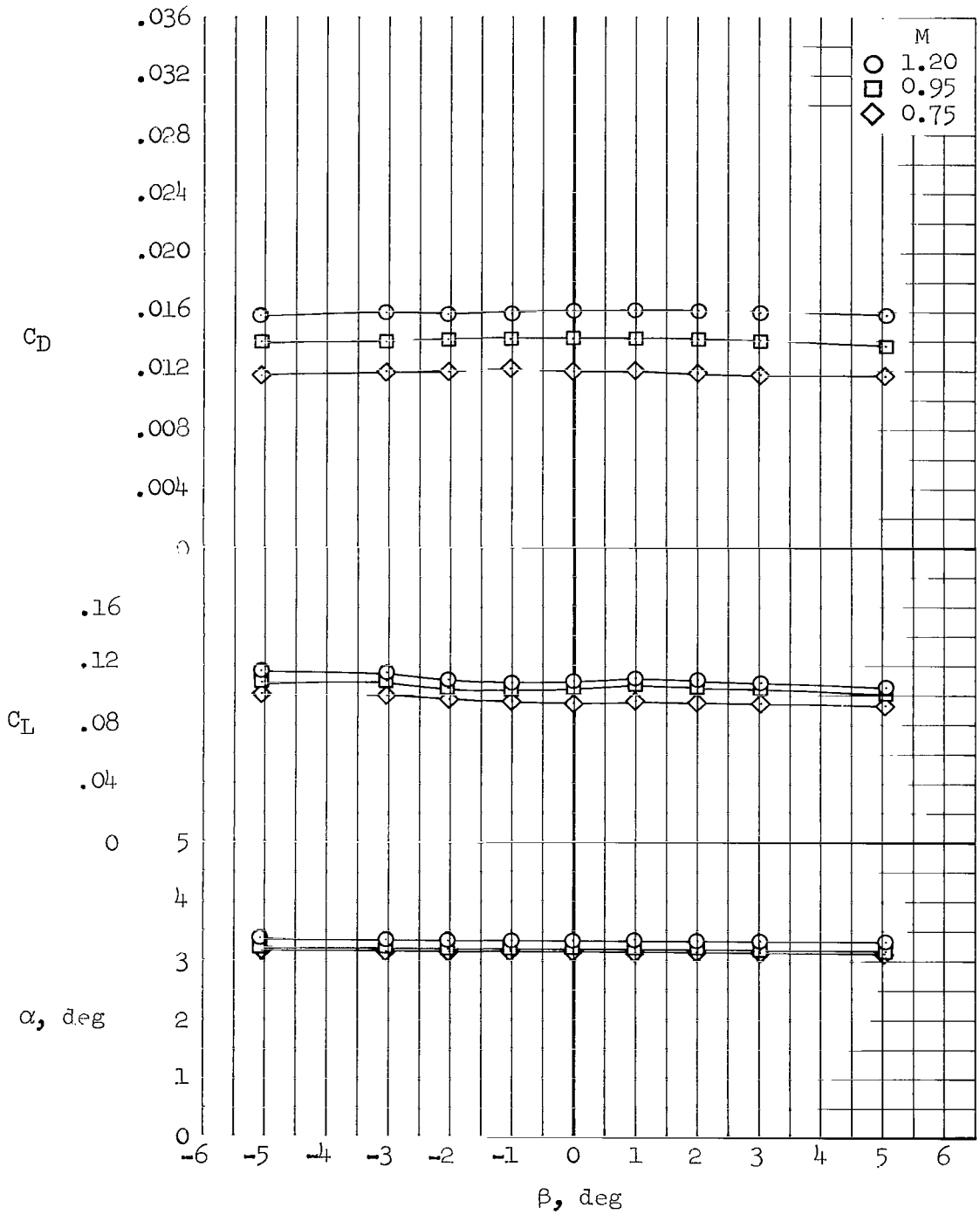

Figure 15.- Effects of sideslip angle on the lift and drag characteristics of configuration $W_1E_1B_2K_1N_2C_1V_1G_7$, $\delta_y = 0°$.

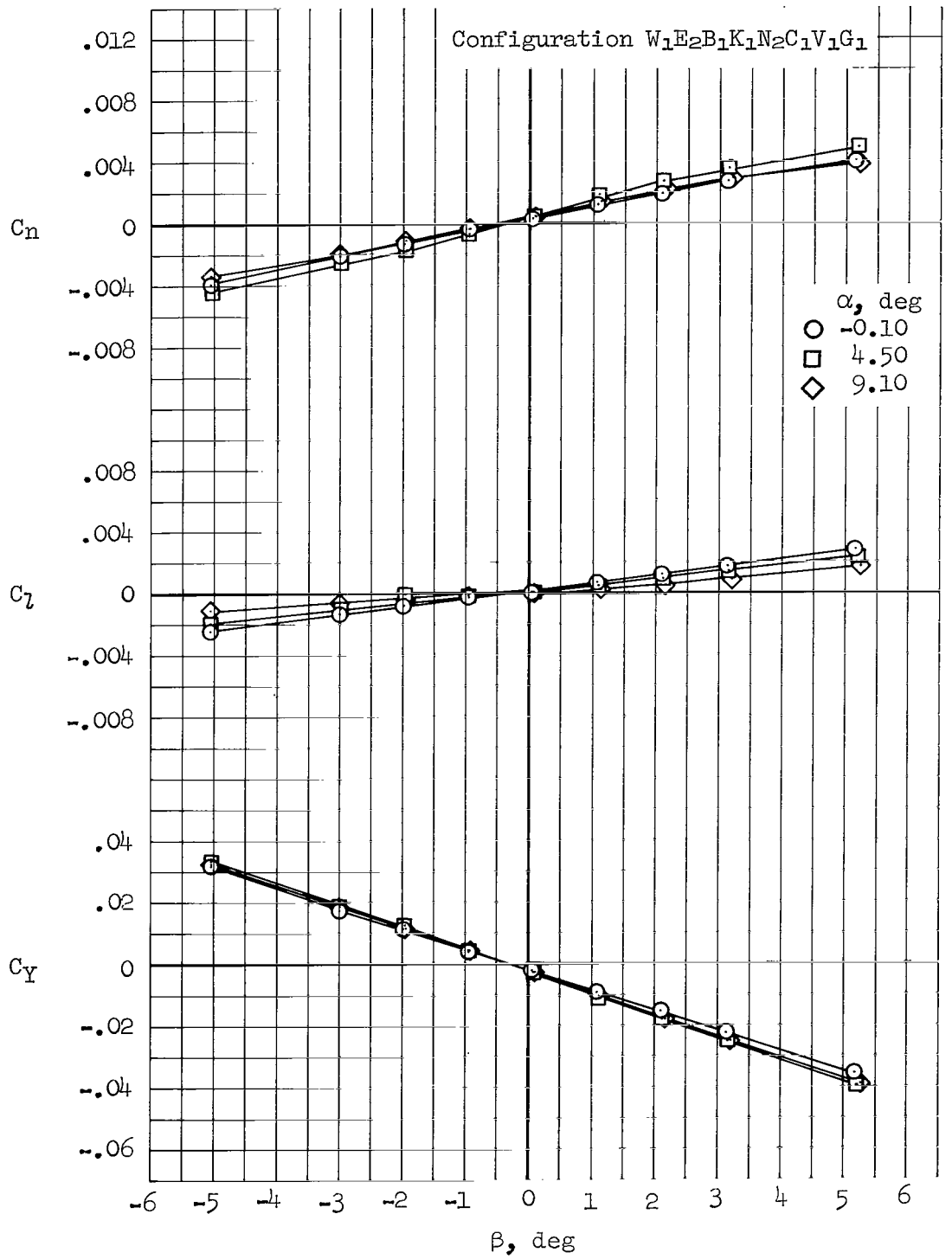

(a) M = 2.53, δ_y = 65°

Figure 16.- Effects of angle of attack on lateral-directional characteristics.

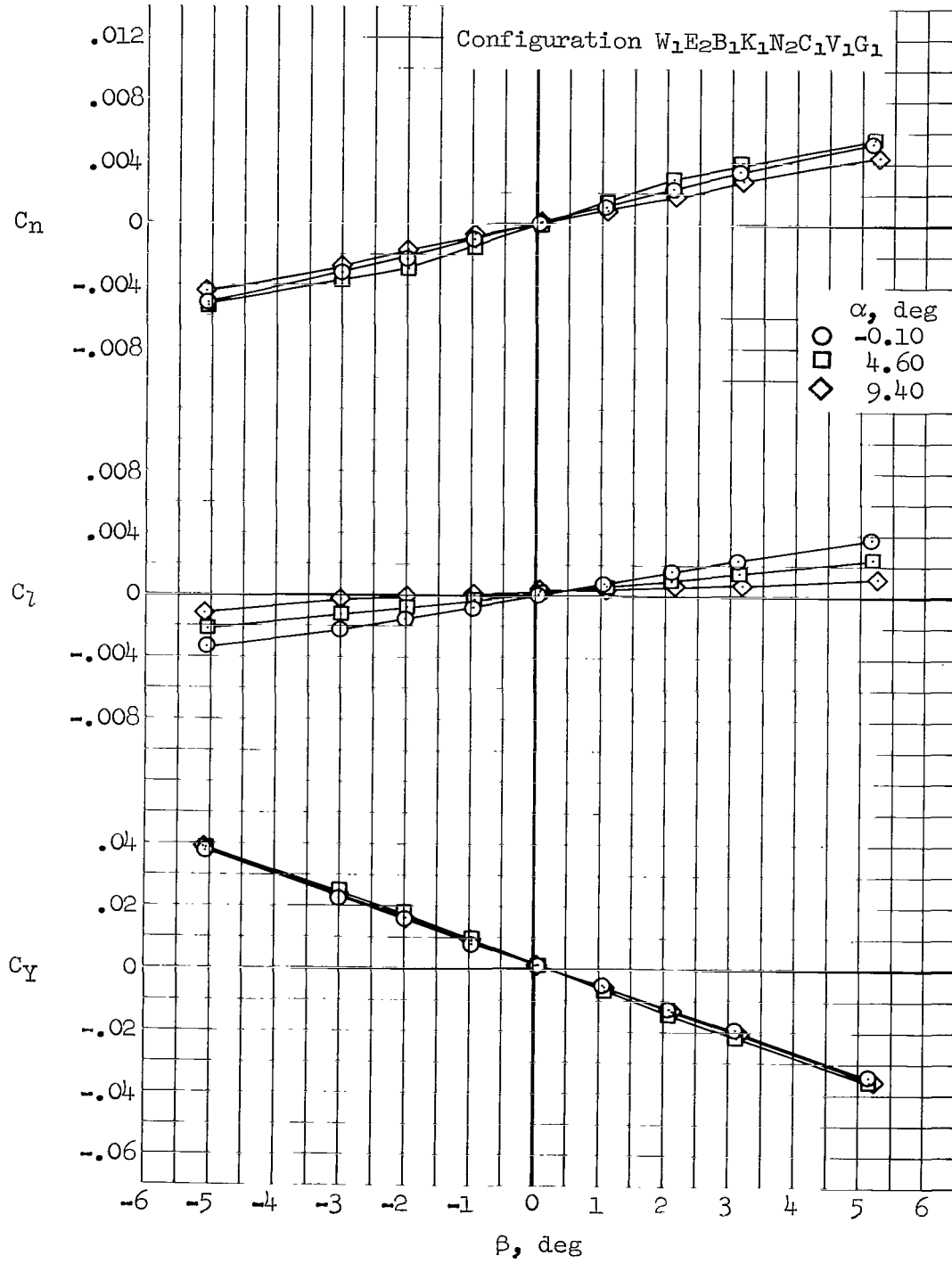

(b) M = 2.10, δ_y = 65°

Figure 16.- Continued.

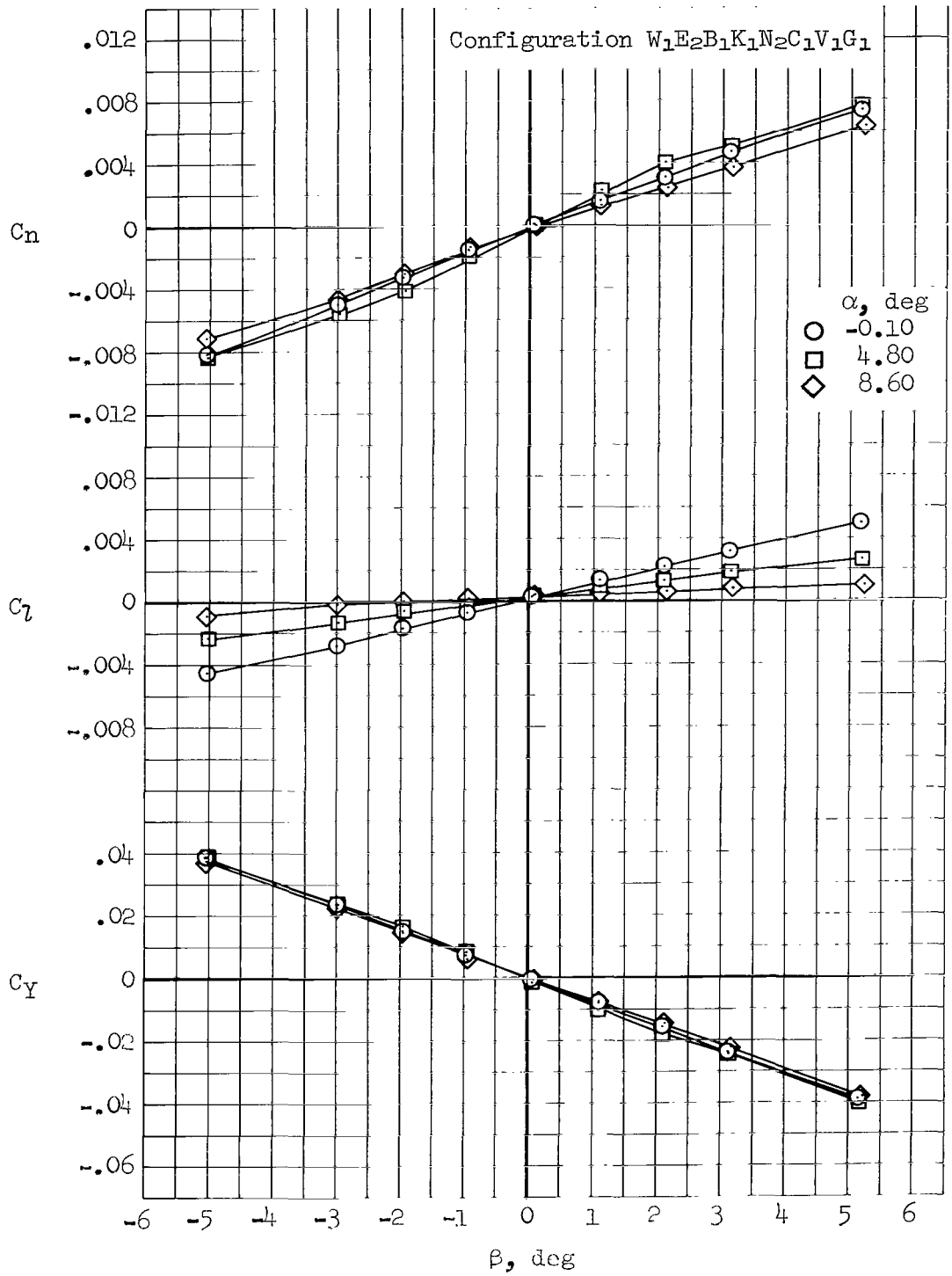

(c) M = 1.60, δ_y = 65°

Figure 16.- Continued.

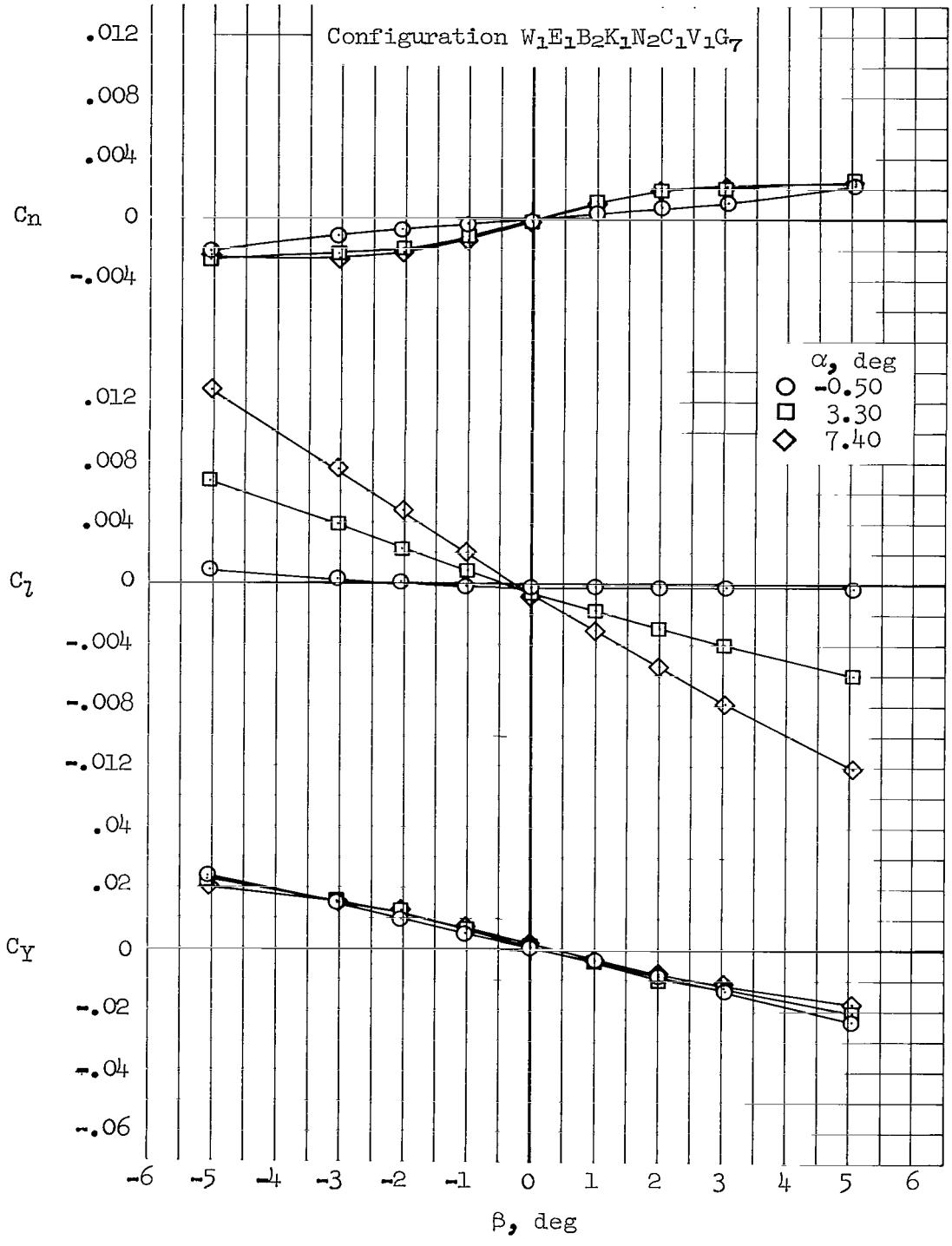

(d) M = 1.20, δ_y = 0°

Figure 16.- Continued.

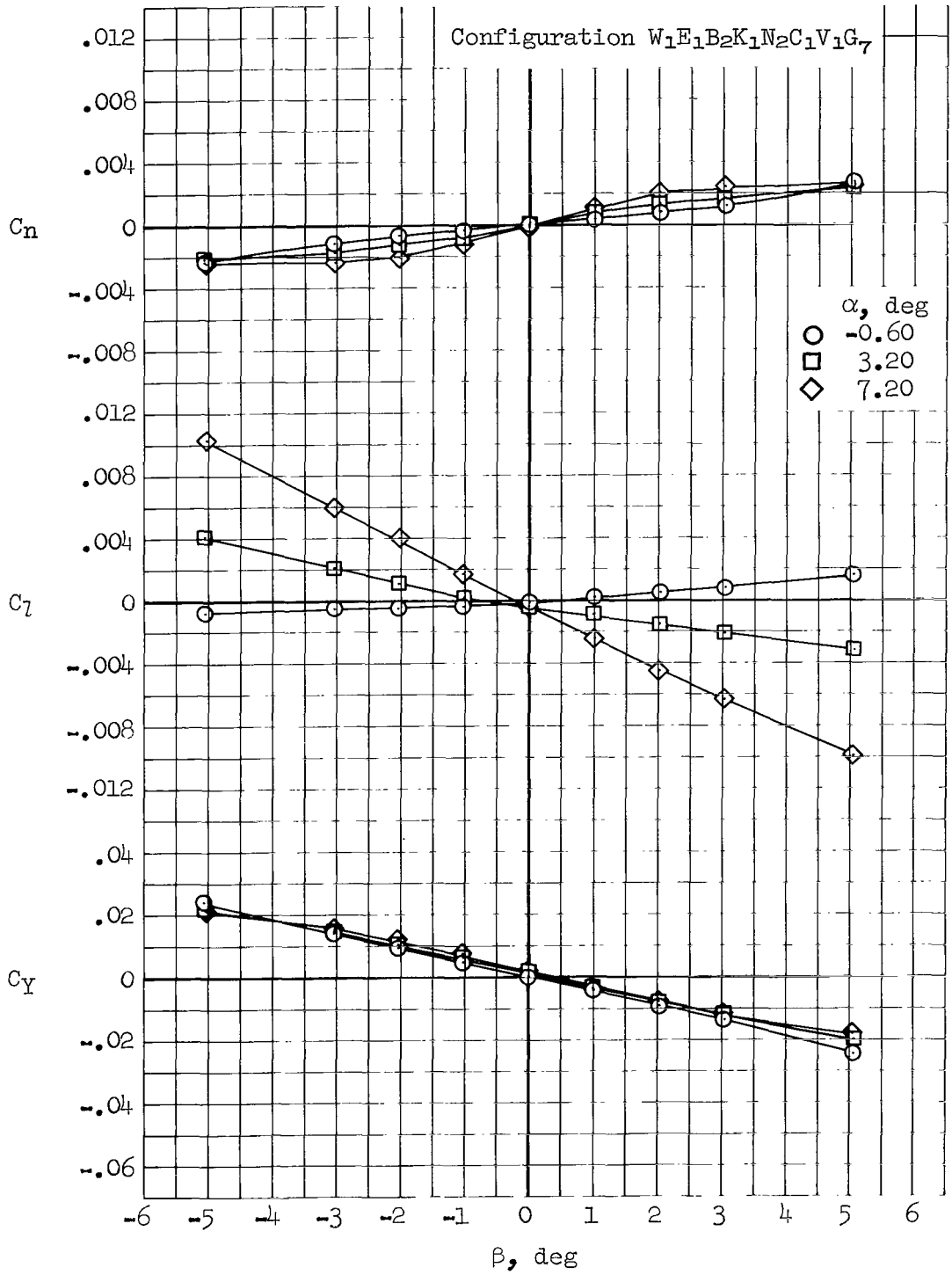

(e) M = 0.95, δ_y = 0°

Figure 16.- Continued.

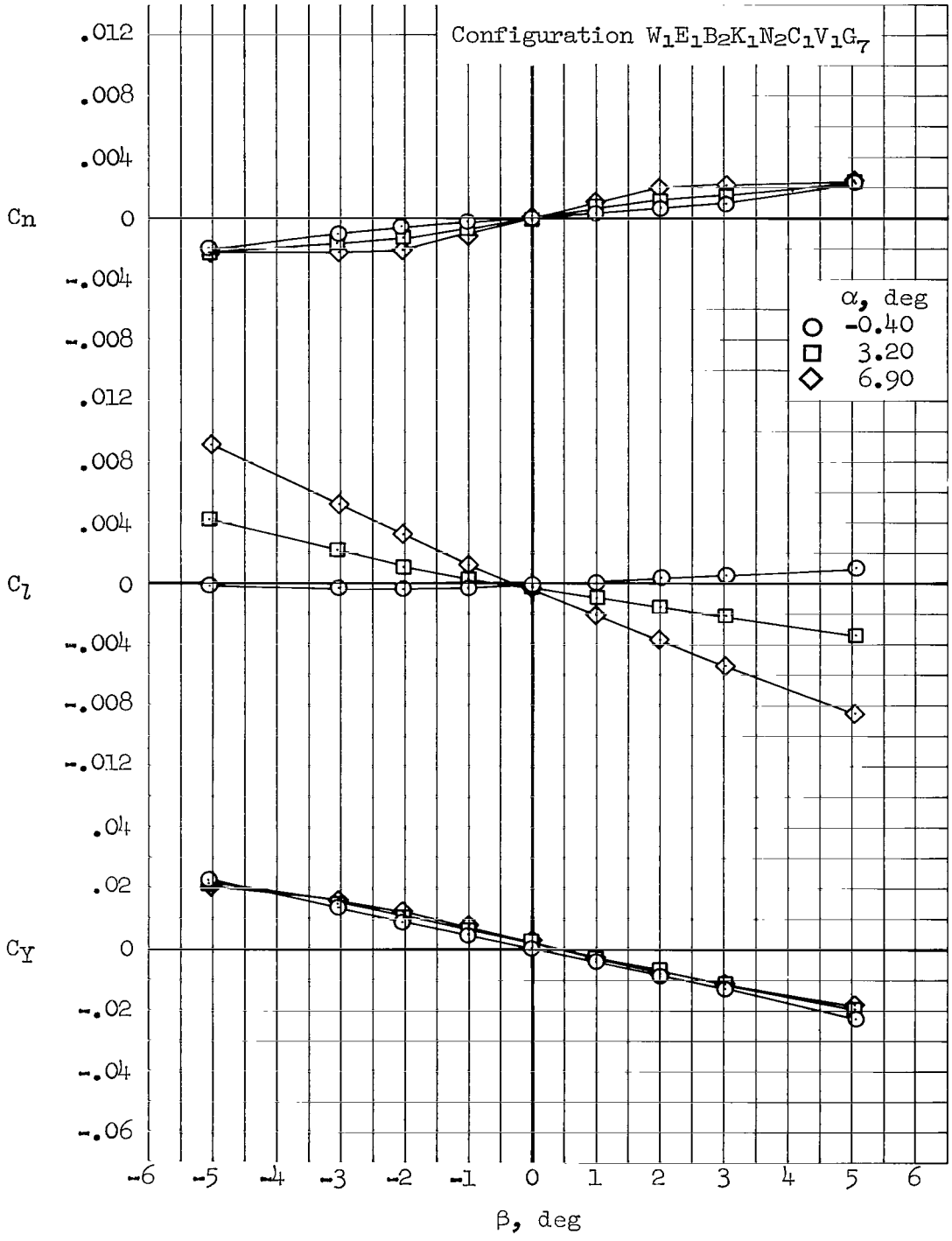

(f) M = 0.75, δ_y = 0°

Figure 16.- Concluded.

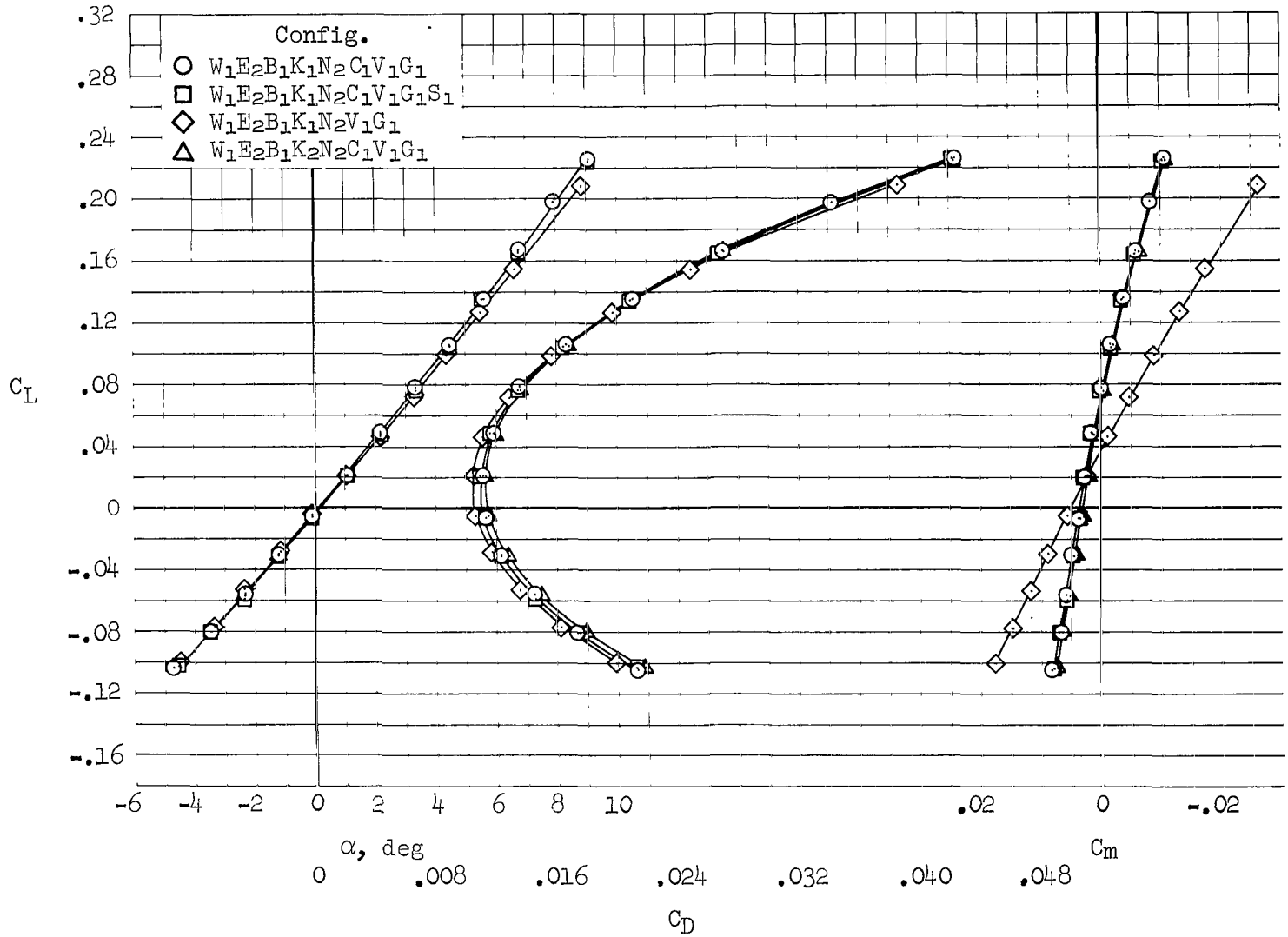

(a) M = 2.53, δ_y = 65°

Figure 17.- Effects of various component configurations on longitudinal characteristics.

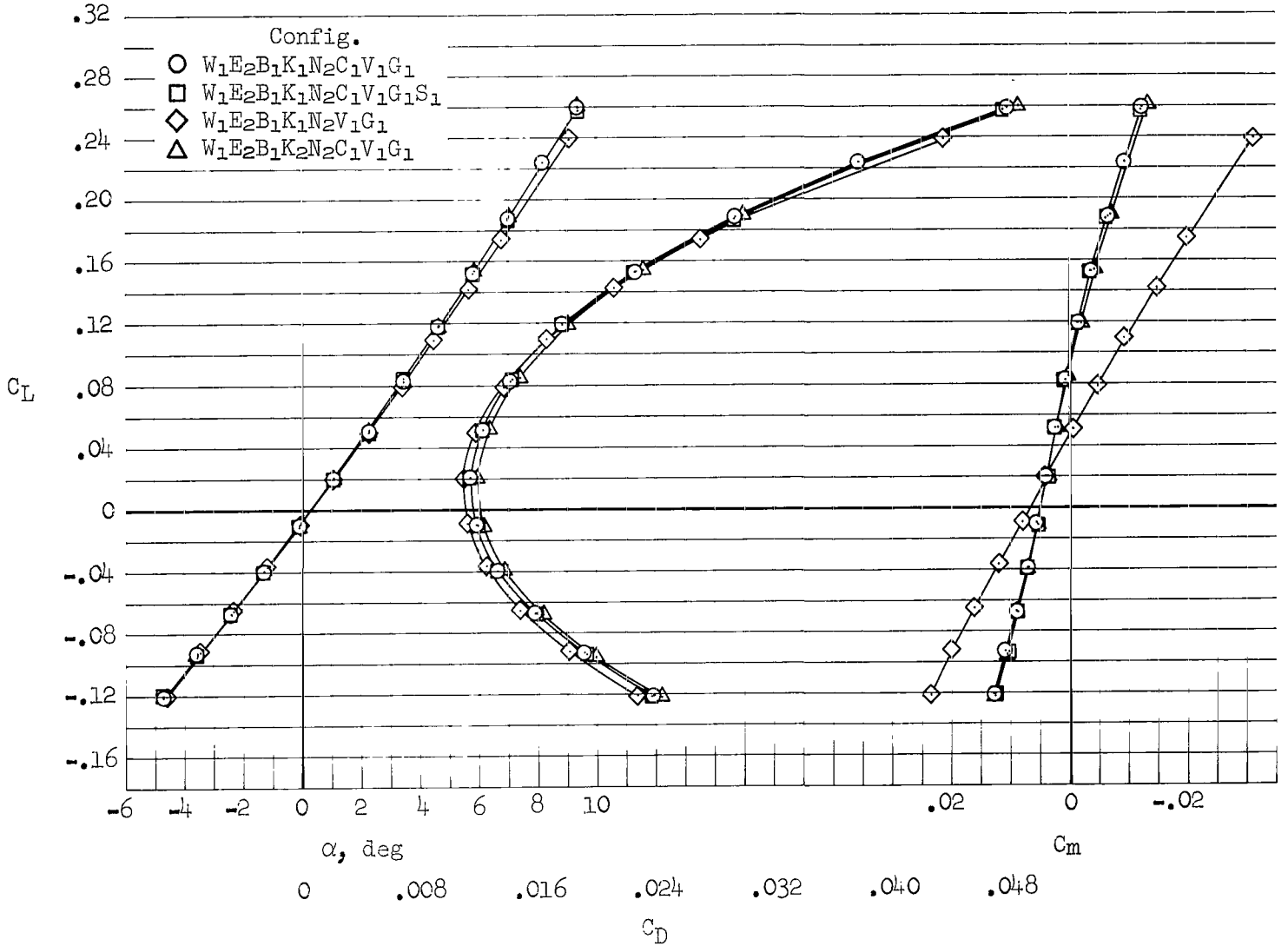

(b) M = 2.10, δ_y = 65°

Figure 17.- Continued.

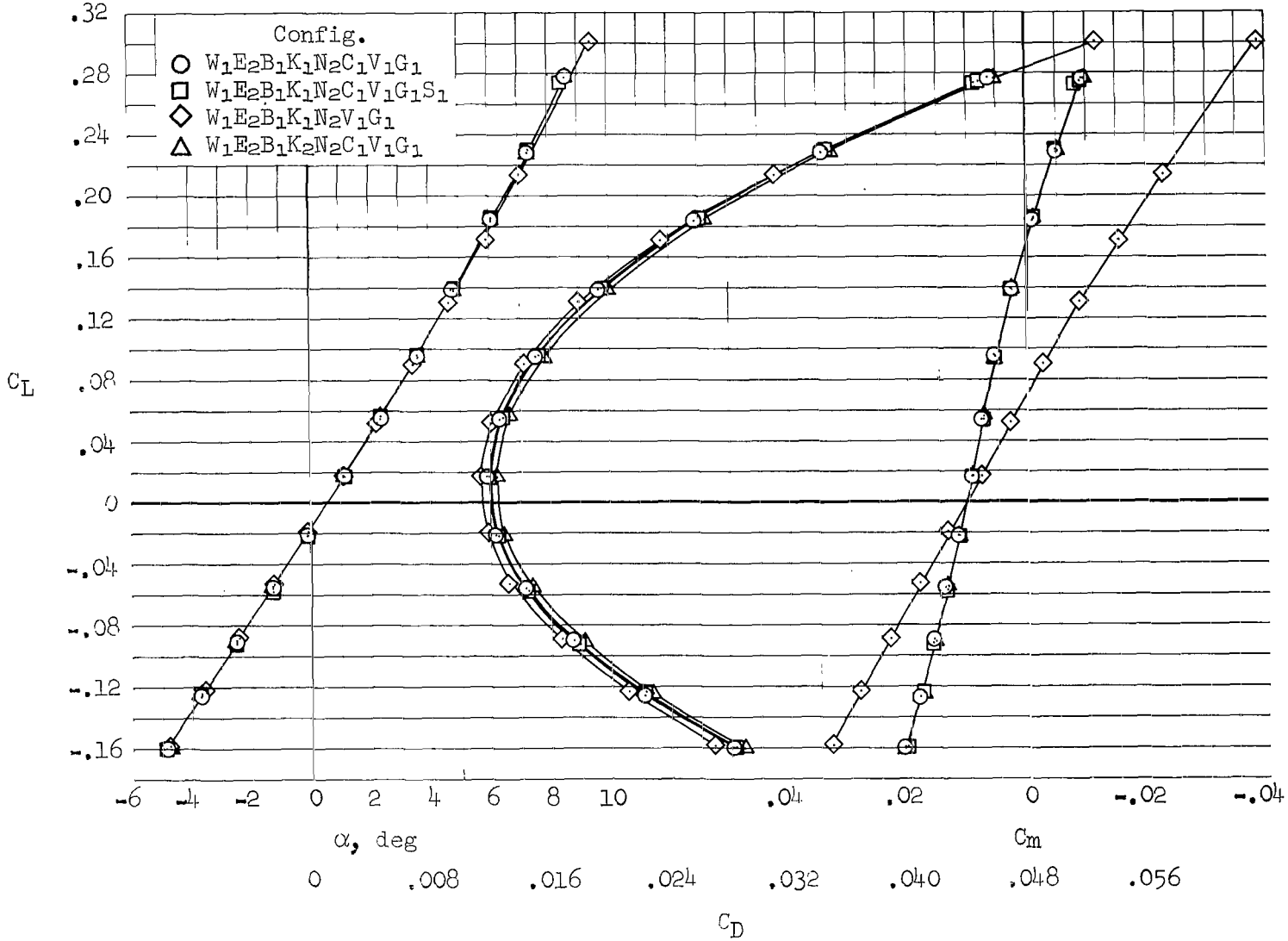

(c) M = 1.60, δ_y = 65°

Figure 17.- Continued.

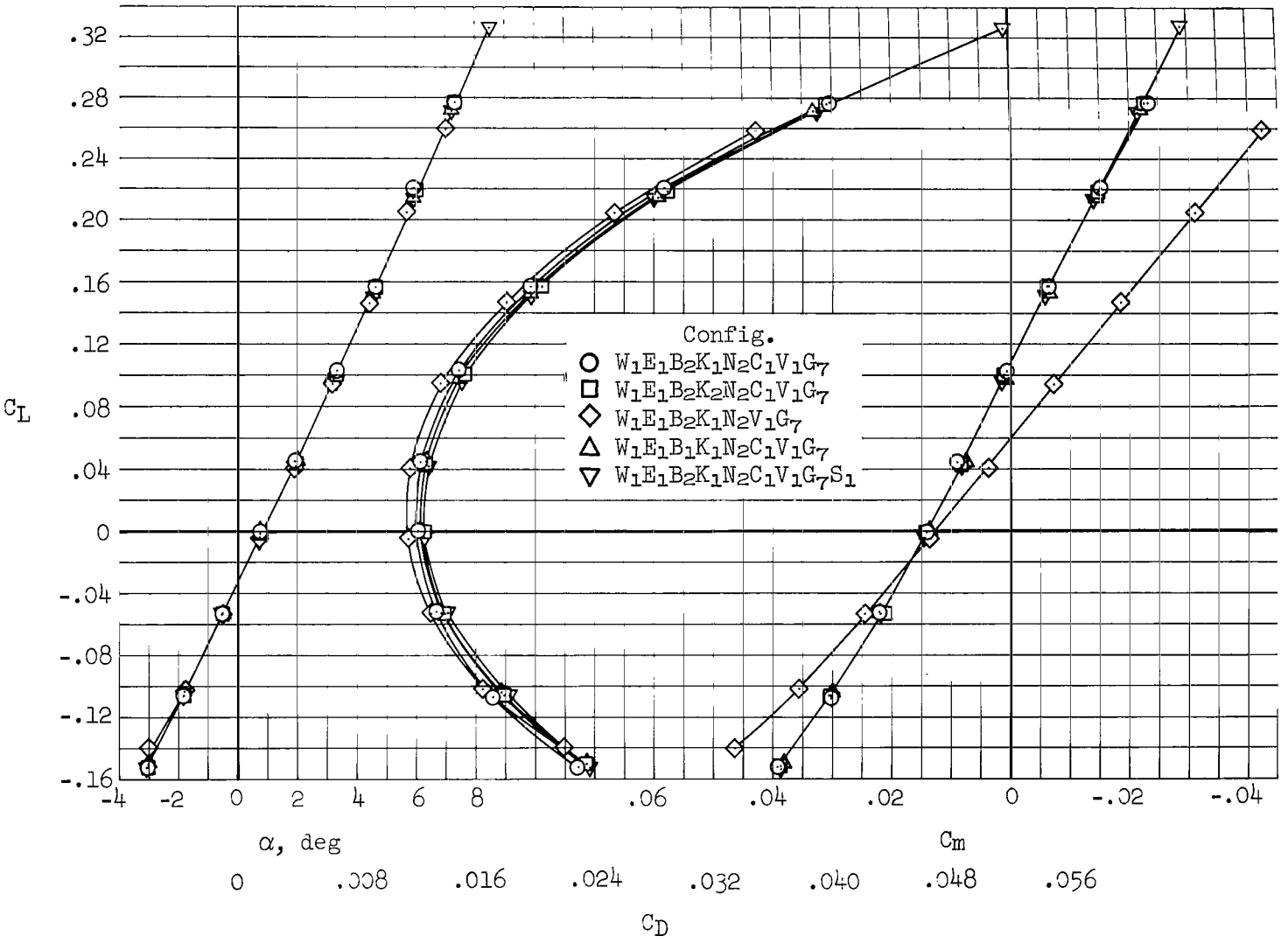

(d) M = 1.40, δ_y = 0°

Figure 17.- Continued.

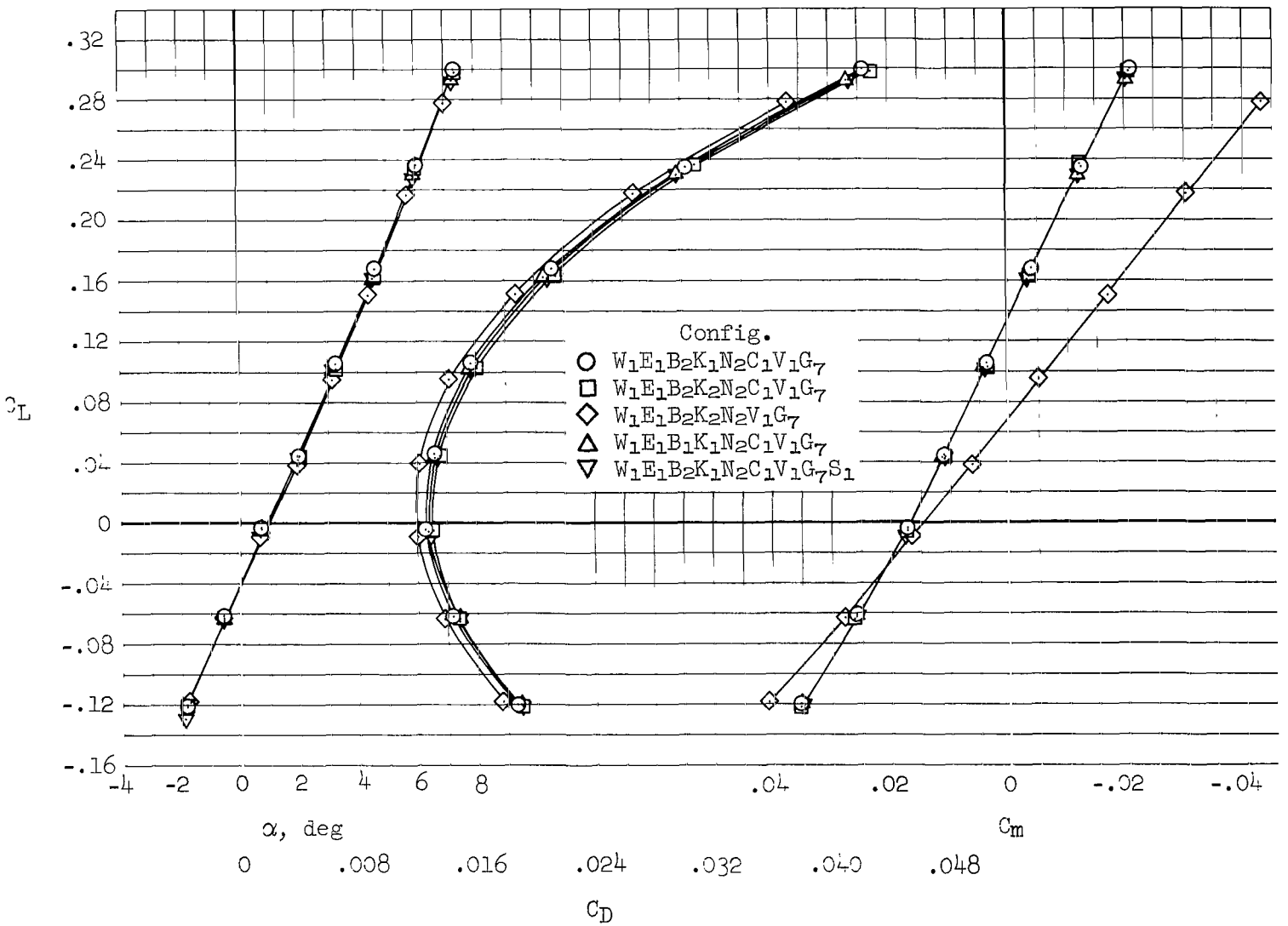

(e) M = 1.20, δ_y = 0°

Figure 17.- Continued.

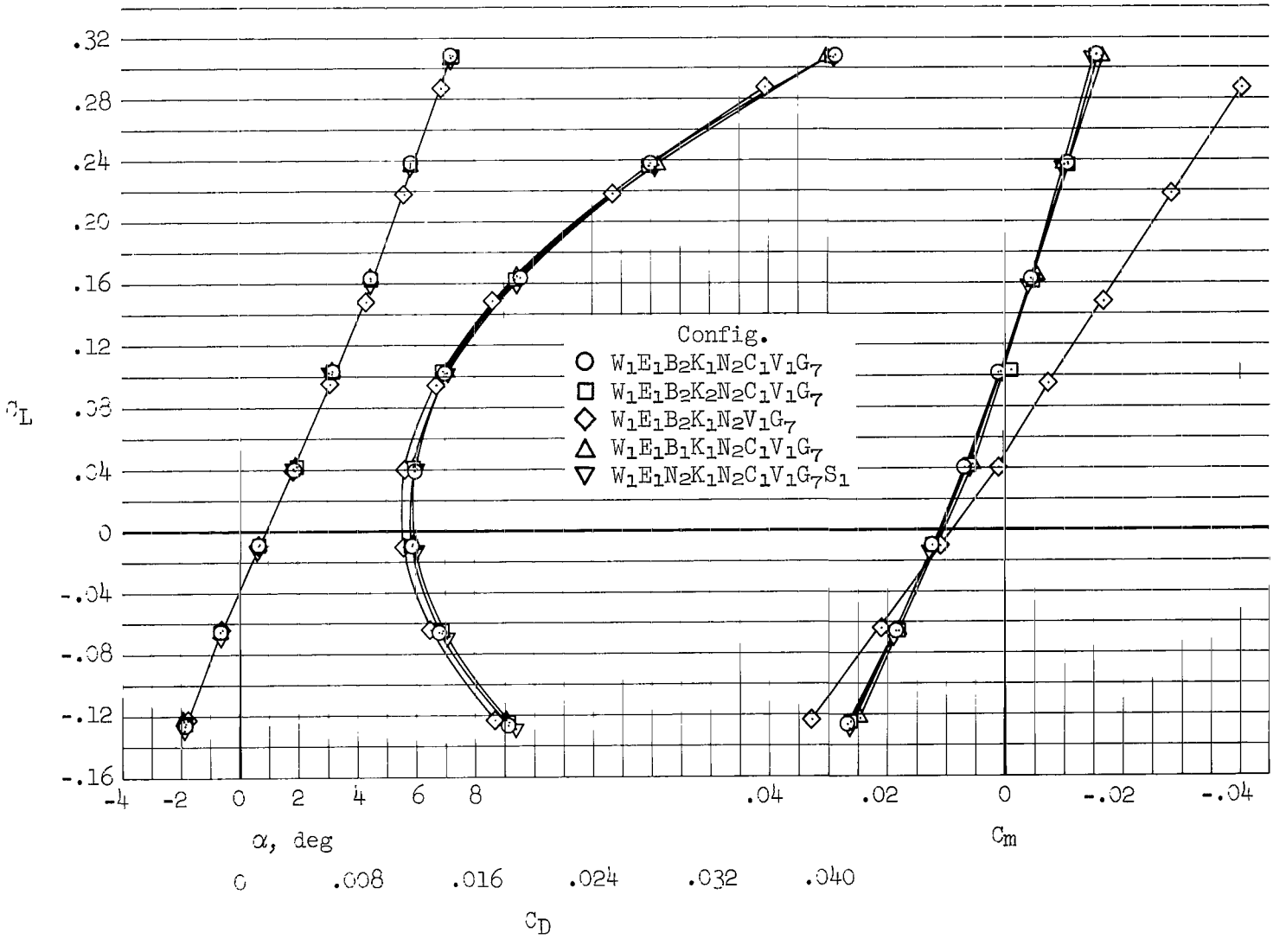

(f) M = 0.95, δ_y = 0°

Figure 17.- Continued.

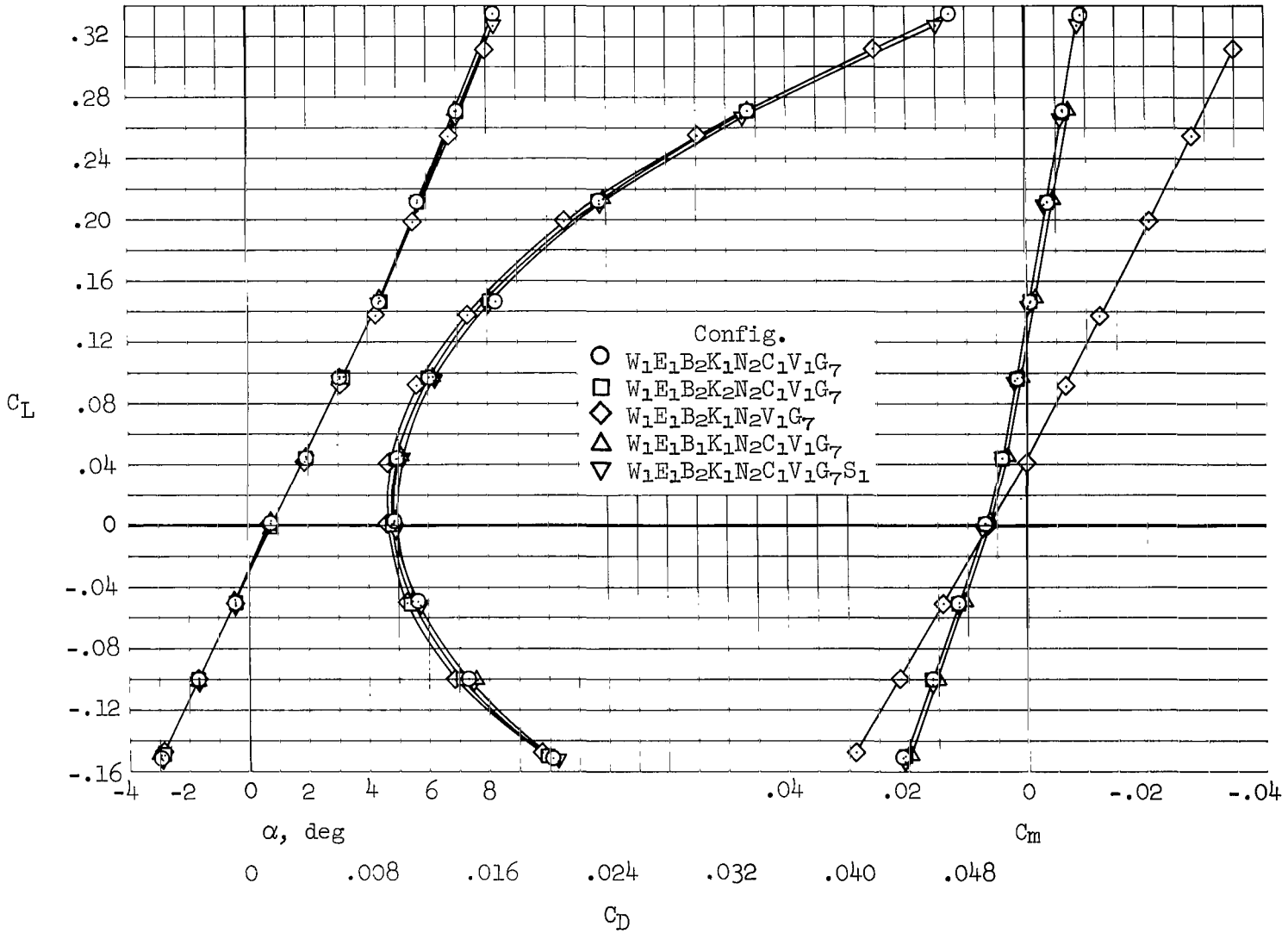

(g) M = 0.80, δ_y = 0°

Figure 17.- Continued.

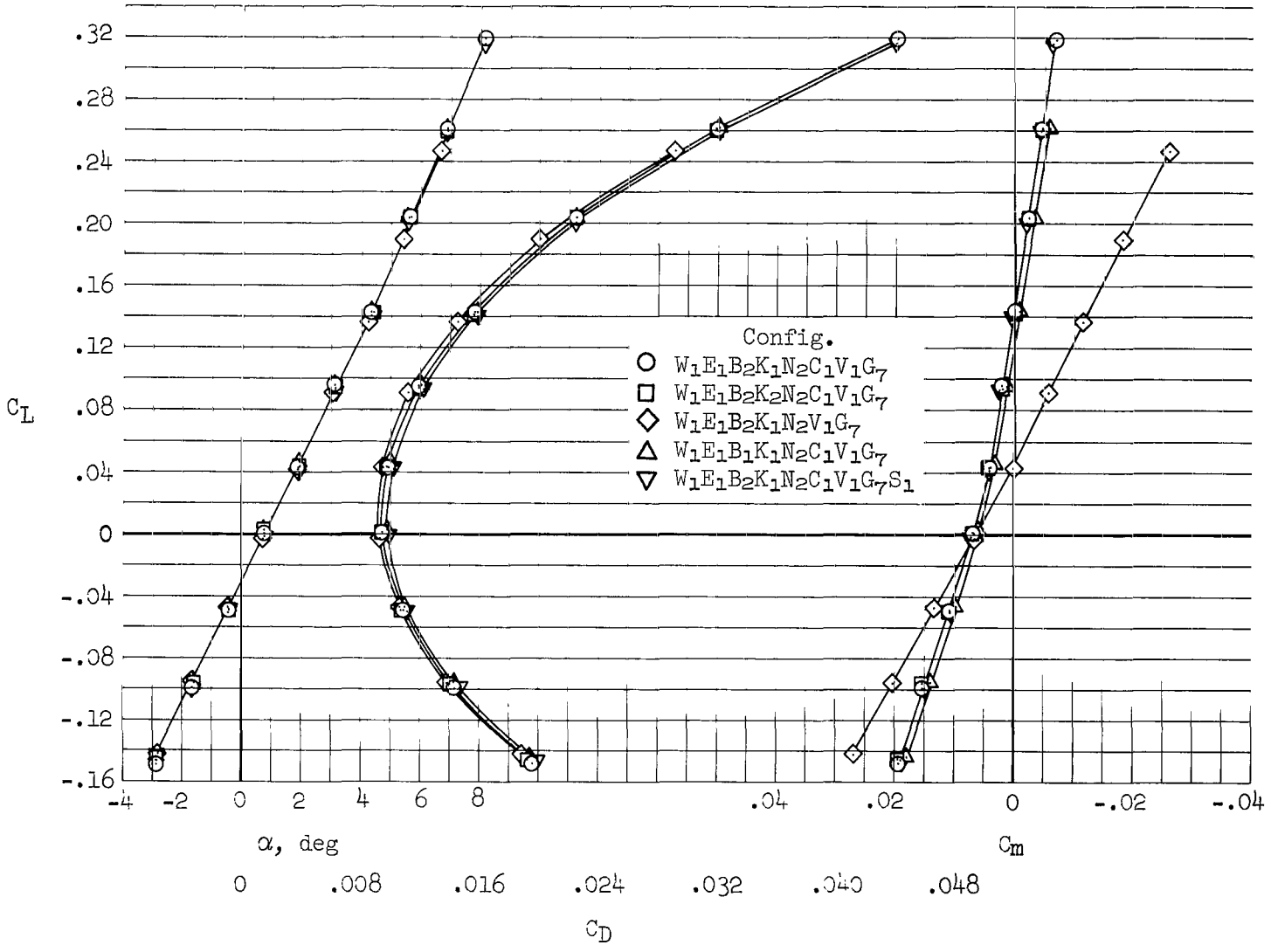

(h) M = 0.75, δ_y = 0°

Figure 17.- Continued.

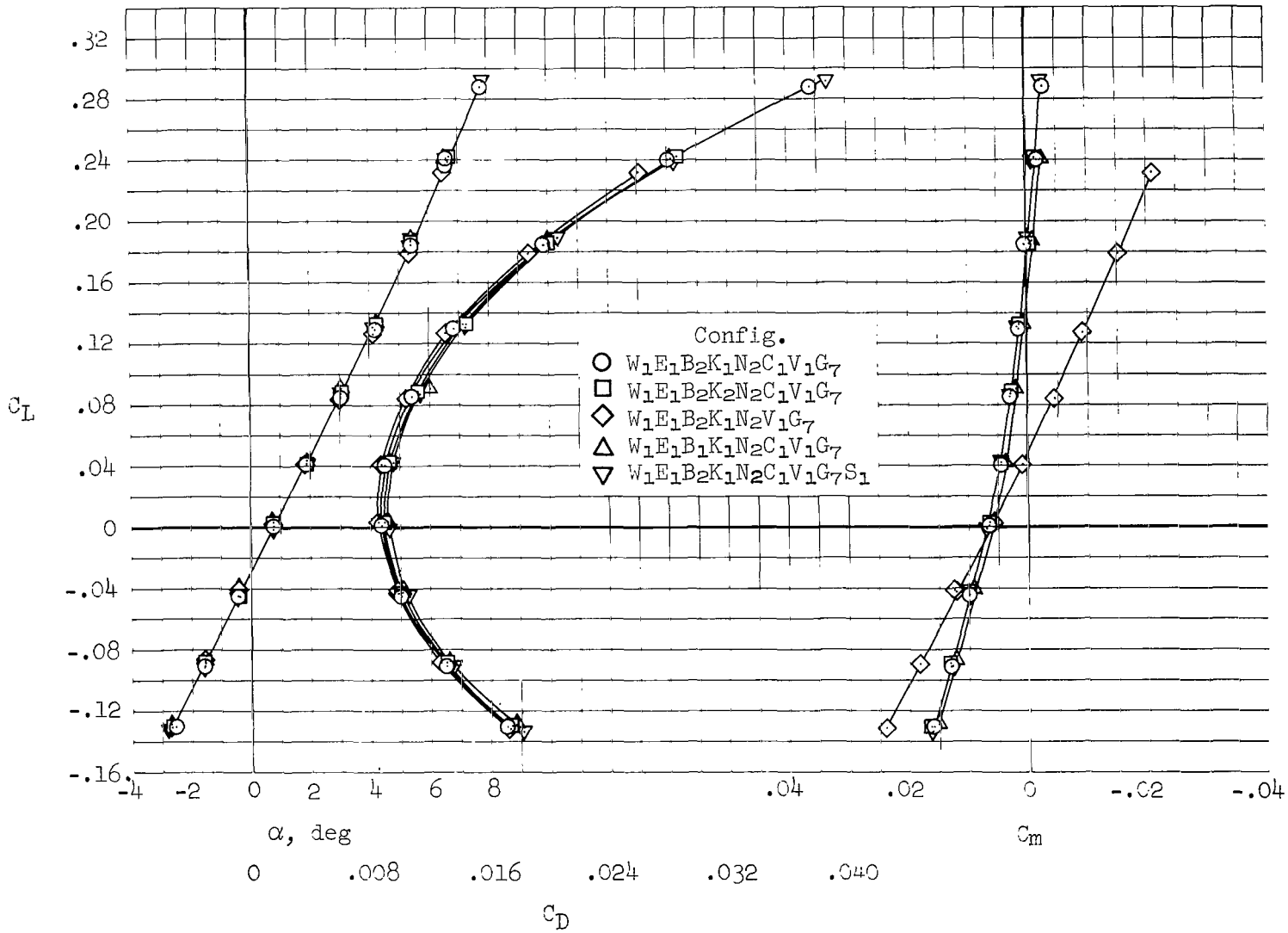

(i) M = 0.60, δ_y = 0°

Figure 17.- Concluded.

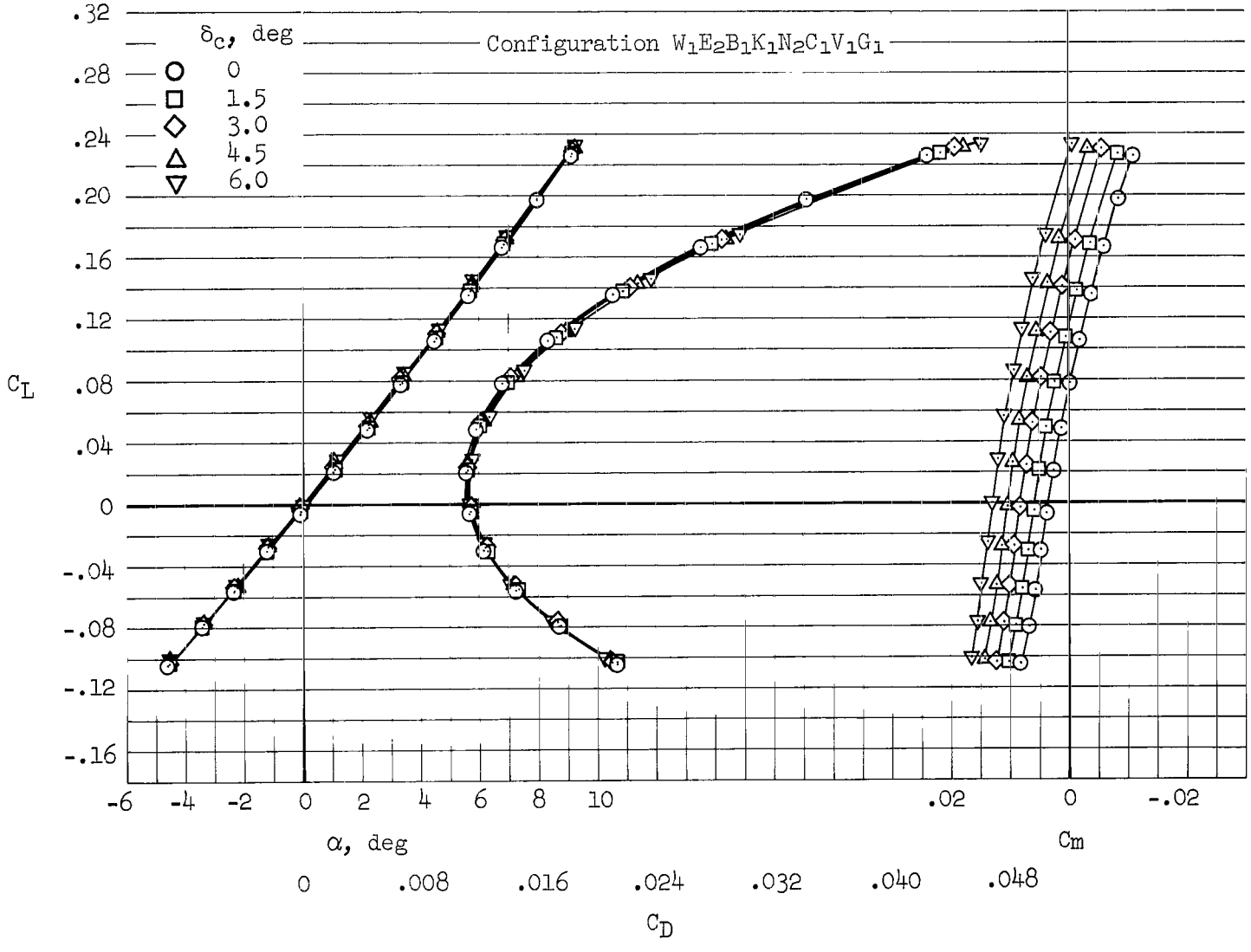

(a) M = 2.53, δ_y = 65°

Figure 18.- Effects of canard deflection on longitudinal characteristics.

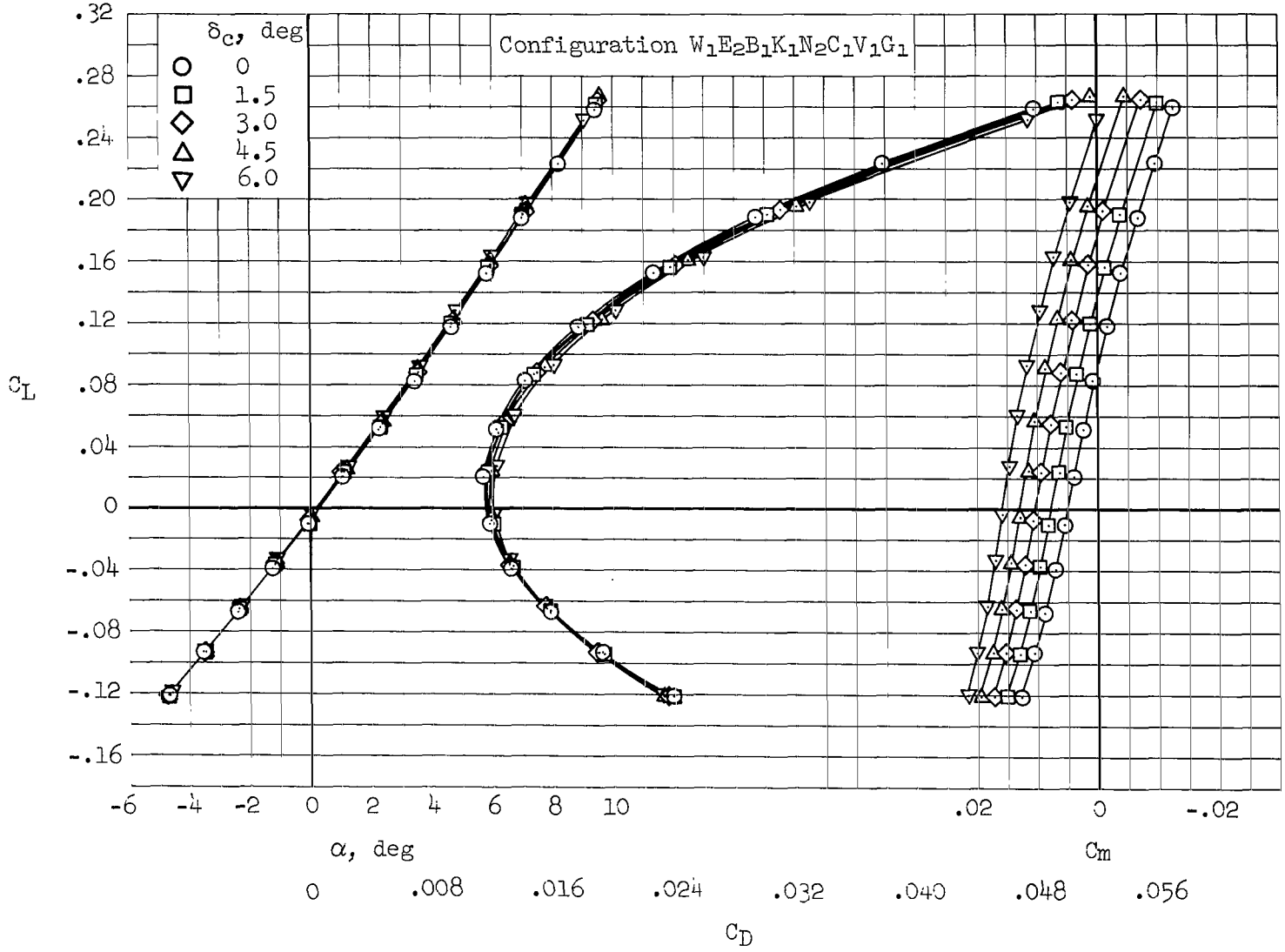

(b) M = 2.10, δ_y = 65°

Figure 18.- Continued.

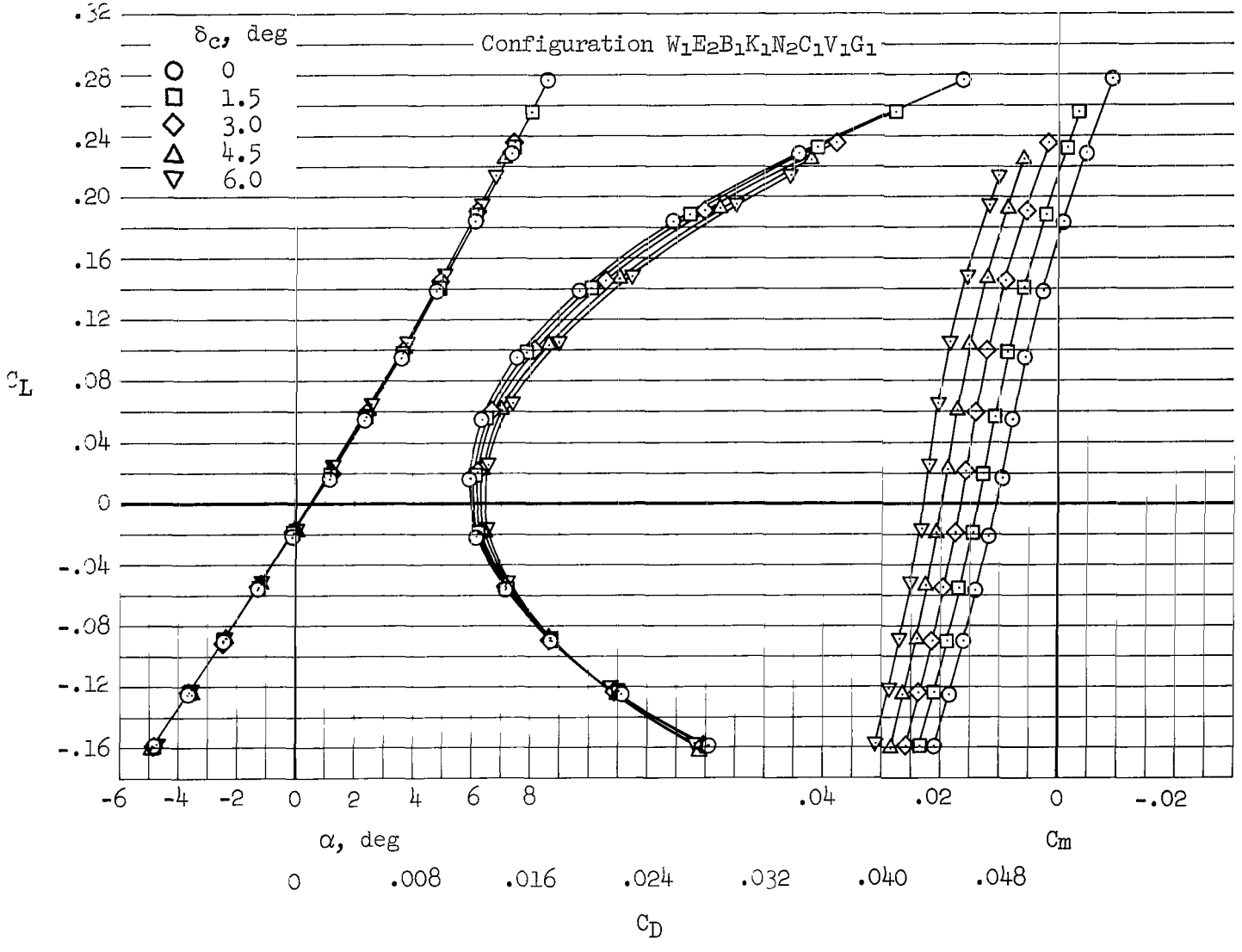

(c) M = 1.60, δ_y = 65°

Figure 18.- Continued.

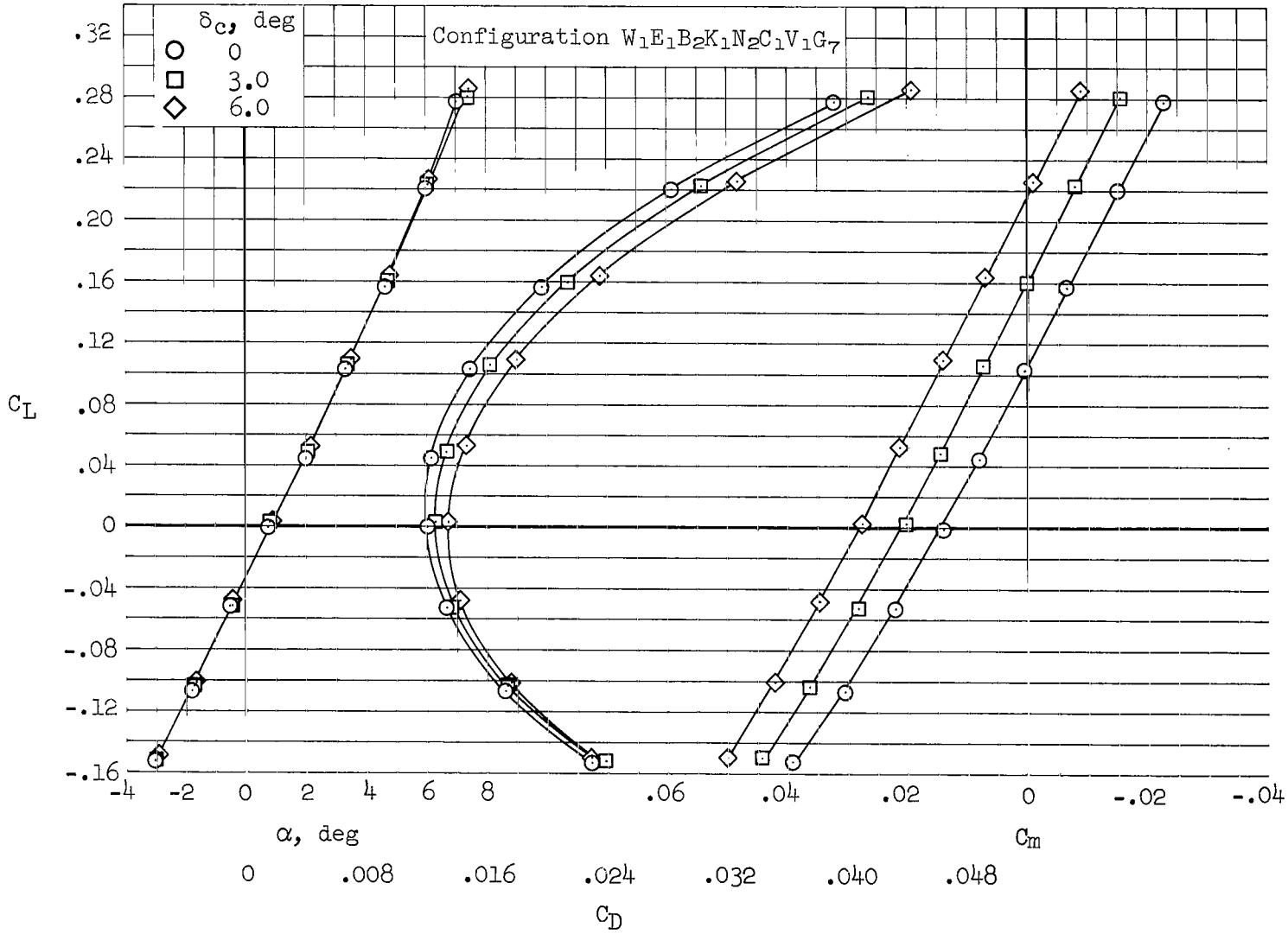

(d) M = 1.40, δ_y = 0°

Figure 18.- Continued.

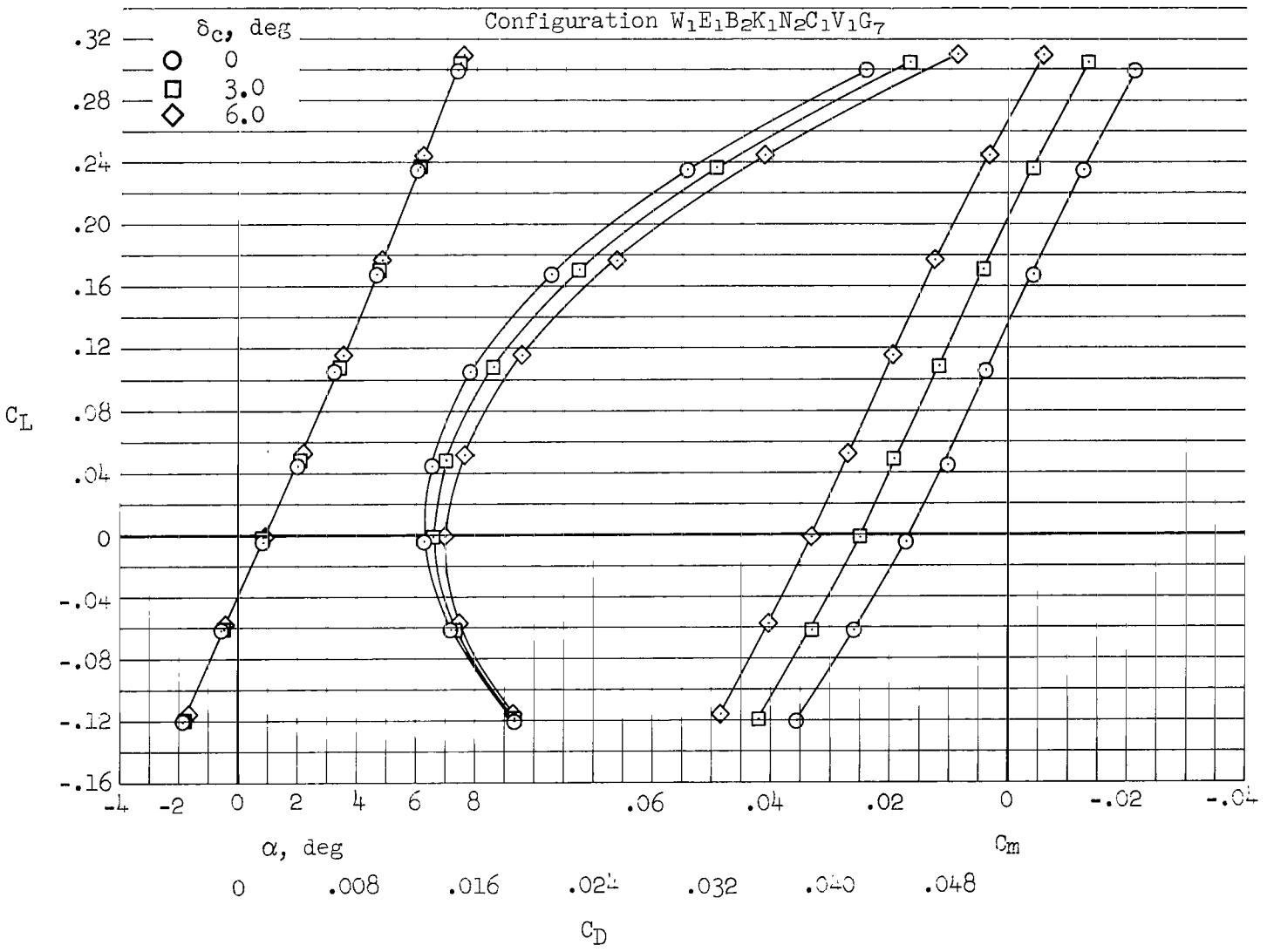

(e) M = 1.20, δ_y = 0°

Figure 18.- Continued.

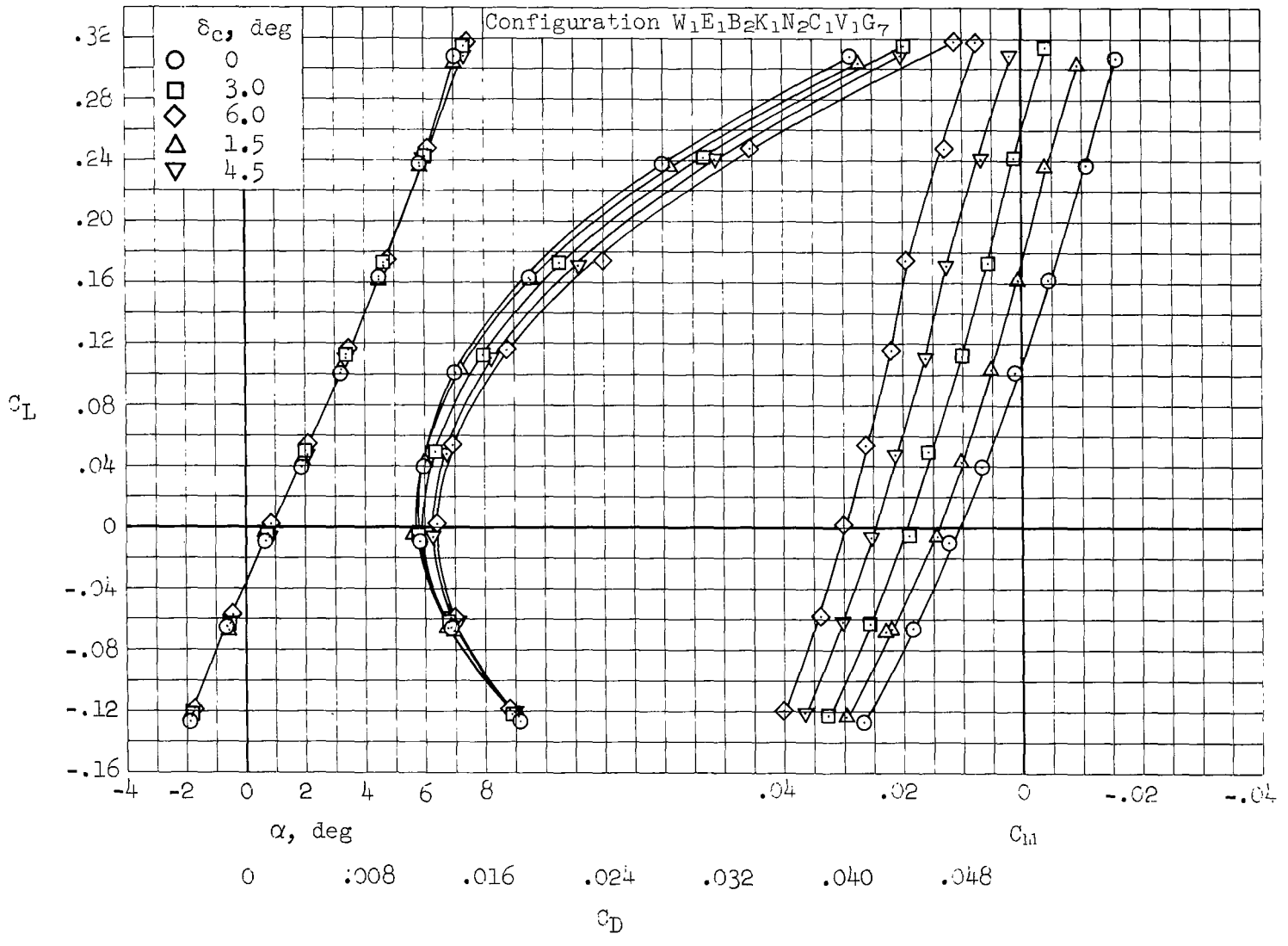

(f) M = 0.95, δ_y = 0°

Figure 18.- Continued.

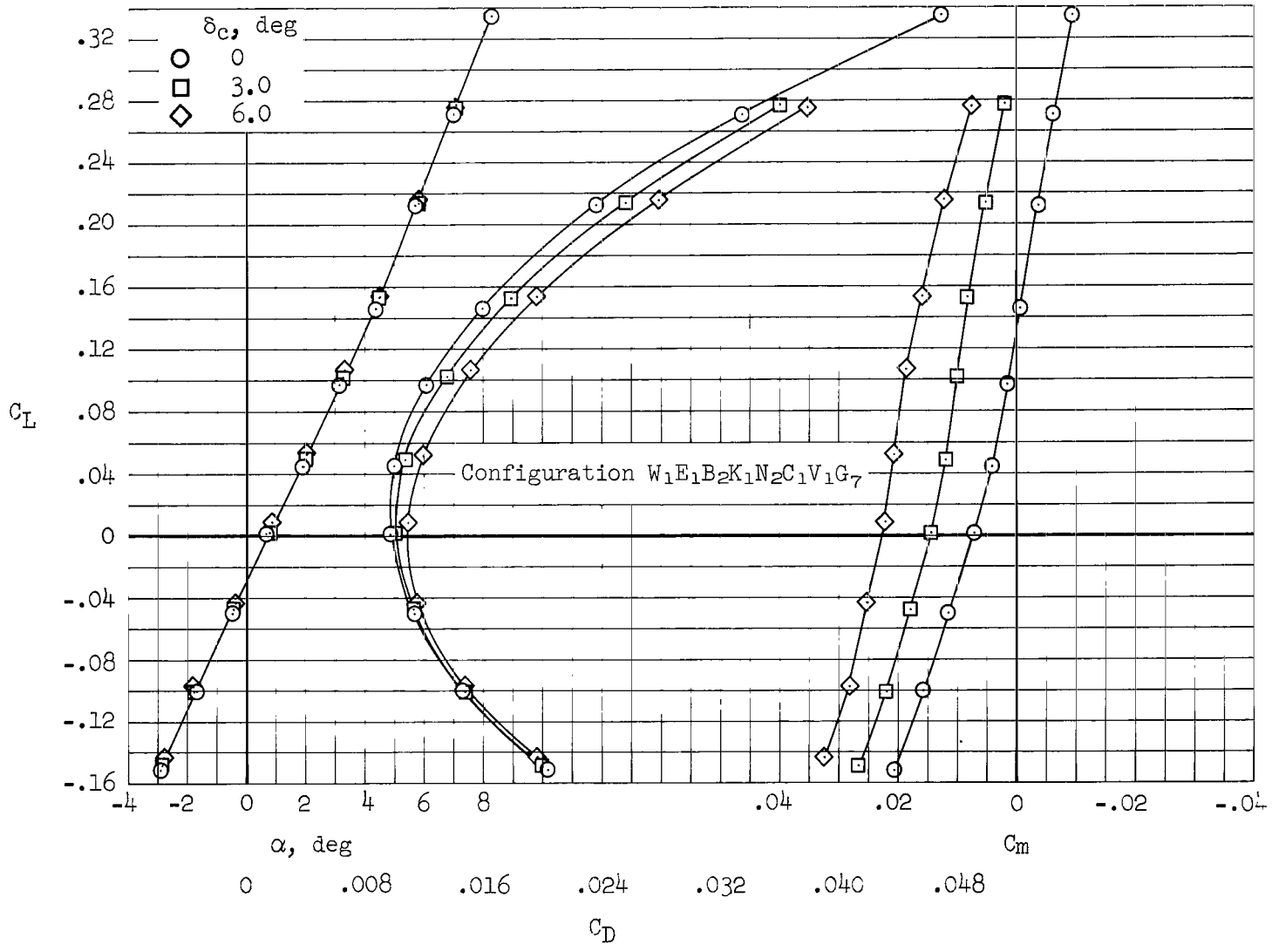

(g) M = 0.80, δ_y = 0°

Figure 18.- Continued.

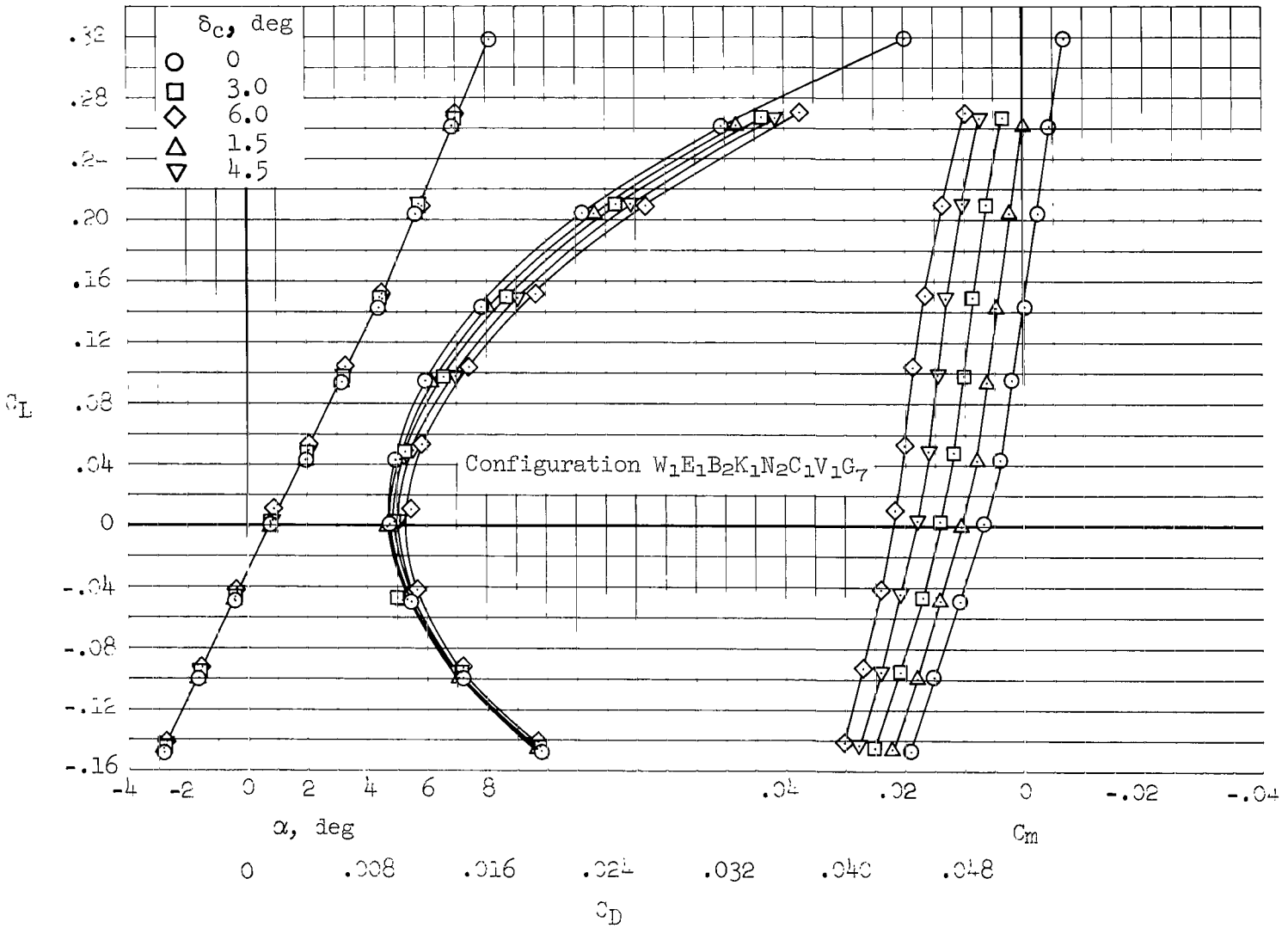

(h) M = 0.75, δ_y = 0°

Figure 18.- Continued.

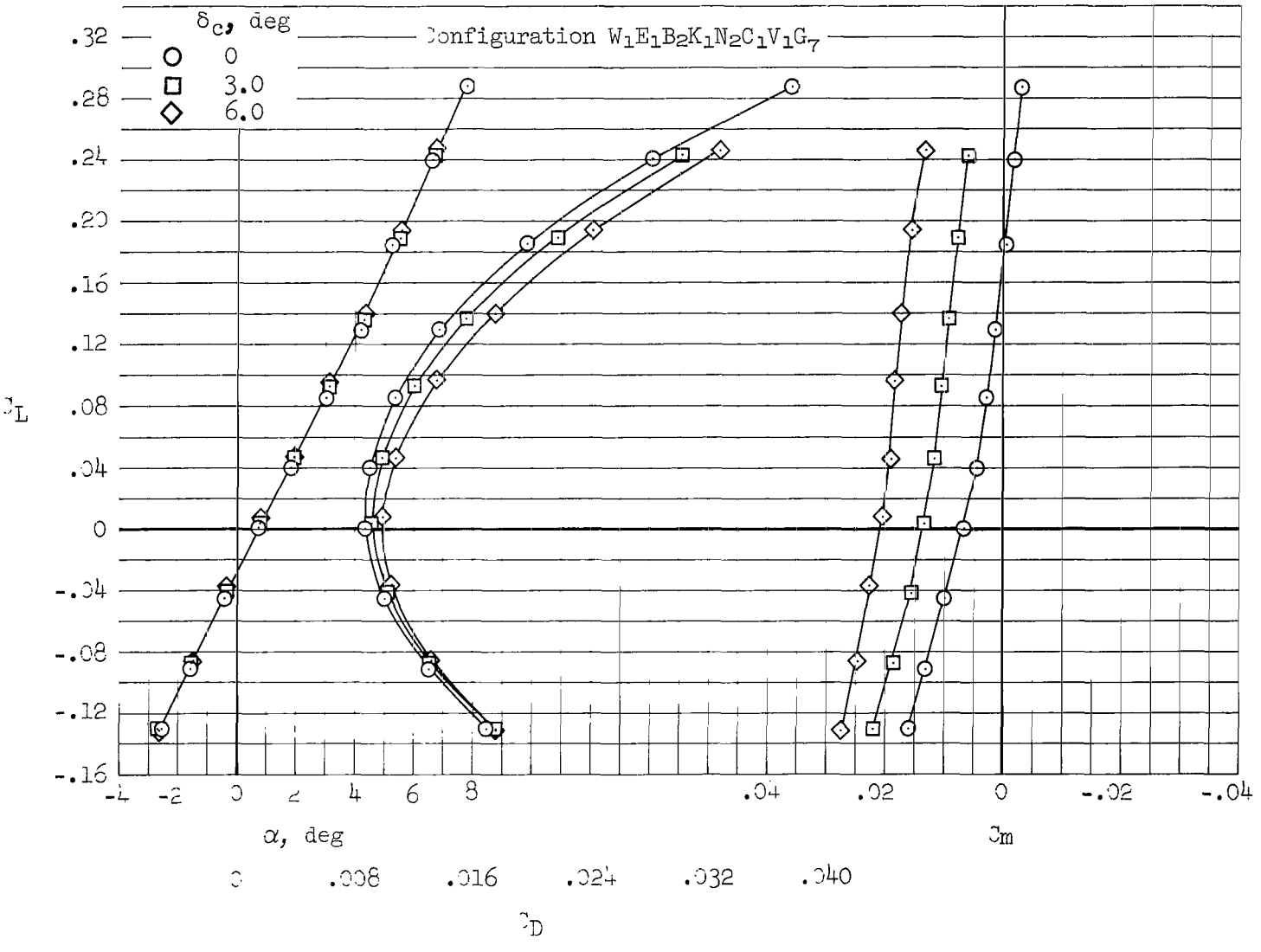

(i) M = 0.60, δ_y = 0°

Figure 18.- Concluded.

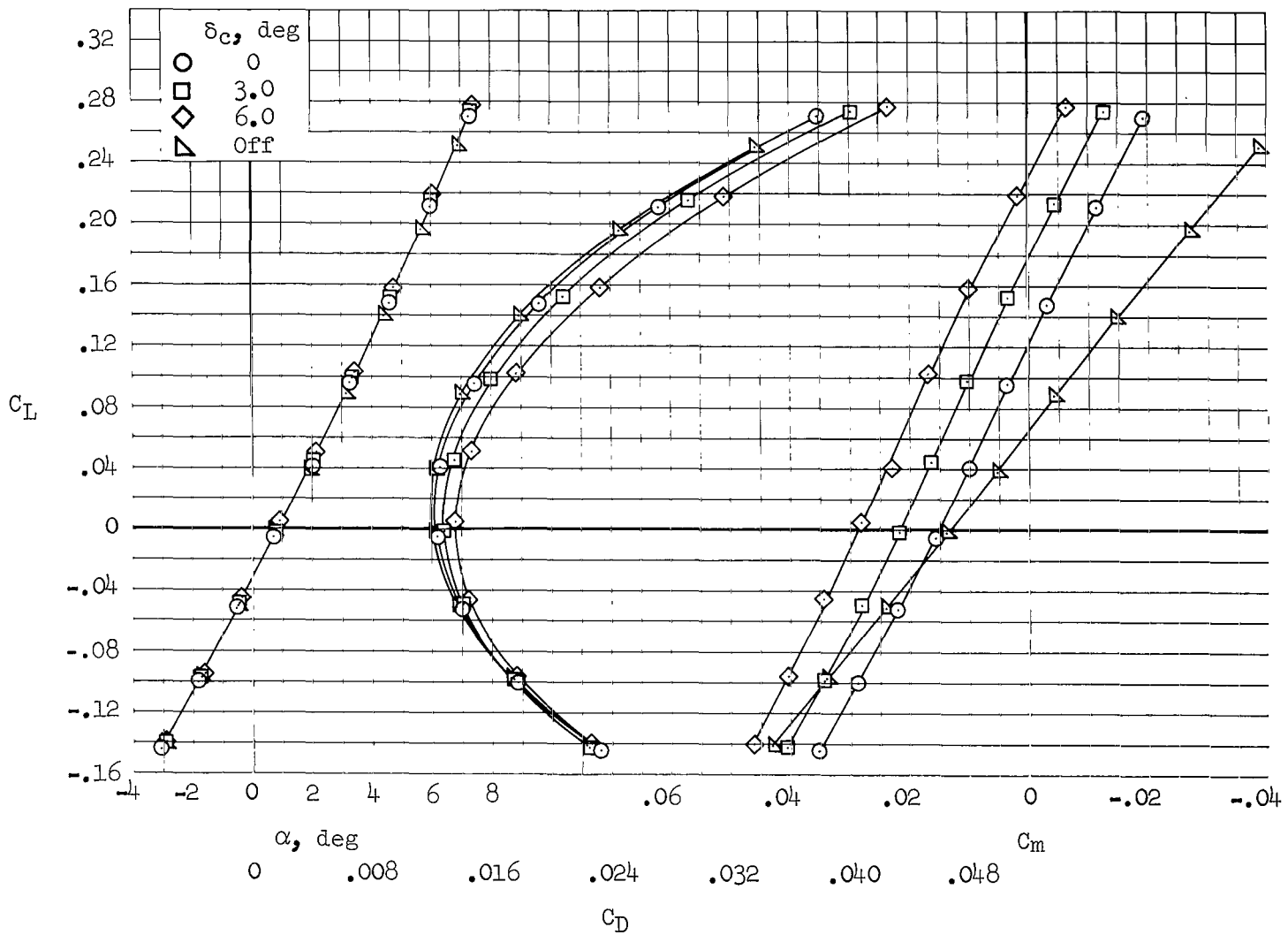

(a) M = 1.40

Figure 19.- Effects of canard component and deflection on longitudinal characteristics; configuration $W_1E_2B_2K_1N_2C_1V_1G_7$, δ_y = 25°.

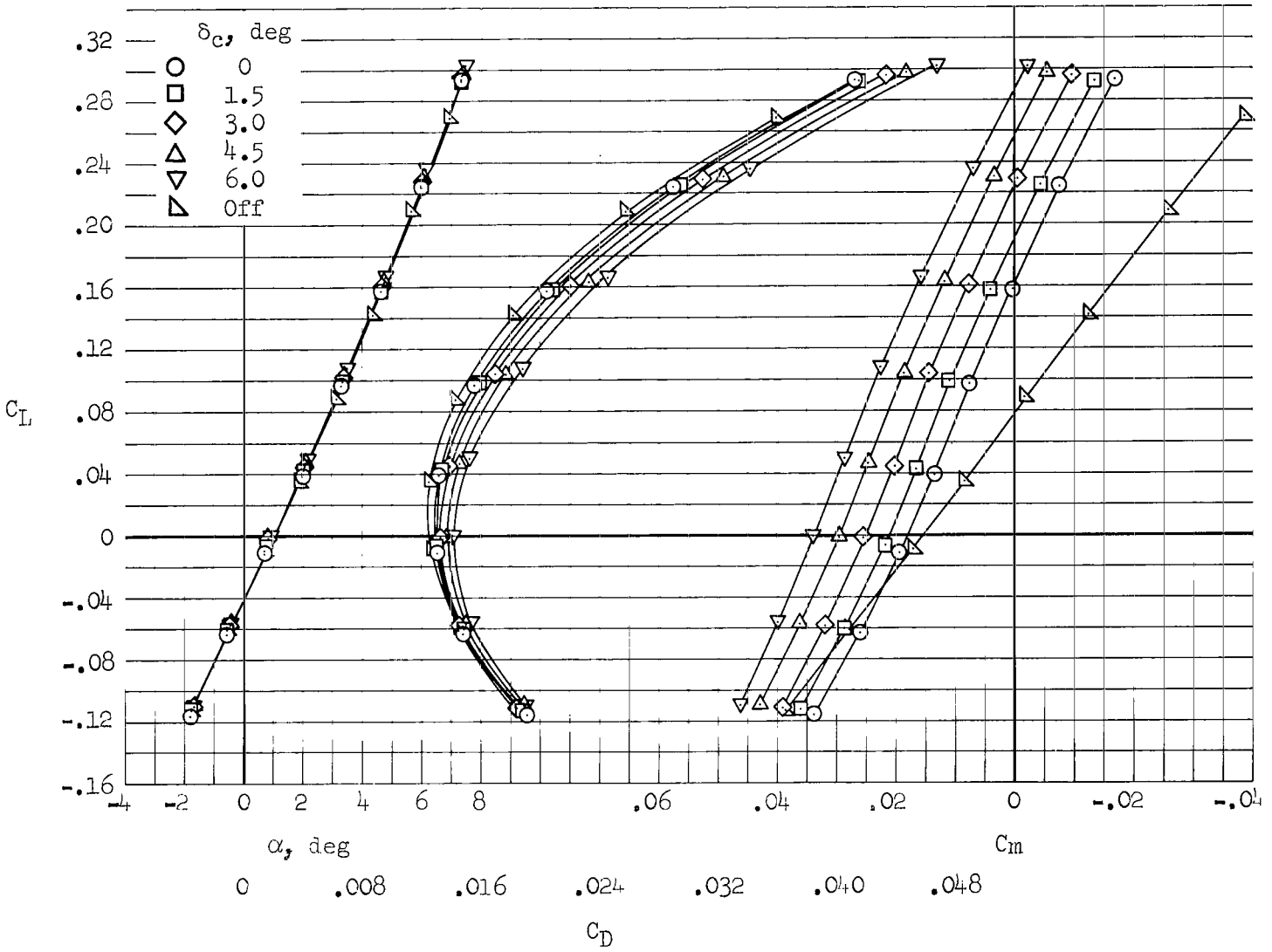

(b) M = 1.20

Figure 19.- Continued.

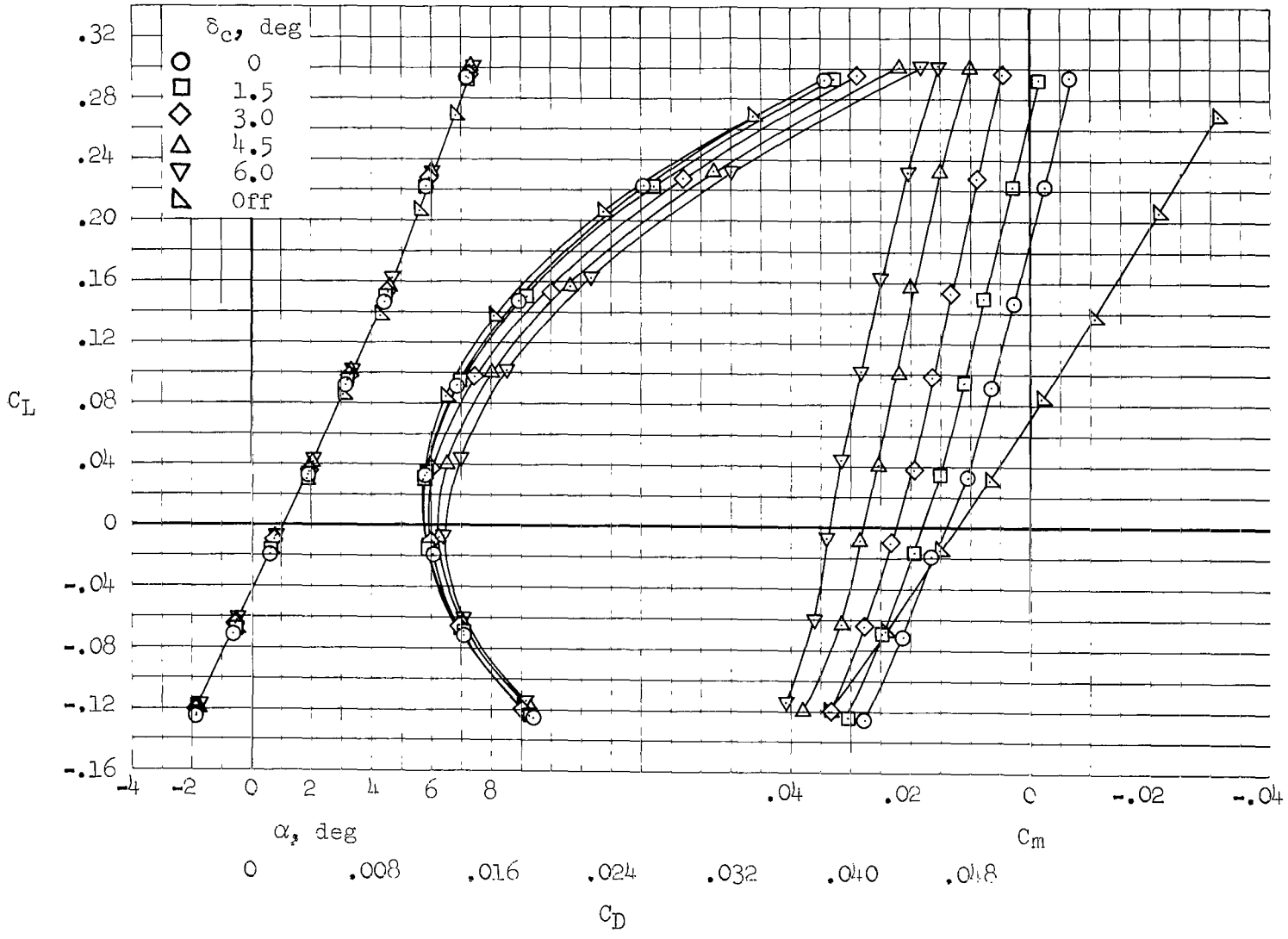

(c) M = 0.95

Figure 19.- Continued.

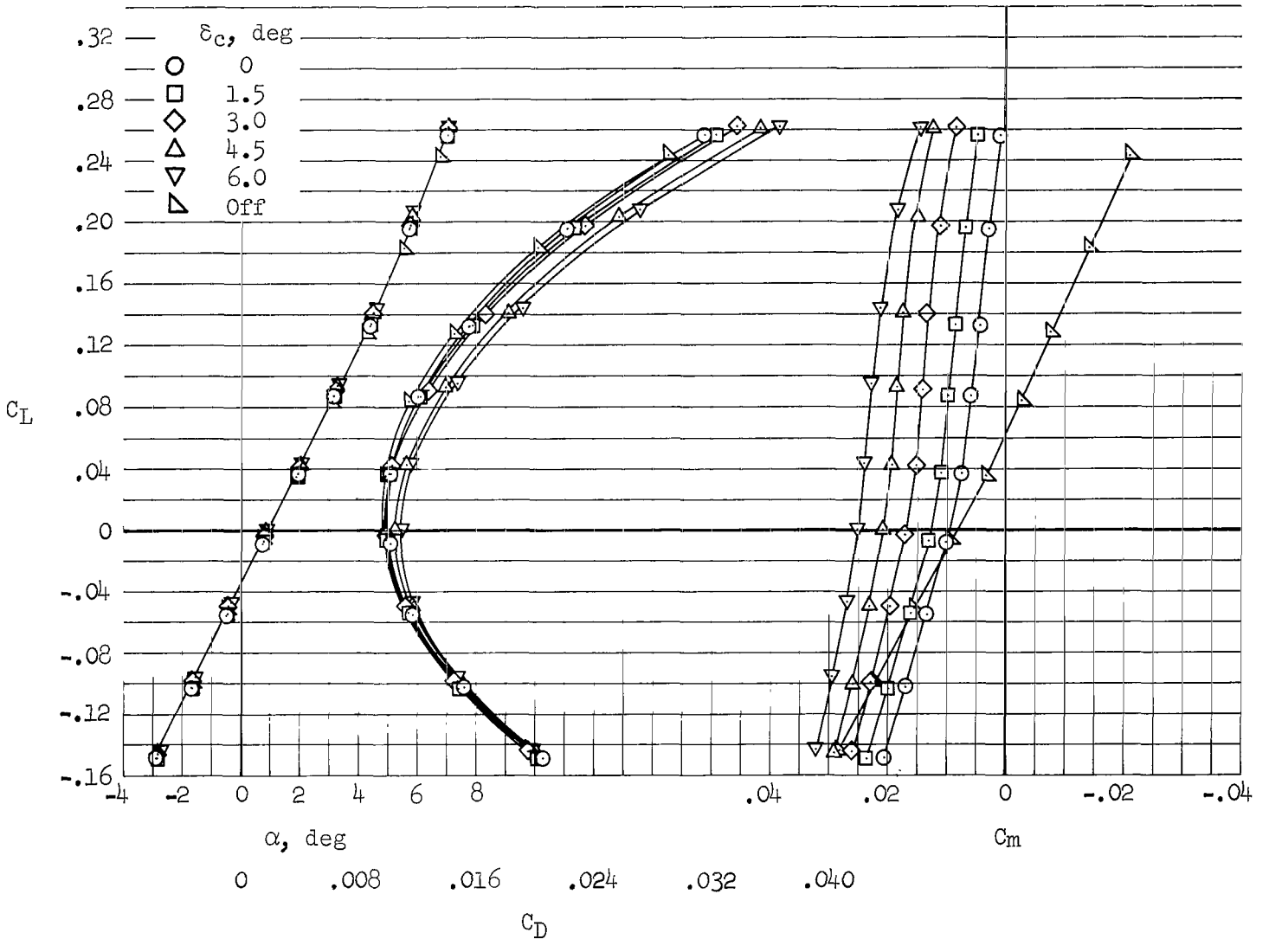

(d) M = 0.80

Figure 19.- Concluded.

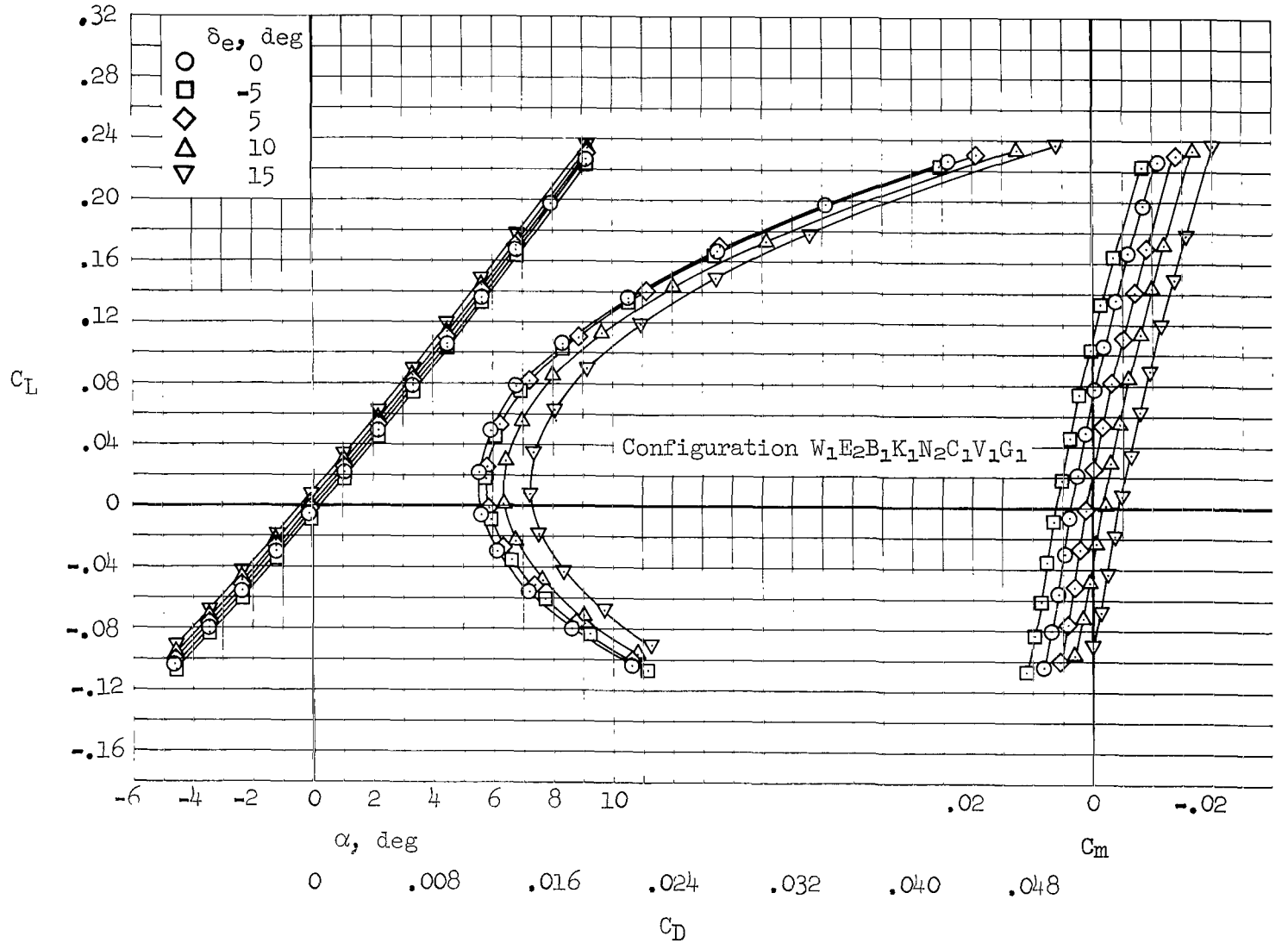

(a) M = 2.53, δ_y = 65°

Figure 20.- Effects on longitudinal characteristics of various pitch-trim-and-control deflection of the elevons.

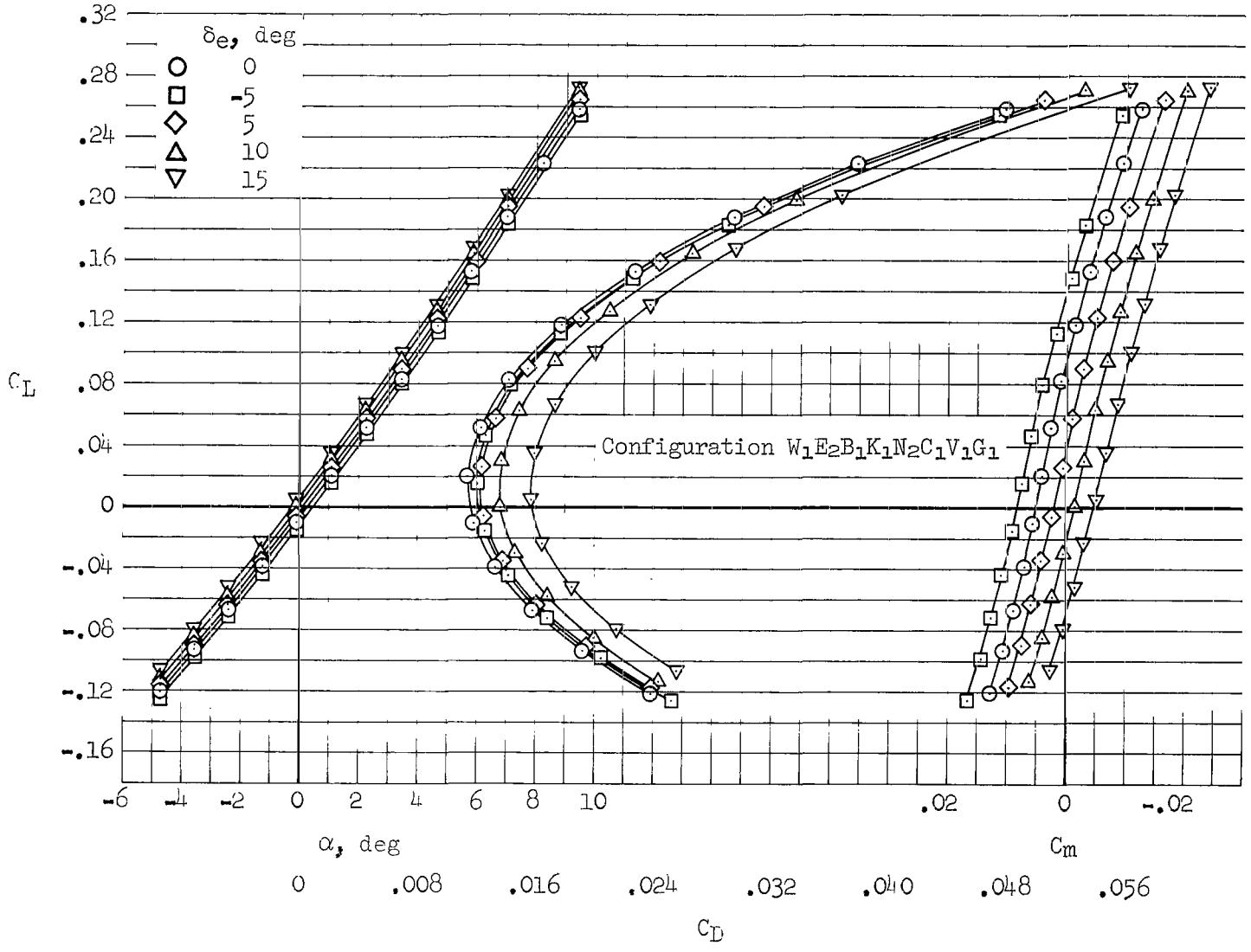

(b) M = 2.10, δ_y = 65°

Figure 20.- Continued.

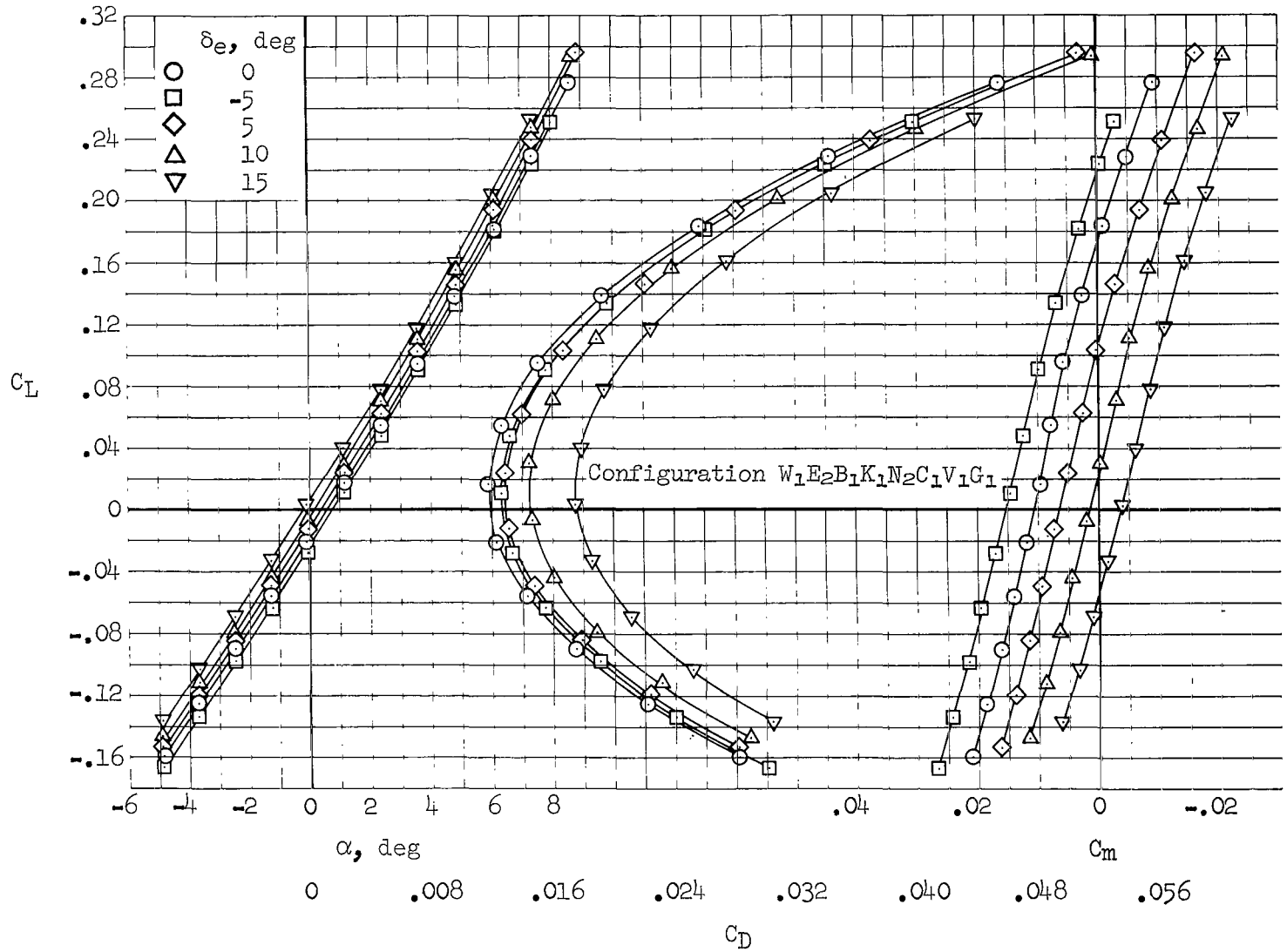

(c) M = 1.60, δ_y = 65°

Figure 20.- Continued.

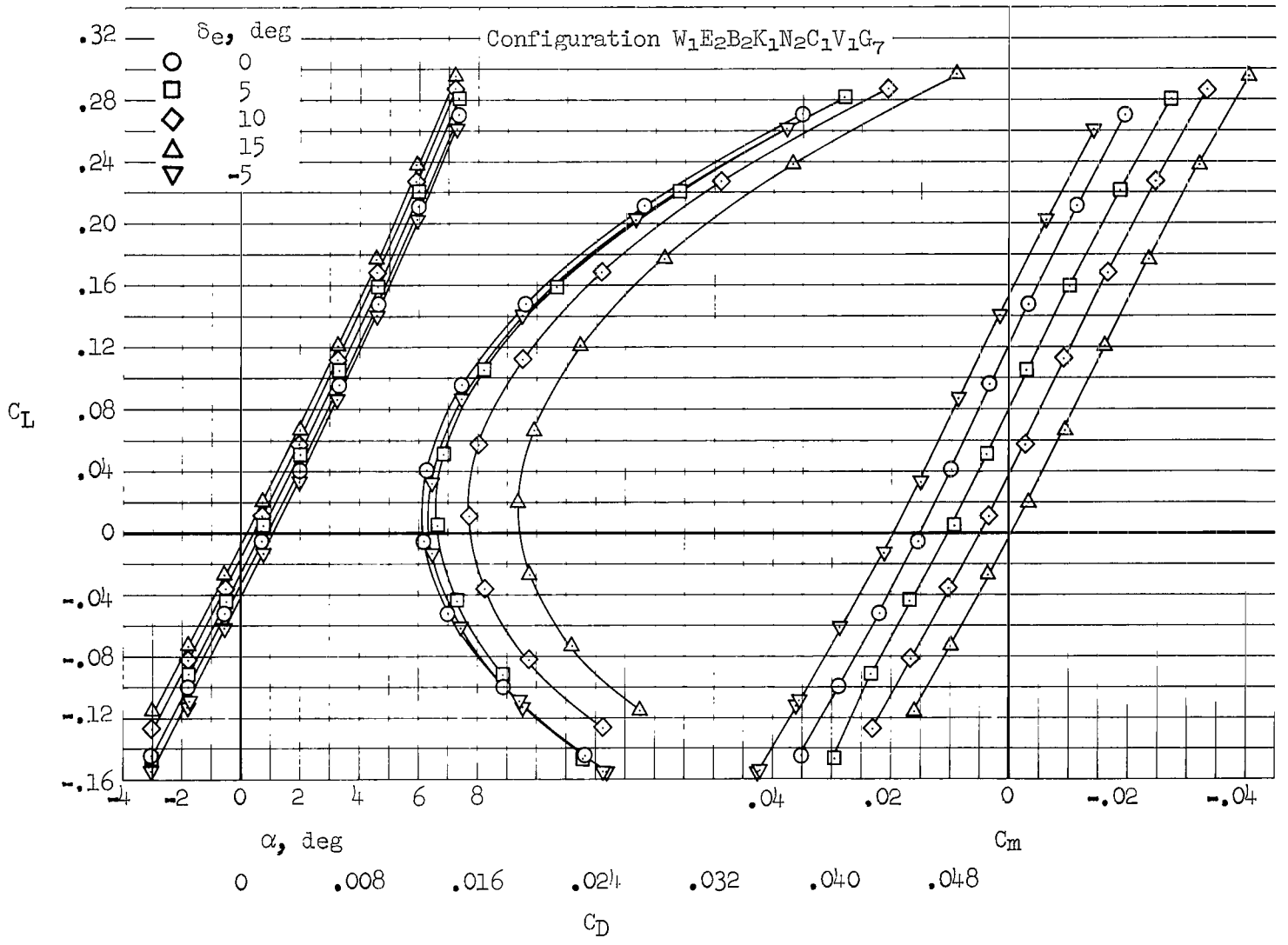

(d) M = 1.40, δ_y = 25°

Figure 20.- Continued.

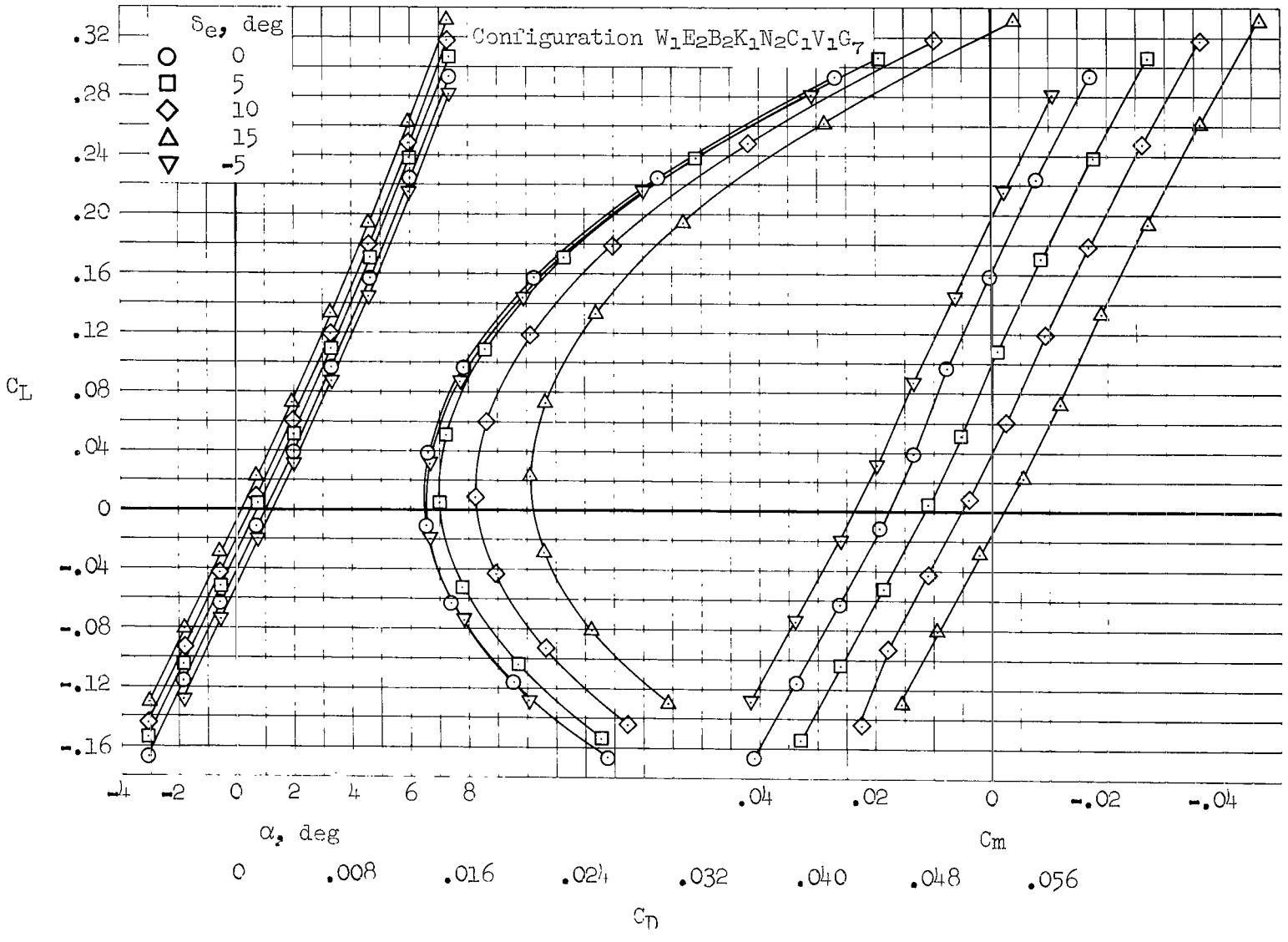

(e) M = 1.20, δ_y = 25°

Figure 20.- Continued.

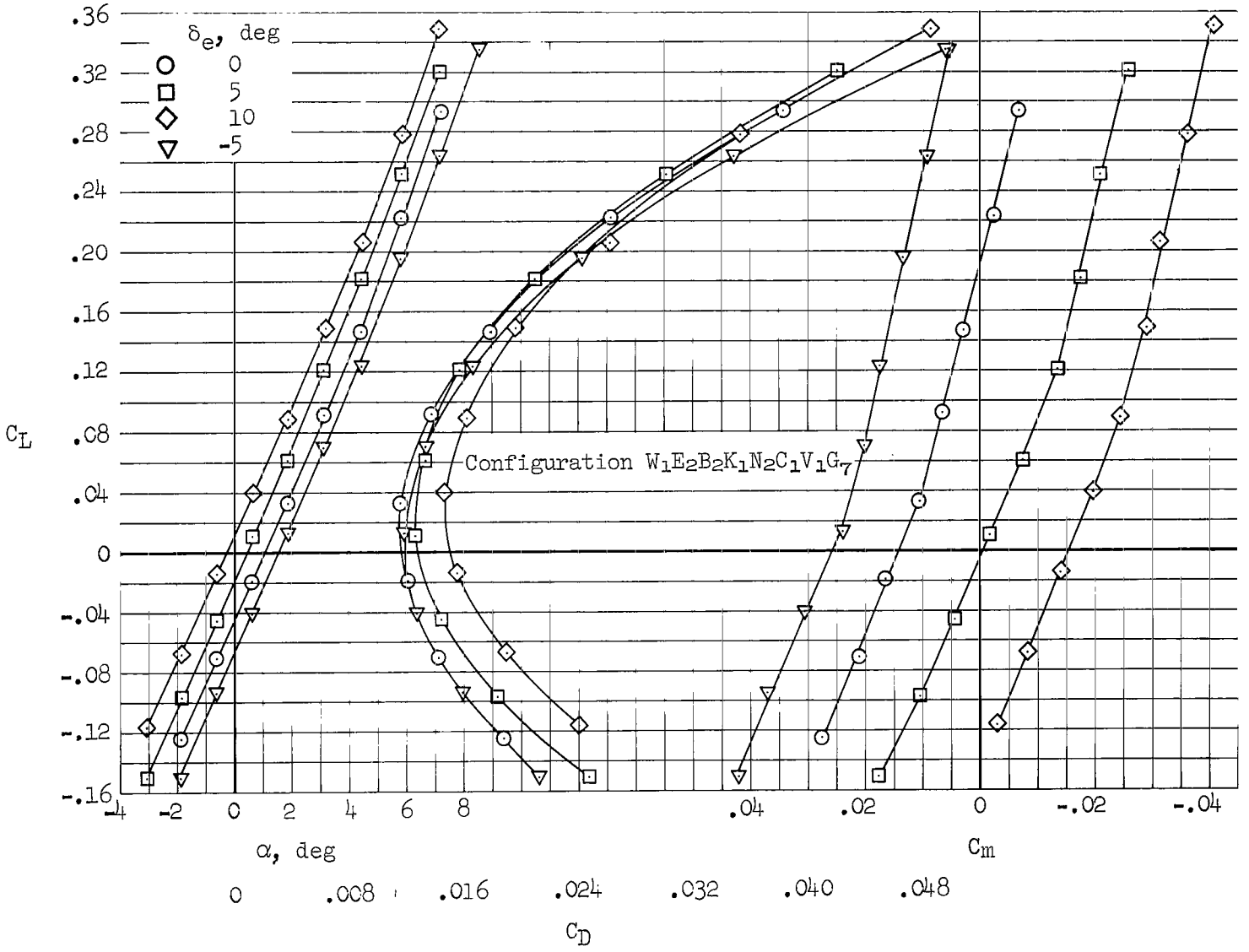

(f) M = 0.95, δ_y = 25°

Figure 20.- Continued.

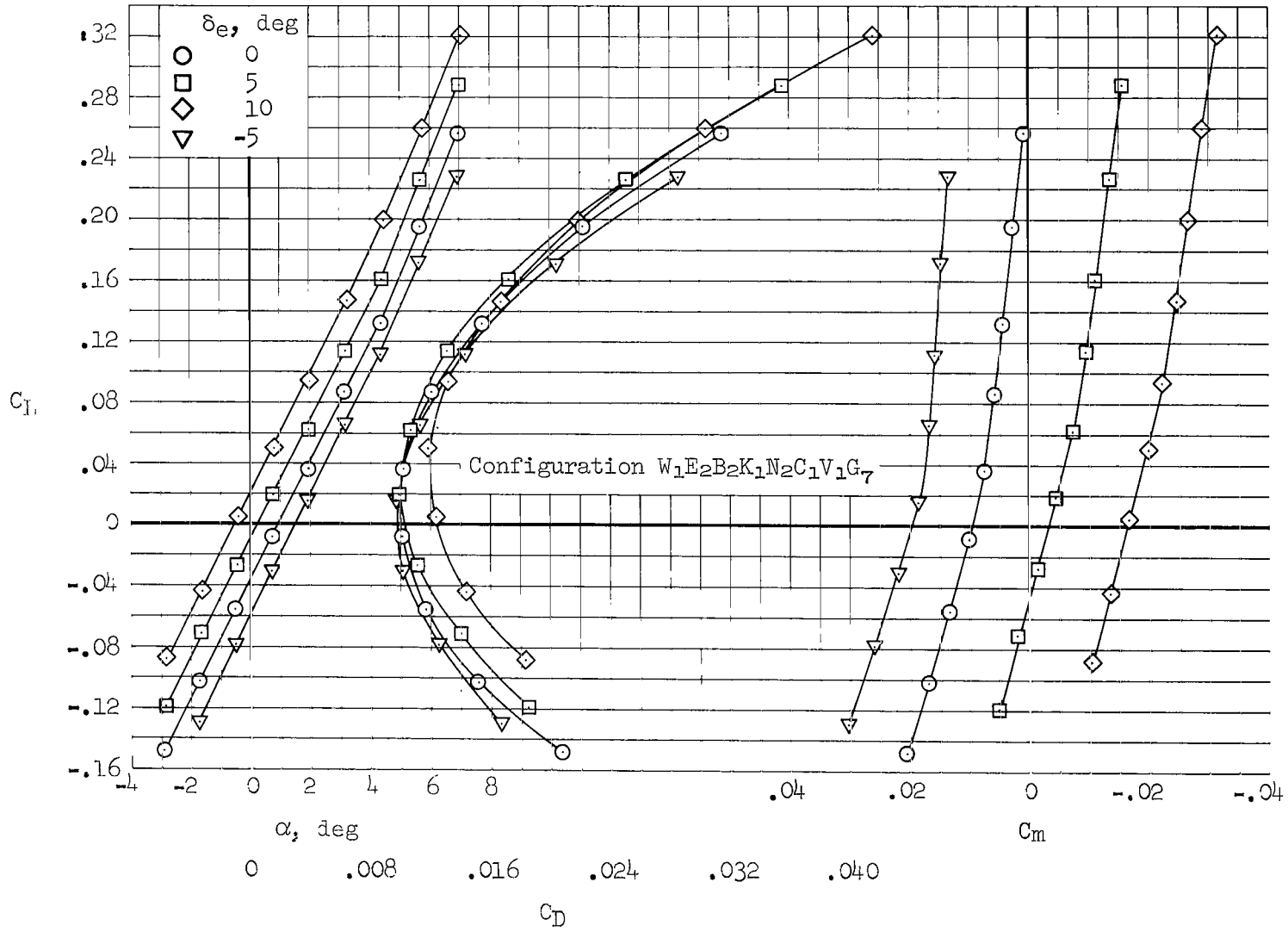

(g) M = 0.80, δ_y = 25°

Figure 20.- Continued.

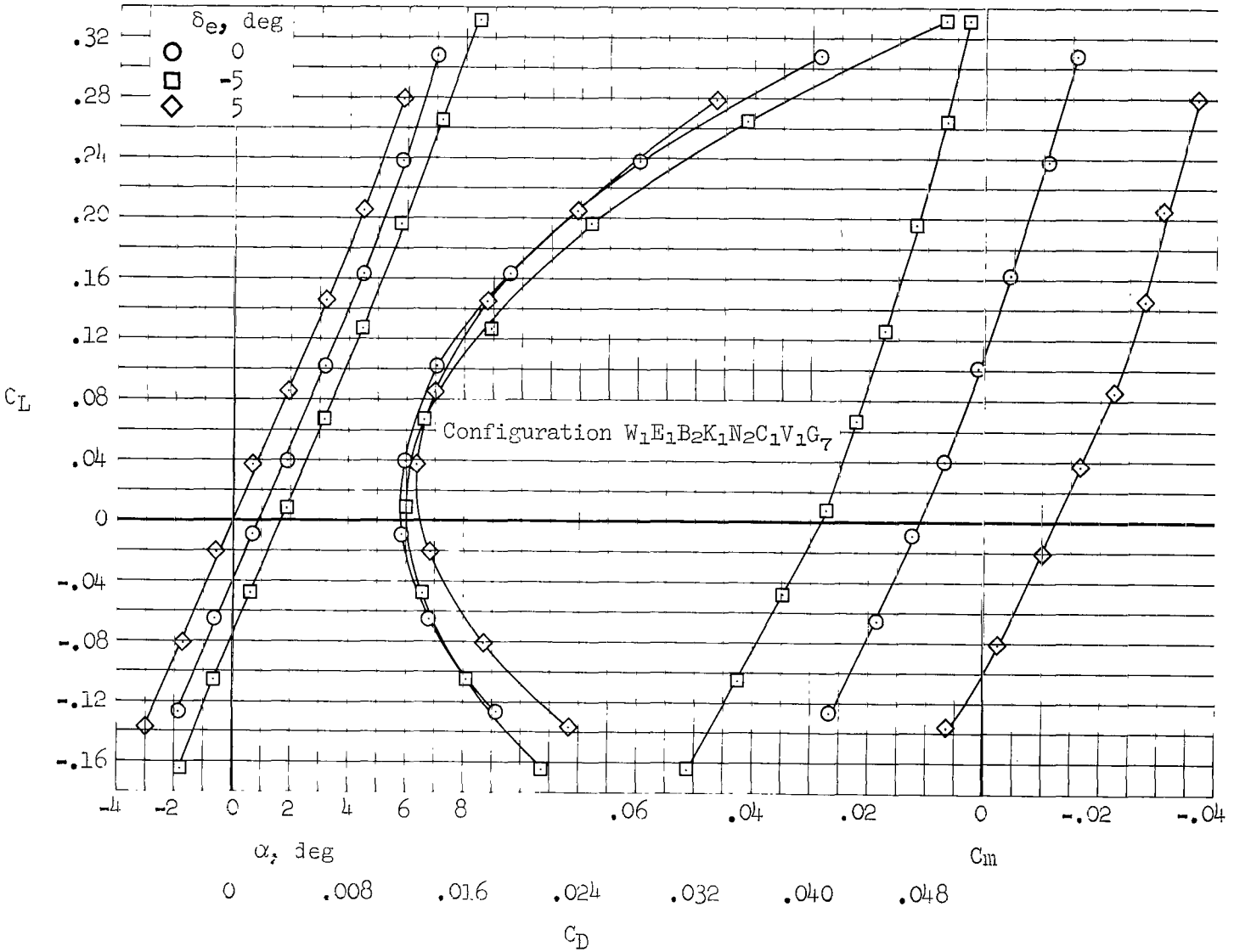

(h) M - 0.95, δ_y = 0°

Figure 20.- Continued.

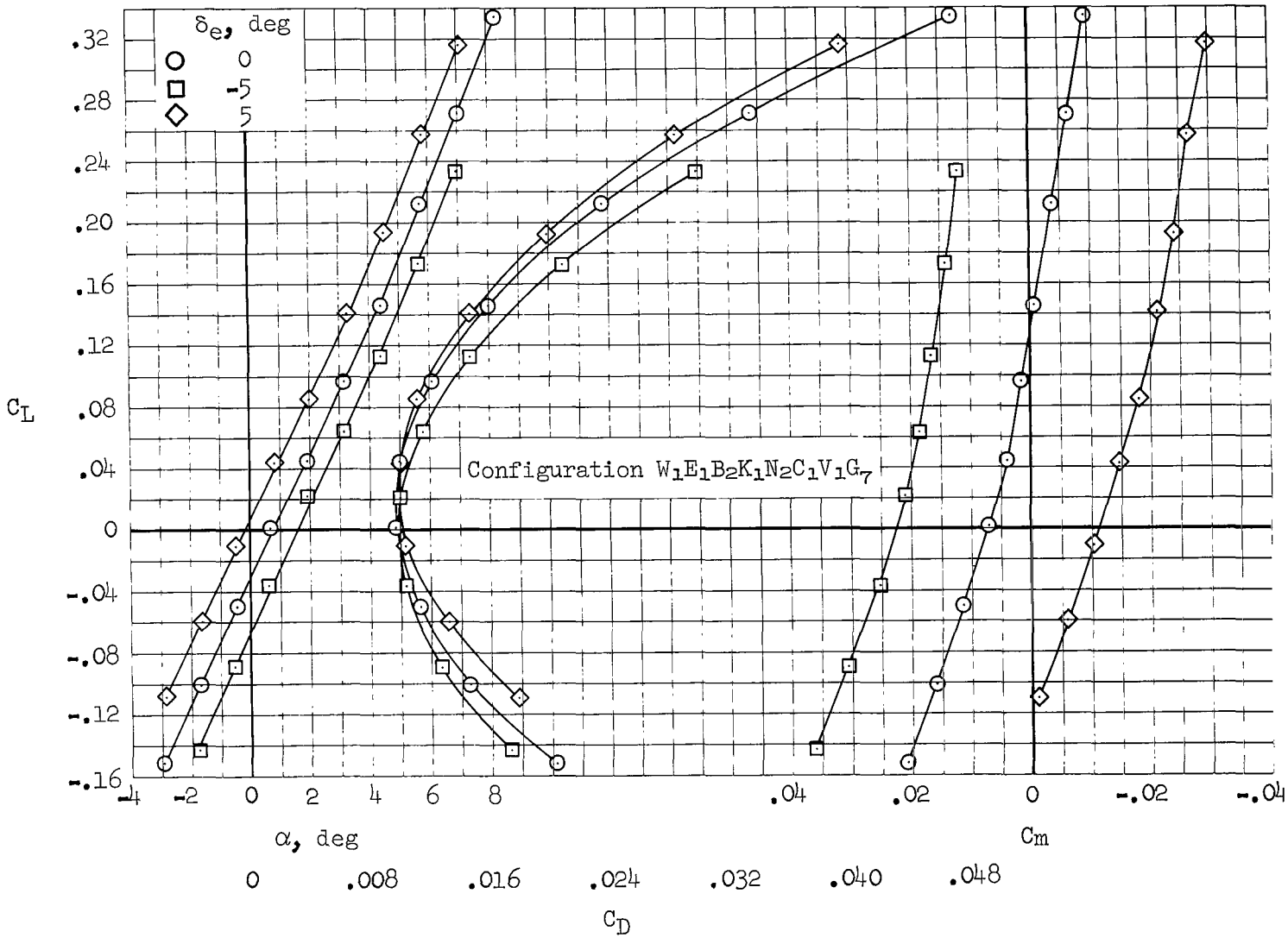

(i) M = 0.80, δ_y = 0°

Figure 20.- Continued.

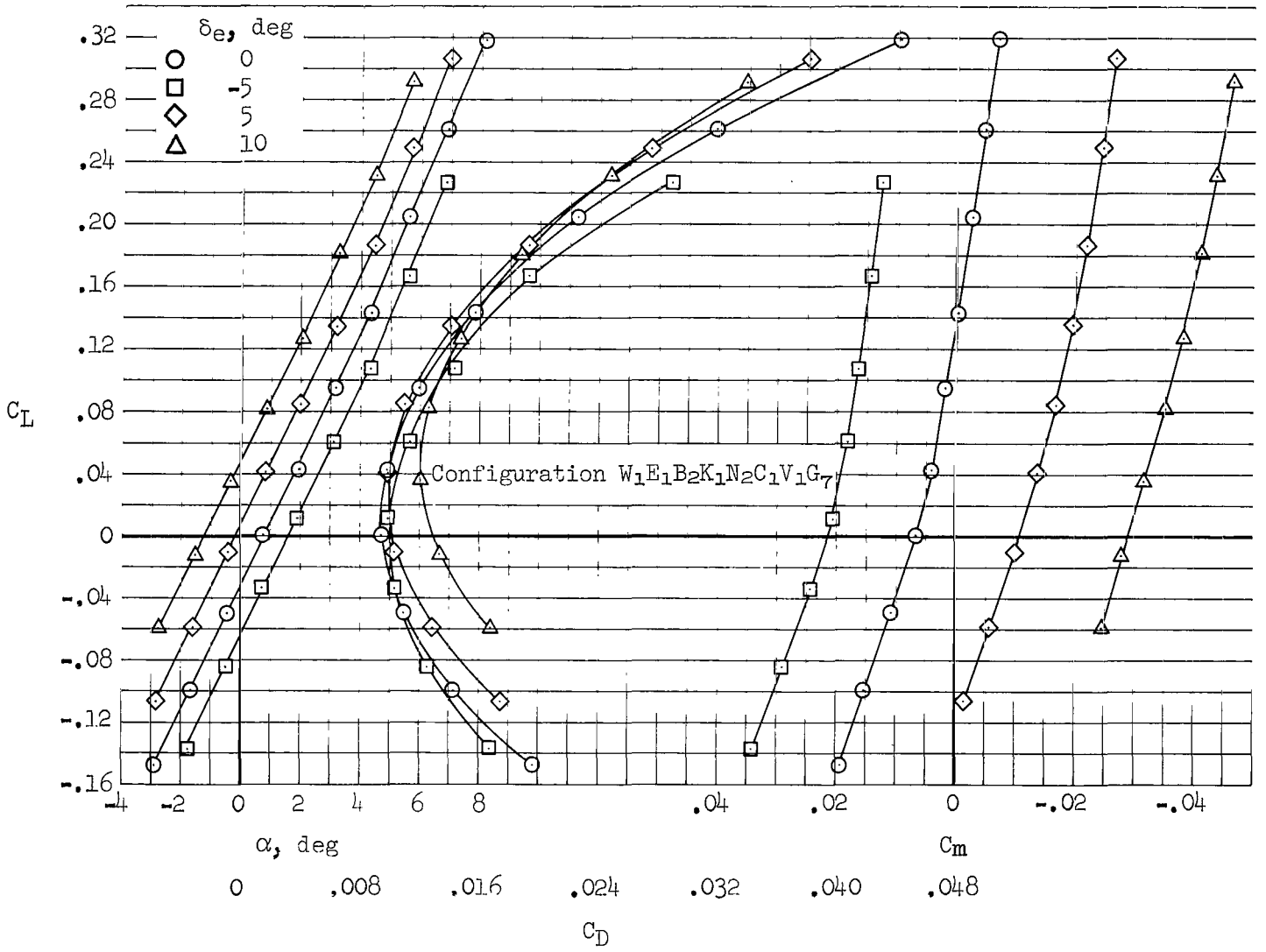

(j) M = 0.75, δ_y = 0°

Figure 20.- Continued.

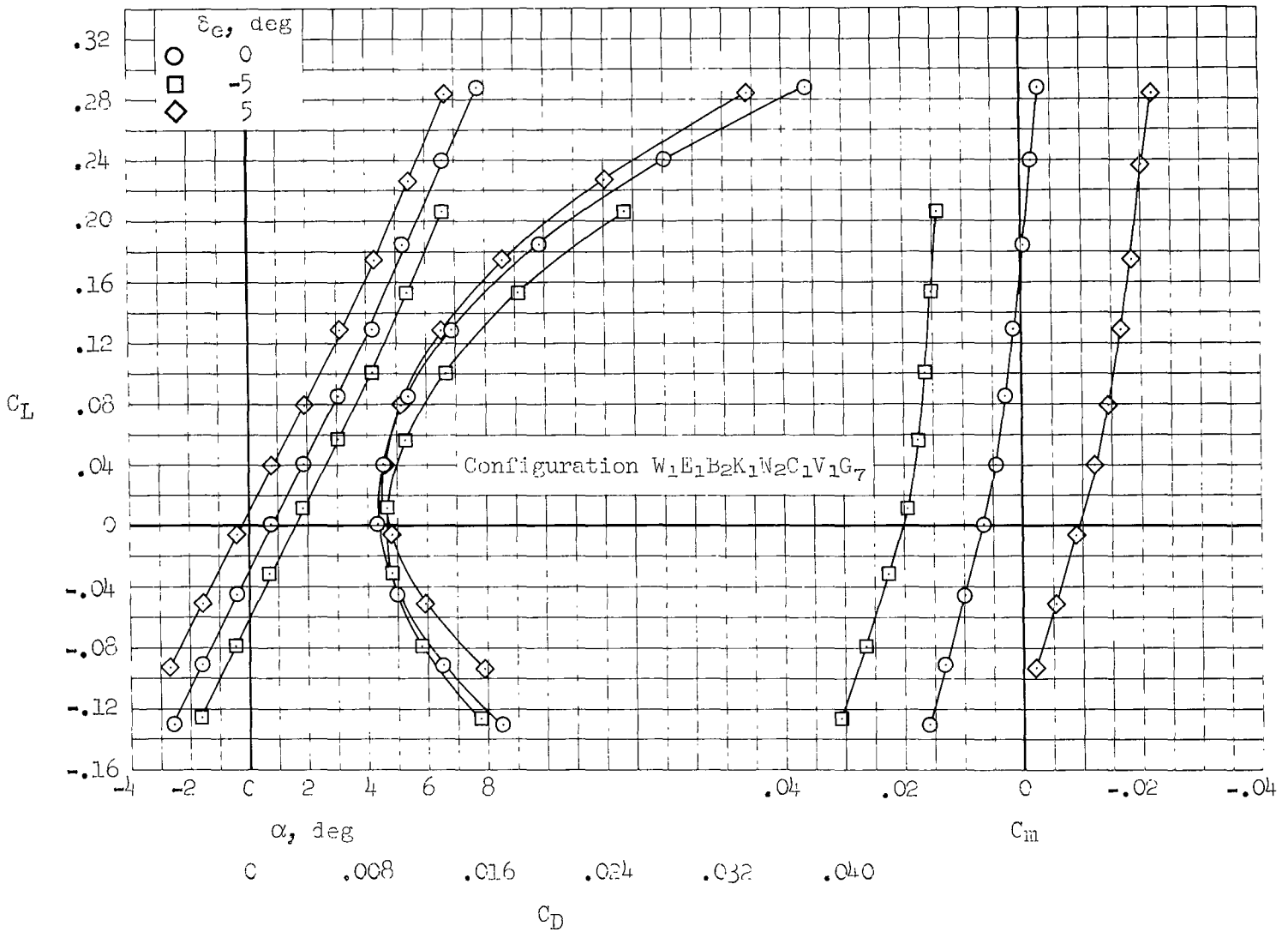

(k) M = 0.60, δ_y = 0°

Figure 20.- Concluded.

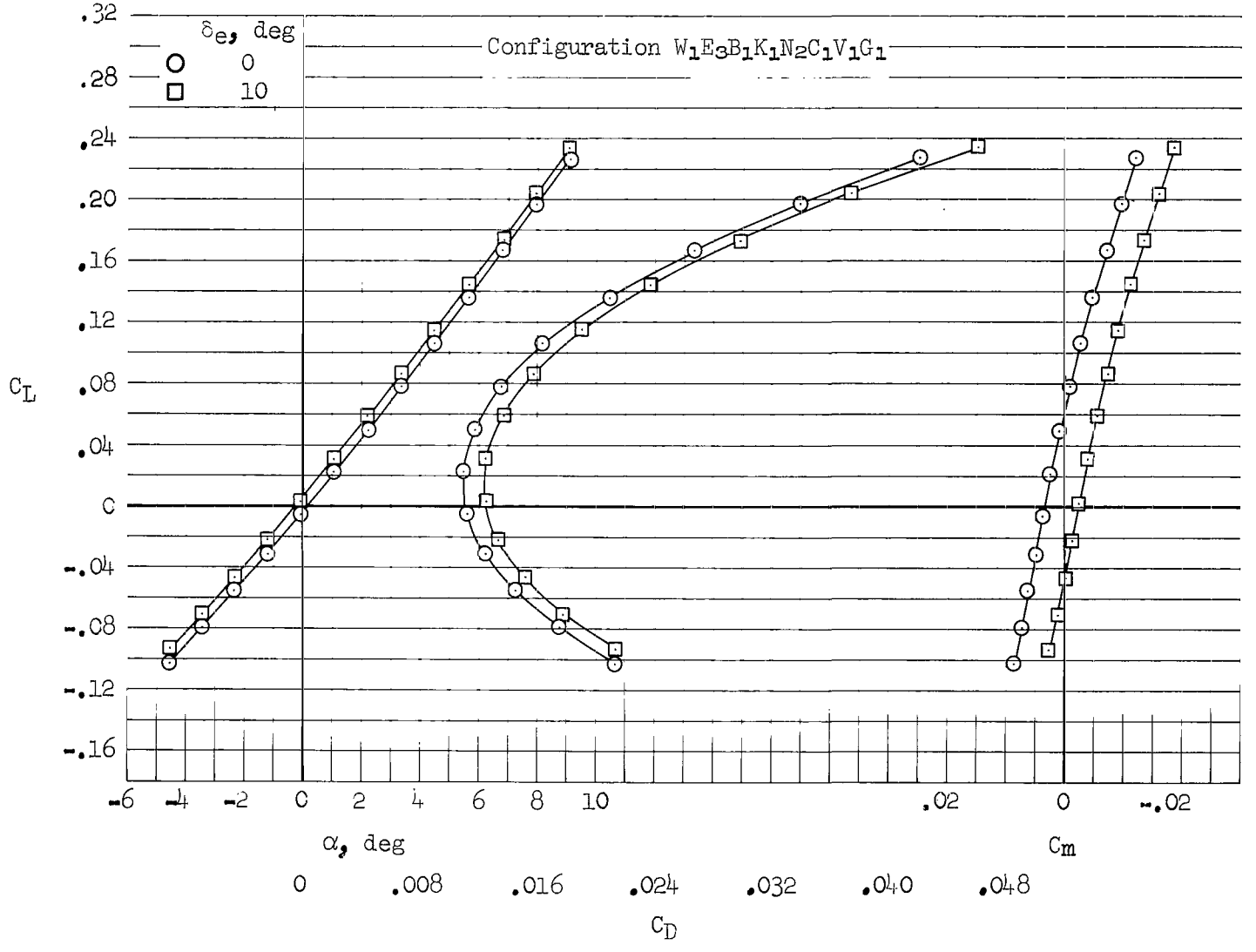

(a) M = 2.53, δ_y = 75°

Figure 21.- Longitudinal results for the developmental-elevon configuration segmentation gaps filled and taped.

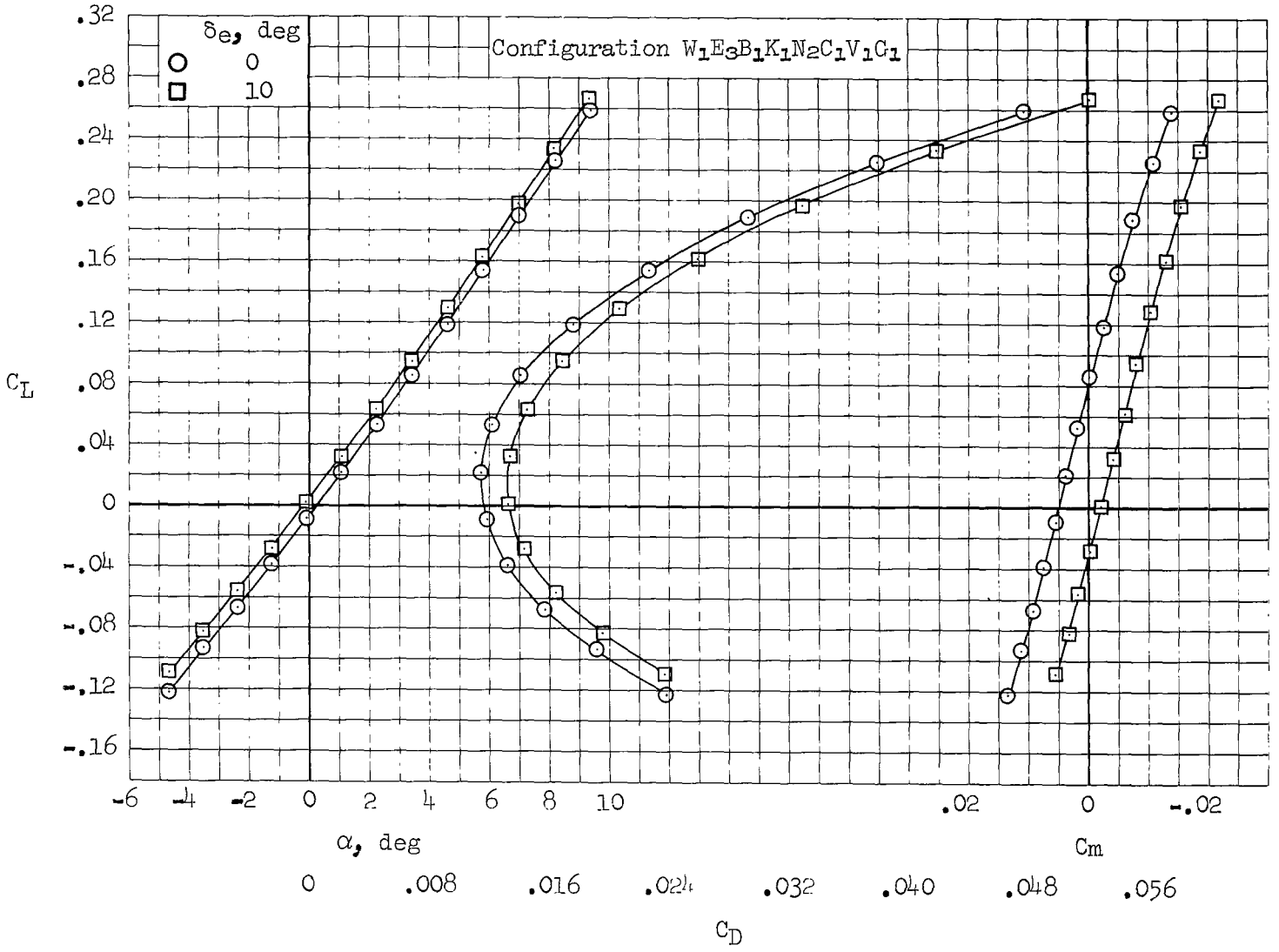

(b) M = 2.10, δ_Y = 65°

Figure 21.- Continued.

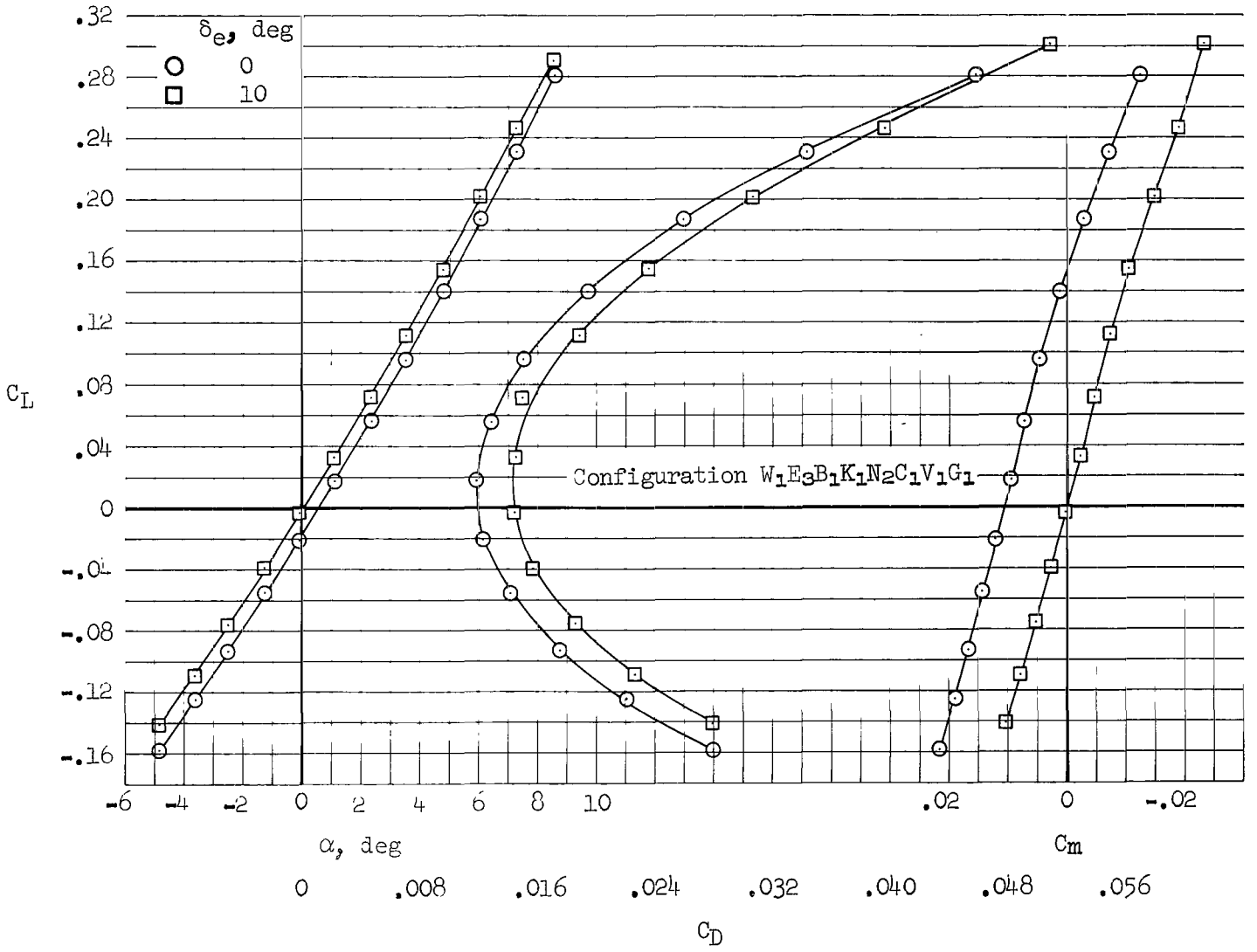

(c) M = 1.60, δ_y = 65°

Figure 21.- Continued.

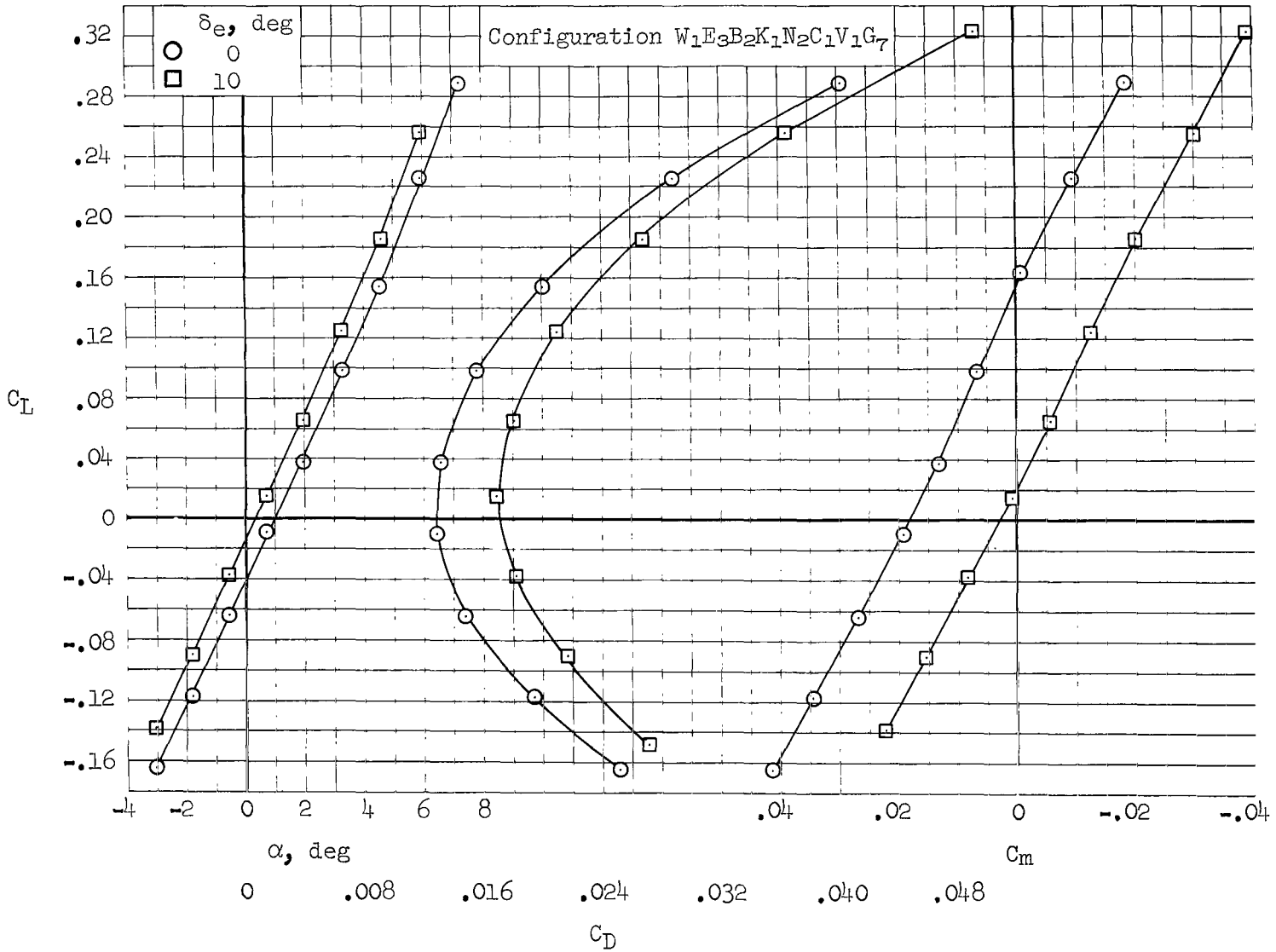

(d) M = 1.20, δ_y = 25°

Figure 21.- Continued.

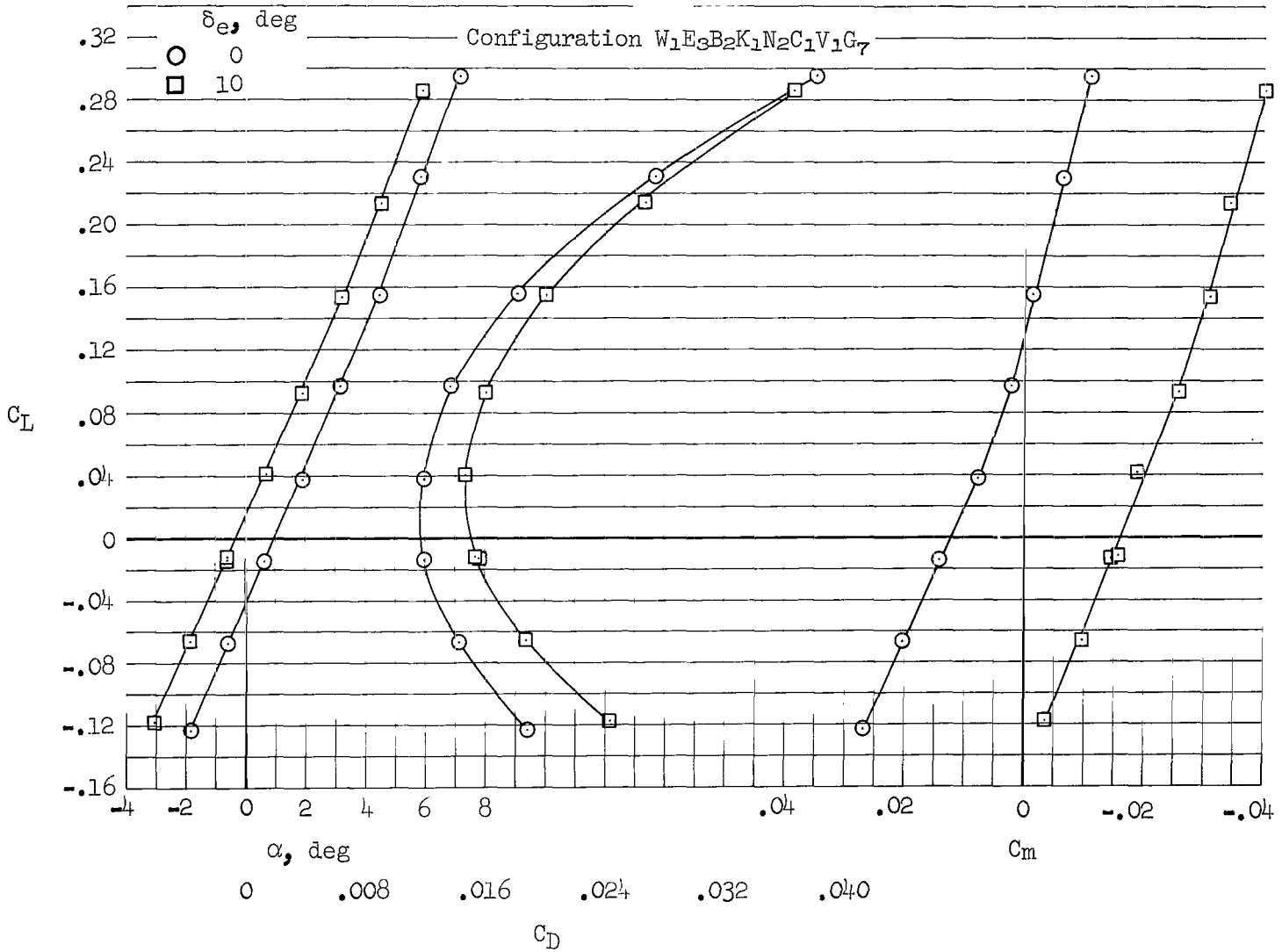

(e) M = 0.95, δ_y = 25°

Figure 21.- Concluded.

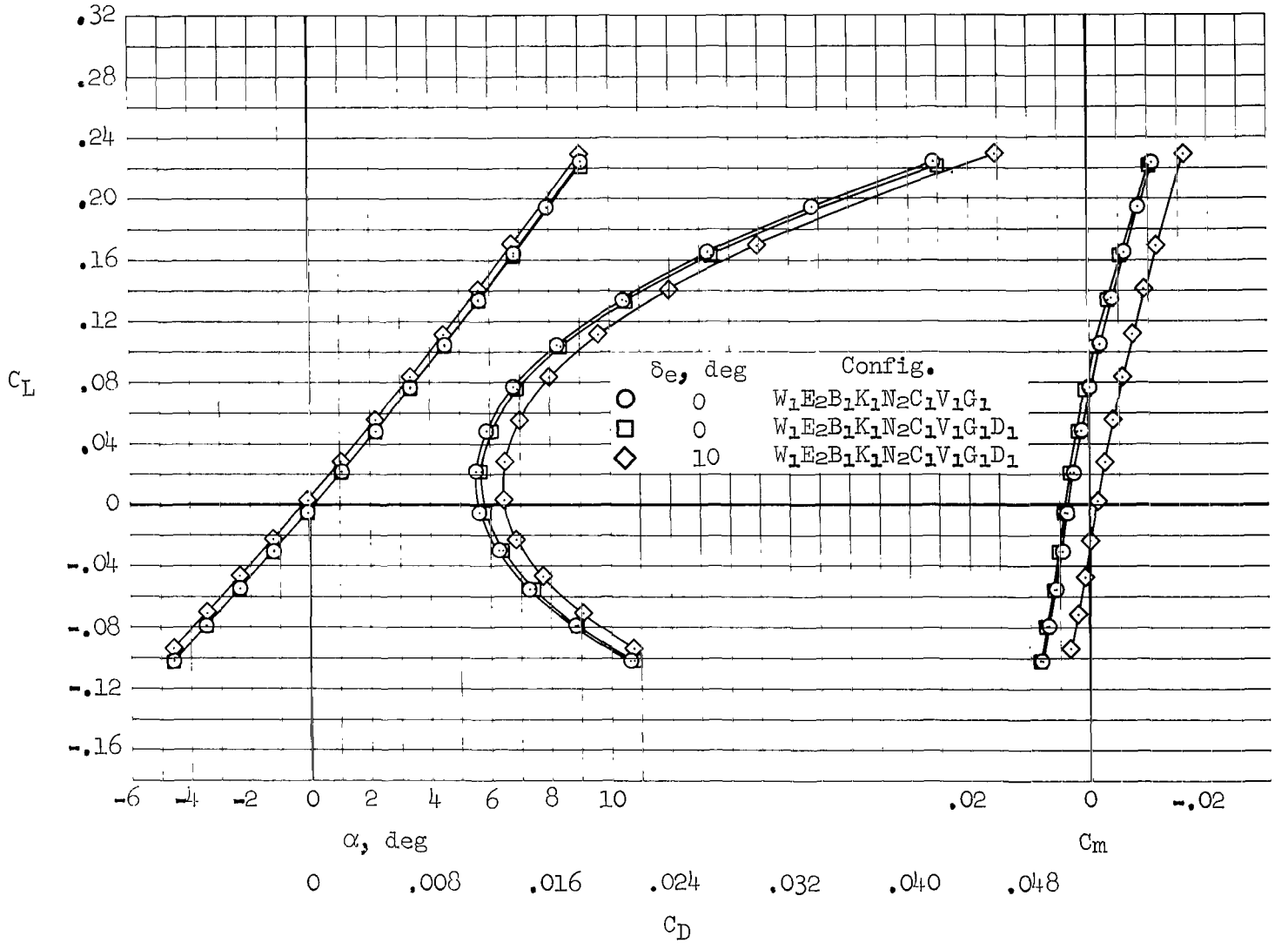

(a) M = 2.53, δ_y = 65°

Figure 22.- Effects on the longitudinal characteristics of adding the bleed dump and deflecting the elevon with the bleed dump in position.

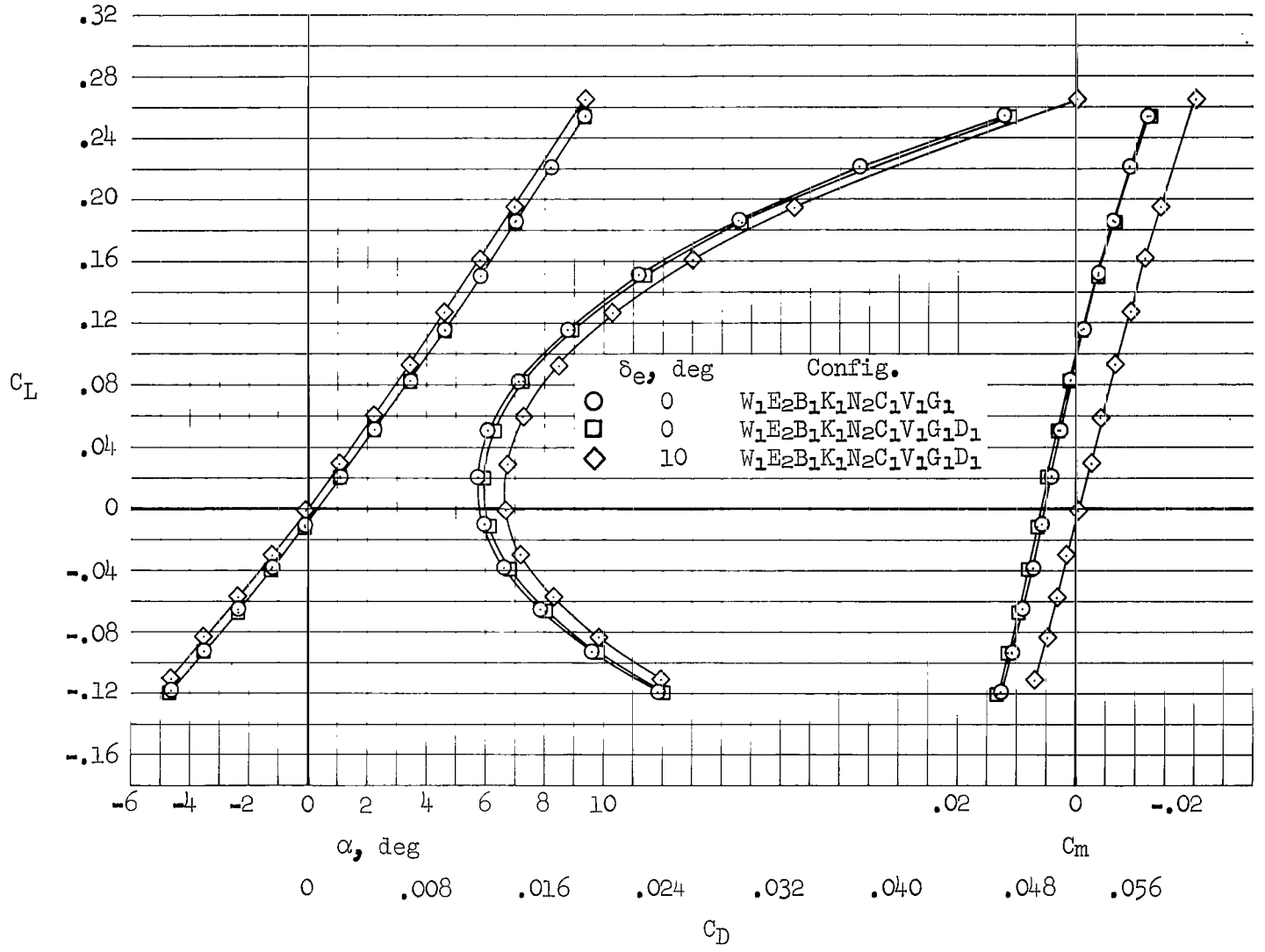

(b) M = 2.10, δ_y = 65°

Figure 22.- Continued.

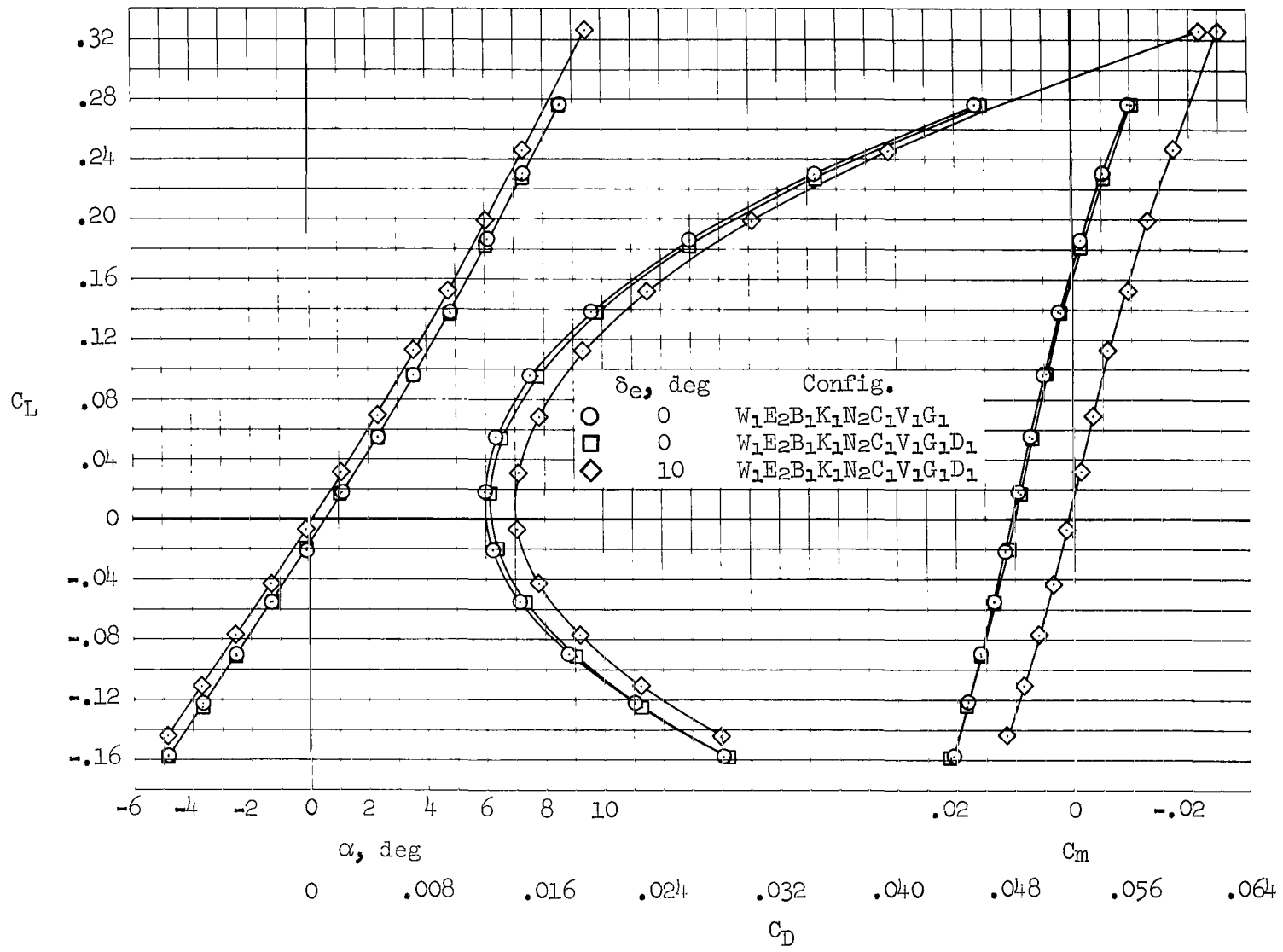

(c) M = 1.60, δ_y = 65°

Figure 22.- Continued.

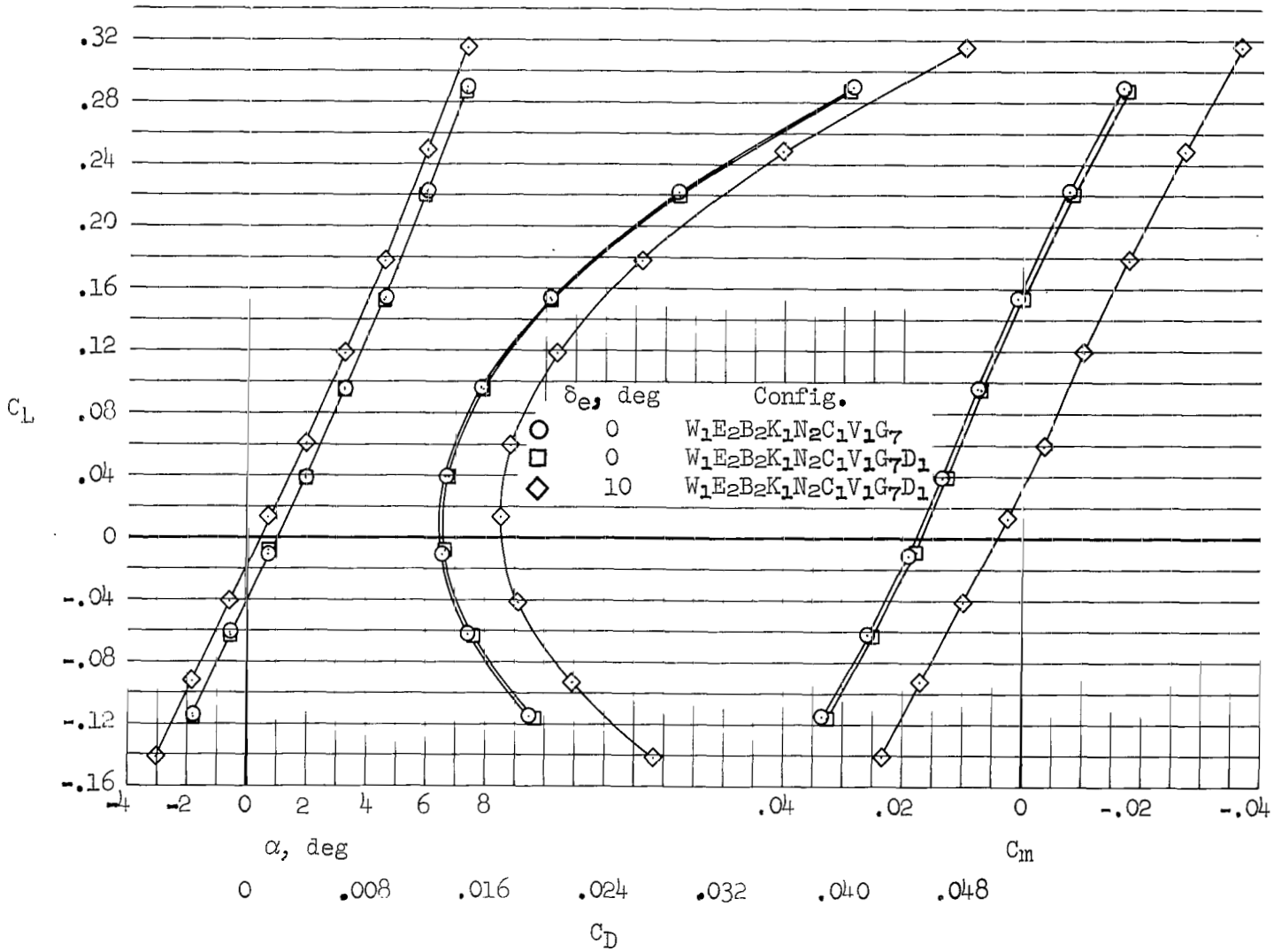

(d) M = 1.20, δ_y = 25°

Figure 22.- Continued.

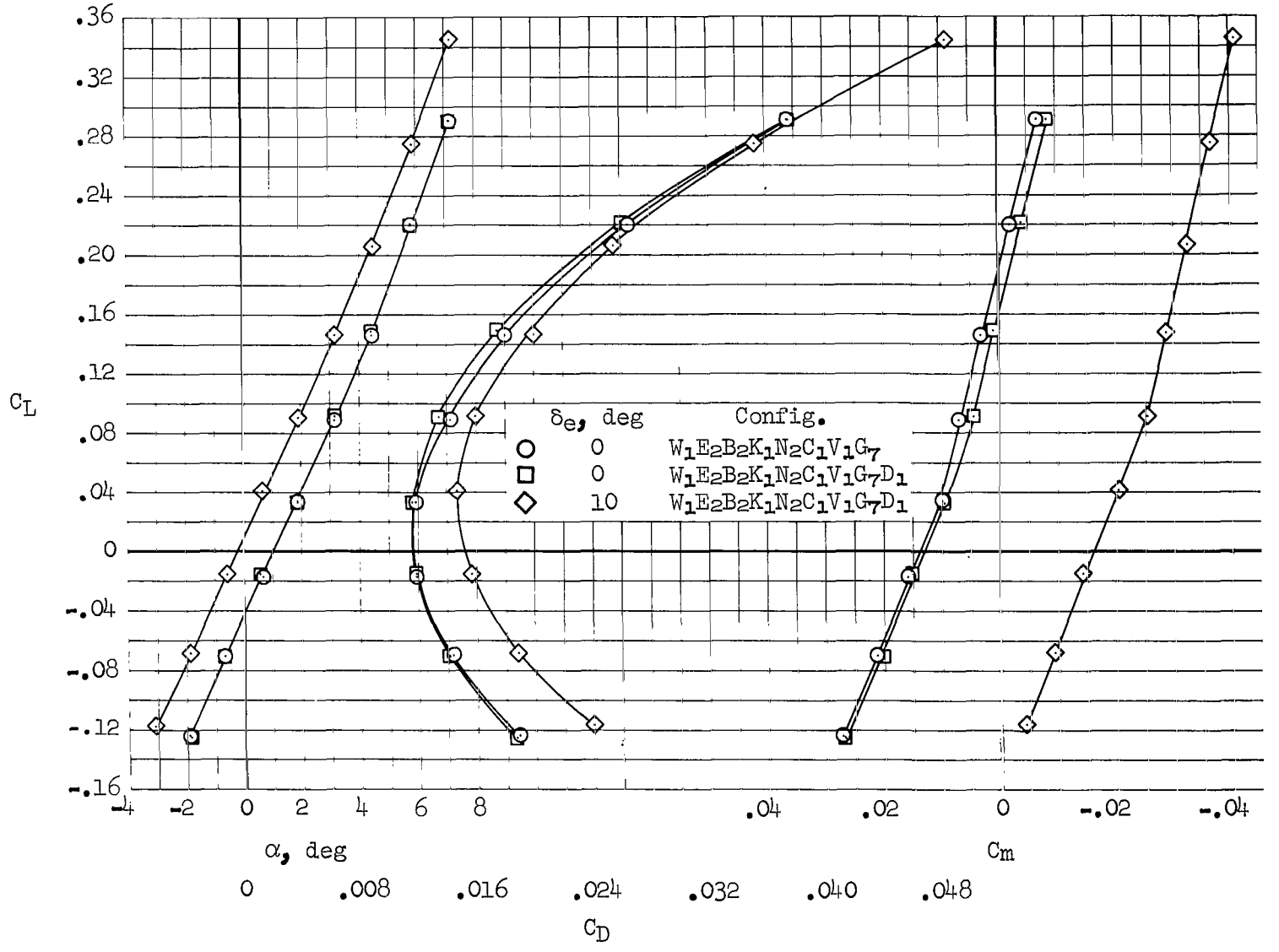

(e) M = 0.95, δ_y = 25°

Figure 22.- Continued.

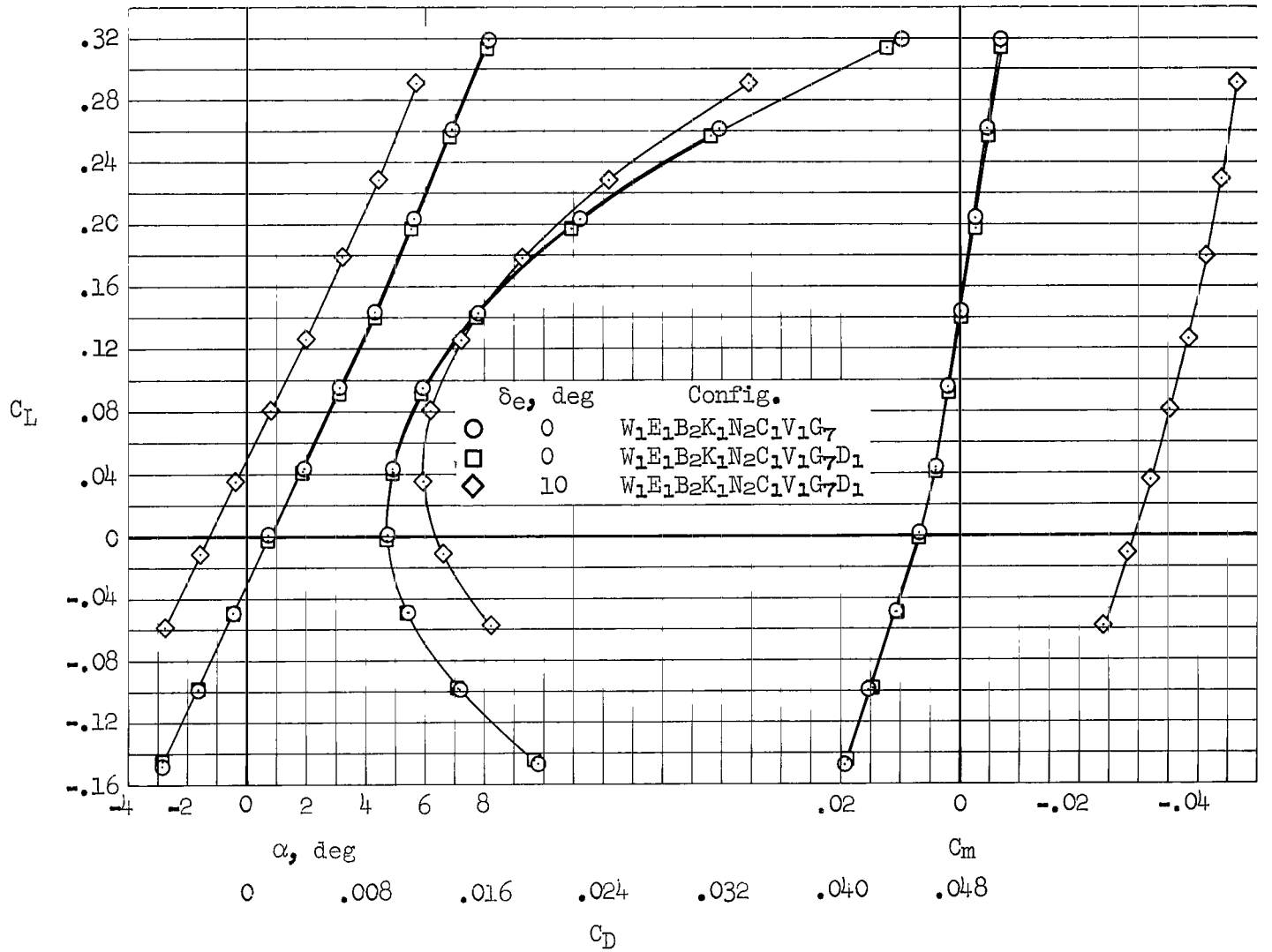

(f) M = 0.75, δ_y = 0°

Figure 22.- Concluded.

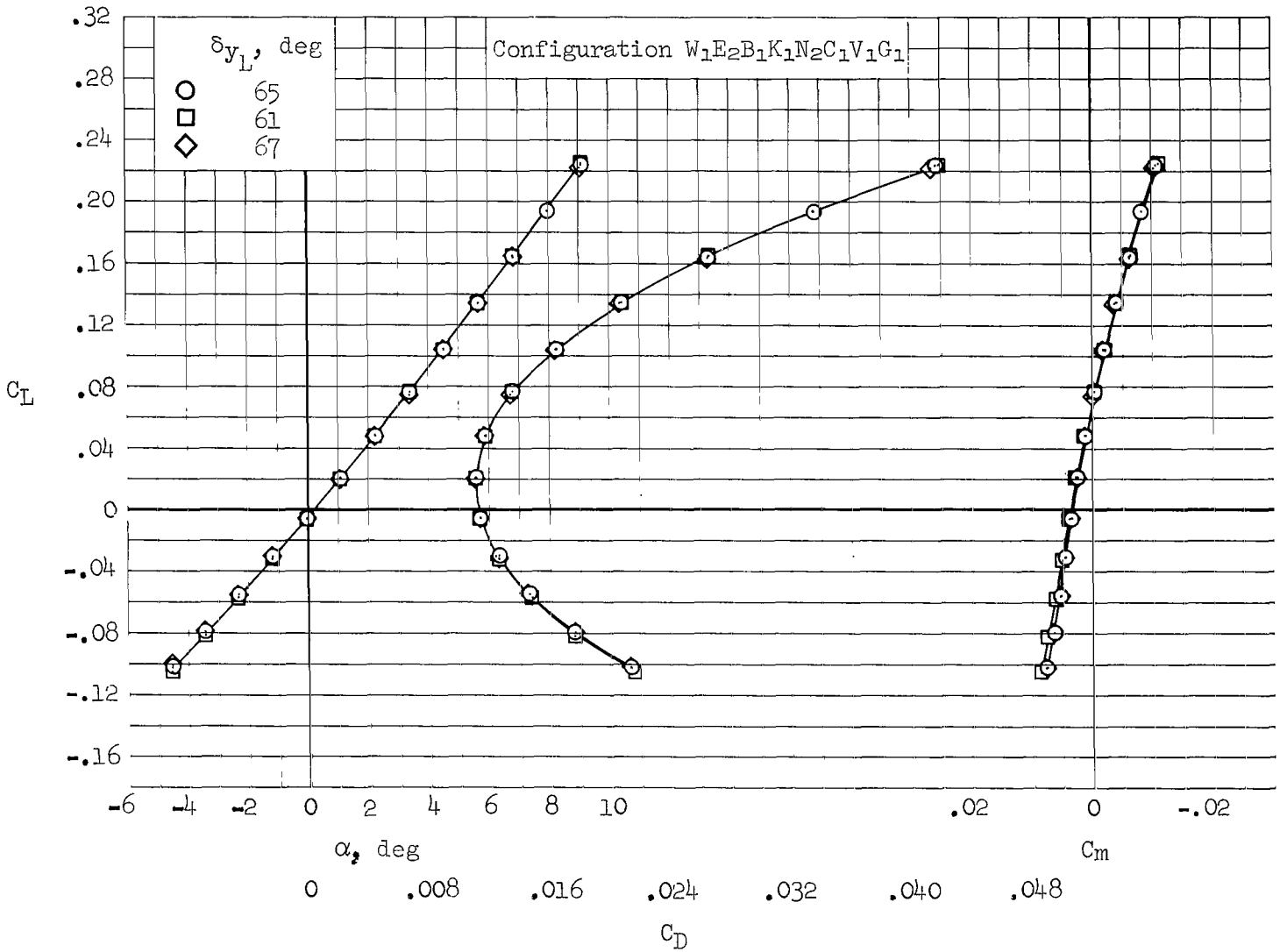

(a) M = 2.53, δ_{y_R} = 65°

Figure 23.- Effects of asymmetric deflection of the wing tips on longitudinal characteristics.

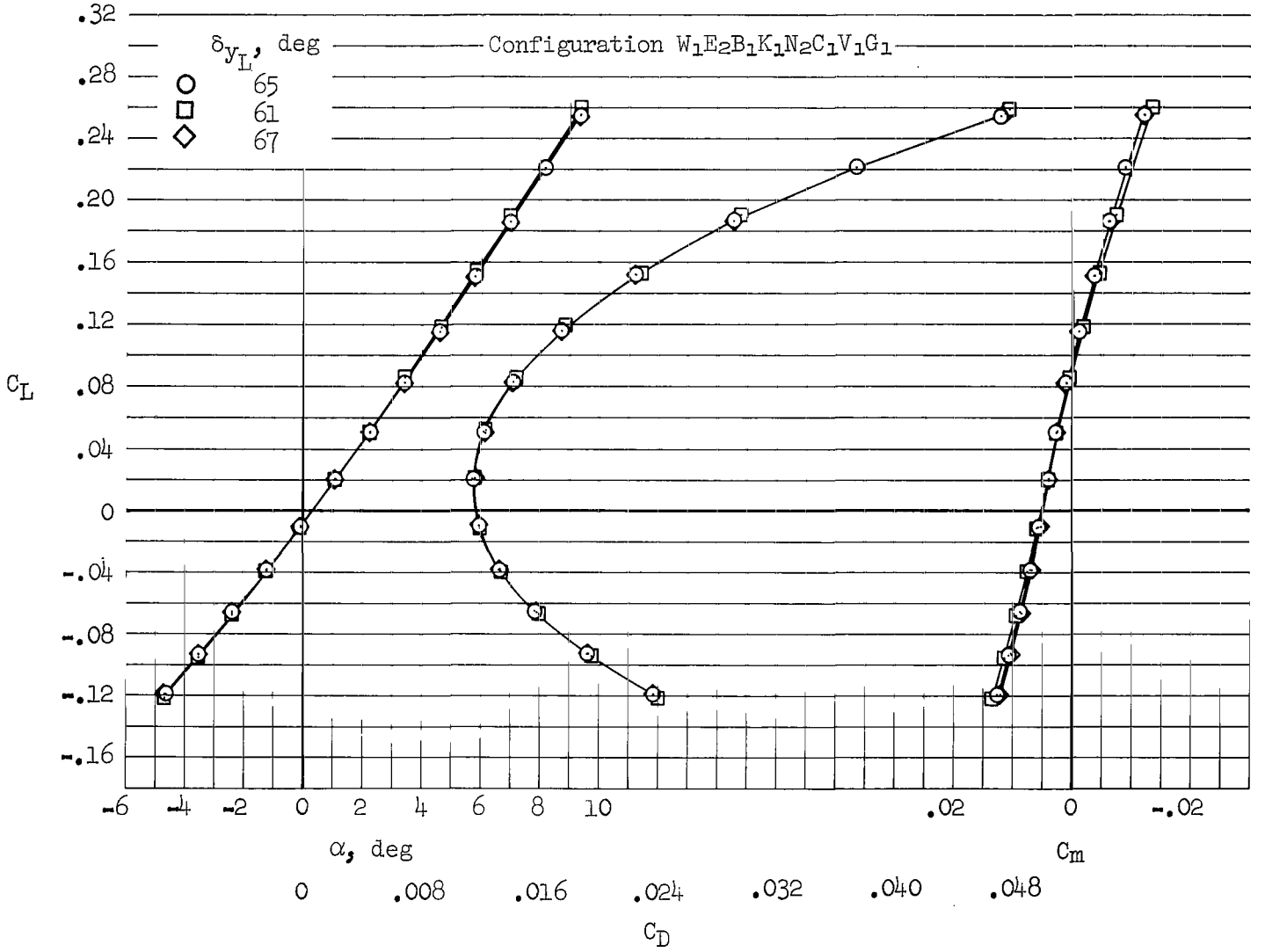

(b) M = 2.10, δ_{y_R} = 65°

Figure 23.- Continued.

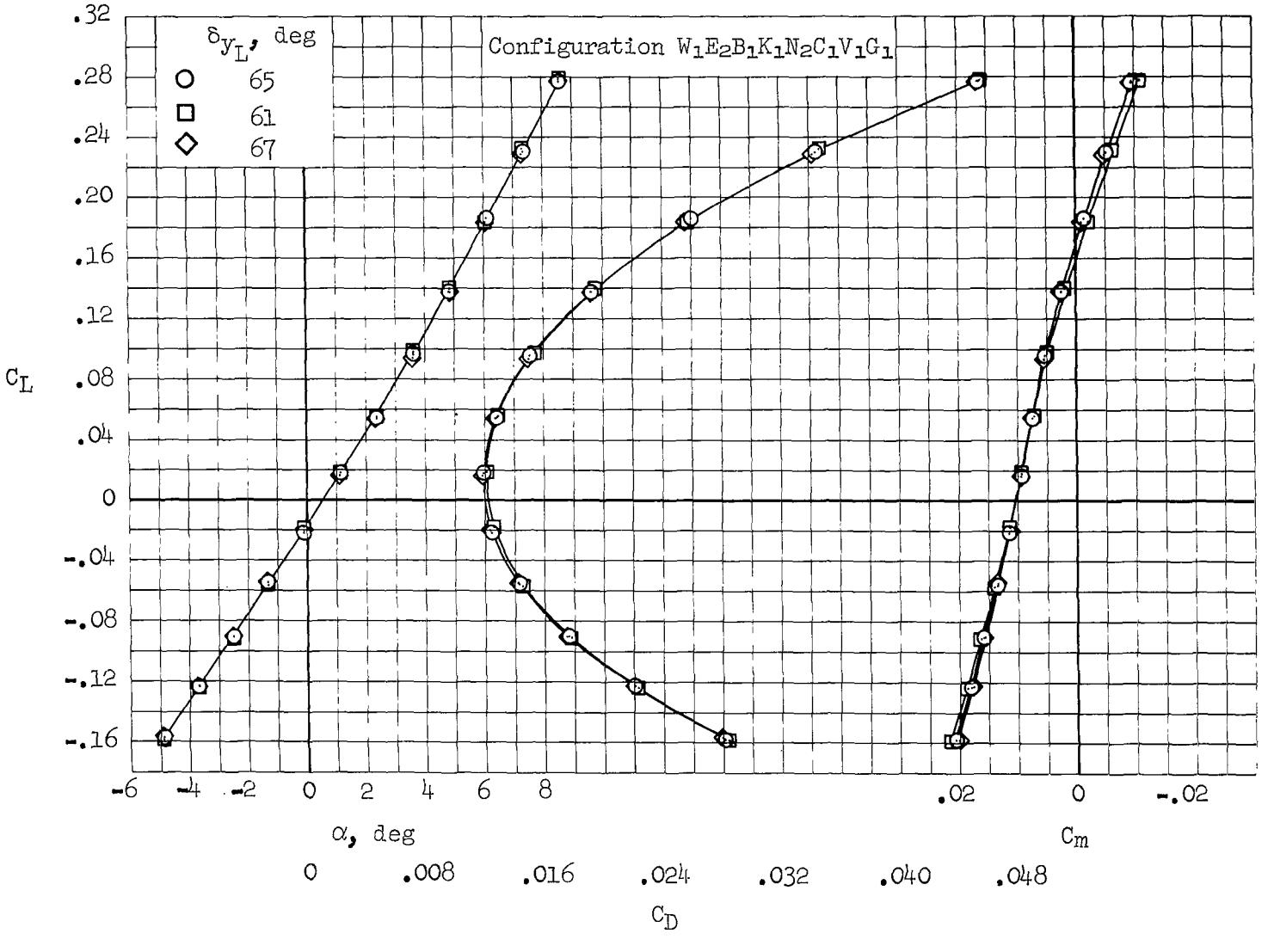

(c) M = 1.60, δ_{Y_R} = 65°

Figure 23.- Continued.

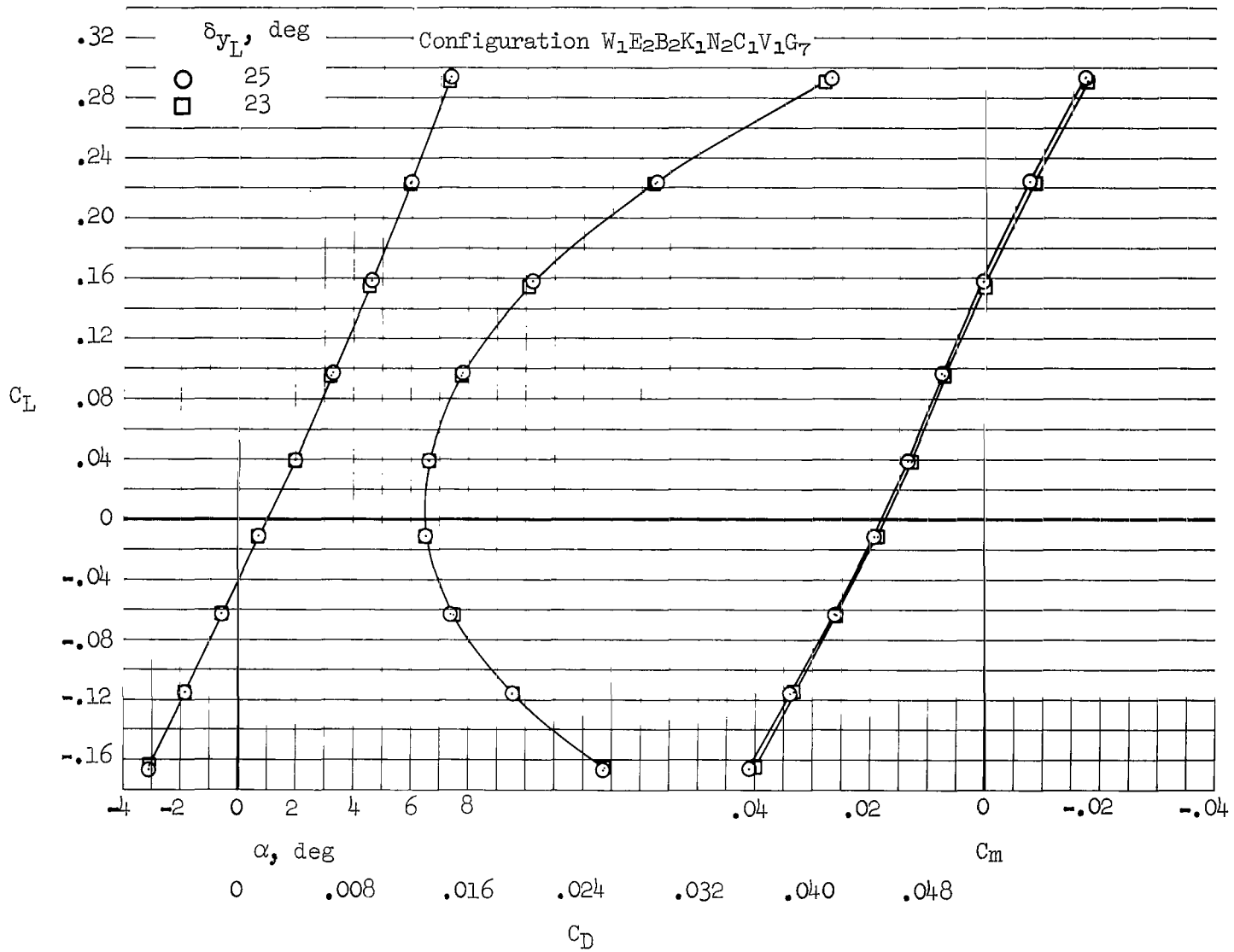

(d) M = 1.20, δ_{y_R} = 25°

Figure 23.- Continued.

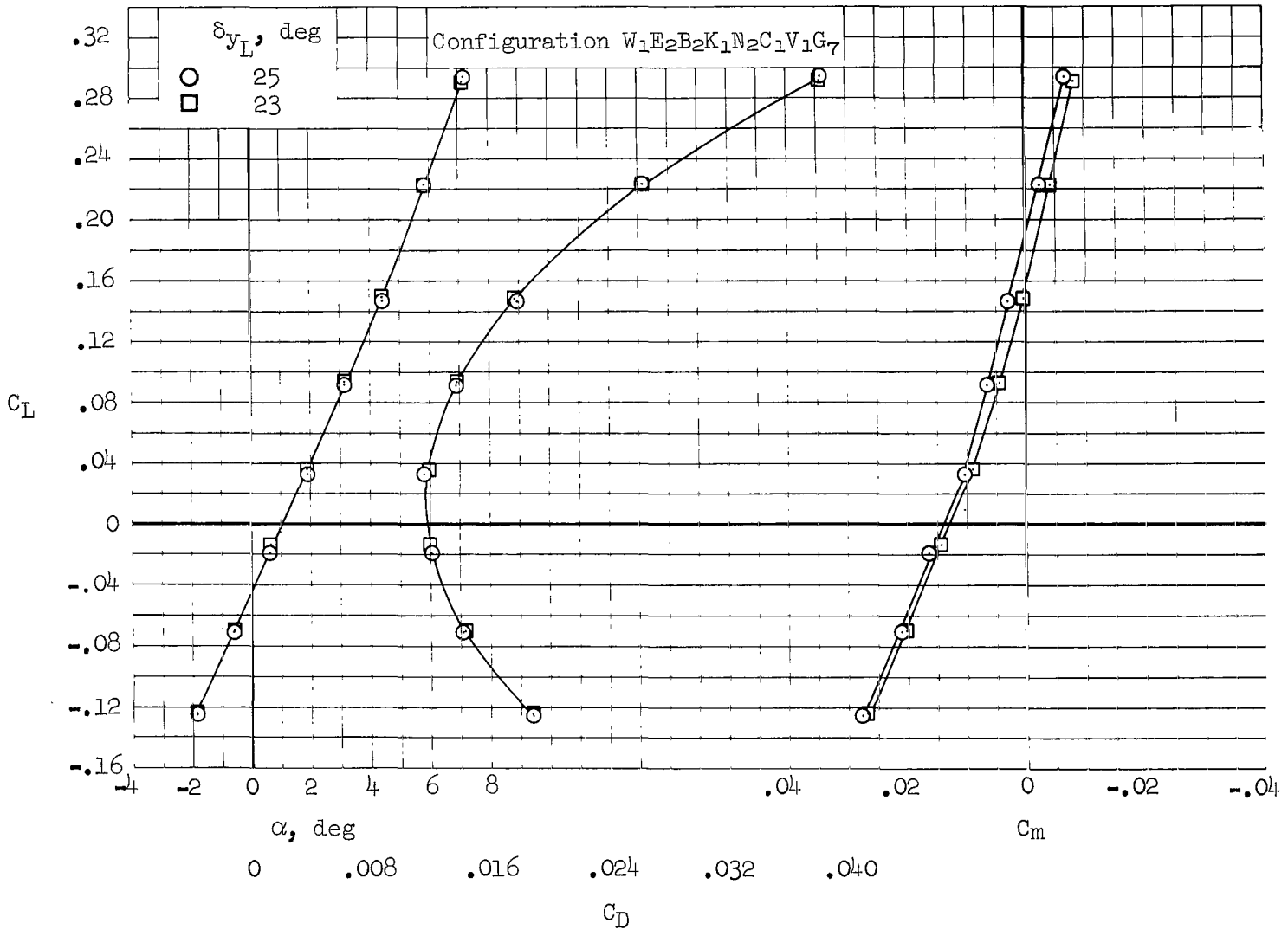

(e) M = 0.95, δ_{y_R} = 25°

Figure 23.- Concluded.

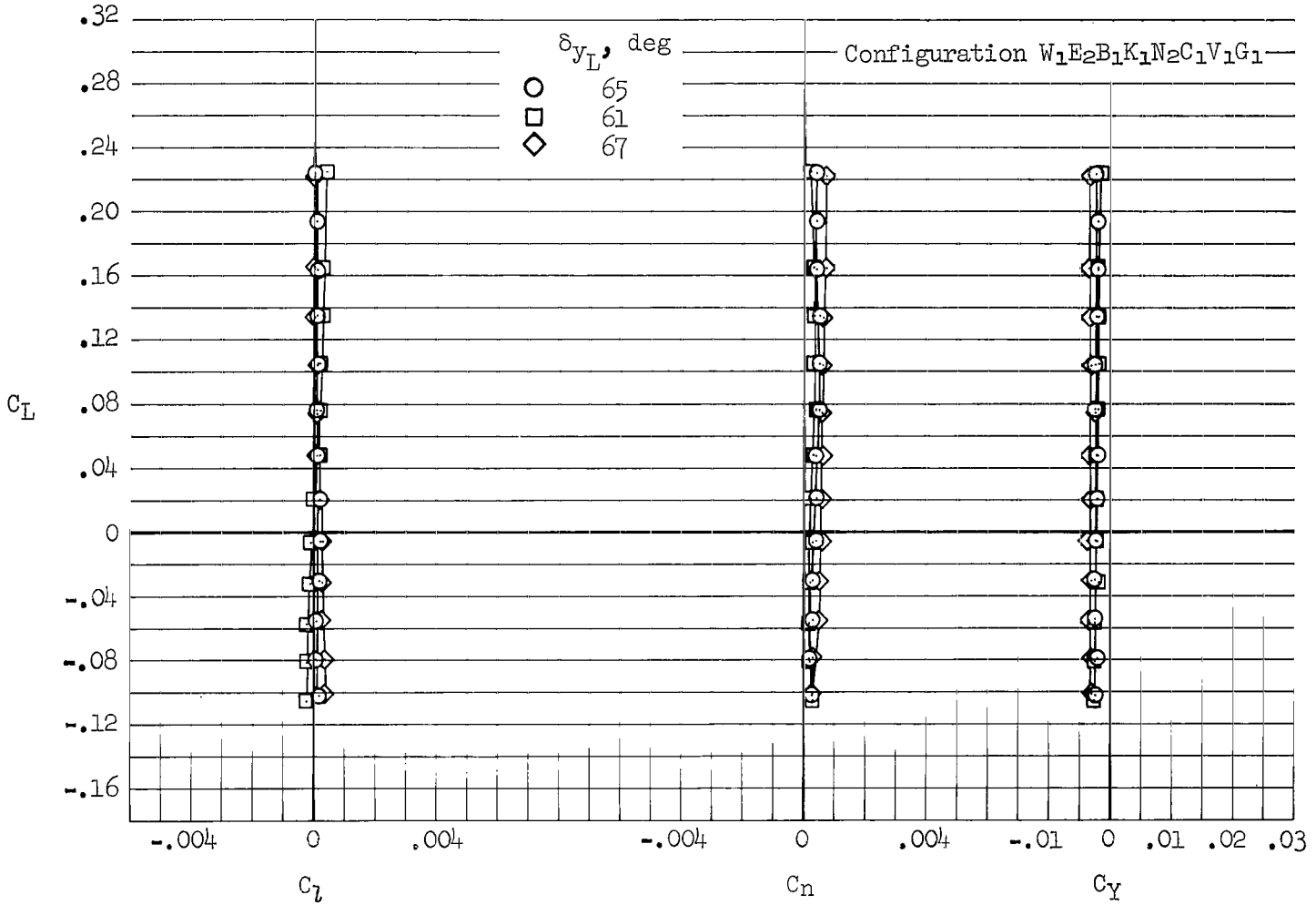

(a) M = 2.53, δ_{y_R} = 65°

Figure 24.- Effects of asymmetric deflection of the wing tips on the rolling-moment, yawing-moment, and side-force characteristics.

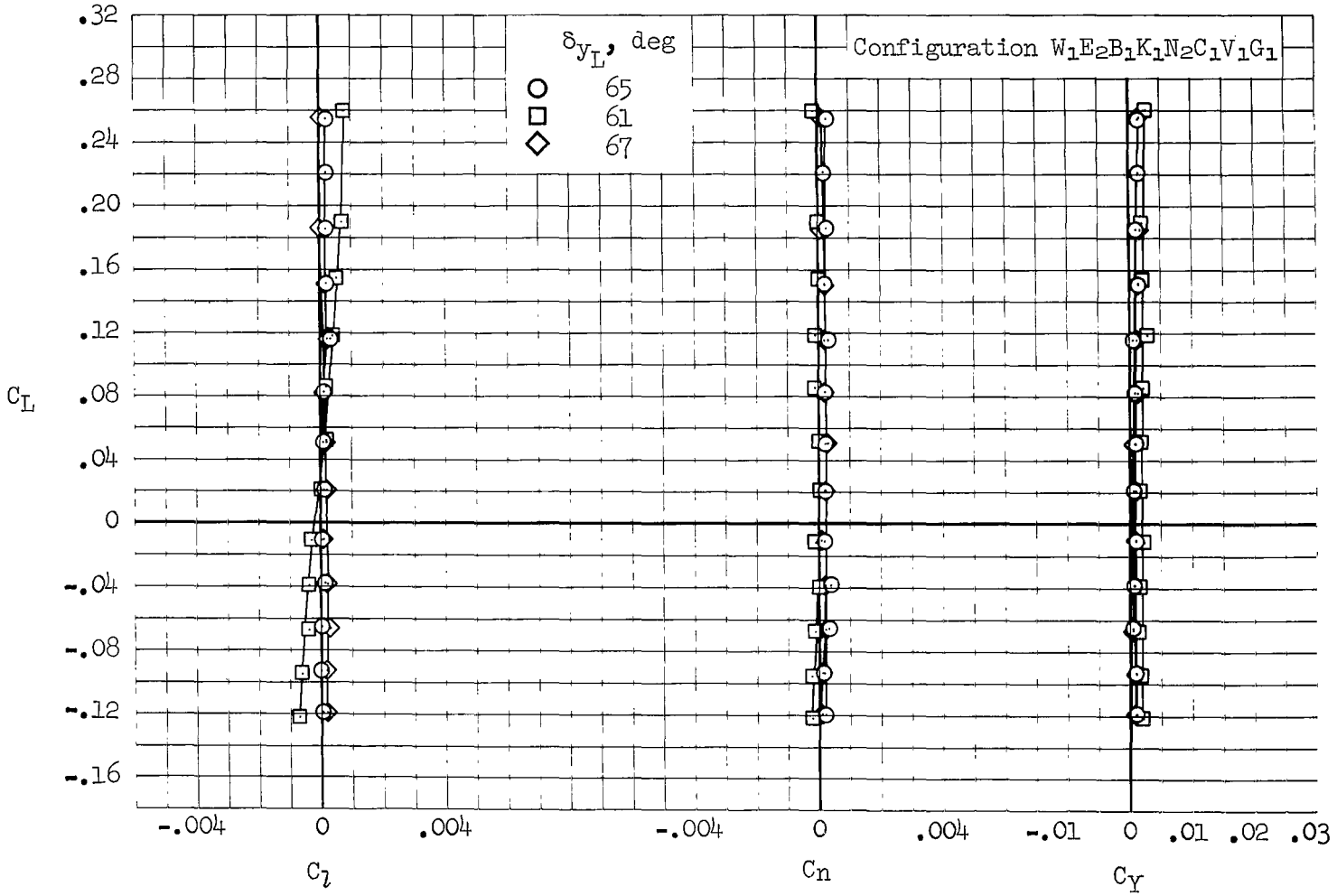

(b) M = 2.10, δ_{y_R} = 65°

Figure 24.- Continued.

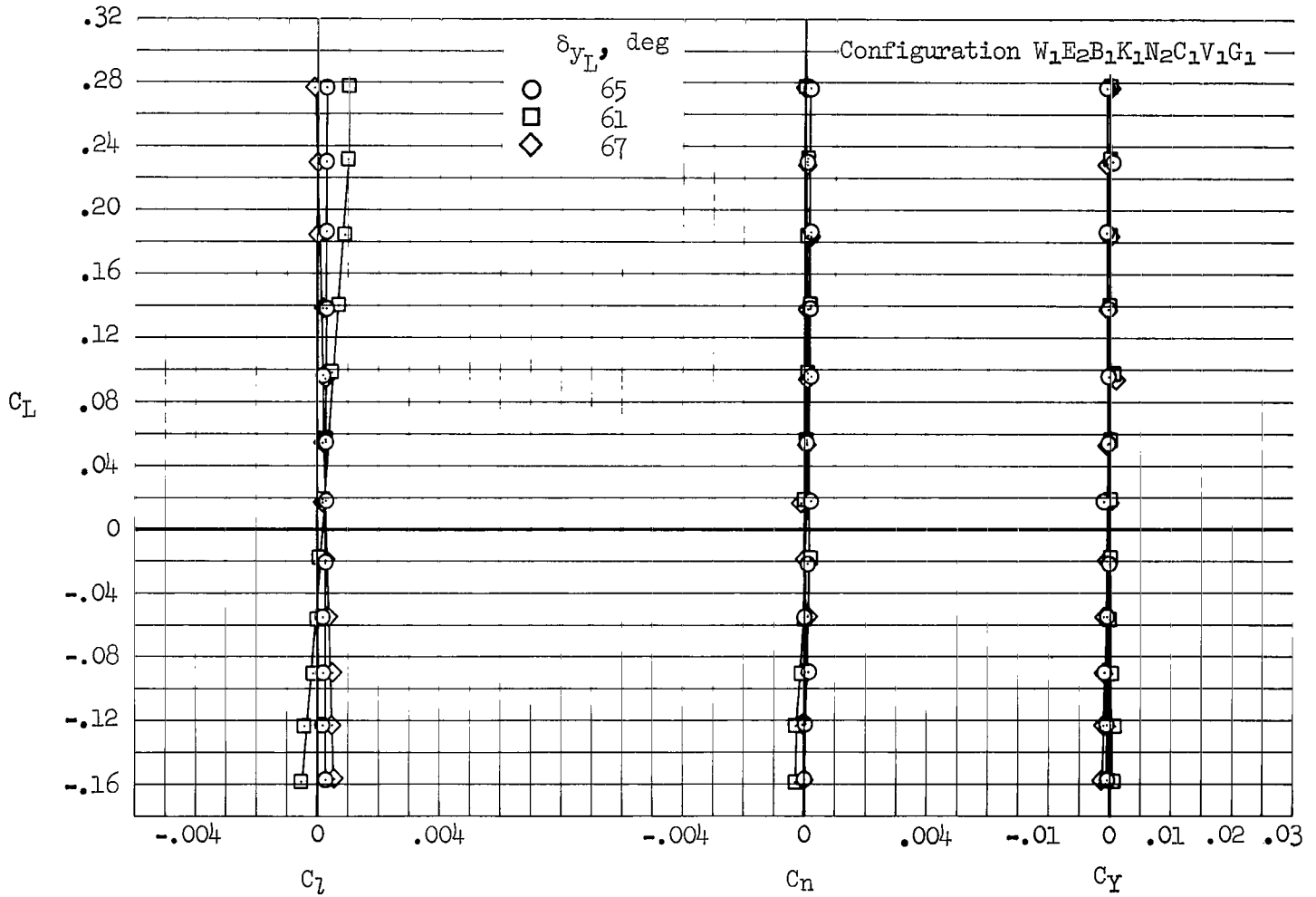

(c) M = 1.60, δ_{y_R} = 65°

Figure 24.- Continued.

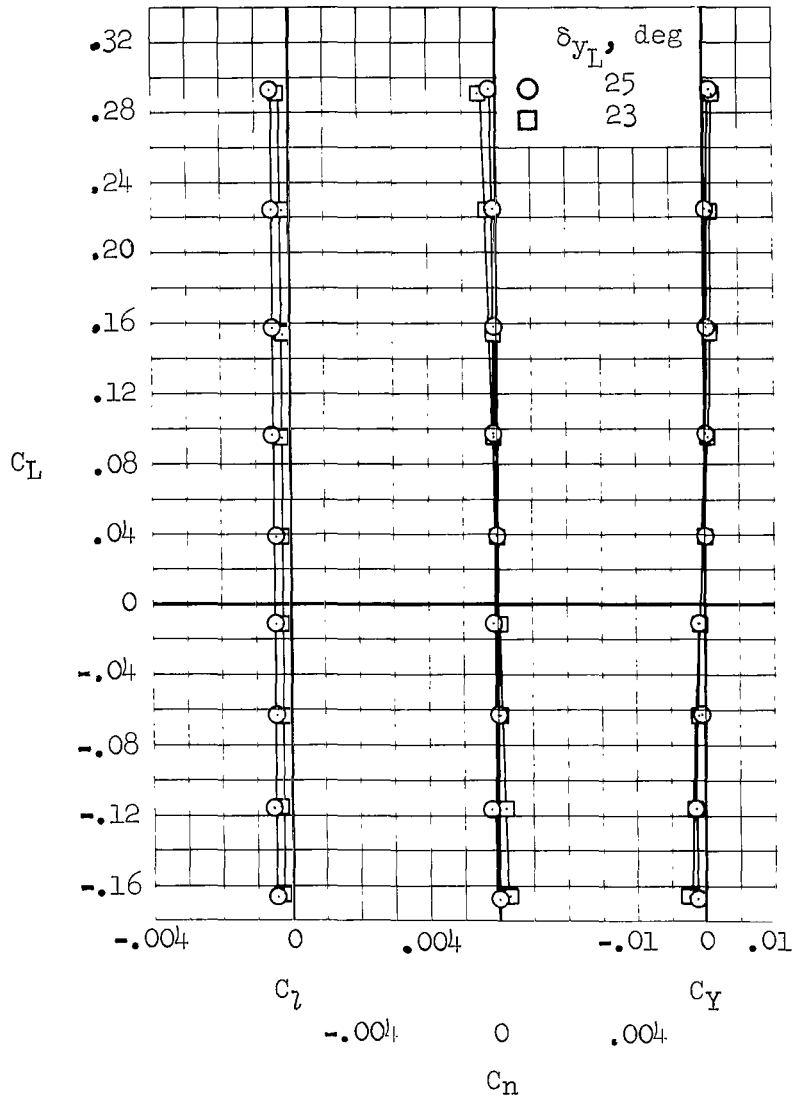

(d) M = 1.20, δ_{y_R} = 25°

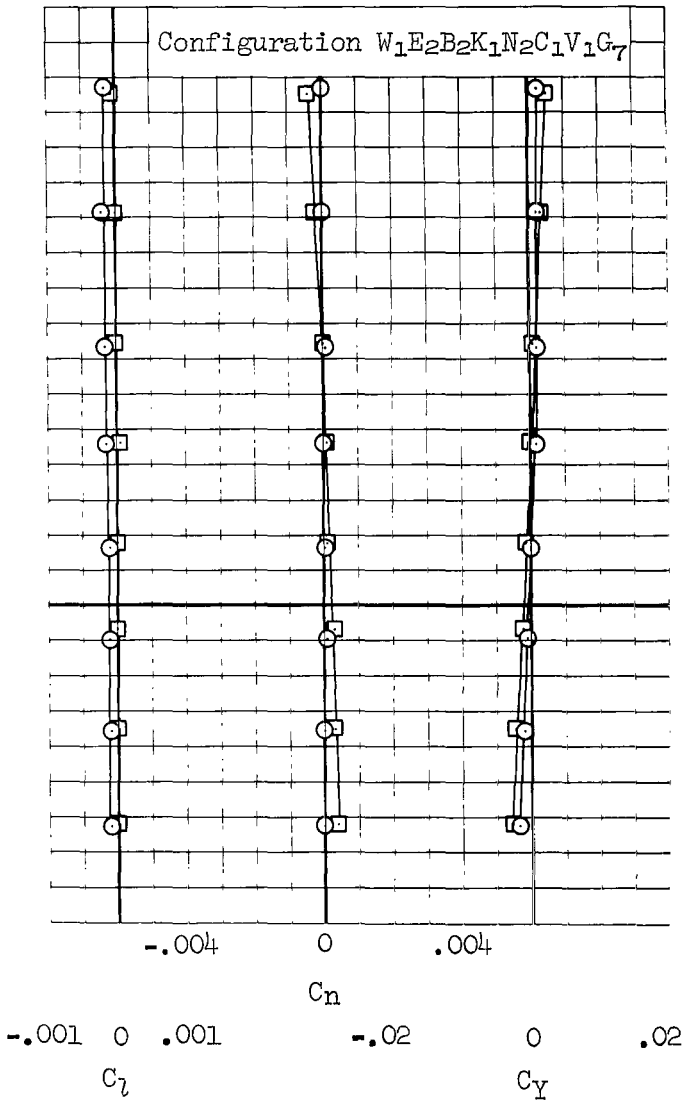

(e) M = 0.95, δ_{y_R} = 25°

Figure 24.- Concluded.

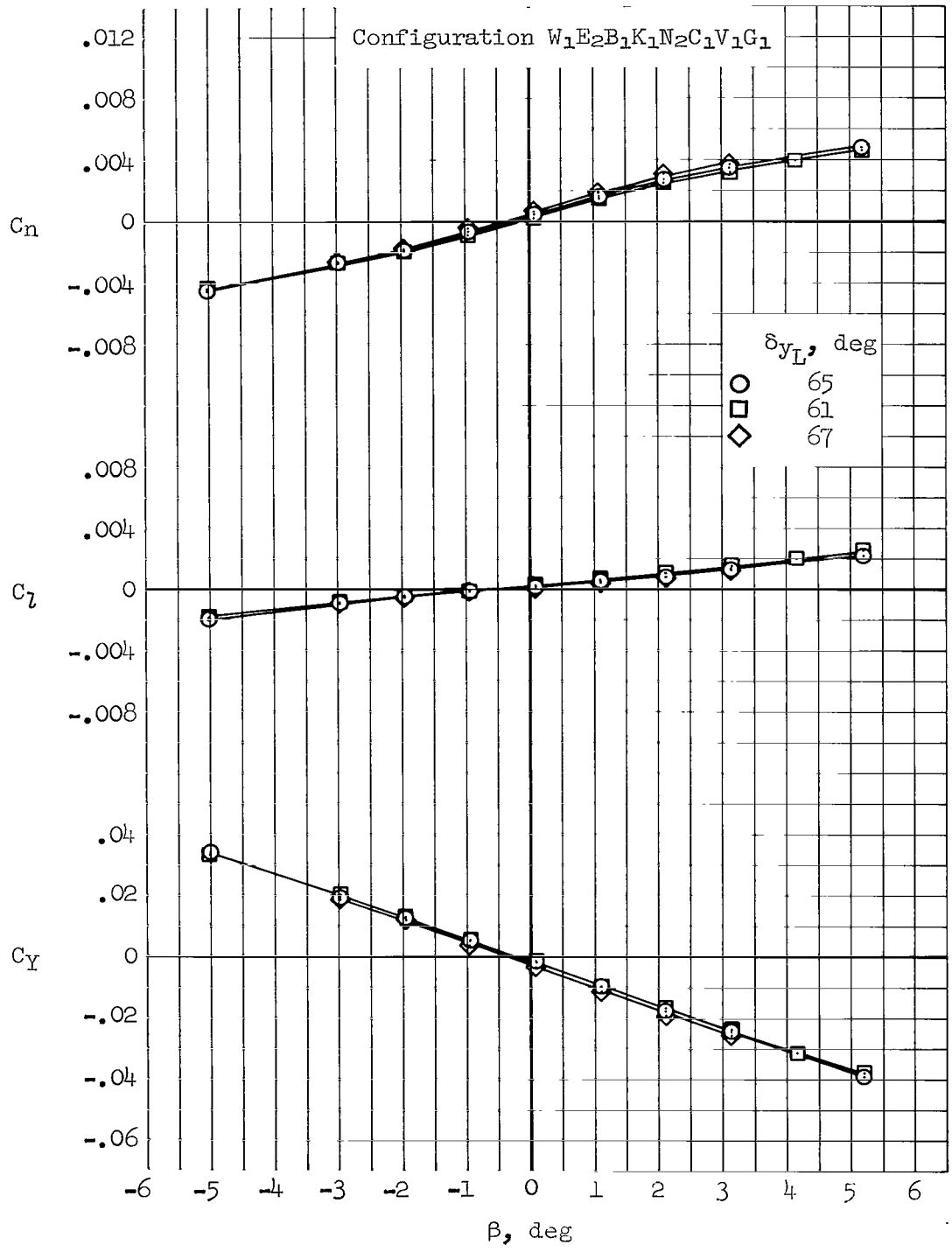

(a) M = 2.53, α = 4.5°, δ_{y_R} = 65°

Figure 25.- Effects on lateral-directional characteristics of asymmetric deflection of the wing tips.

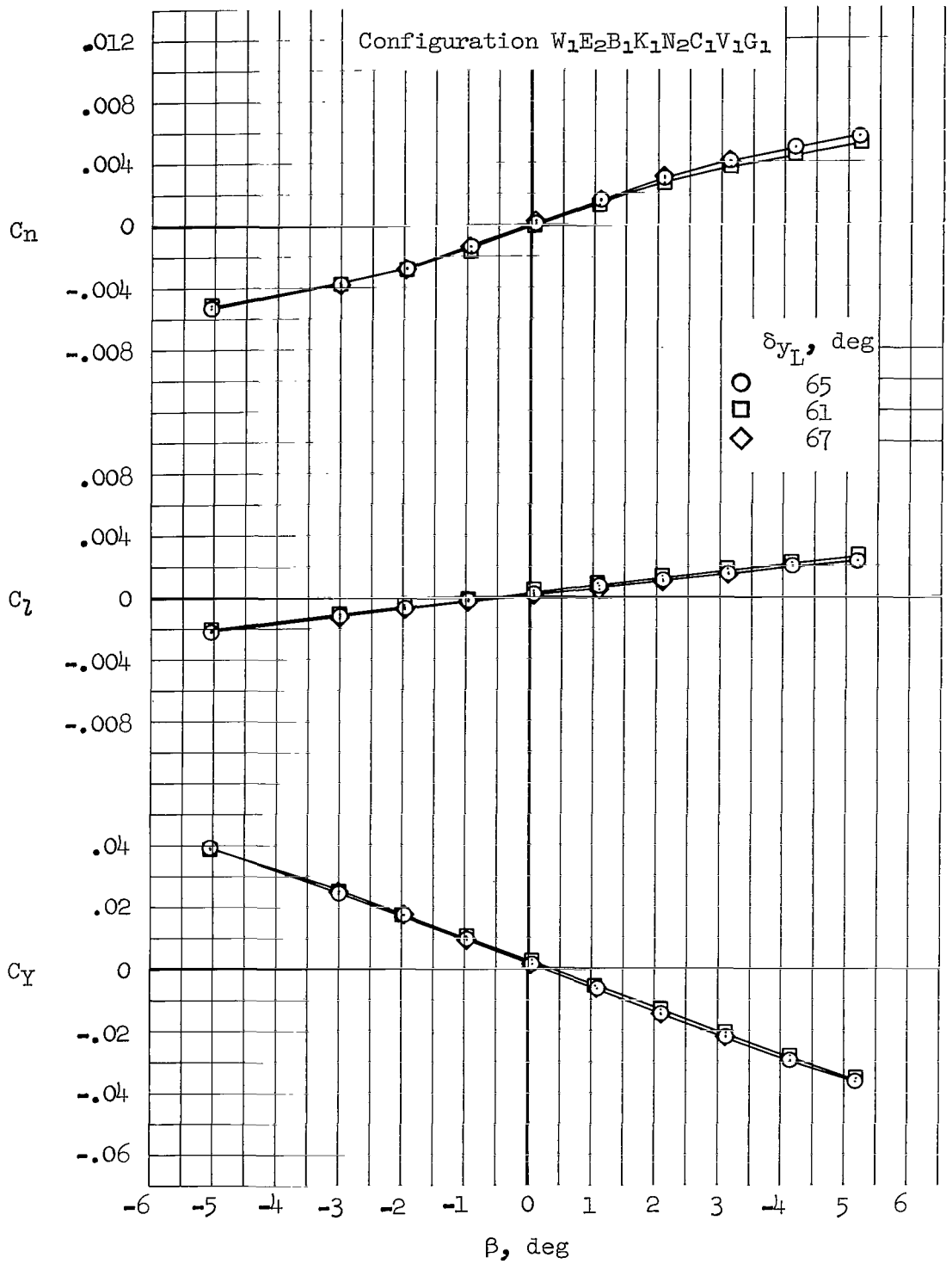

(b) M = 2.10, α = 4.6°, δ_{y_R} = 65°

Figure 25.- Continued.

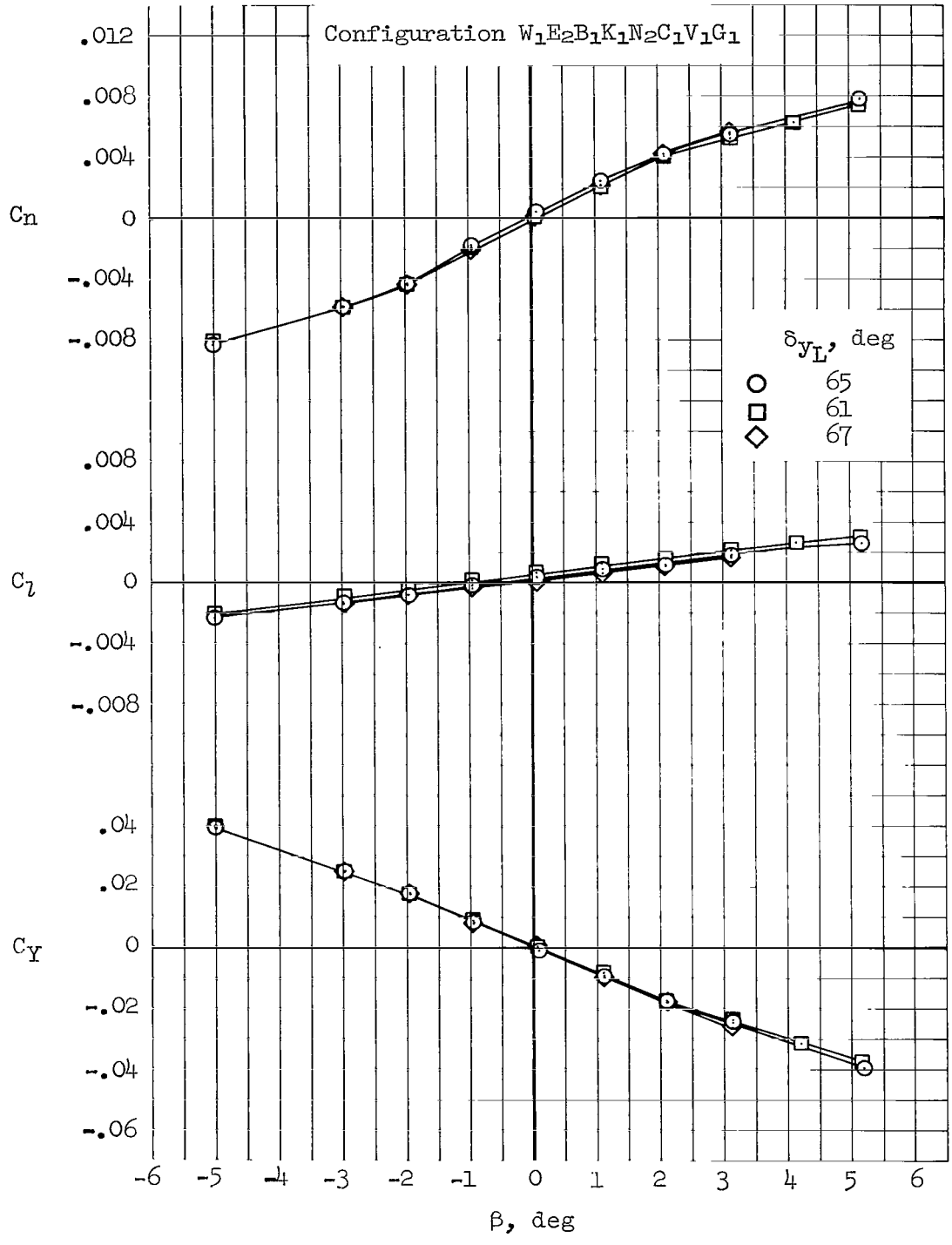

(c) M = 1.60, α = 4.8°, δ_{y_R} = 65°

Figure 25.- Continued.

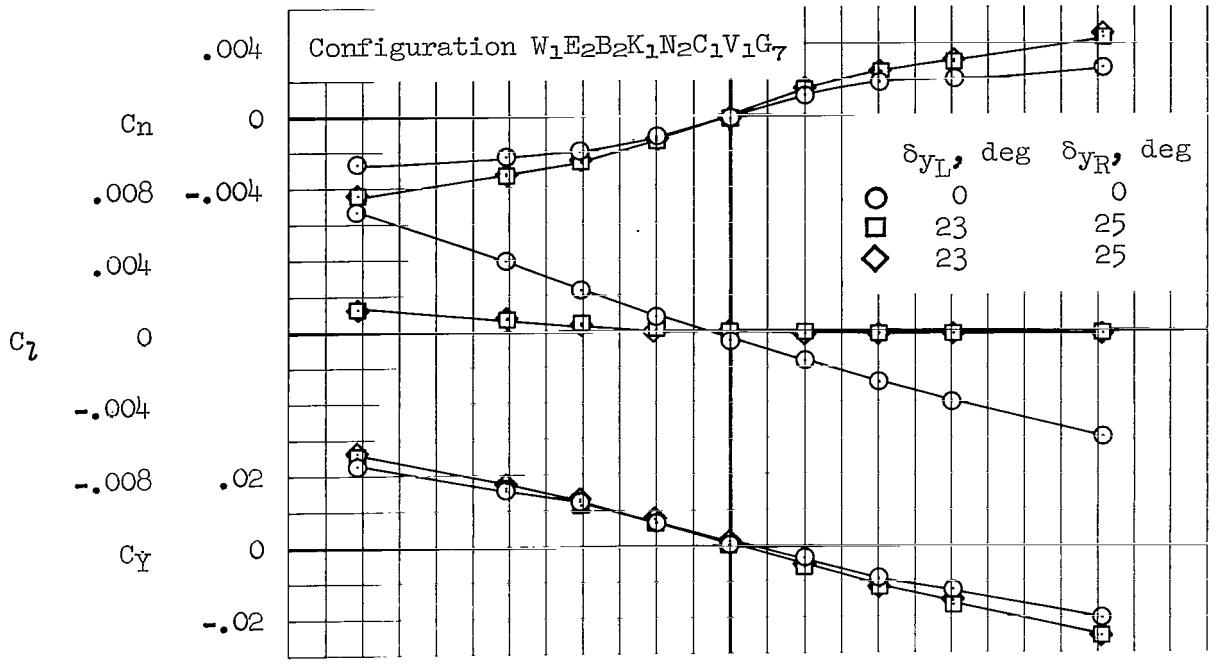

(d) M = 1.20, α = 3.3°

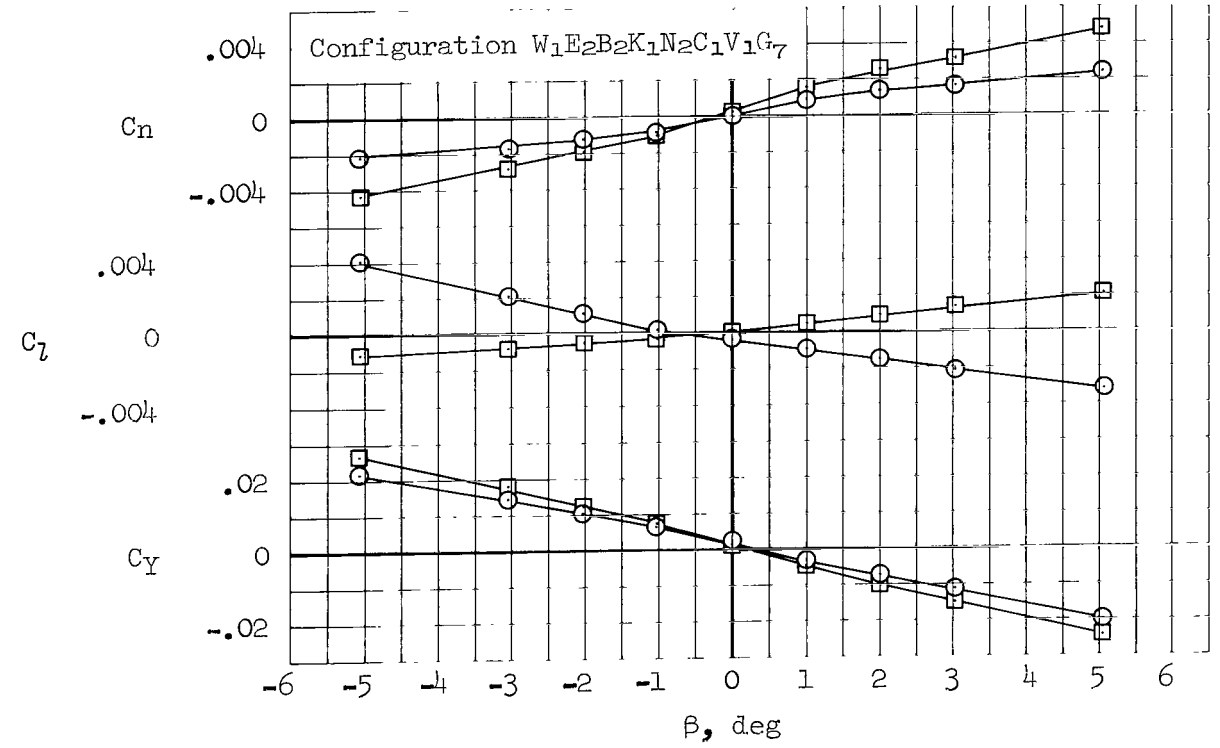

(e) M = 0.95, α = 3.3°

Figure 25.- Concluded.

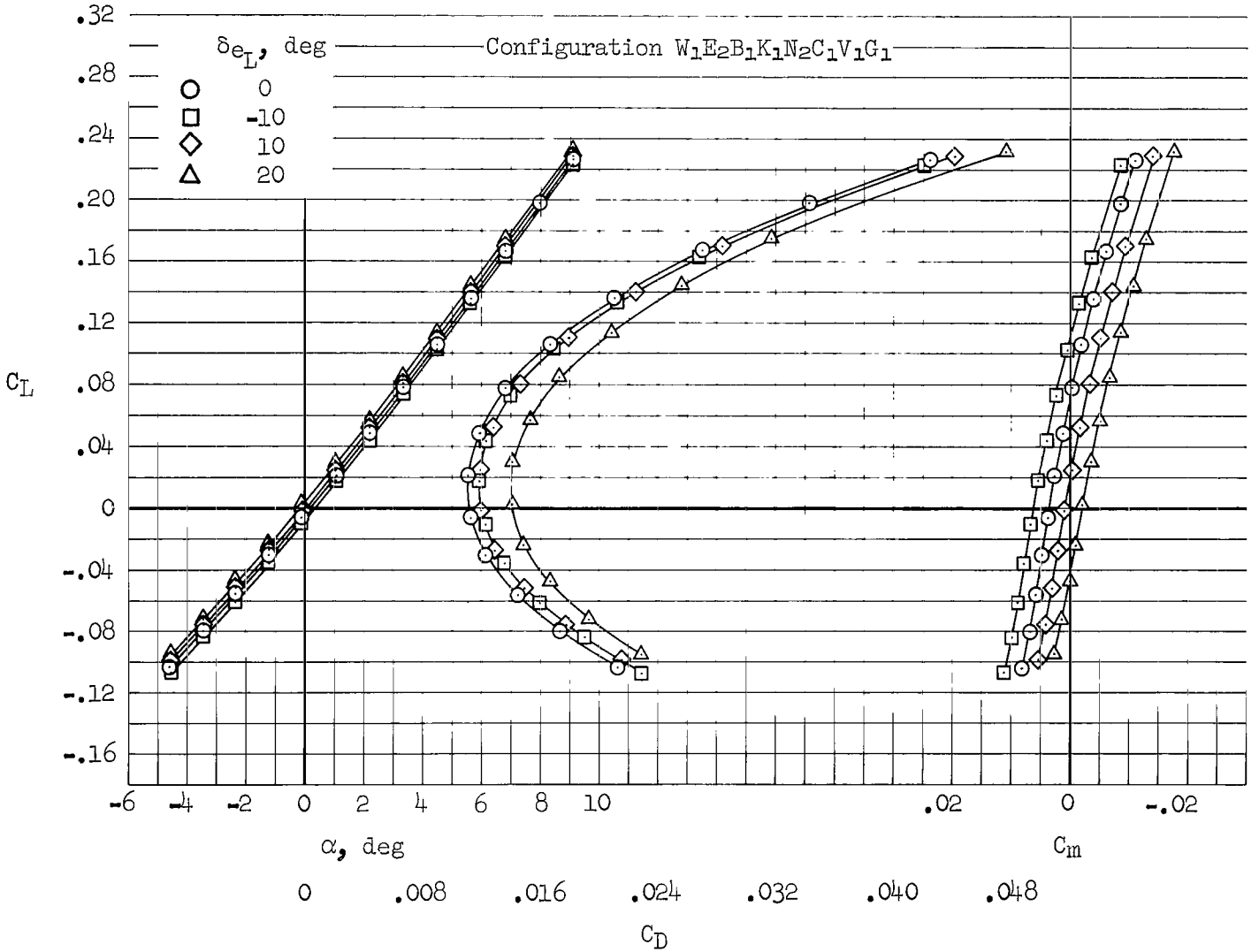

(a) M = 2.53, δ_y = 65°, δ_{e_R} = 0°

Figure 26.- Effects of roll-control deflection of the elevons on longitudinal characteristics.

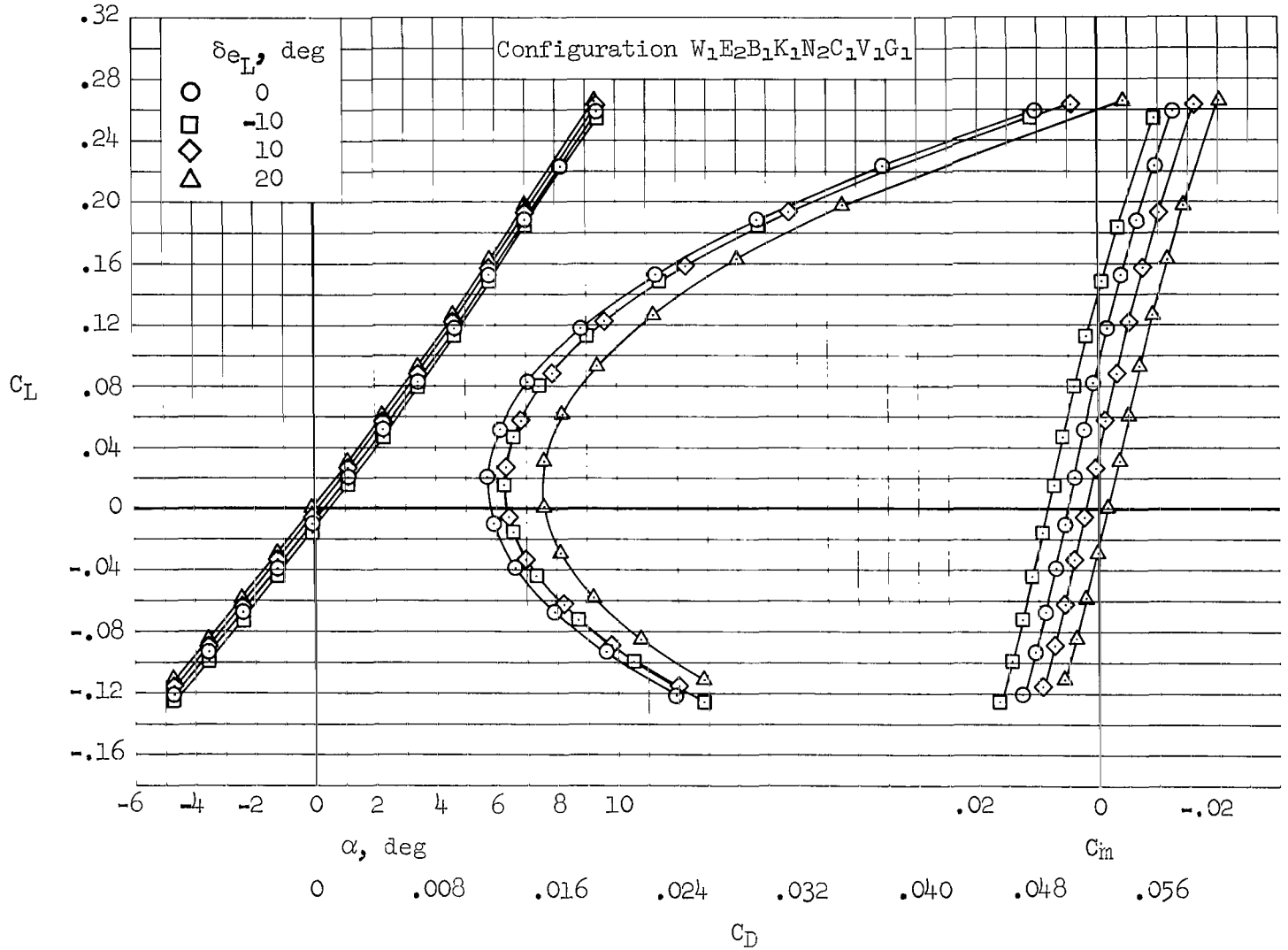

(b) M = 2.10, δ_y = 65°, δ_{e_R} = 0°

Figure 26.- Continued.

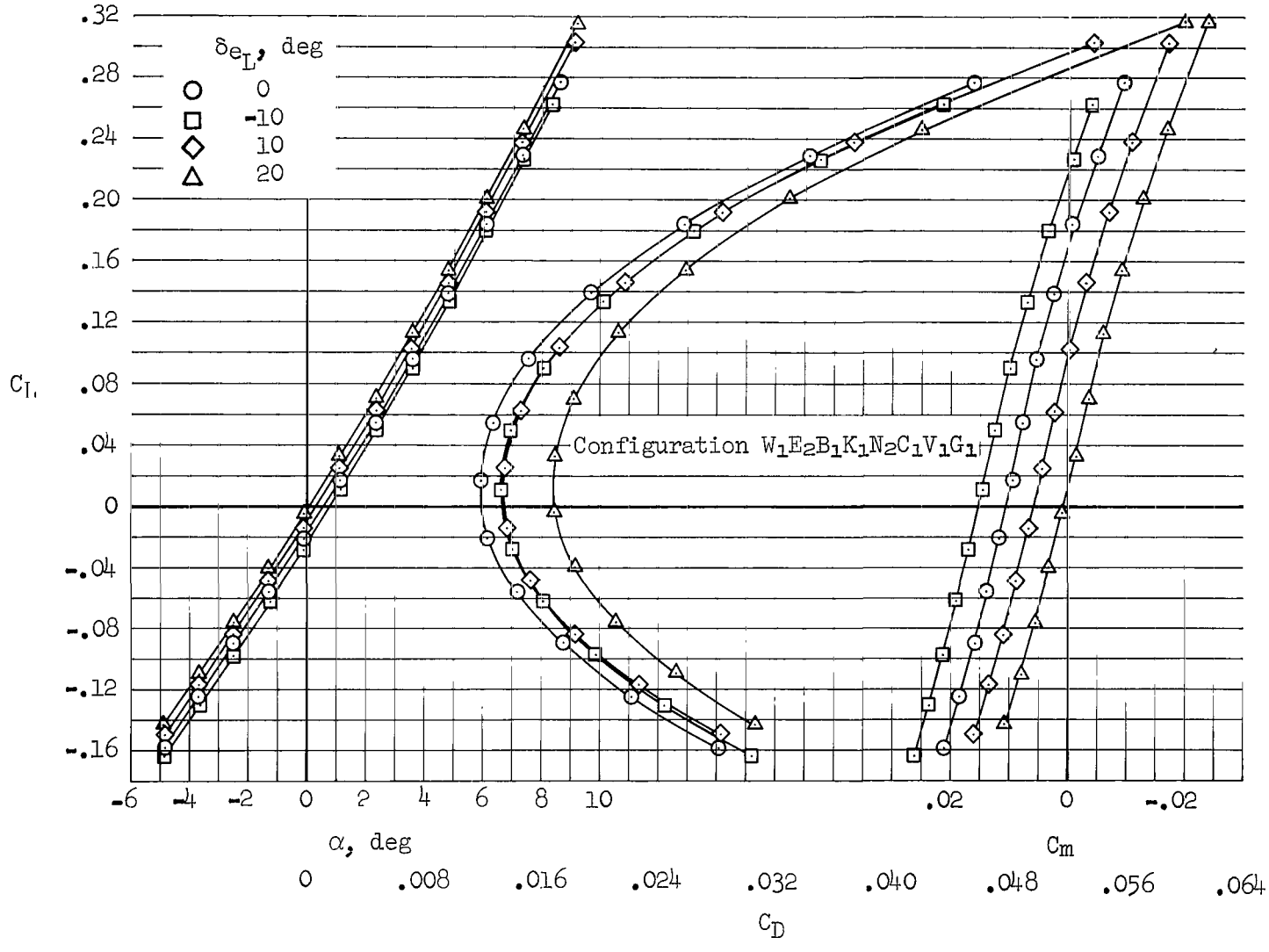

(c) M = 1.60, δ_y = 65°, δ_{e_R} = 0°

Figure 26.- Continued.

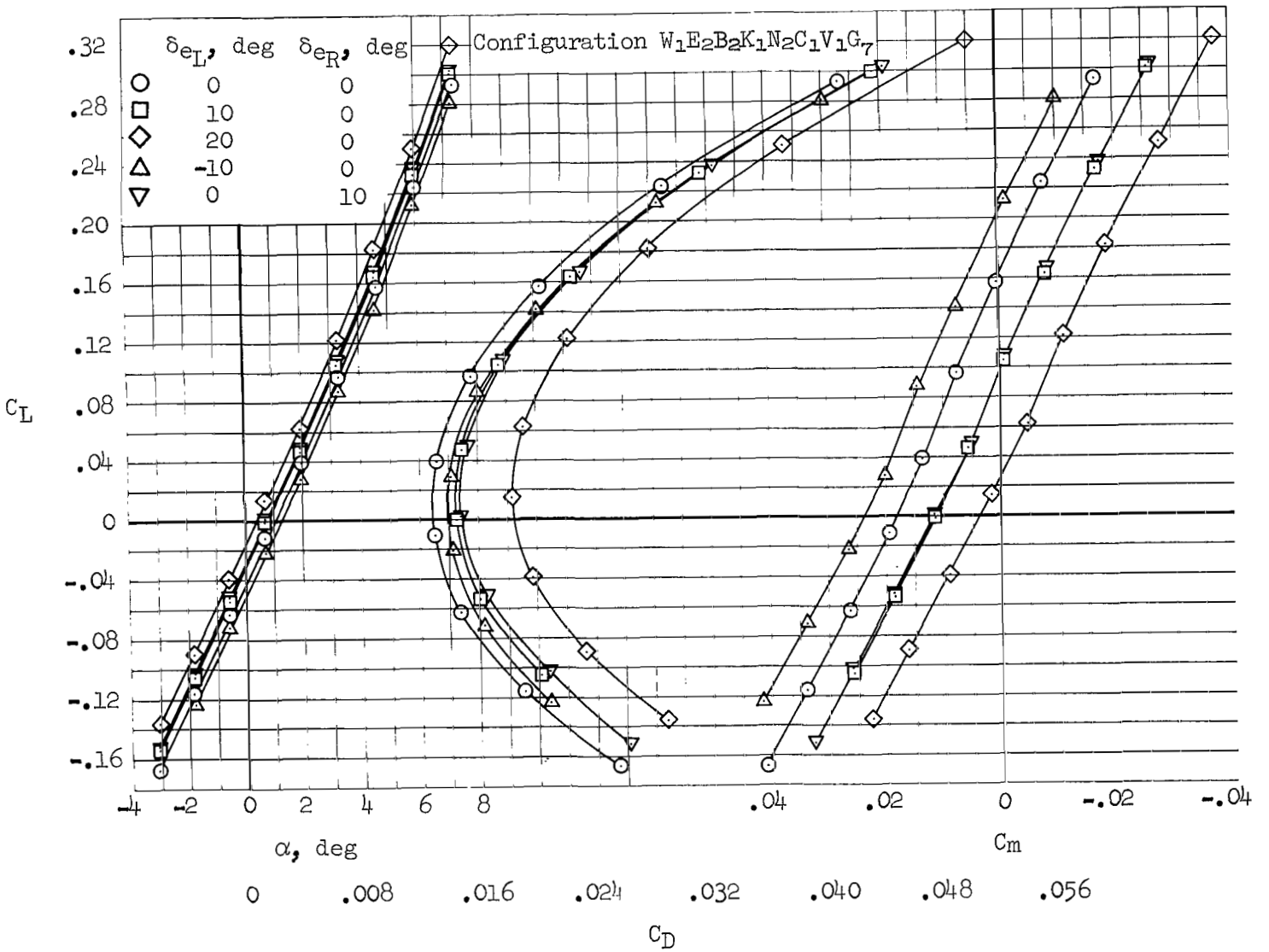

(d) M = 1.20, δ_y = 25°

Figure 26.- Continued.

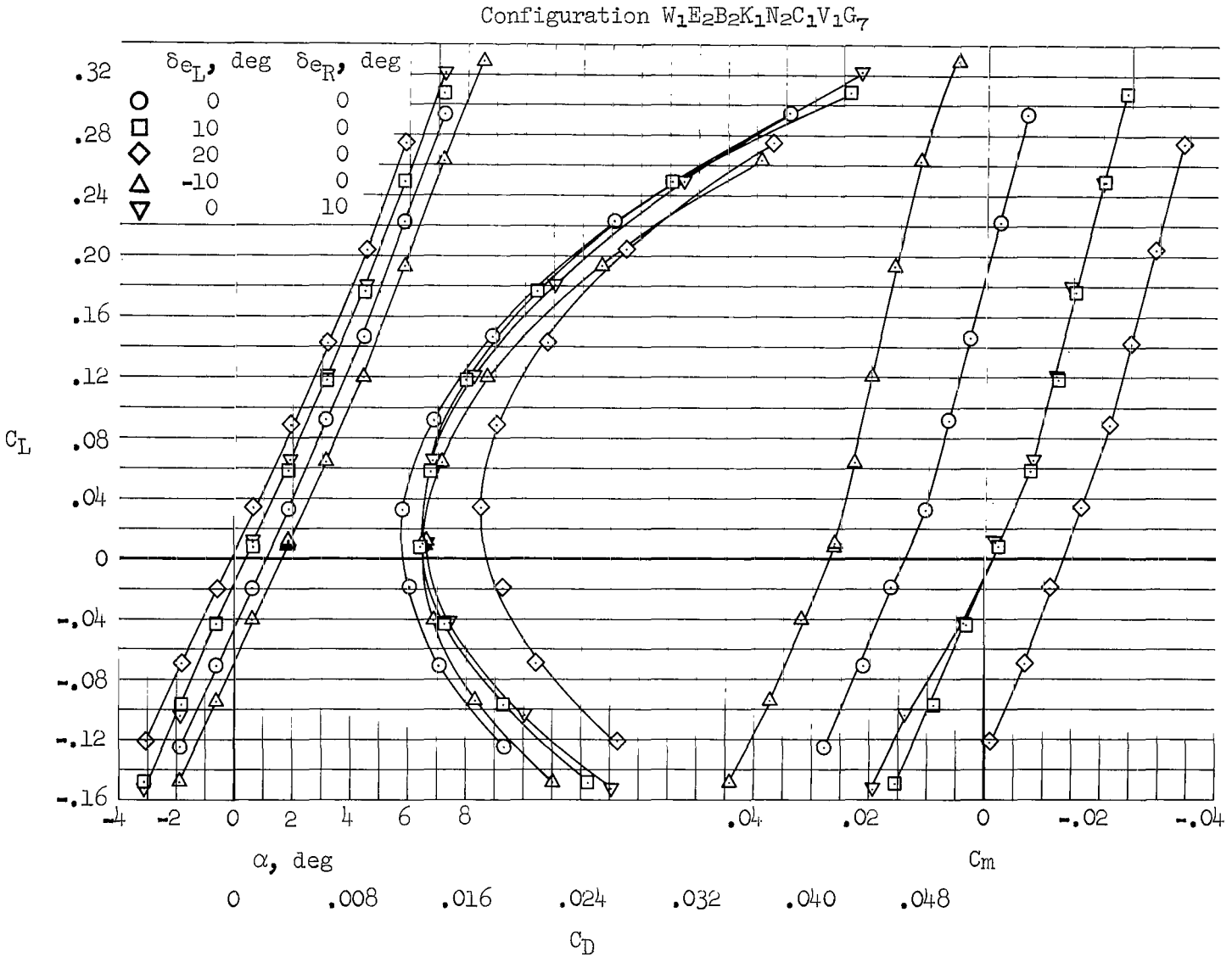

(e) M = 0.95, δ_y = 25°

Figure 26.- Continued.

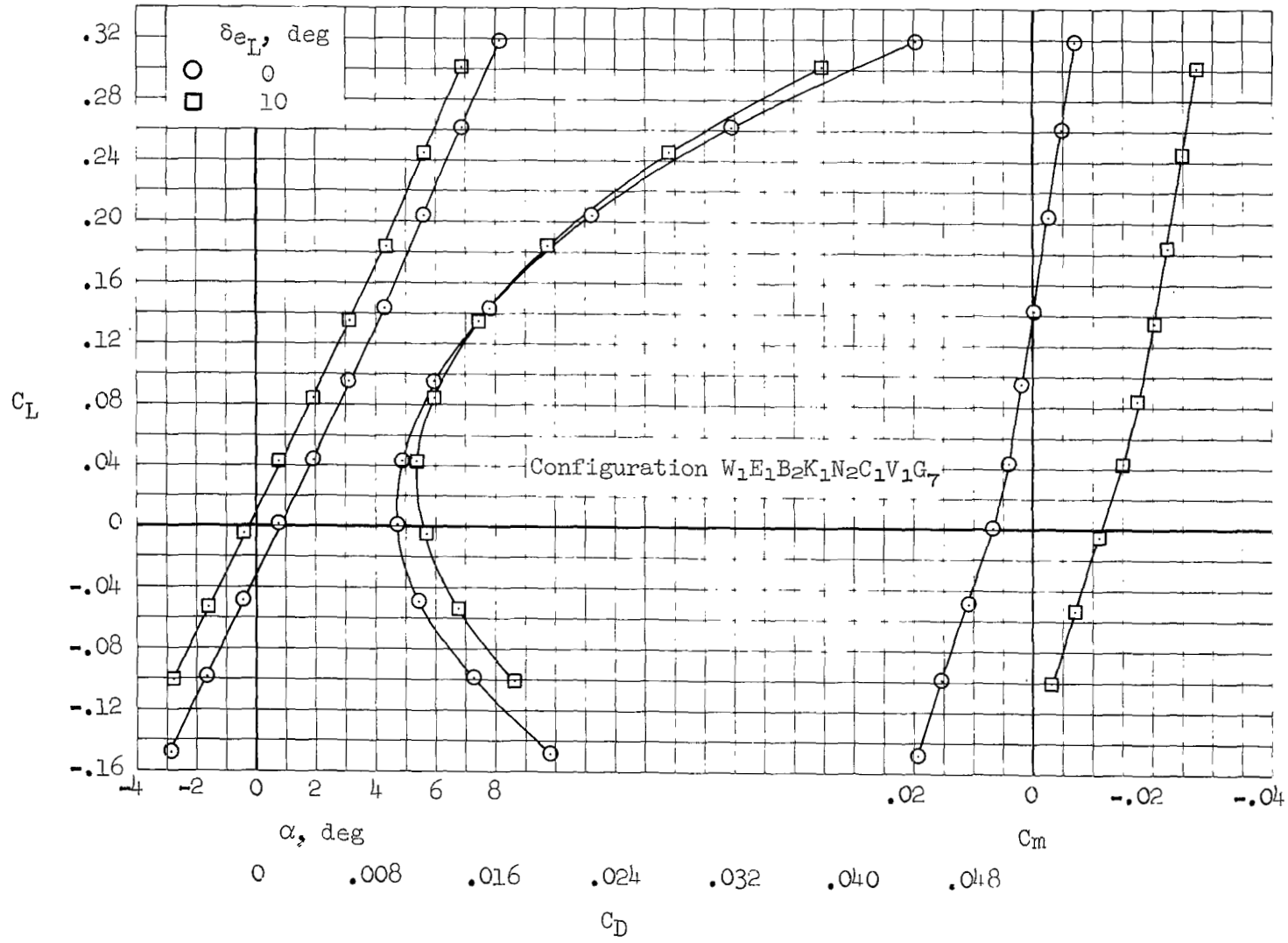

(f) M = 0.75, $\delta_Y = 0°$, $\delta_{e_R} = 0°$

Figure 26.- Concluded.

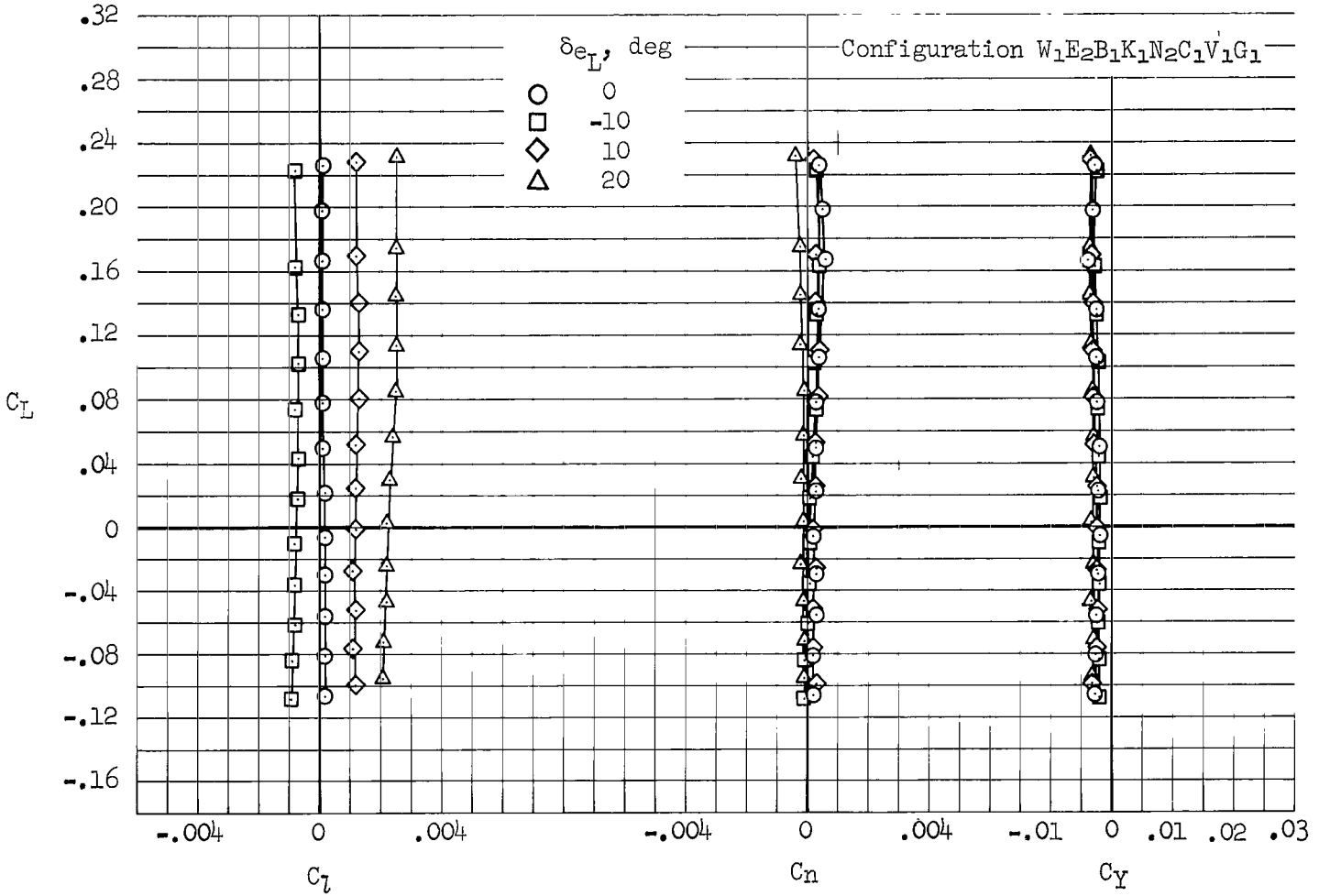

(a) M = 2.53, δ_y = 65°, δ_{e_R} = 0°

Figure 27.- Effects of roll-control deflection of the elevons on the rolling-moment, yawing-moment, and side-force characteristics.

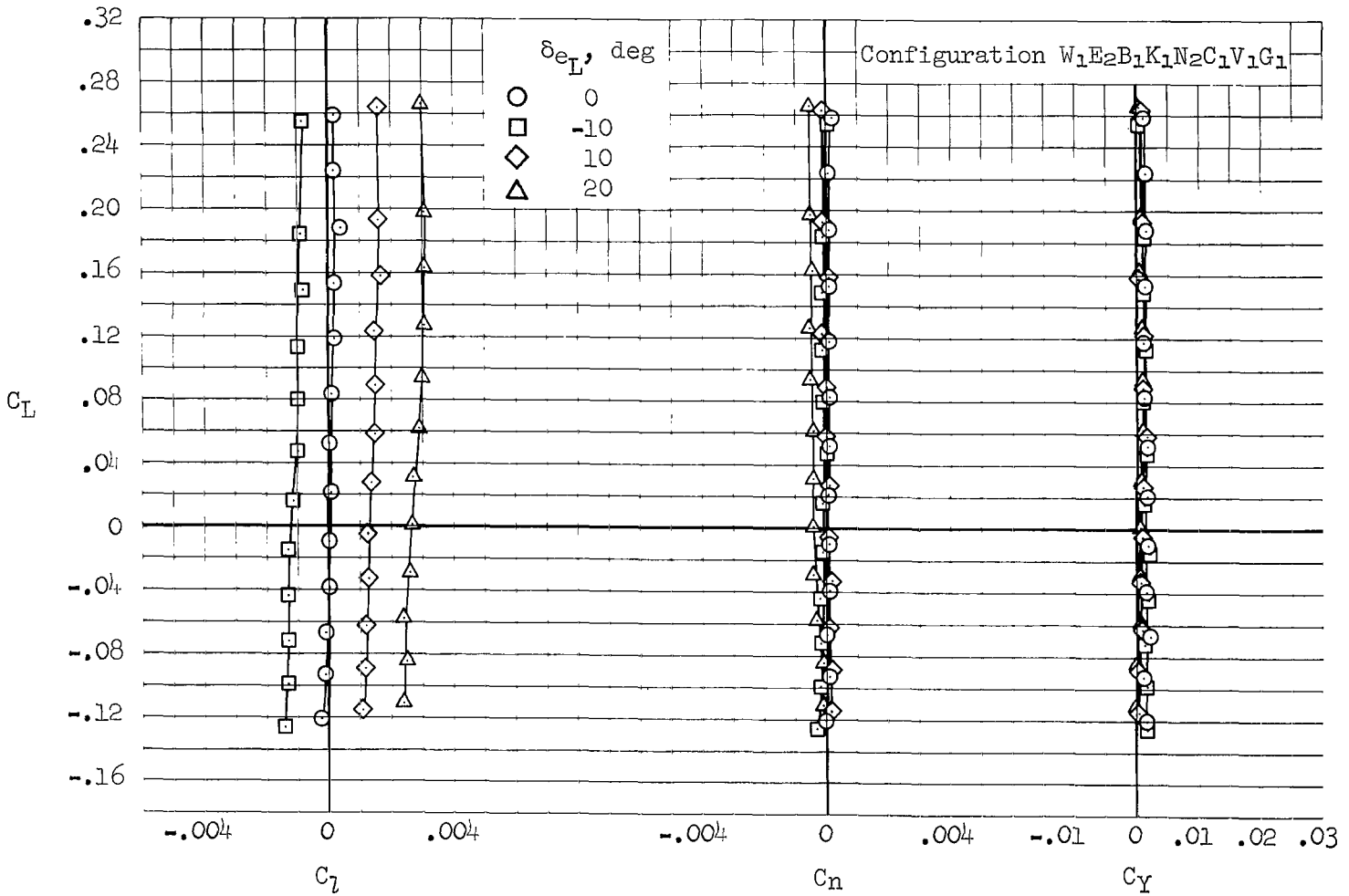

(b) M = 2.10, δ_y = 65°, δ_{e_R} = 0°

Figure 27.- Continued.

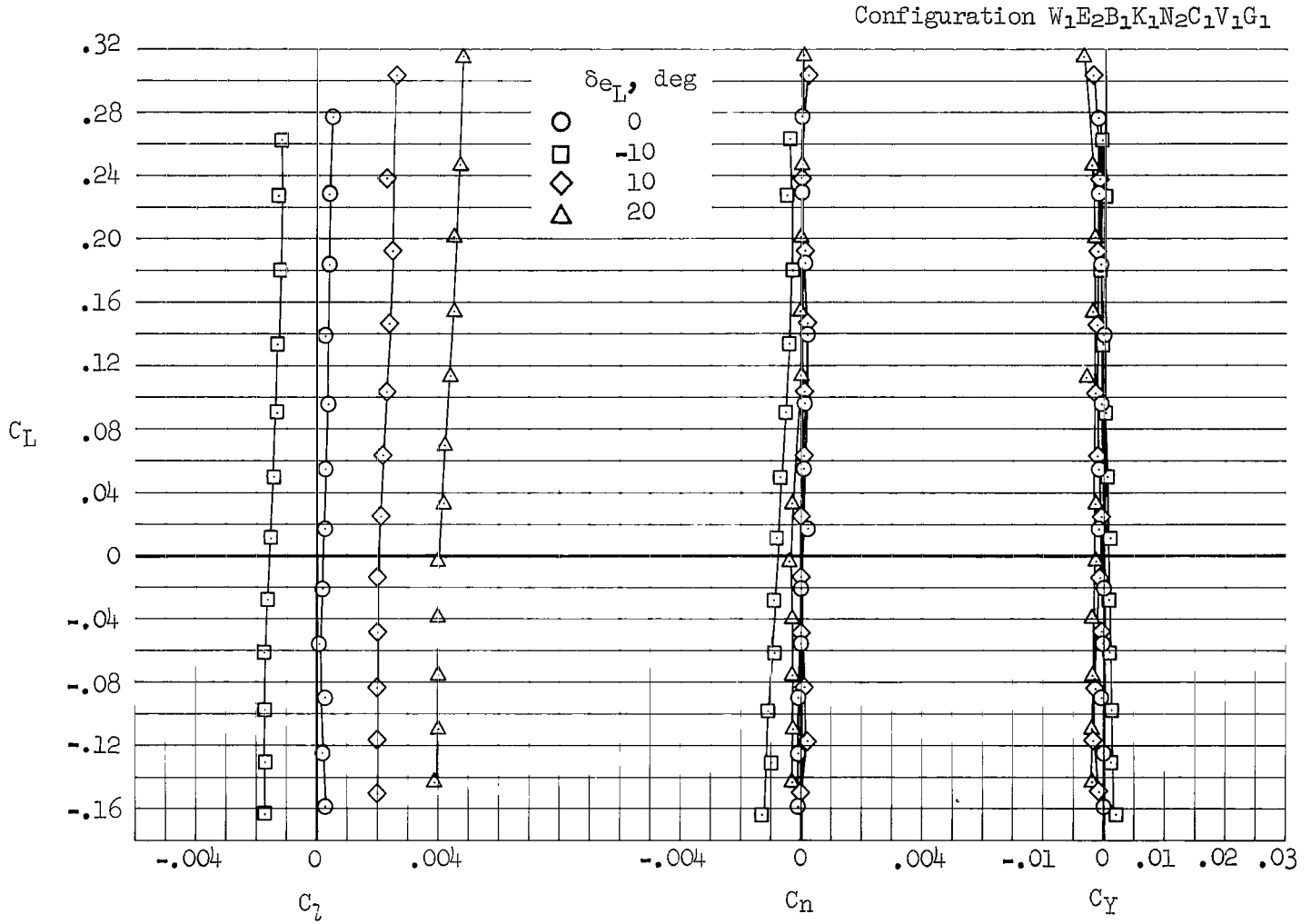

(c) M = 1.60, δ_y = 65°, δ_{e_R} = 0°

Figure 27.- Continued.

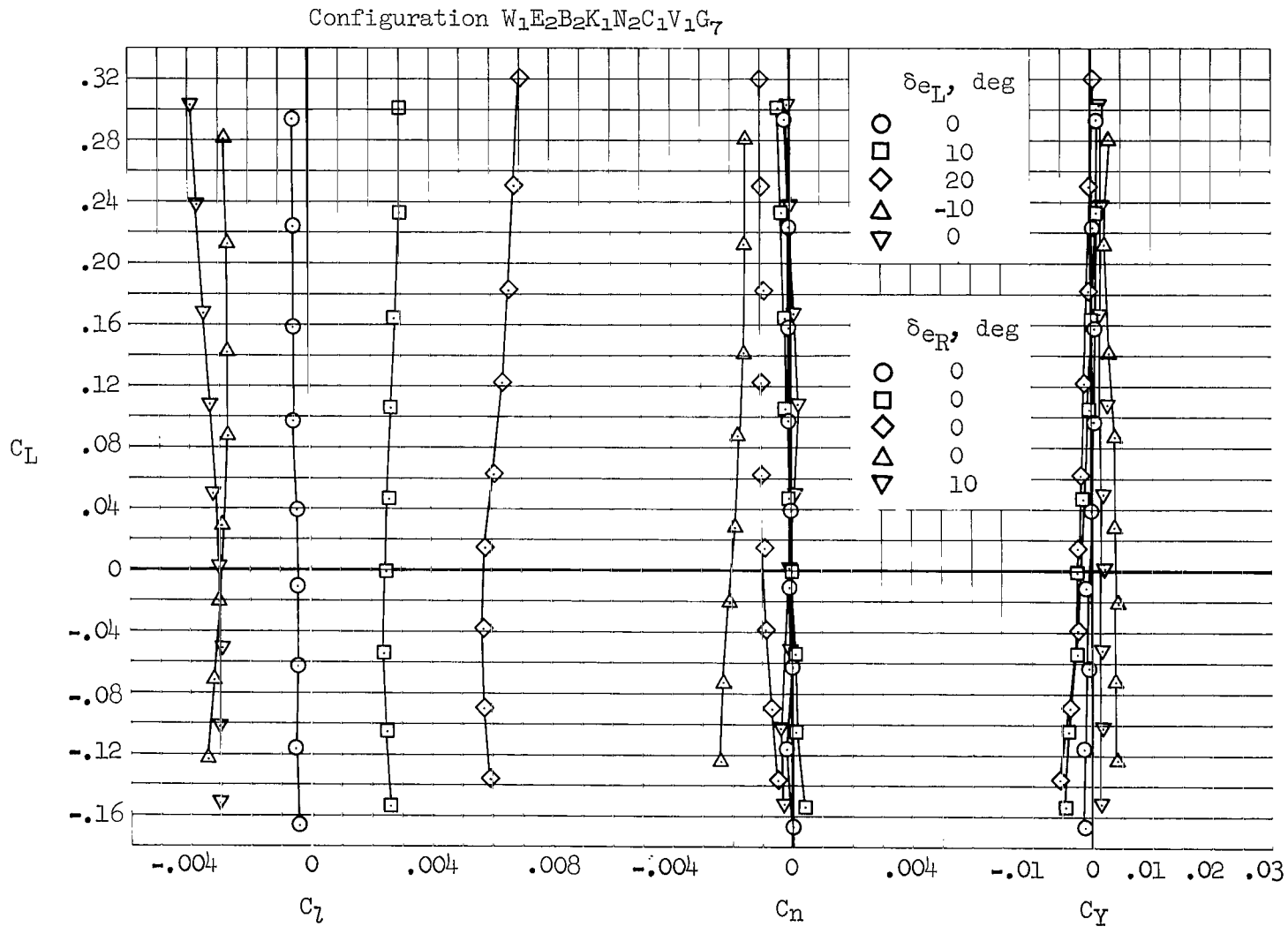

(d) M = 1.20, δ_y = 25°

Figure 27.- Continued.

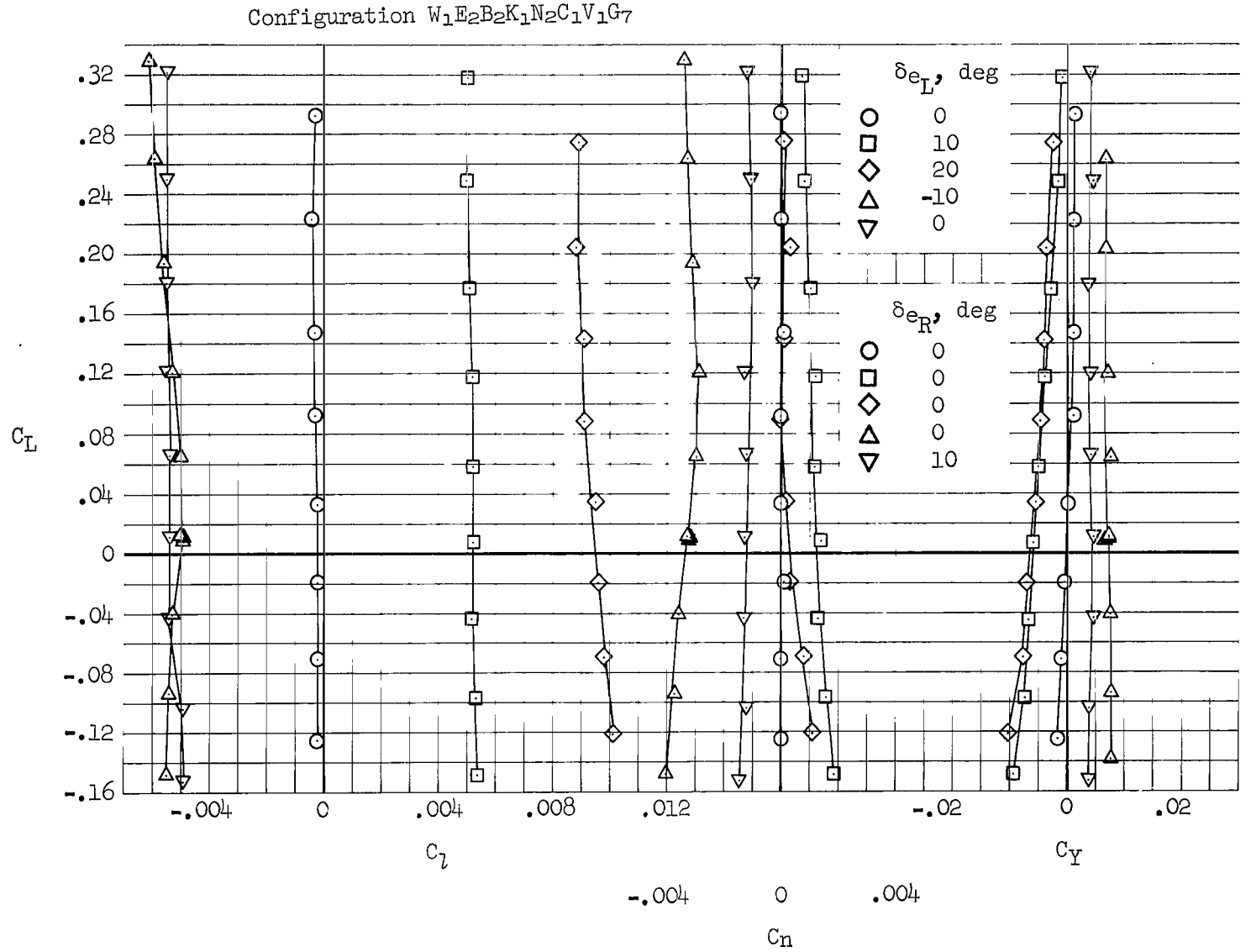

(e) M = 0.95, δ_y = 25°

Figure 27.- Continued.

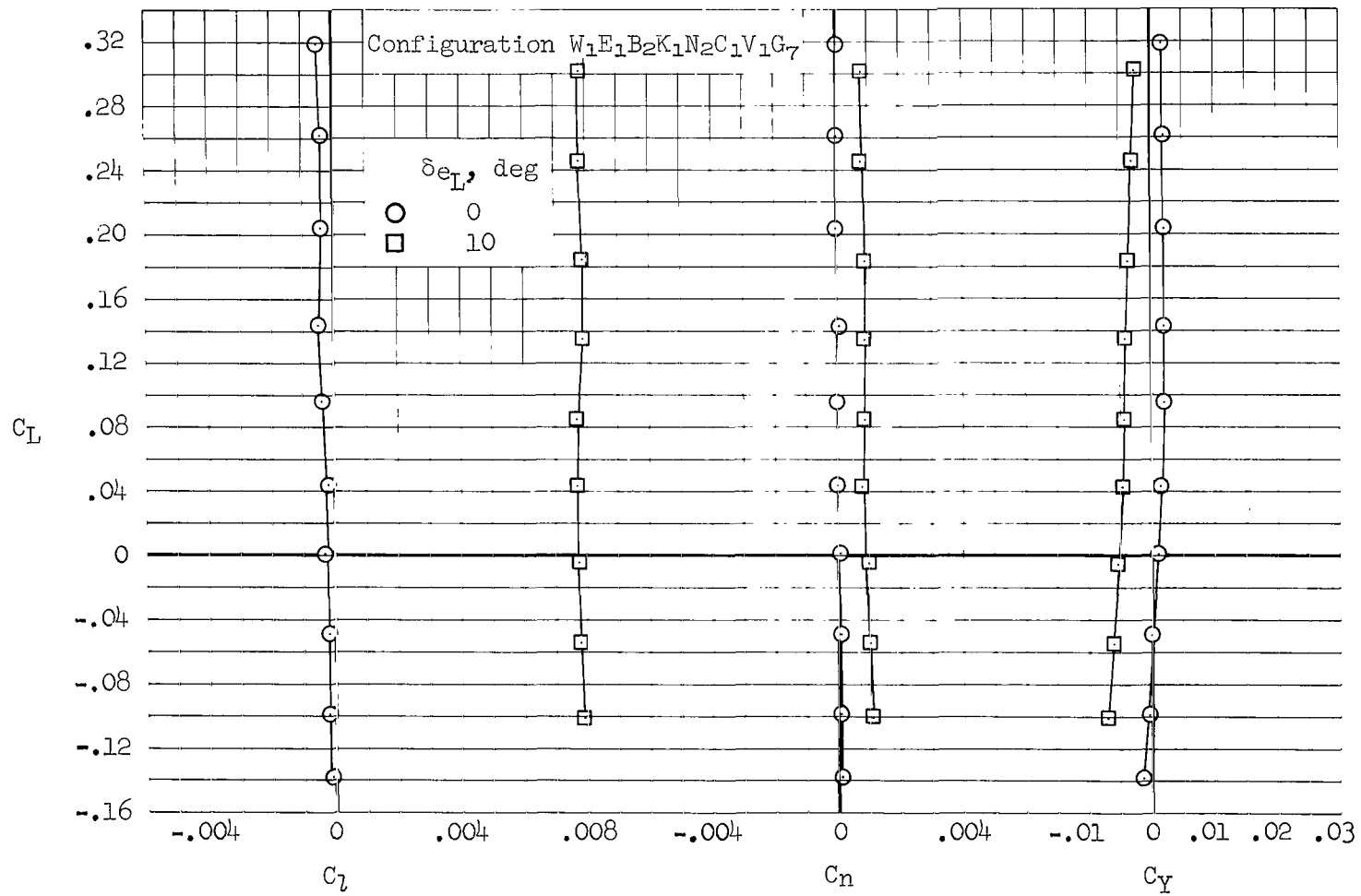

(f) M = 0.75, δ_y = 0°, δ_{e_R} = 0°

Figure 27.- Concluded.

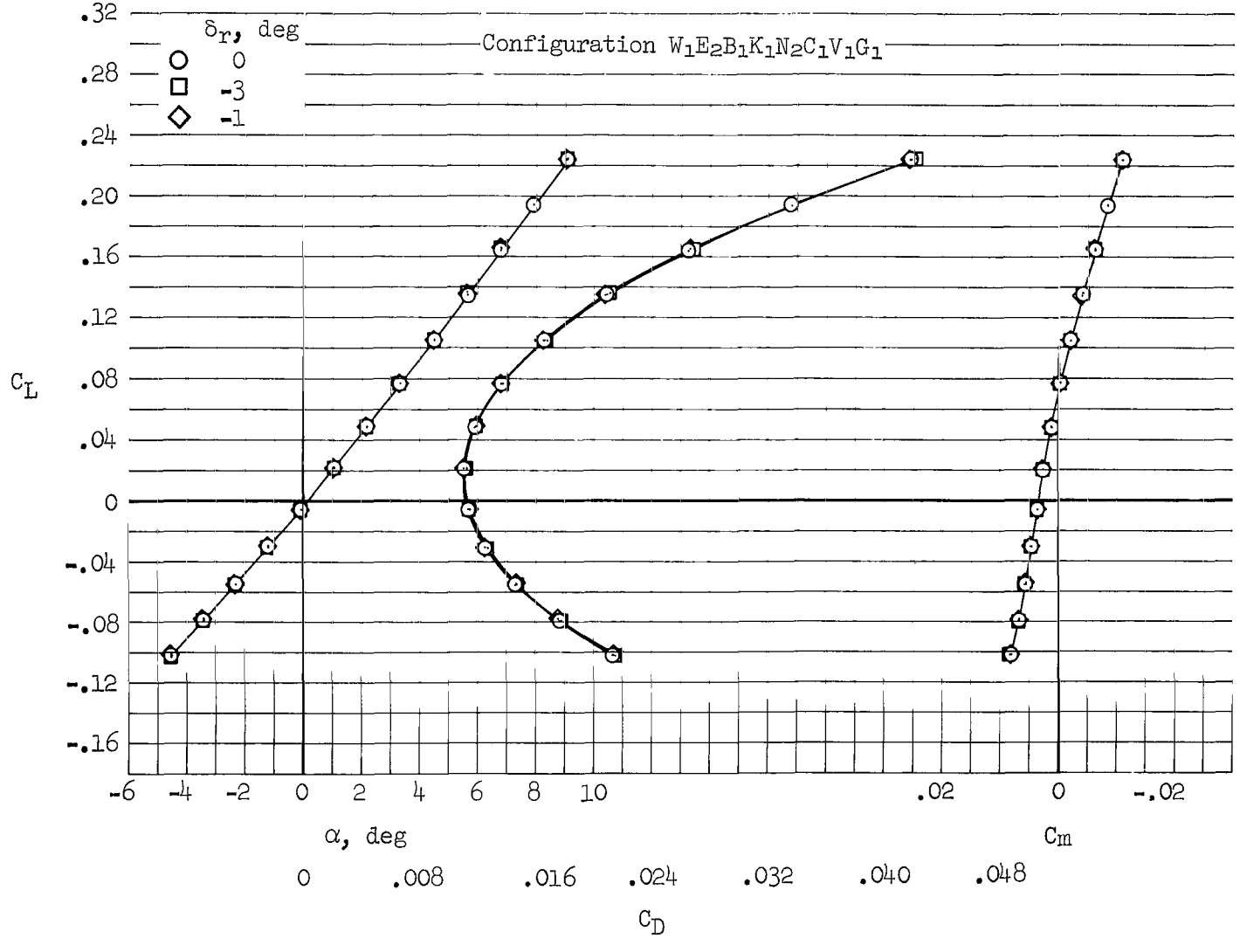

(a) M = 2.53, δ_y = 65°

Figure 28.- Effects of rudder deflection on longitudinal characteristics.

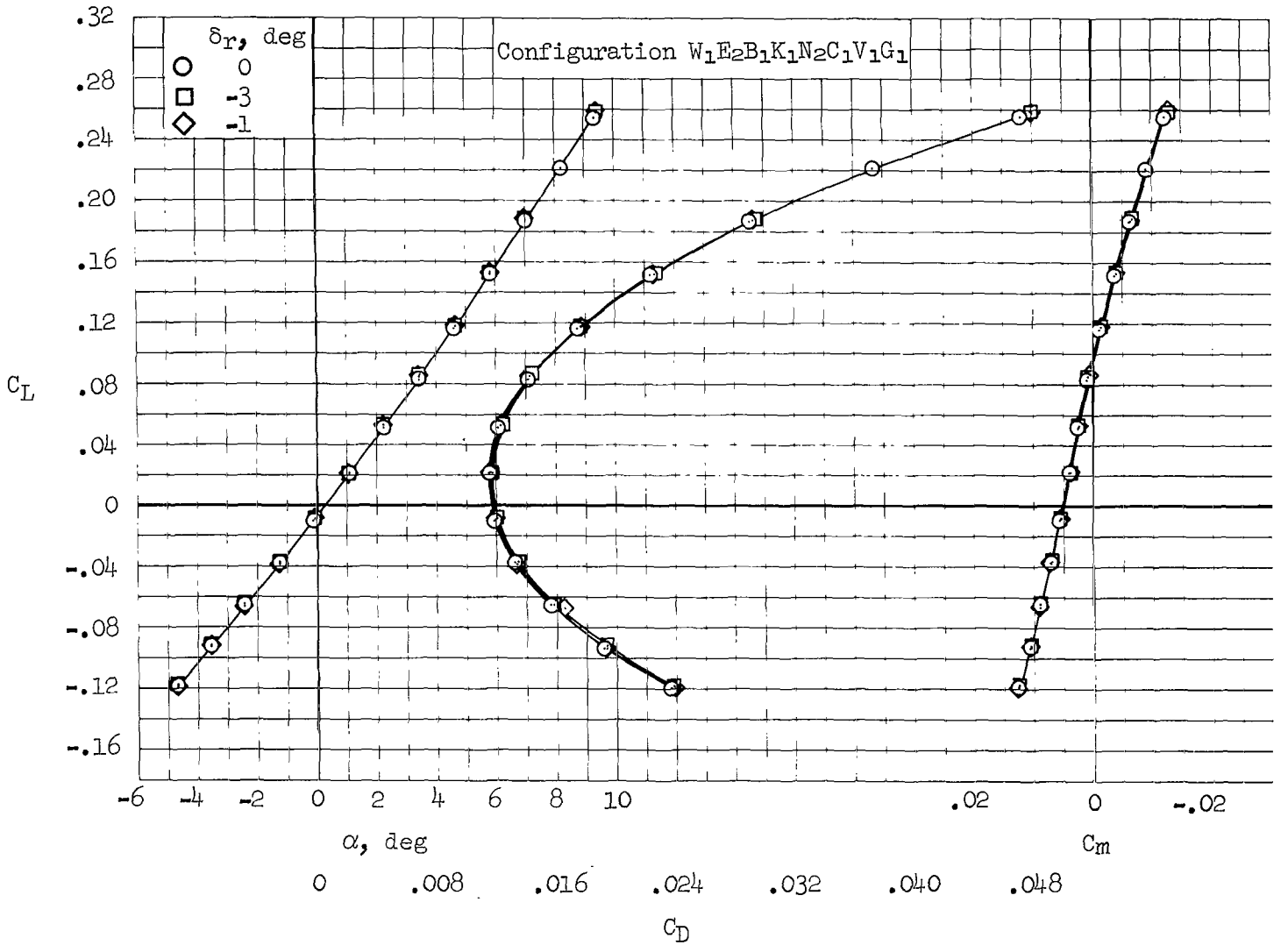

(b) M = 2.10, δ_y = 65°

Figure 28.- Continued.

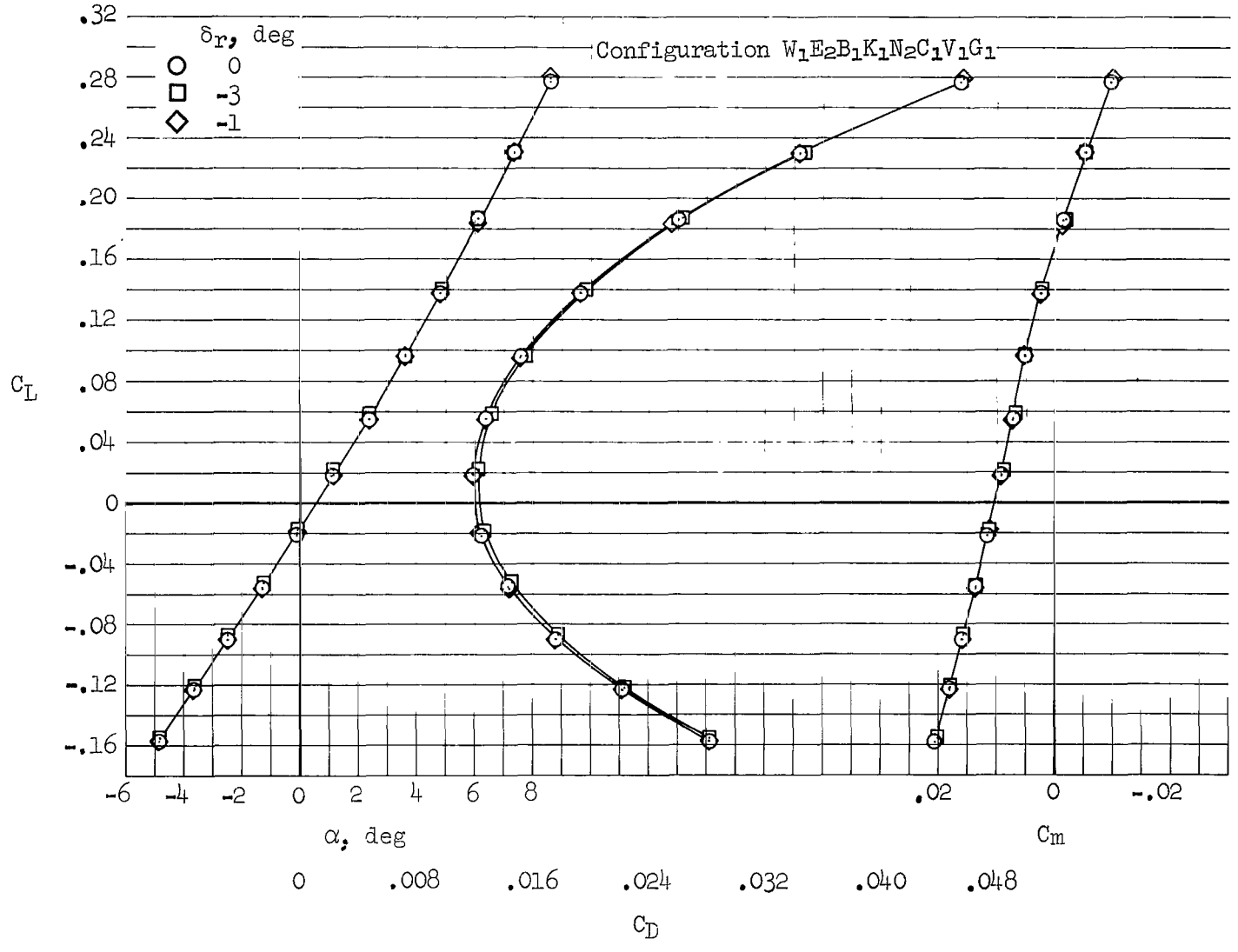

(c) M = 1.60, δ_y = 65°

Figure 28.- Continued.

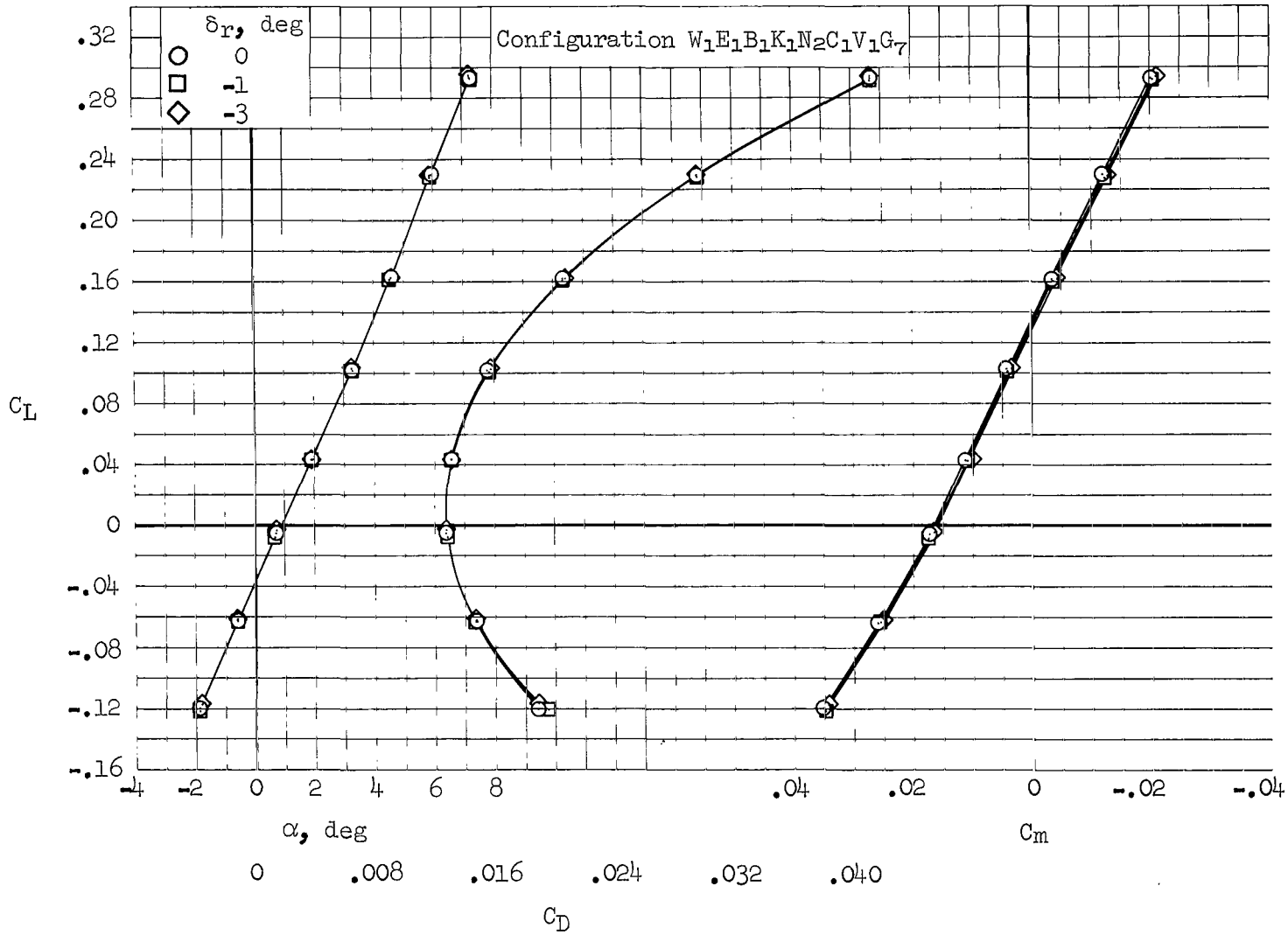

(d) M = 1.20, δ_y = 0°

Figure 28.- Continued.

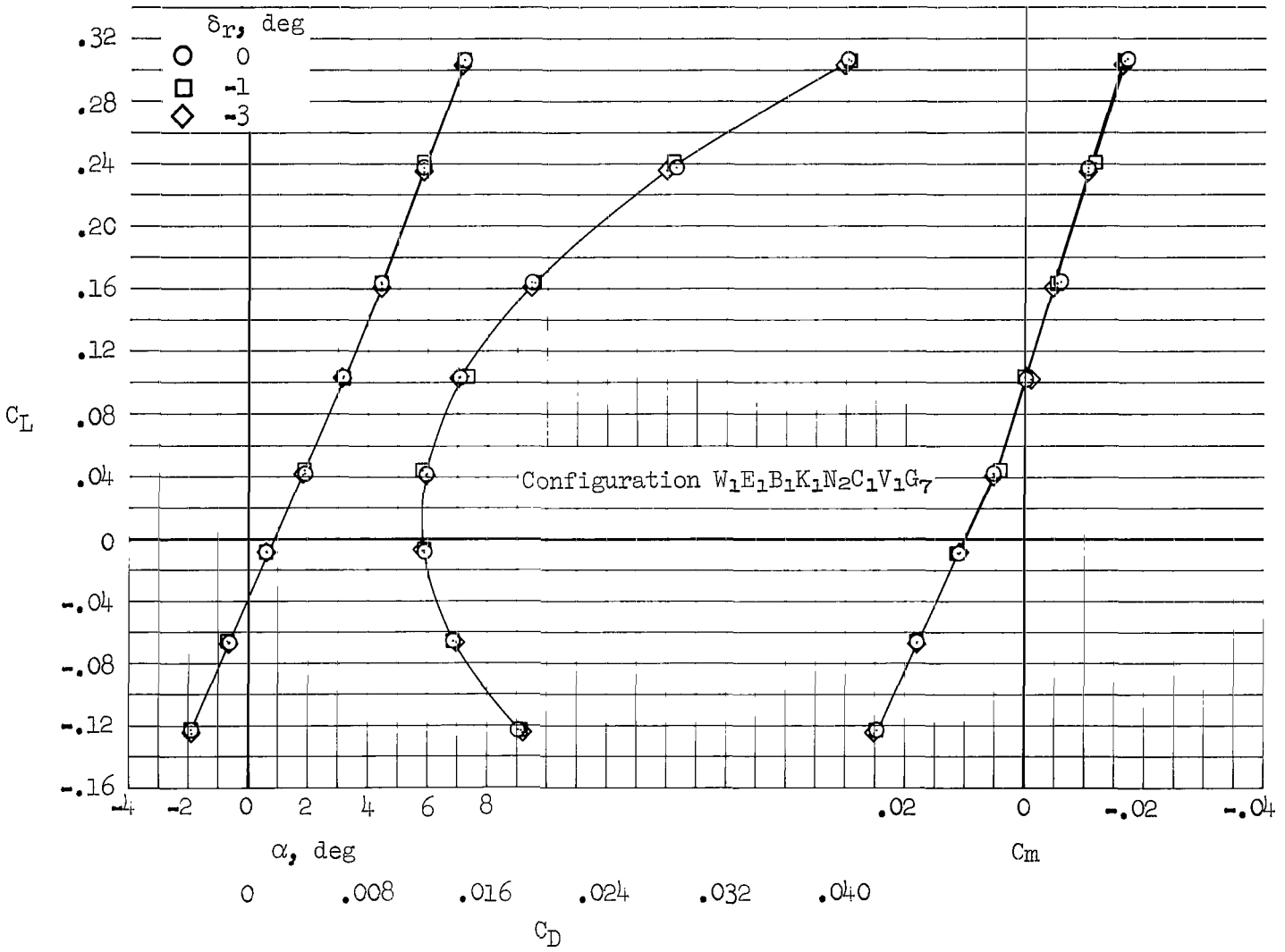

(e) M = 0.95, δ_y = 0°

Figure 28.- Concluded.

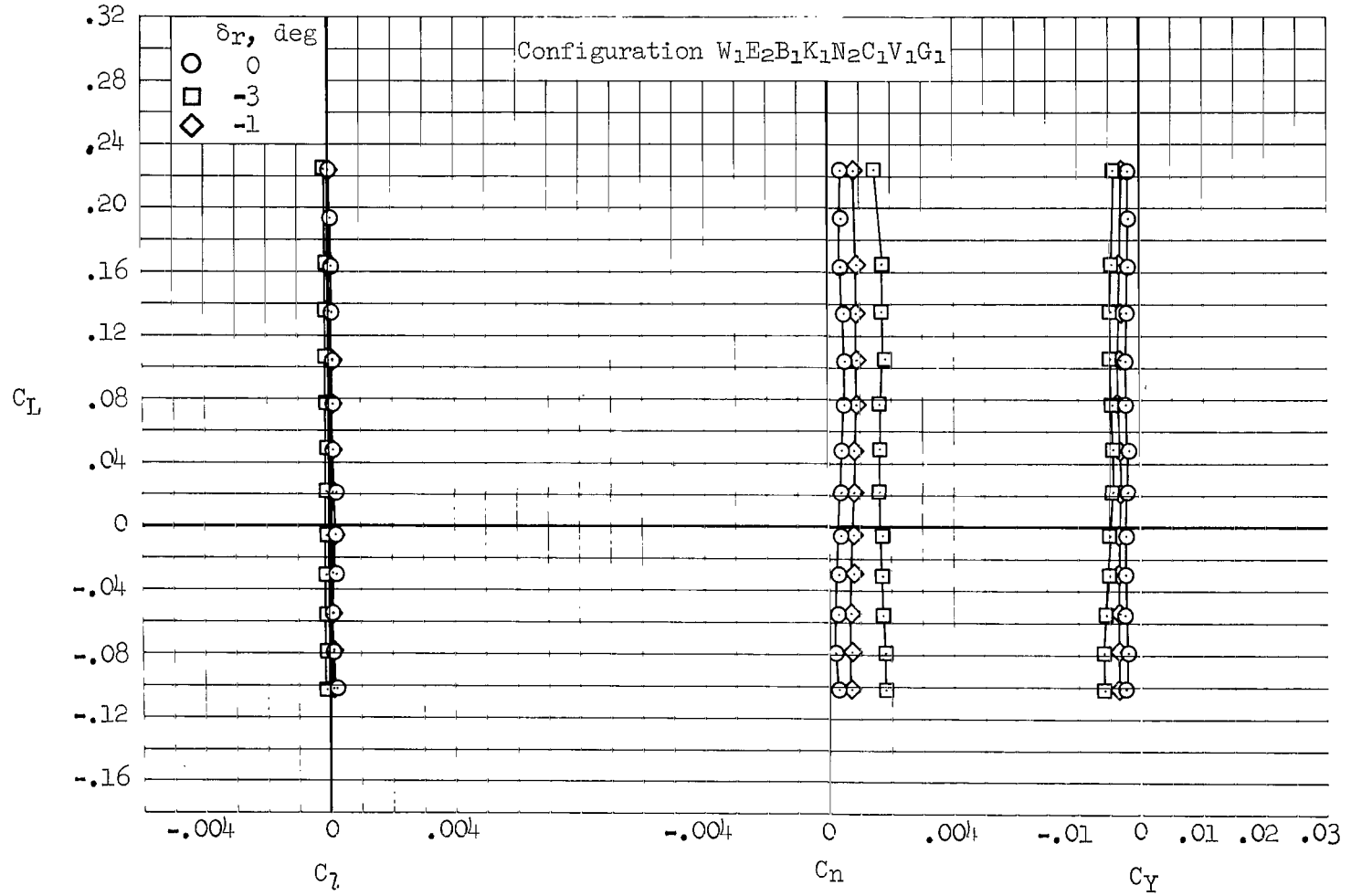

(a) M = 2.53, δ_y = 65°

Figure 29.- Effects of rudder deflection on the rolling-moment, yawing-moment, and side-force characteristics.

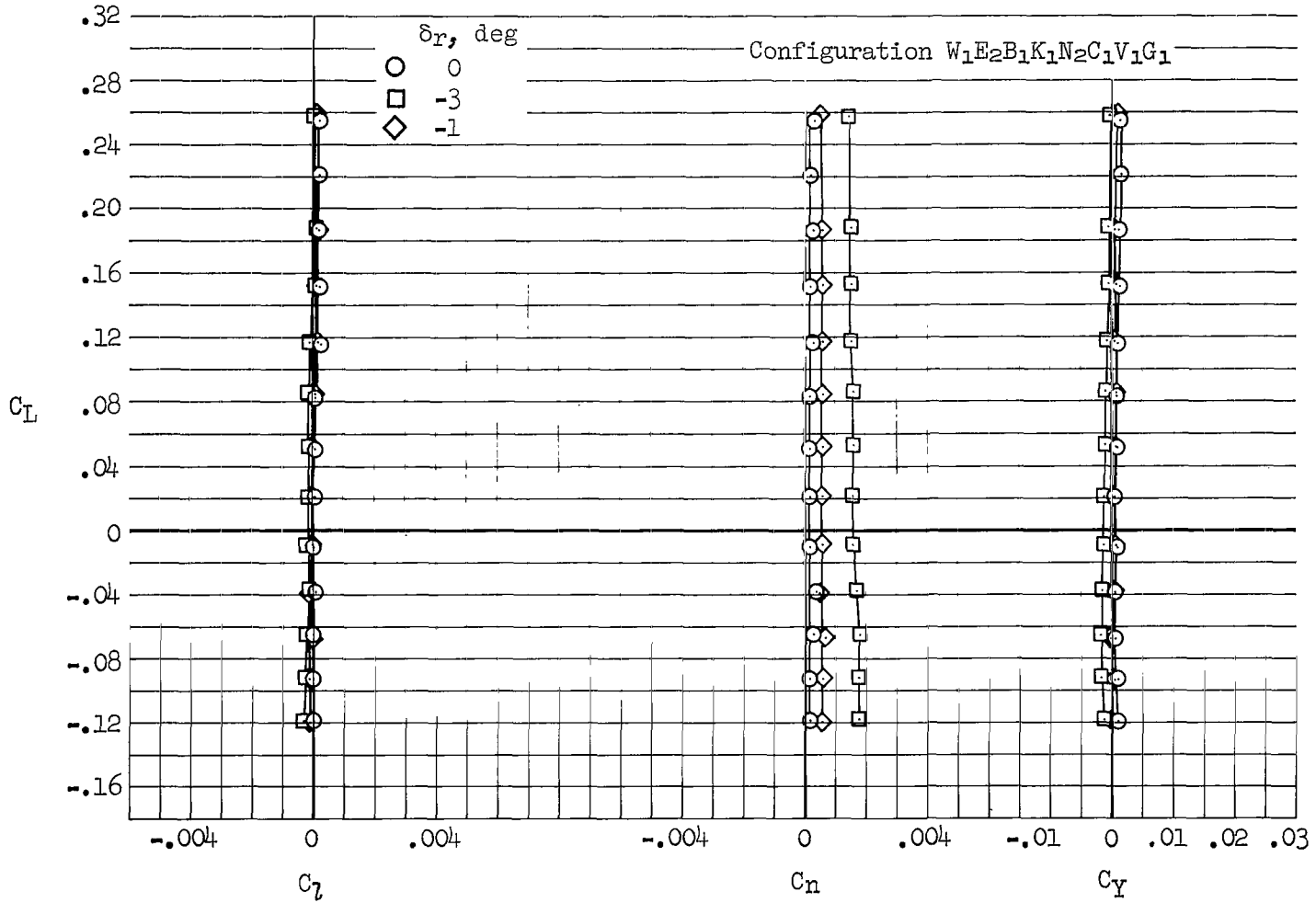

(b) M = 2.10, δ_y = 65°

Figure 29.- Continued.

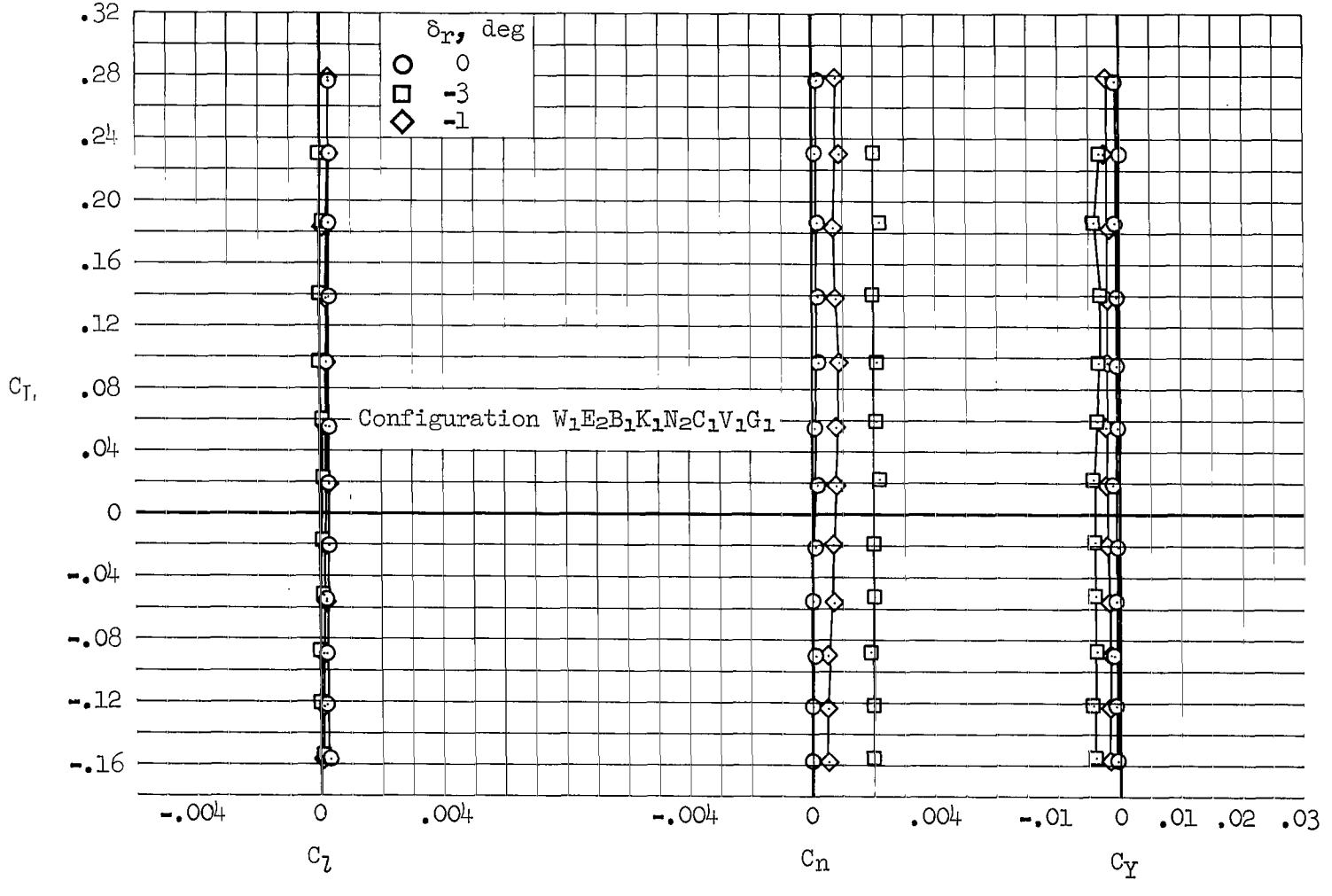

(c) M = 1.60, δ_y = 65°

Figure 29.- Continued.

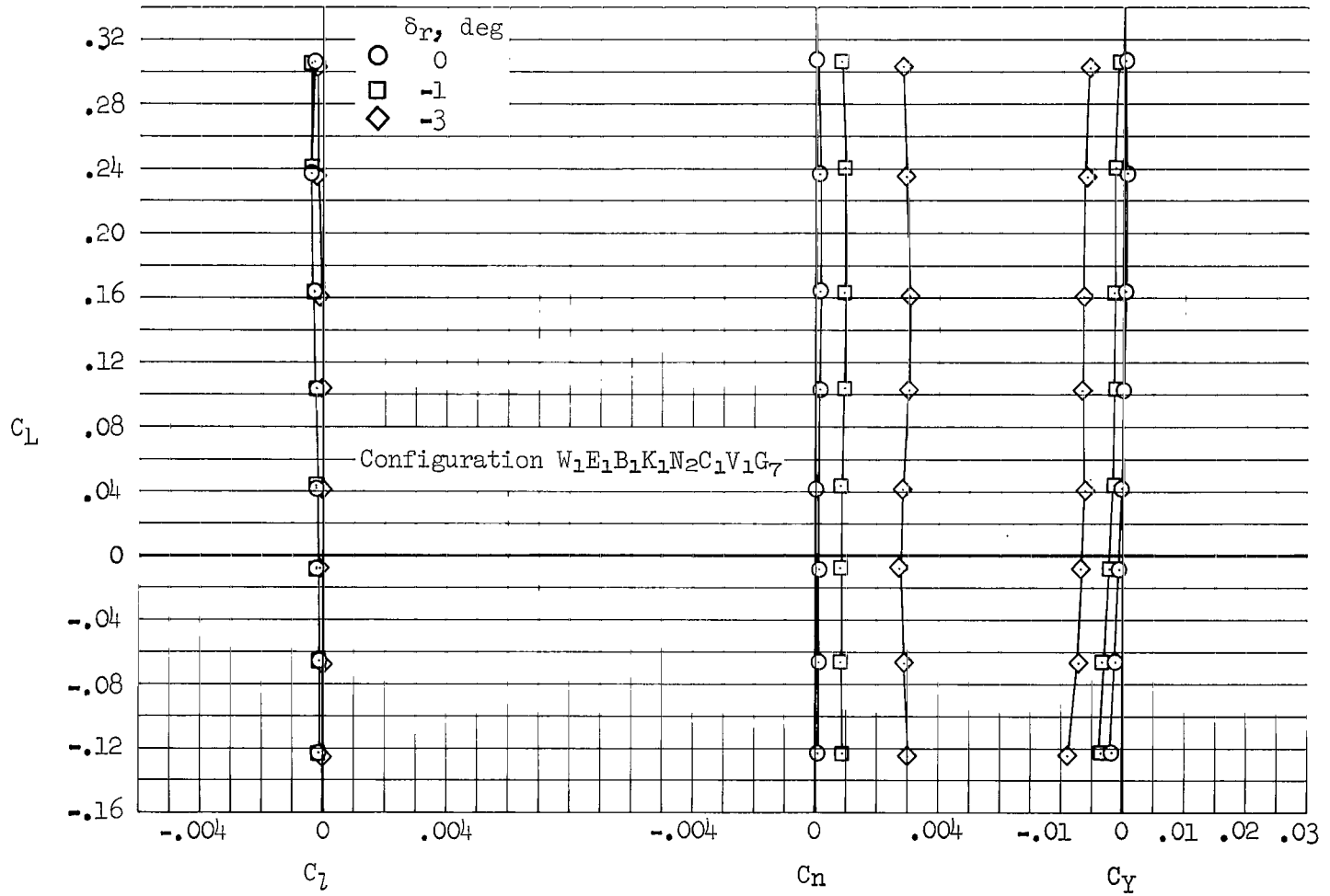

(d) M = 1.20, δ_y = 0°

Figure 29.- Continued.

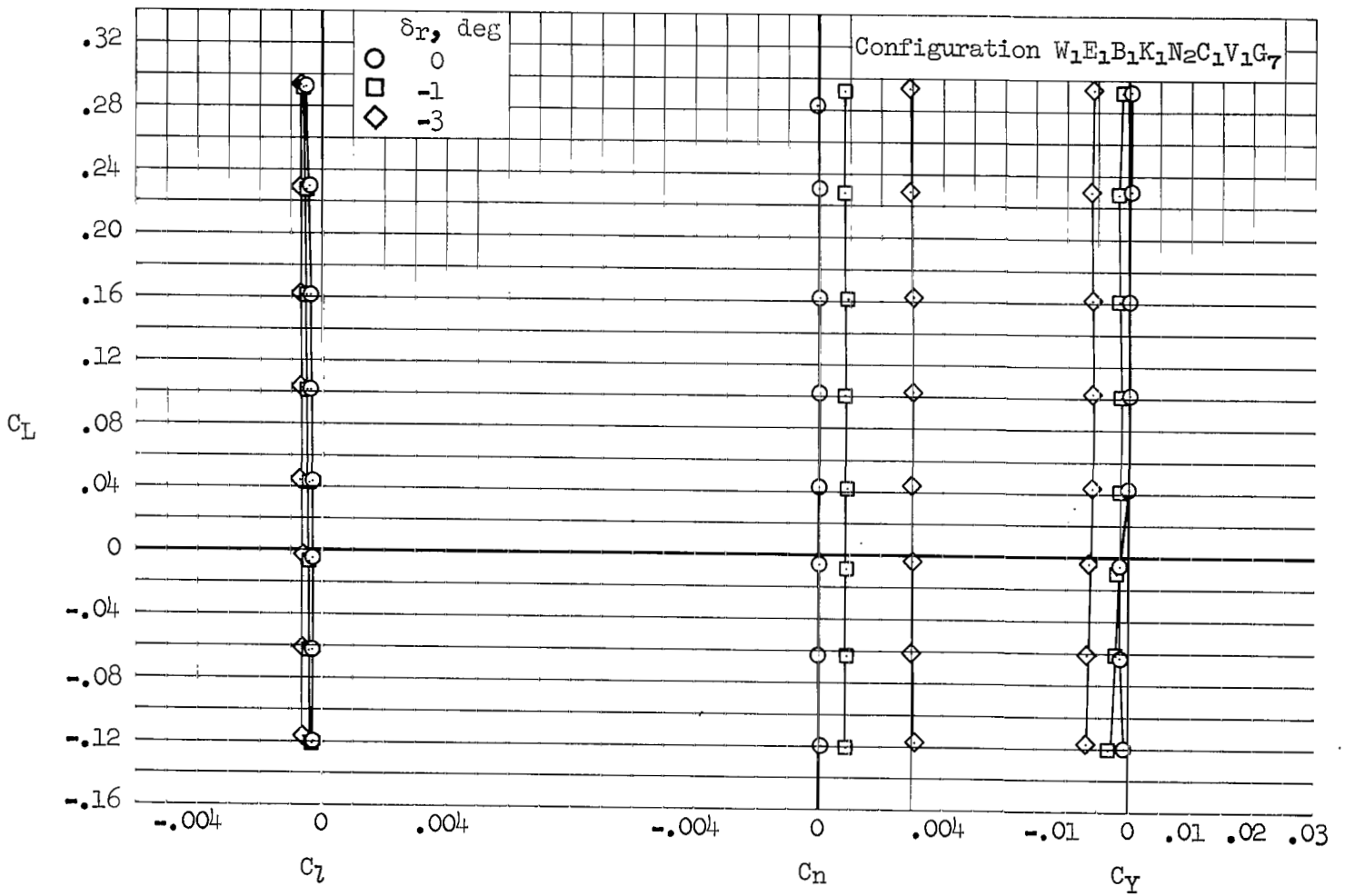

(e) M = 0.95, δ_y = 0°

Figure 29.- Concluded.

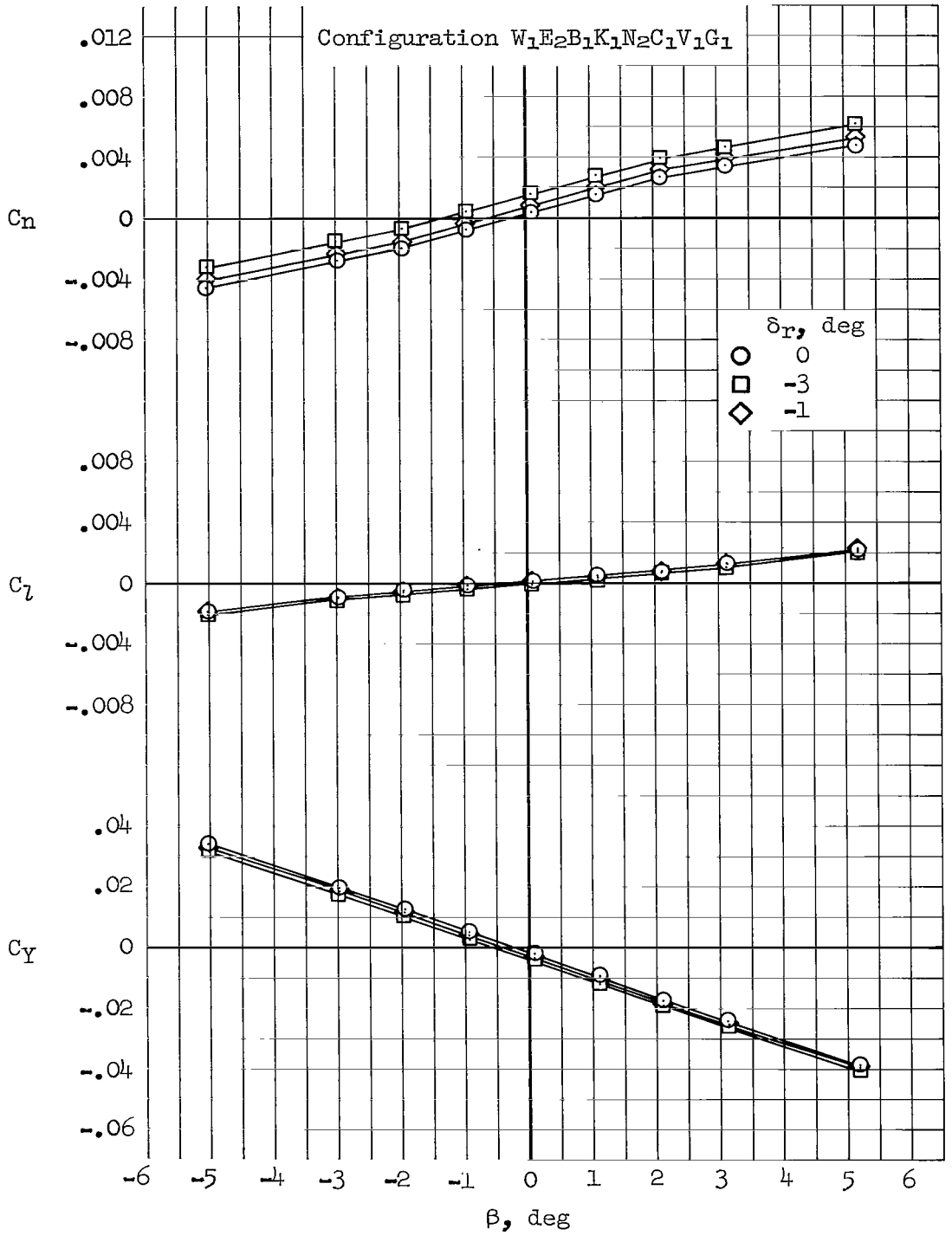

(a) M = 2.53, α = 4.5°, δ_y = 65°

Figure 30.- Effects of rudder deflection on lateral-directional characteristics.

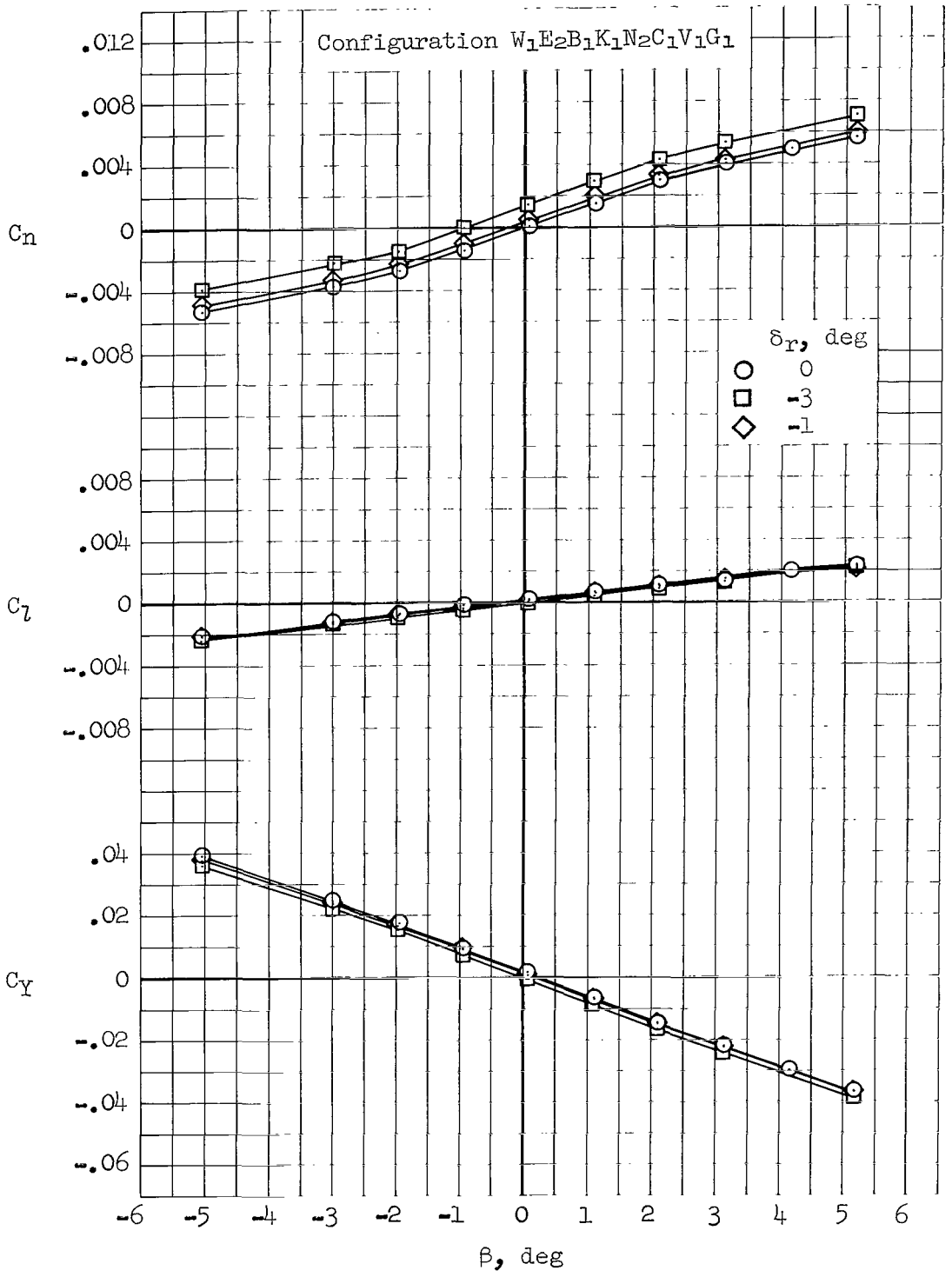

(b) M = 2.10, α = 4.6°, δ_y = 65°

Figure 30.- Continued.

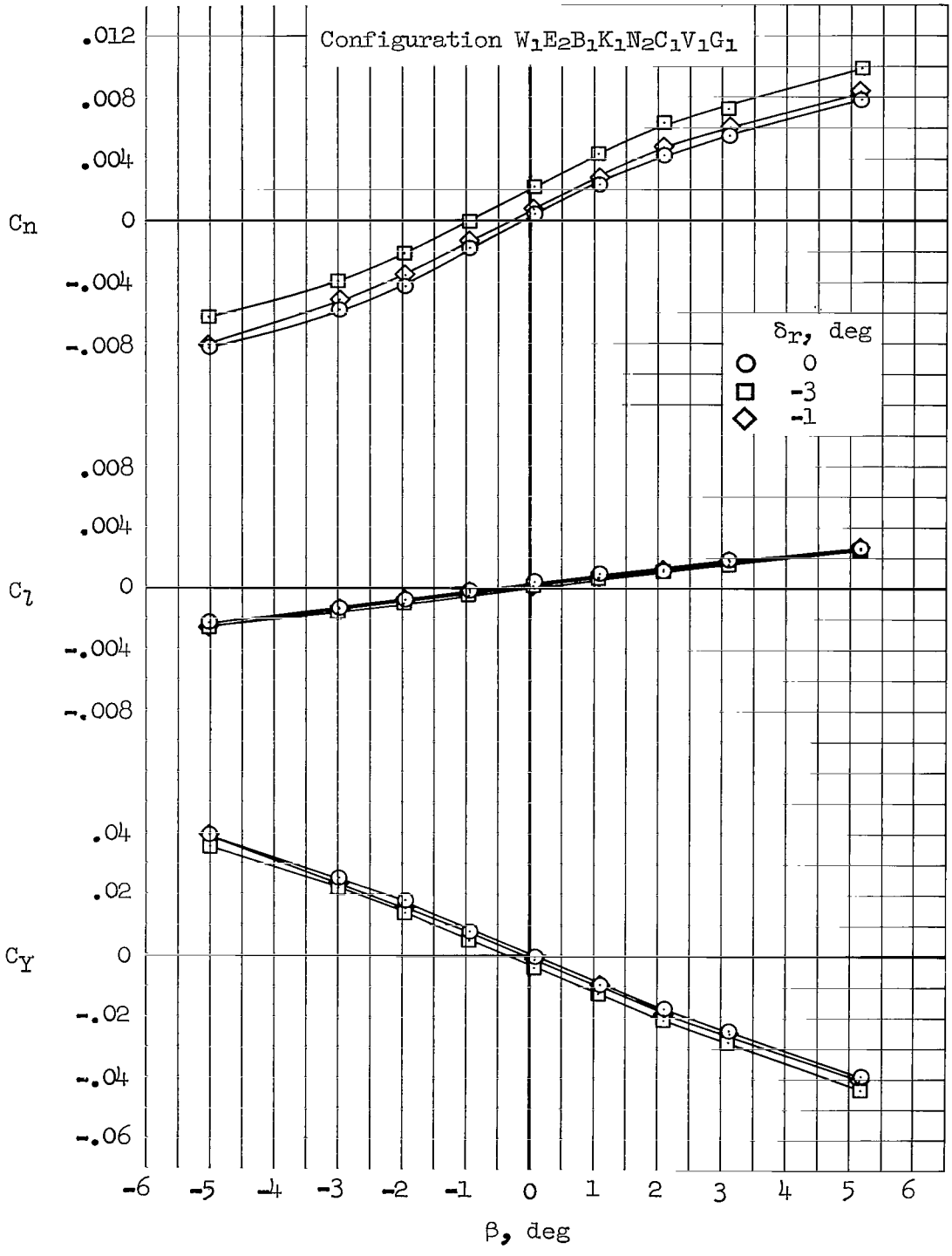

(c) M = 1.60, α = 4.8, δ_y = 65°

Figure 30.- Continued.

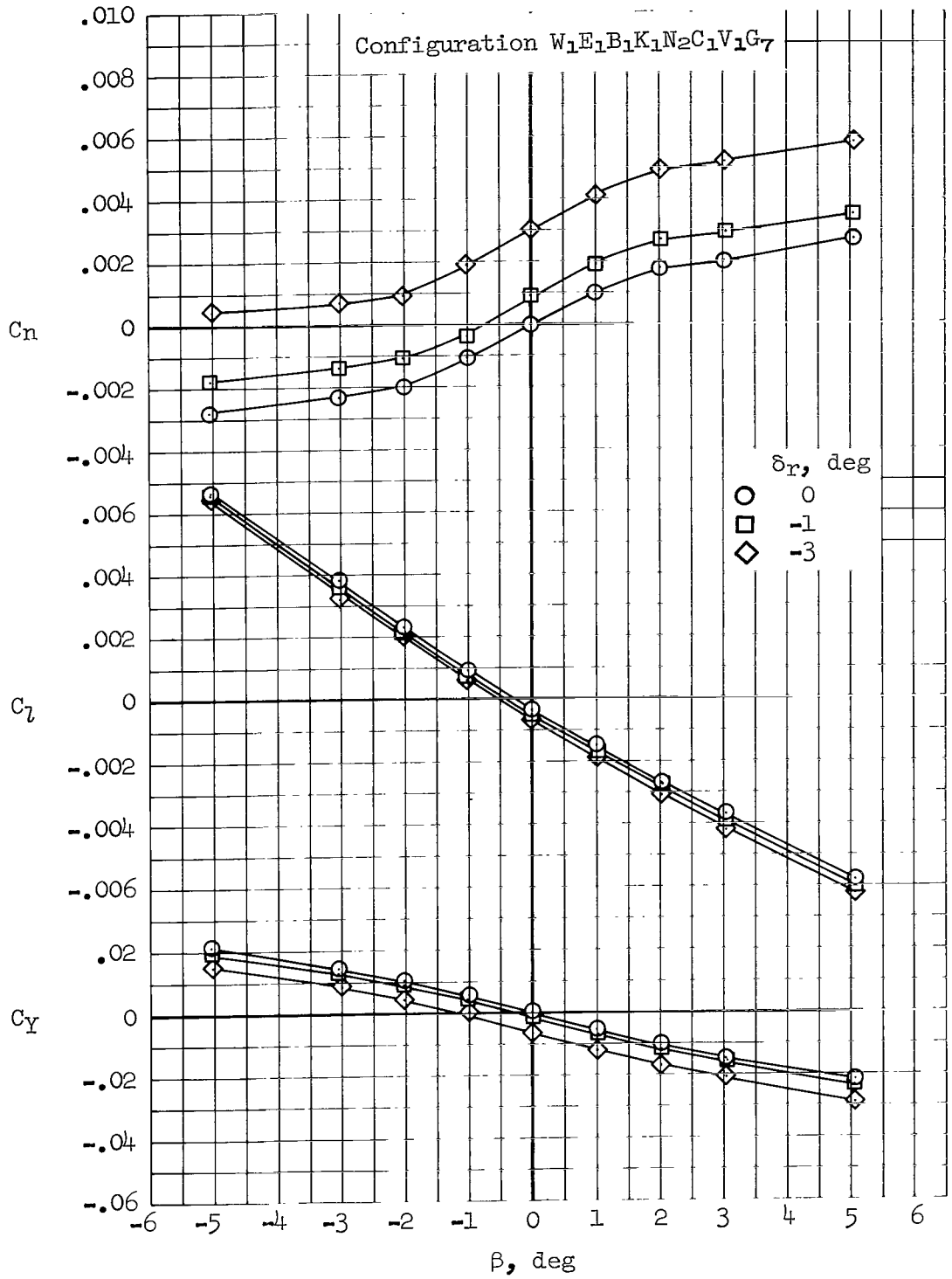

(d) M = 1.20, α = 3.3°, δ_y = 0°

Figure 30.- Continued.

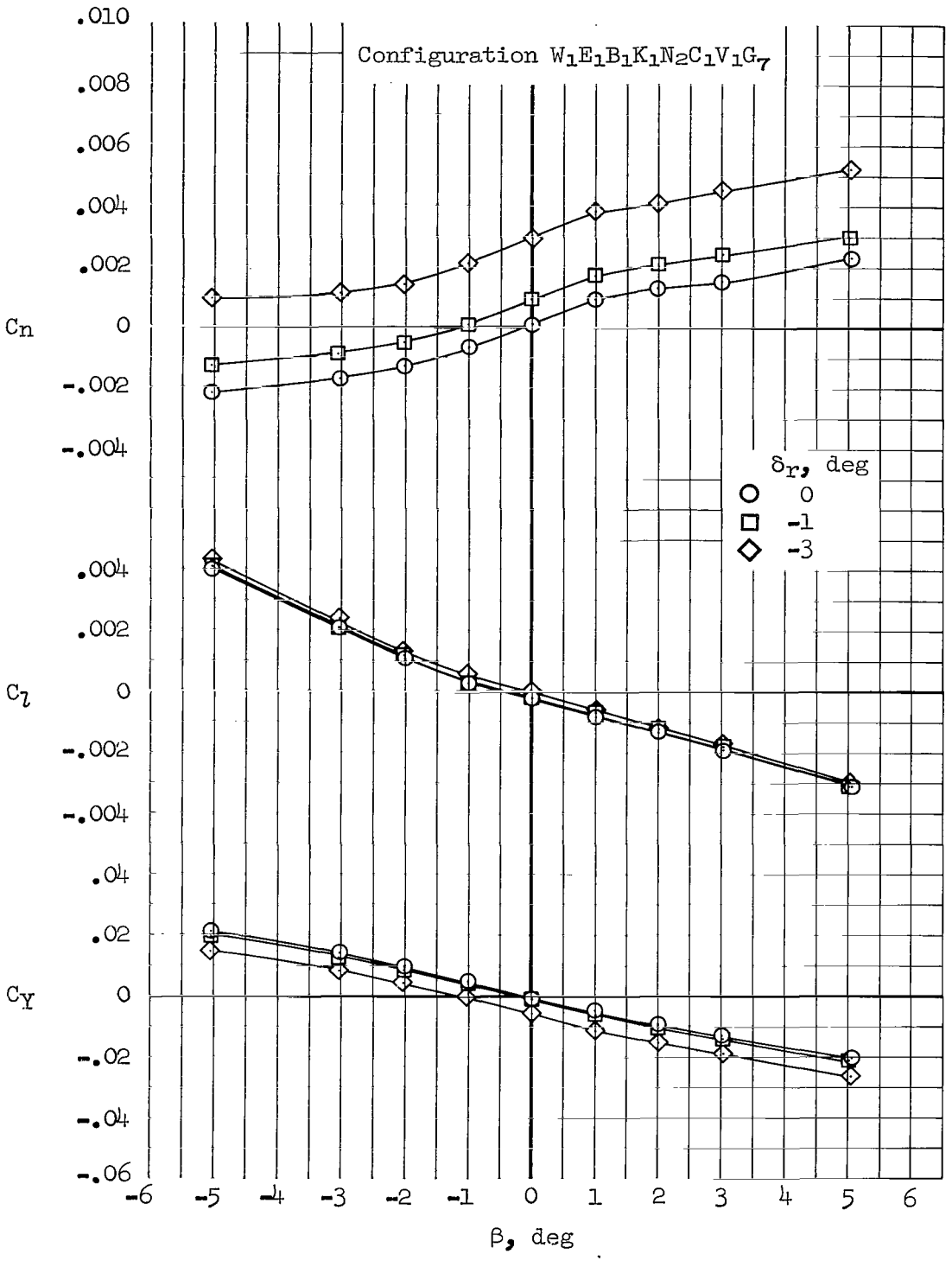

(e) M = 0.95, α = 3.2°, δ_y = 0°

Figure 30.- Concluded.

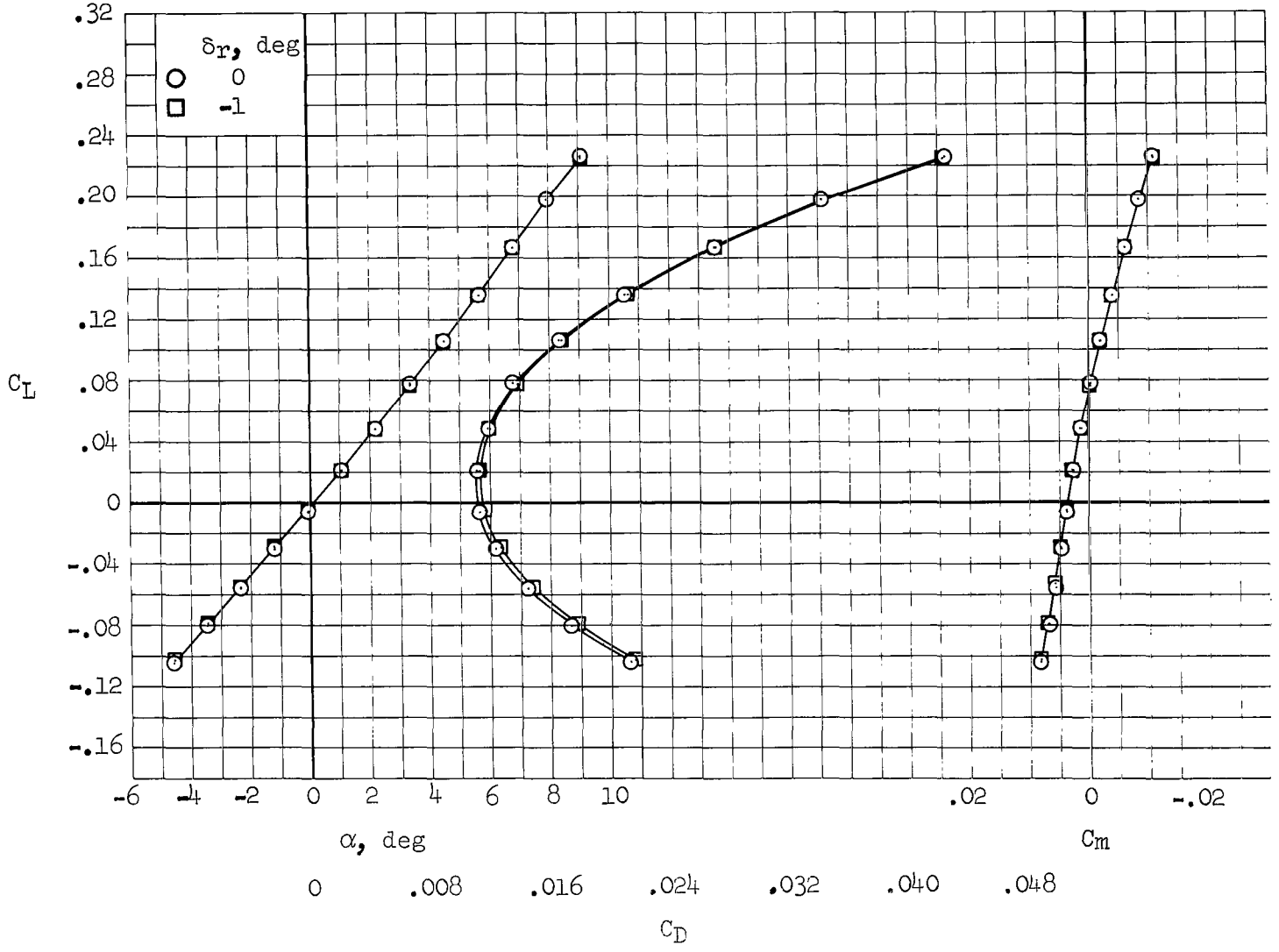

(a) M = 2.53

Figure 31.- Additional data indicating the effects of 1° of rudder deflection on the longitudinal characteristics of configuration $W_1E_2B_1K_1N_2C_1V_1G_1$, δ_y = 65°.

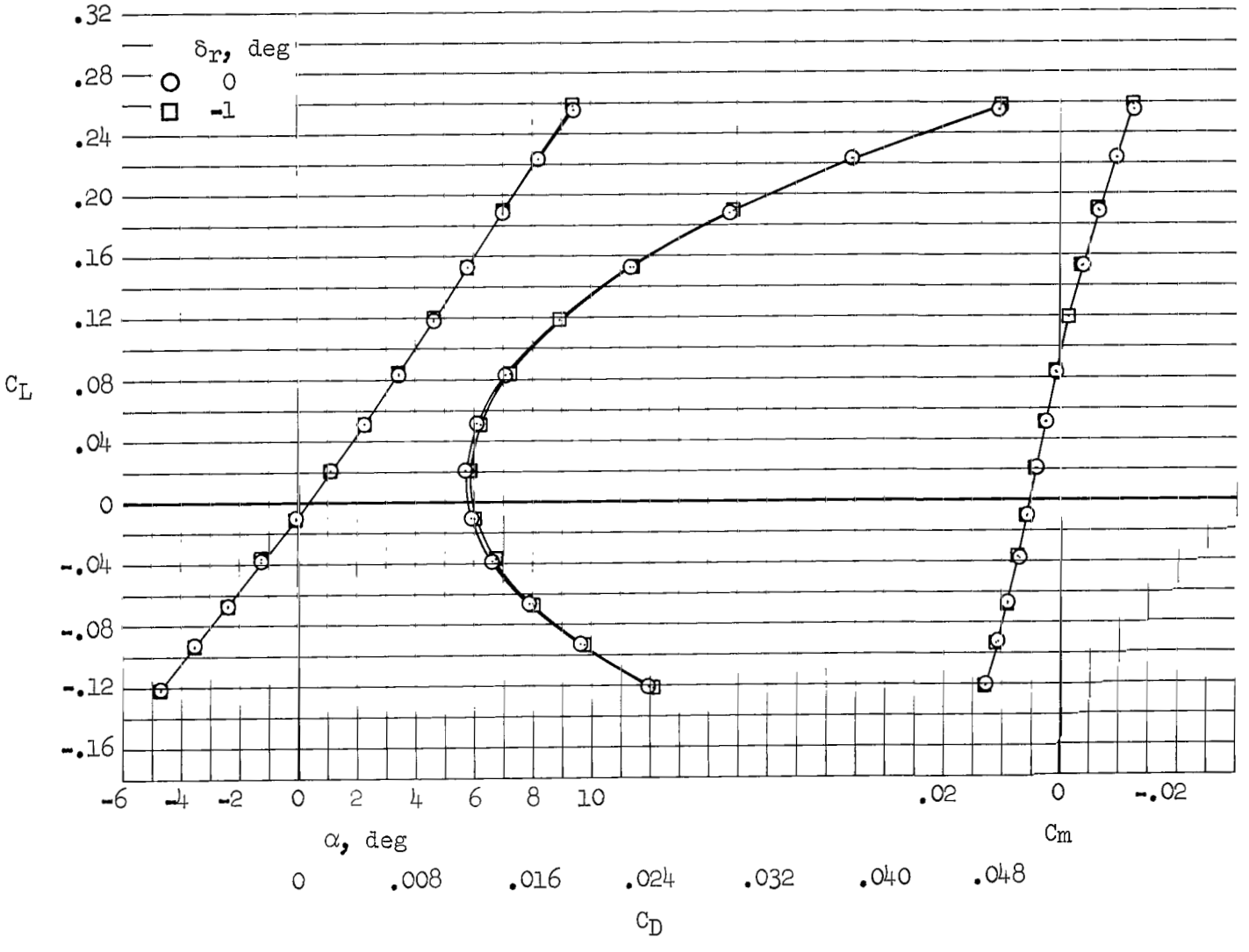

(b) M + 2.10

Figure 31.- Continued.

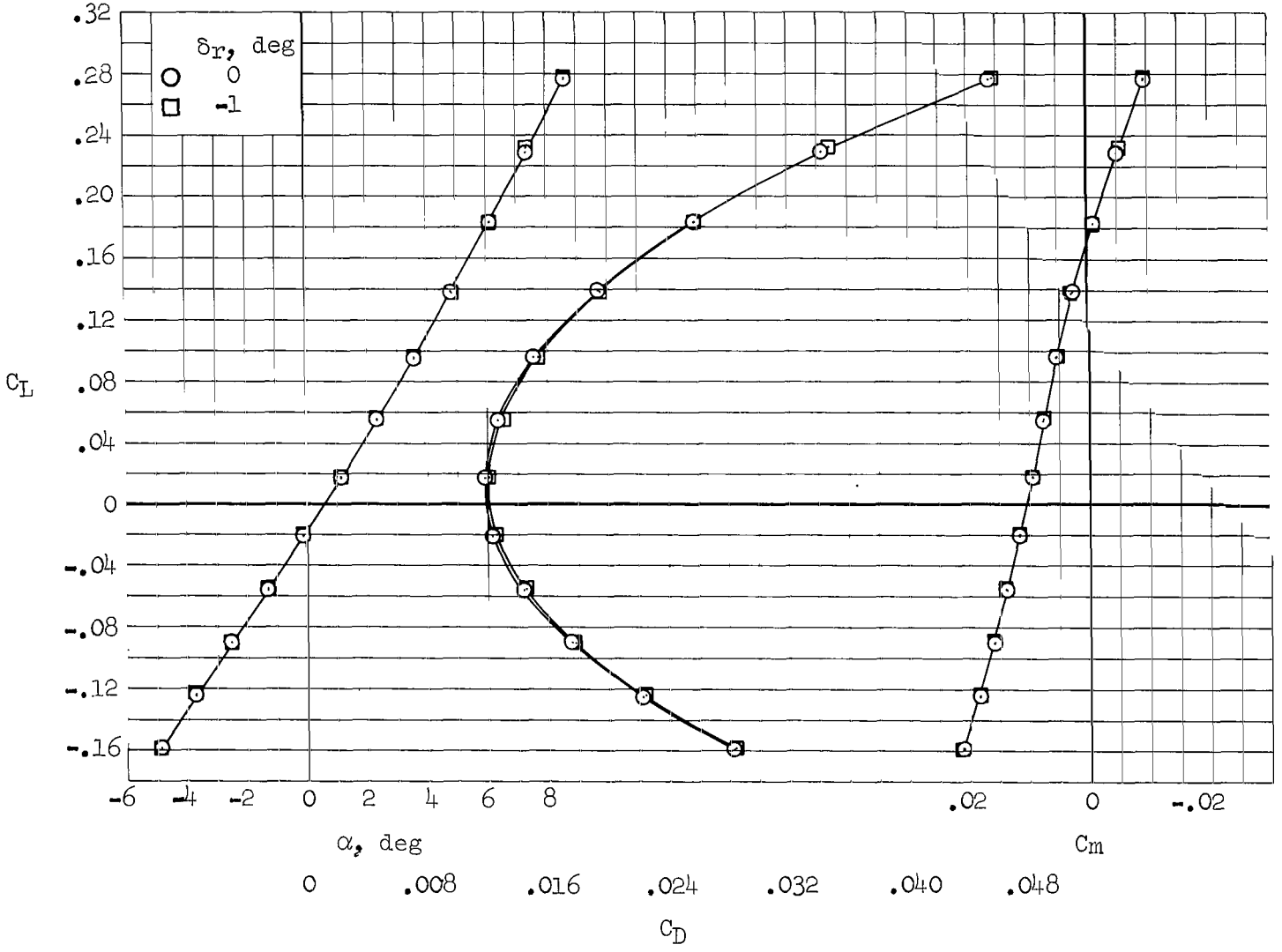

(c) M = 1.60

Figure 31.- Concluded.

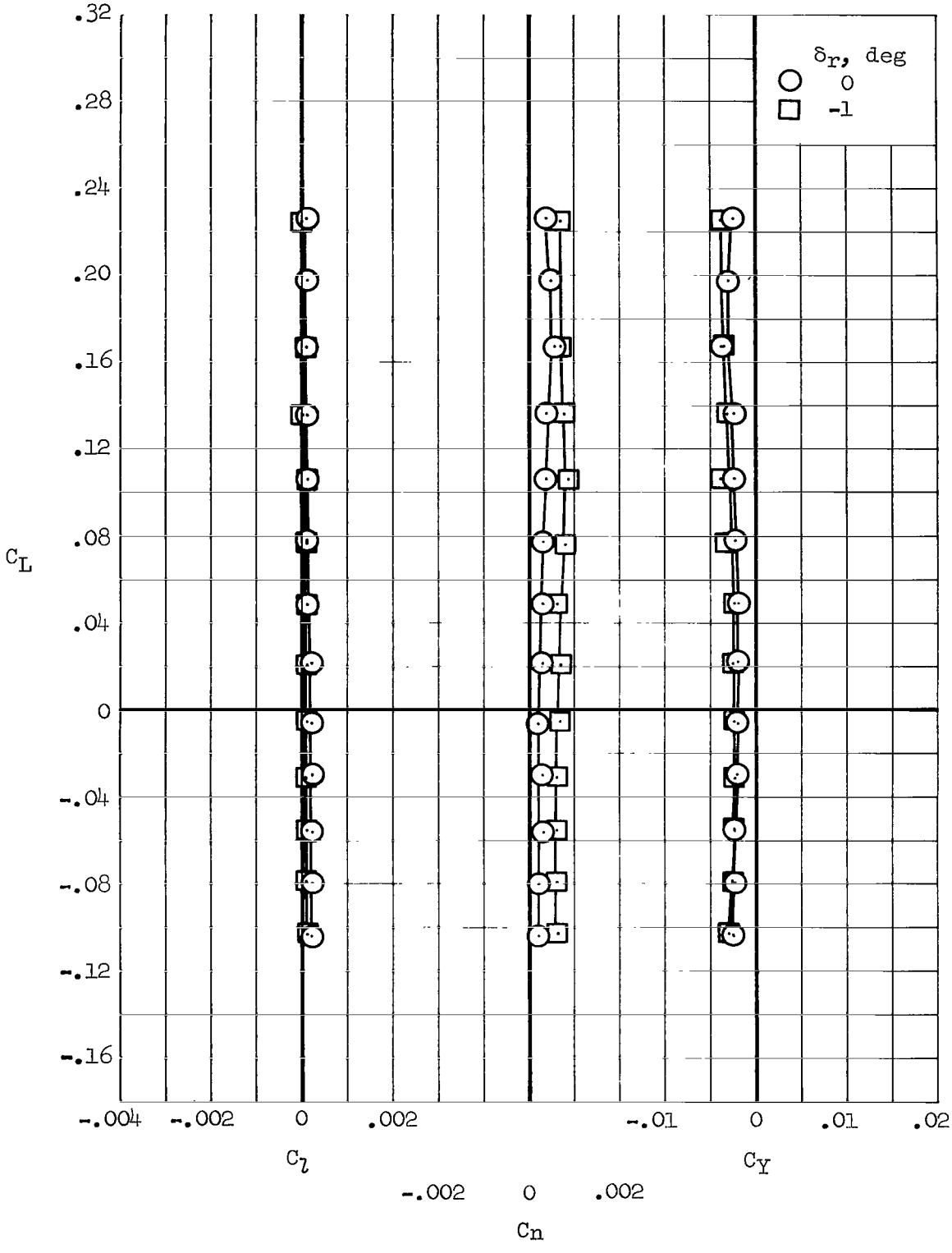

(a) M = 2.53

Figure 32.- Additional data indicating the effects of 1° of rudder deflection on the rolling-moment, yawing-moment, and side-force characteristics of configuration $W_1E_2B_1K_1N_2C_1V_1G_1$, $\delta_y = 65^\circ$.

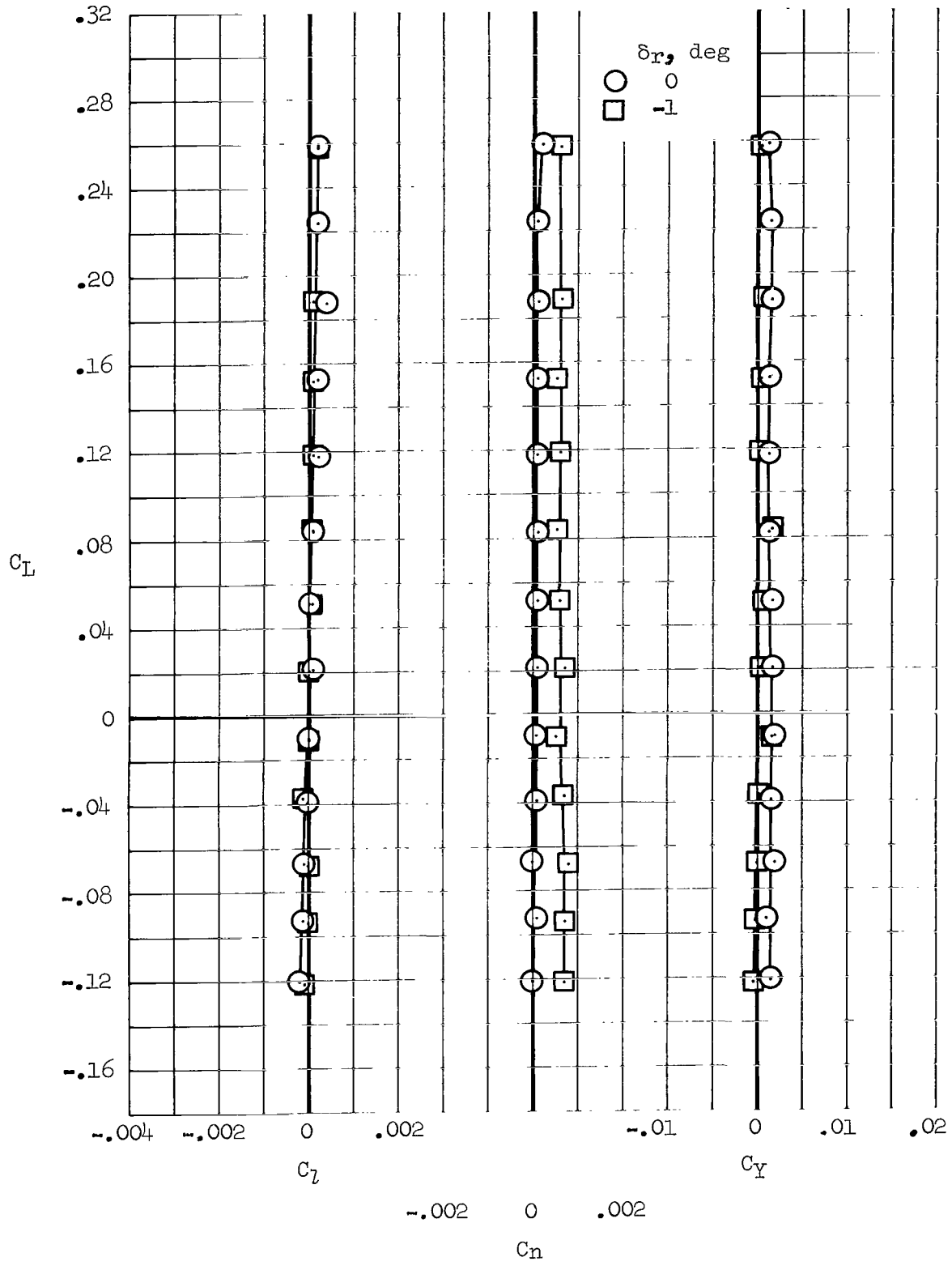

(b) M = 2.10

Figure 32.- Continued.

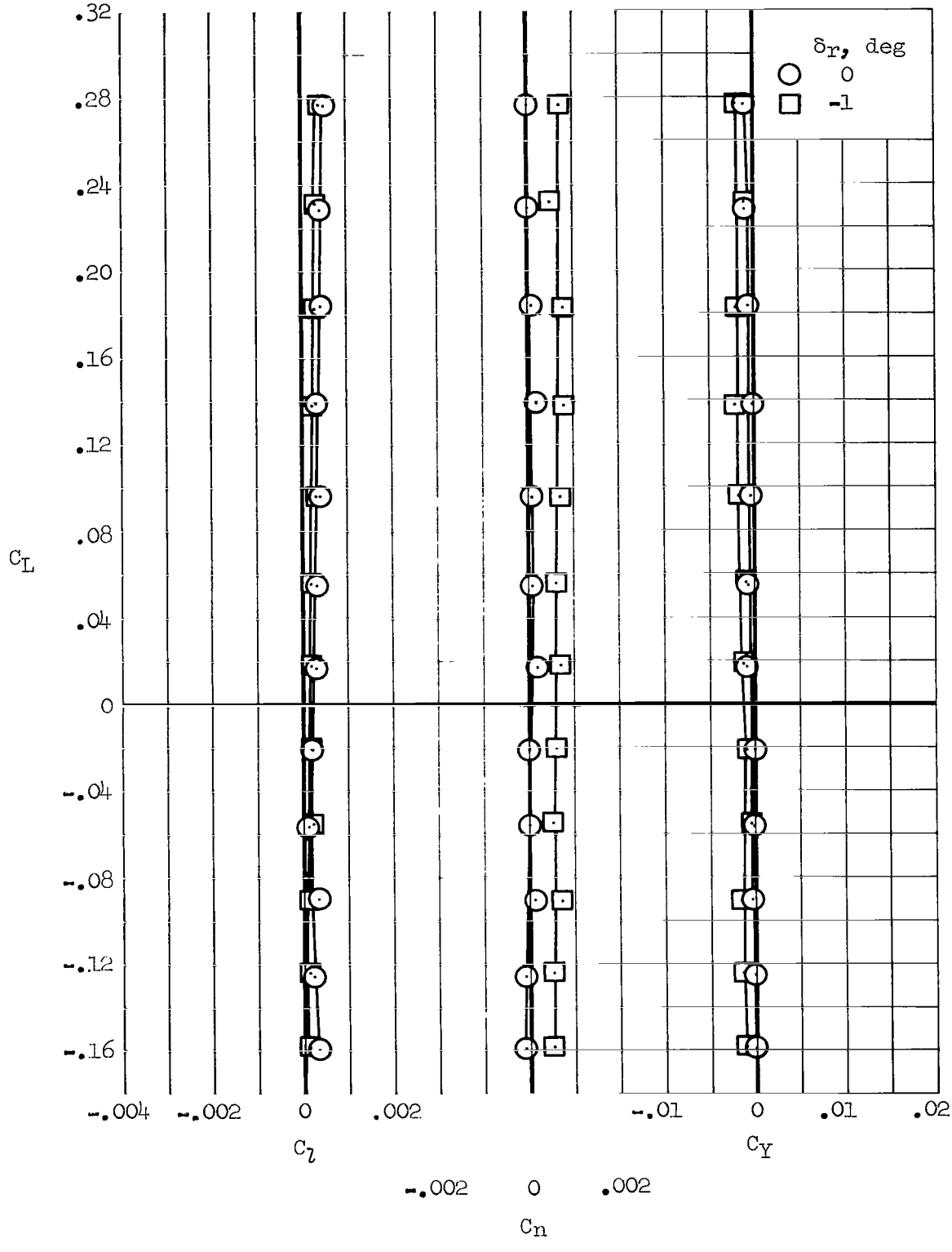

(c) M = 1.60

Figure 32.- Concluded.

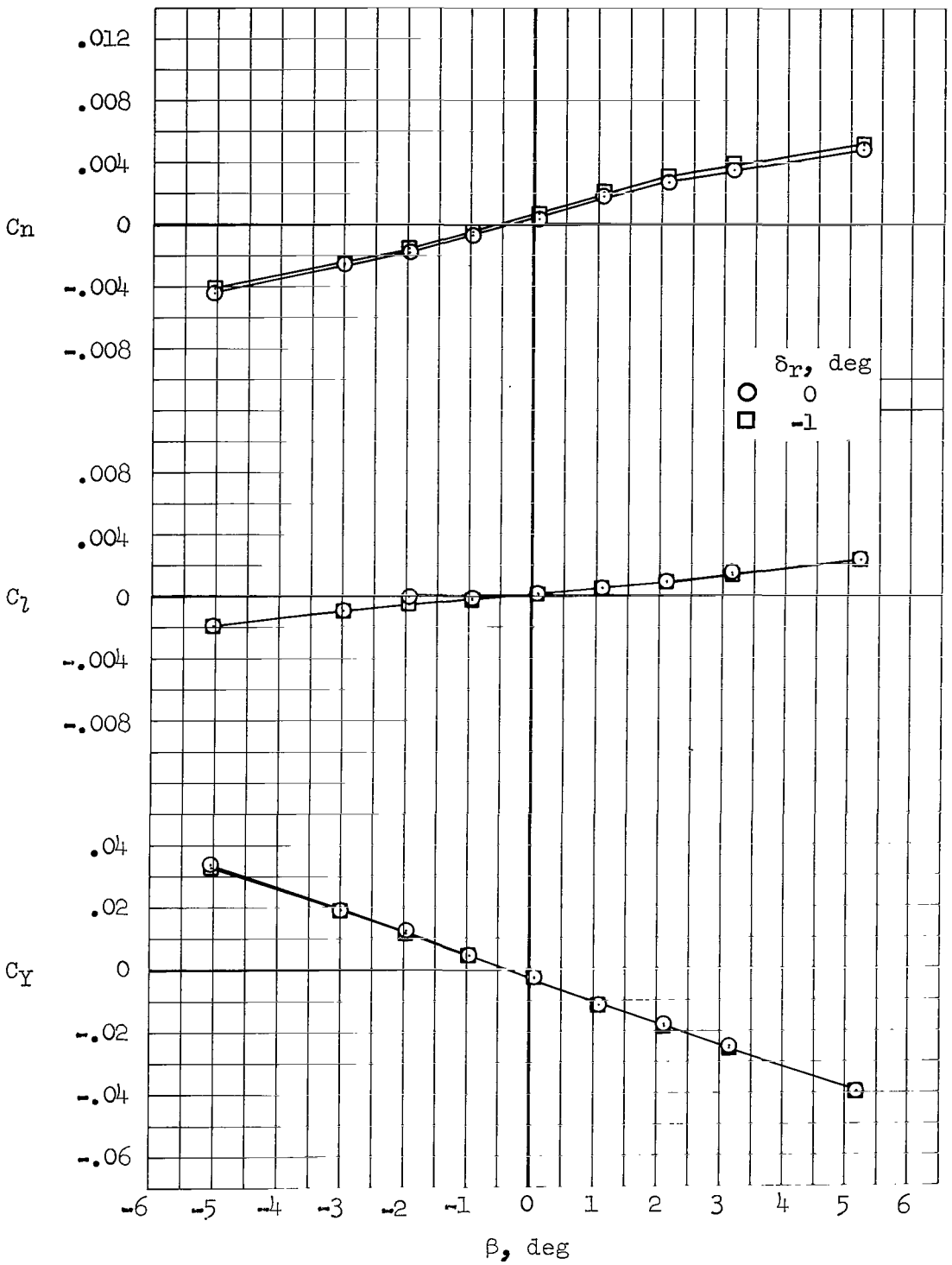

(a) M = 2.53, α = 4.5°

Figure 33.- Additional data indicating the effects of 1° of rudder deflection on the lateral-directional characteristics of configuration $W_1E_2B_1K_1N_2C_1V_1G_1$, δ_y = 65°.

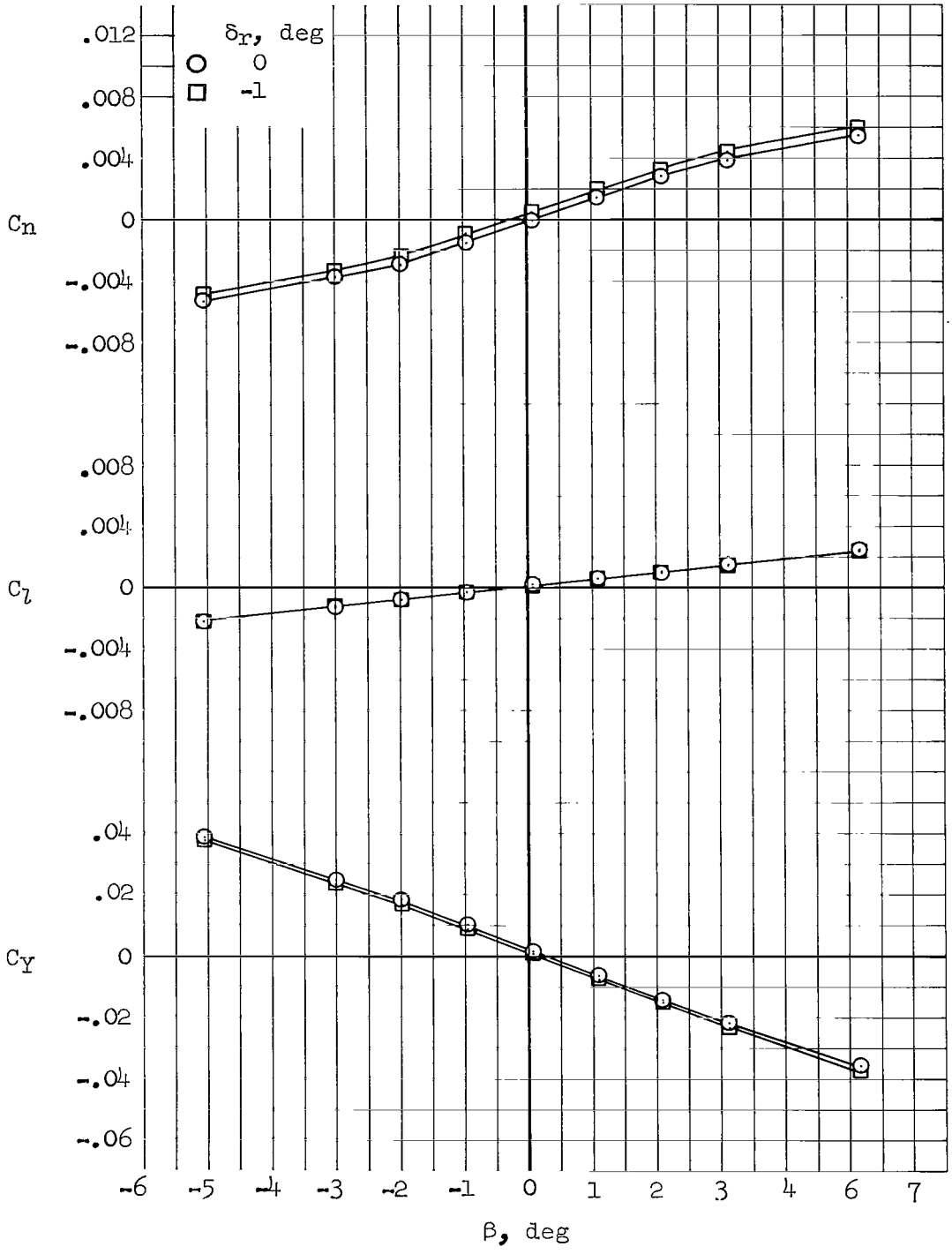

(b) M = 2.10, α = 4.6°

Figure 33.- Continued.

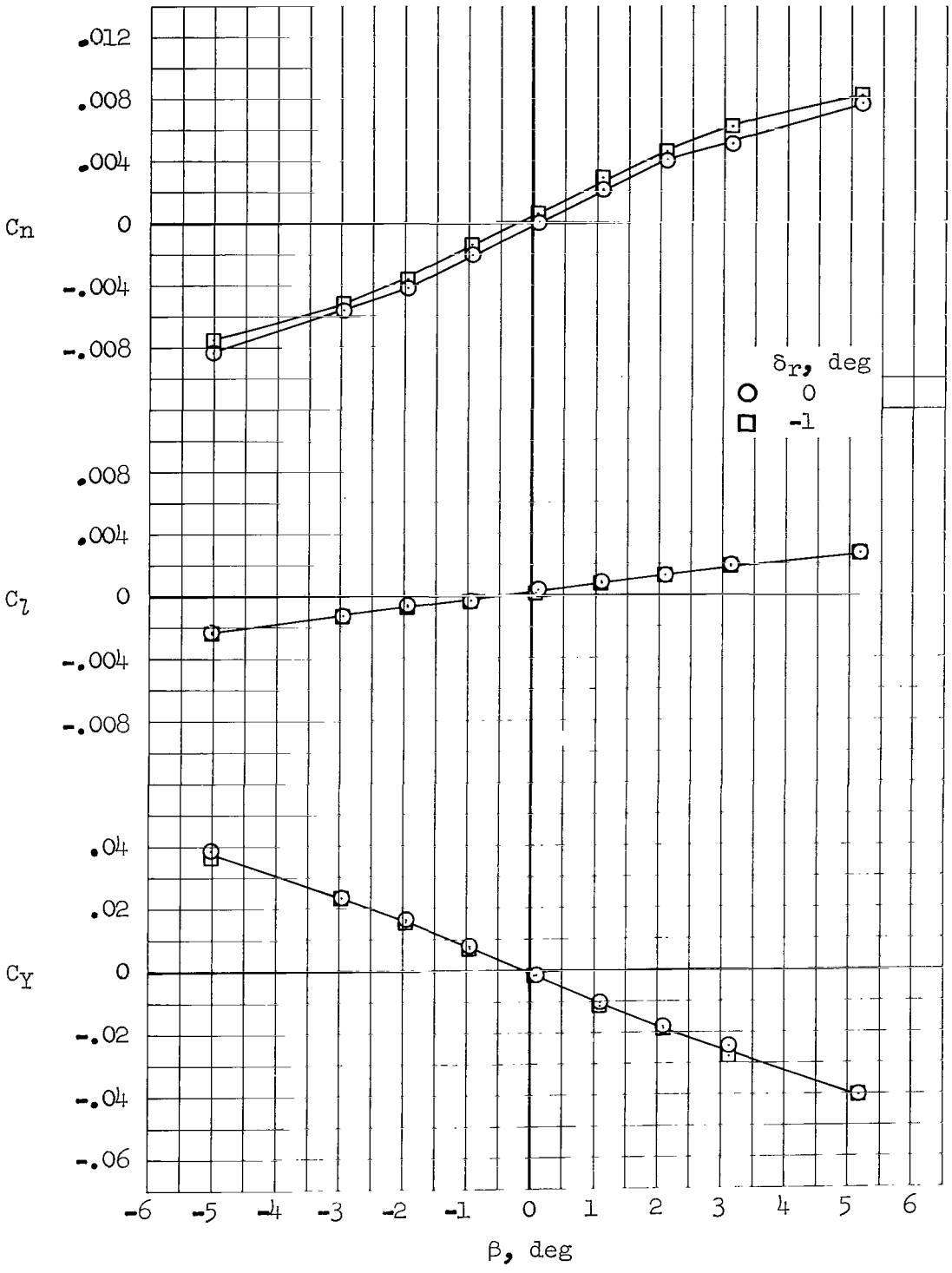

(c) M = 1.60, α = 4.8°

Figure 33.- Concluded.

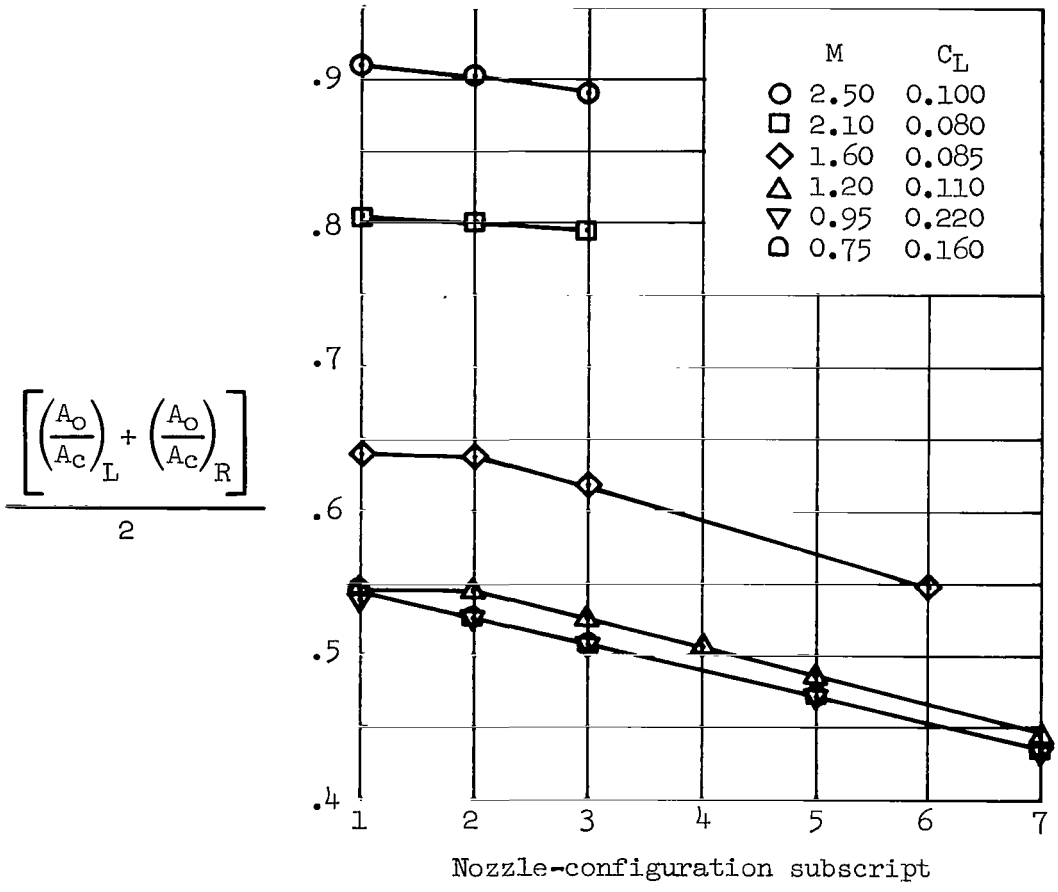

Figure 34.- Average of left- and right-duct mass-flow ratios for various duct flow nozzles at lift coefficients and Mach numbers approximately speed-power stabilized flight-test conditions.

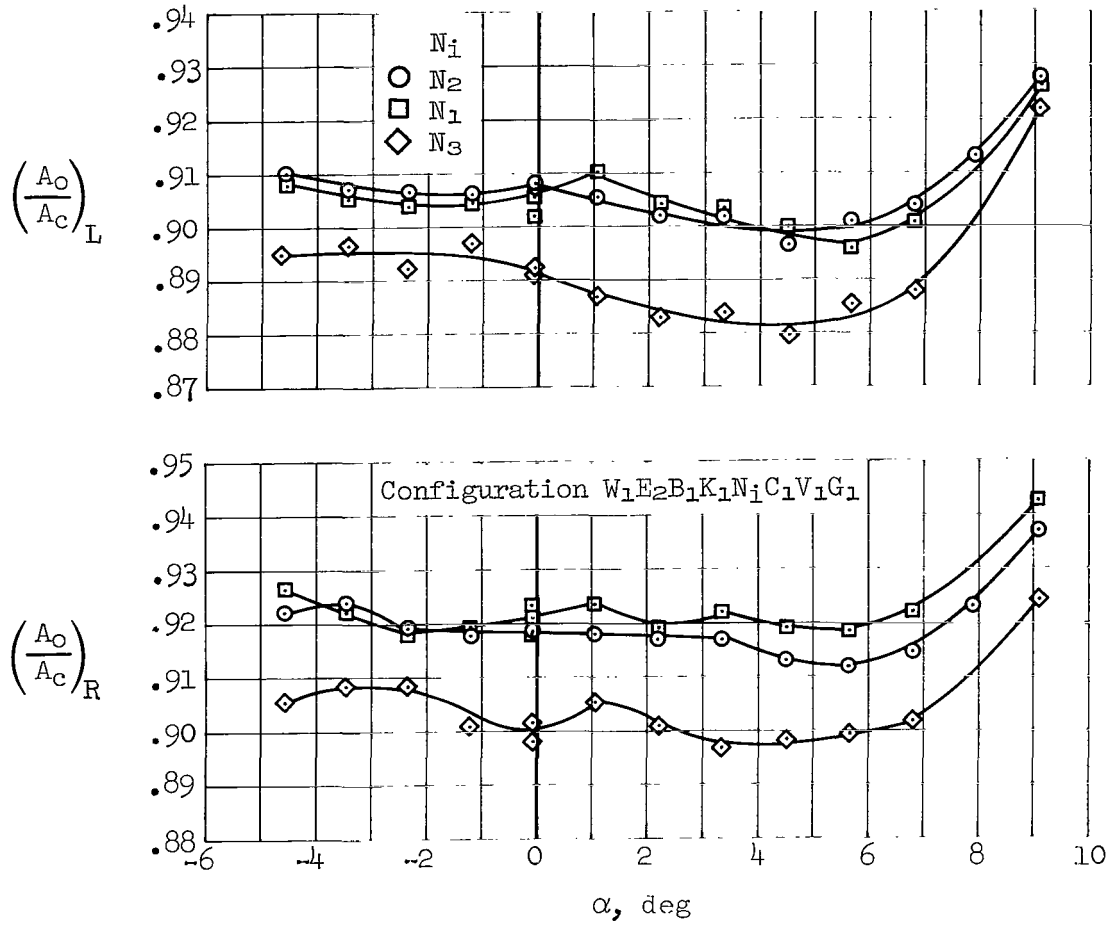

(a) M = 2.53, δ_y = 65°

Figure 35.- Effects of various nozzle configurations and angle-of-attack variation on inlet mass-flow ratios.

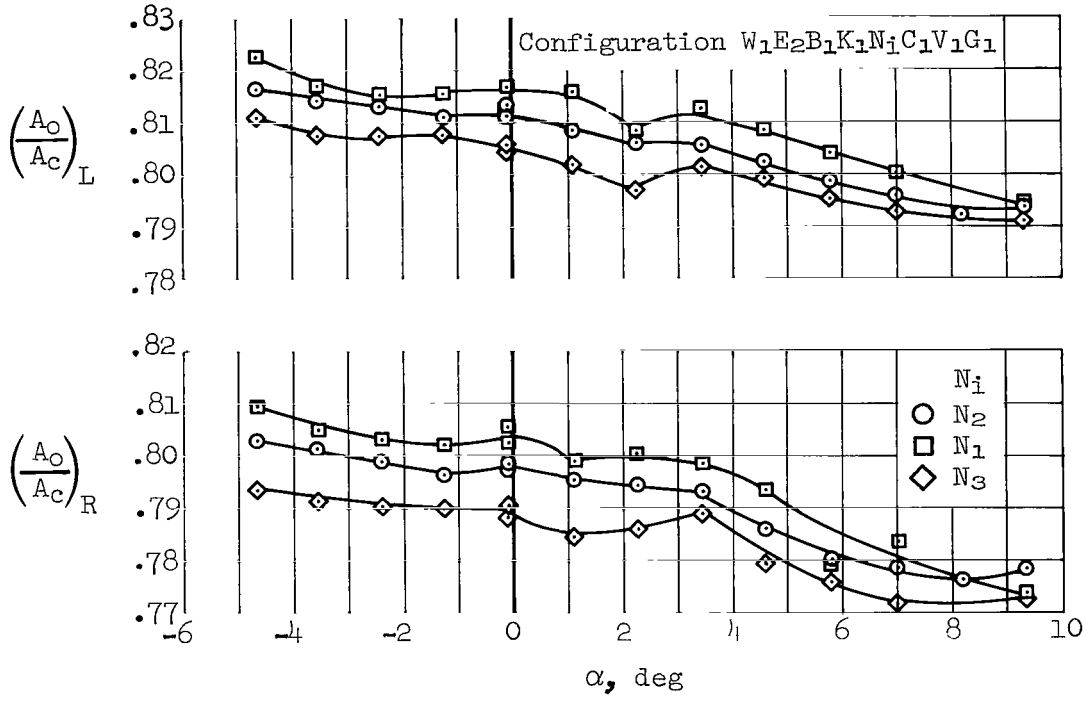

(b) M = 2.10, δ_y = 65°

Figure 35.- Continued.

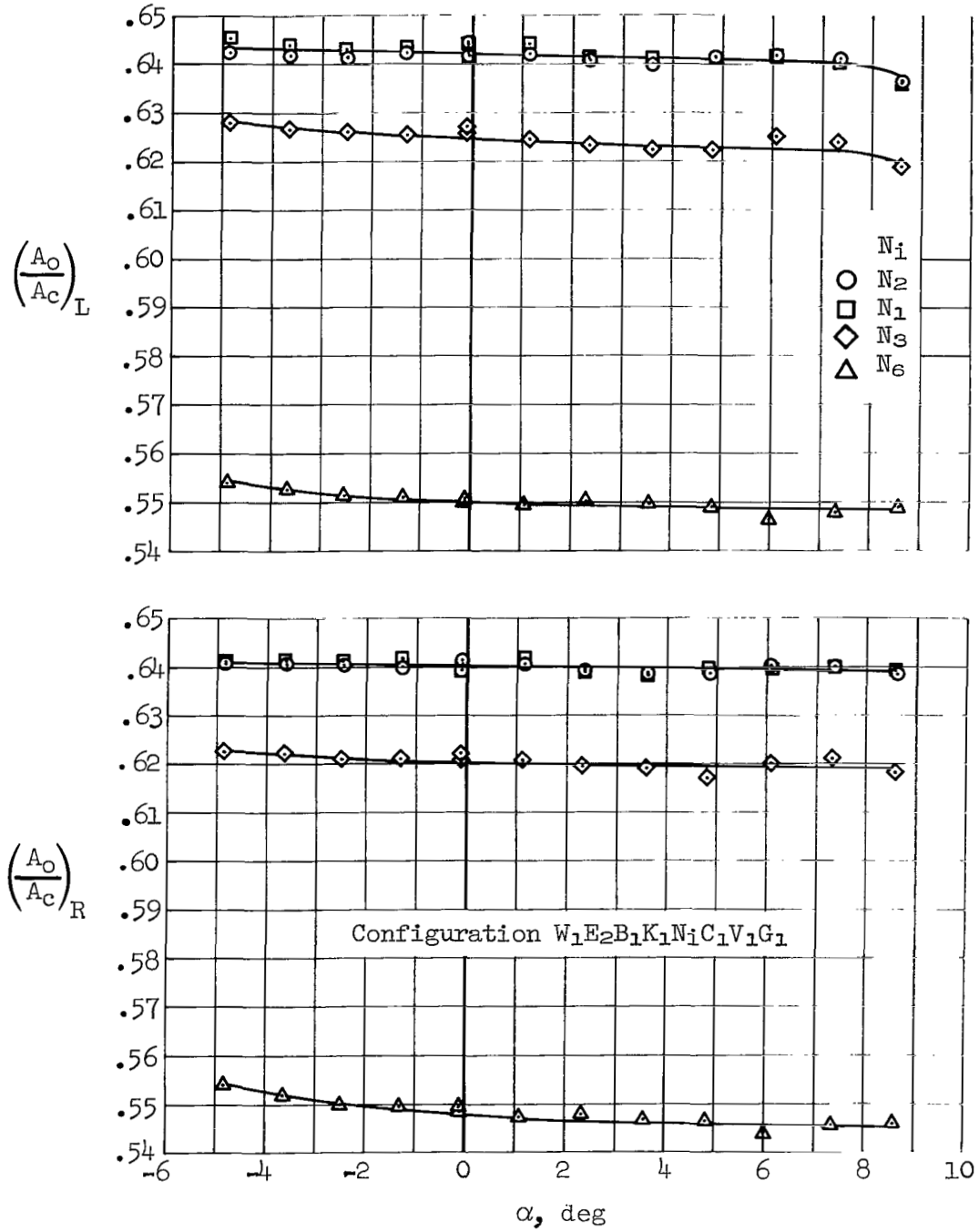

(c) M = 1.60, δ_y = 65°

Figure 35.- Continued.

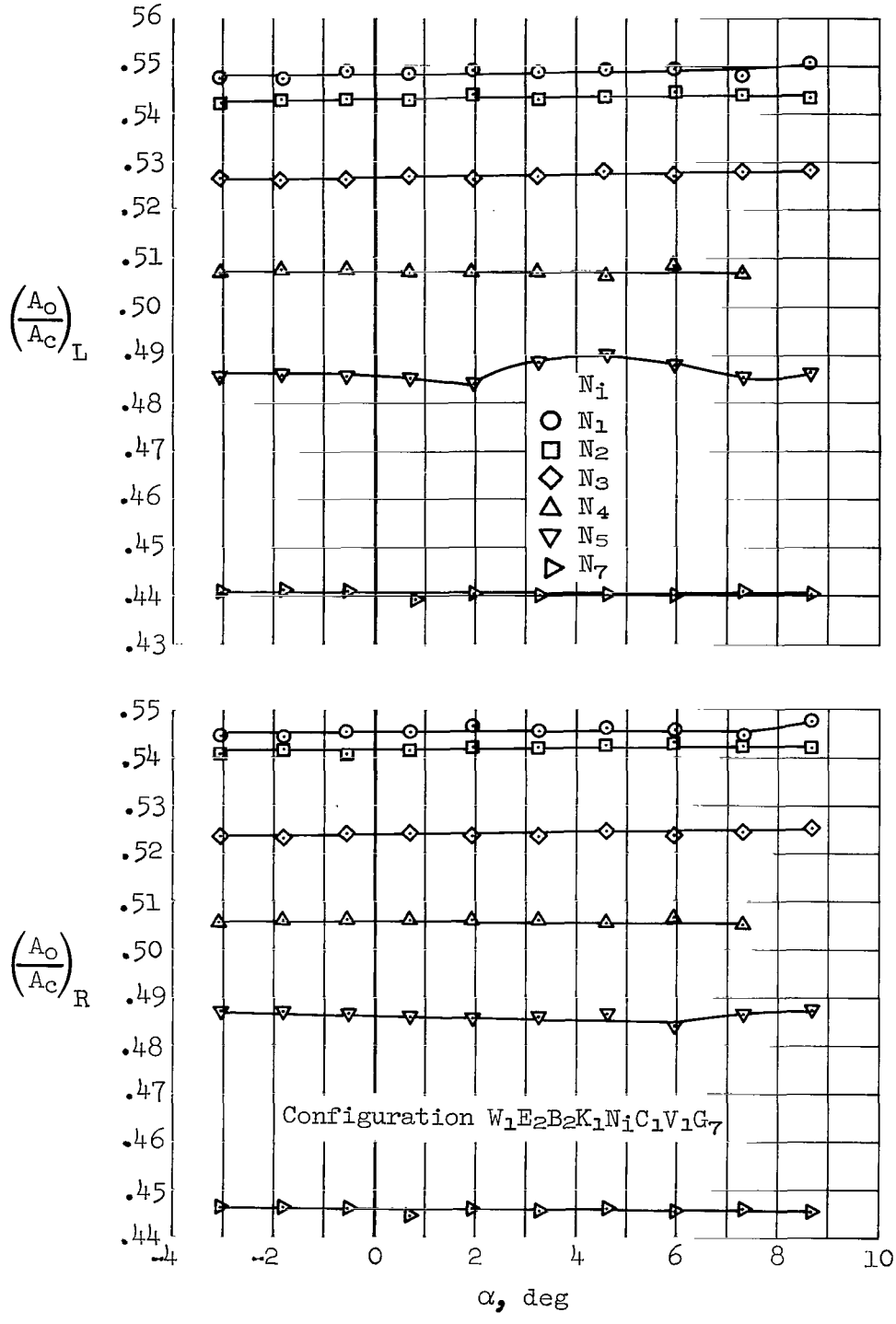

(d) M = 1.20, δ_y = 25°

Figure 35.- Continued.

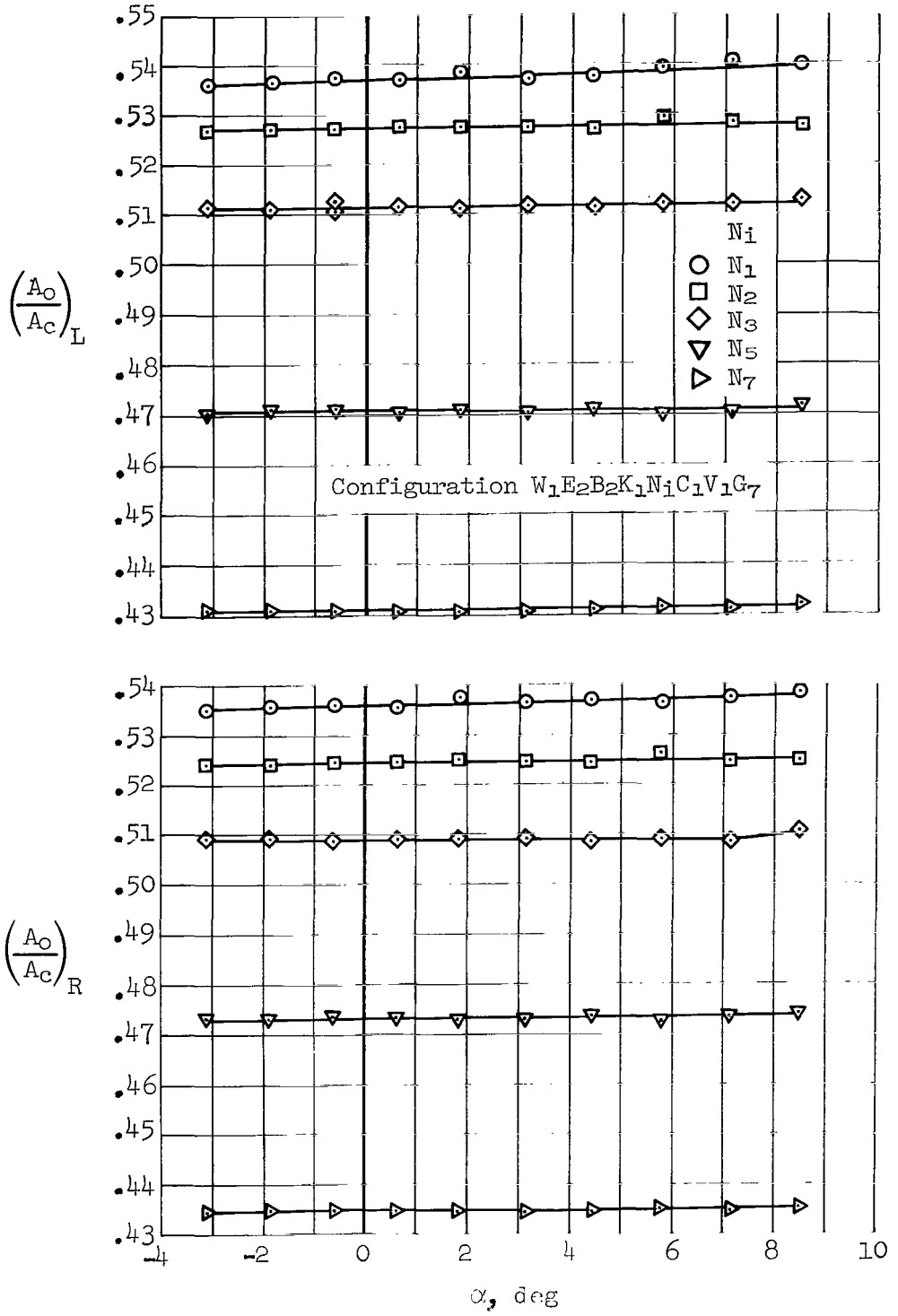

(e) M = 0.95, δ_y = 25°

Figure 35.- Continued.

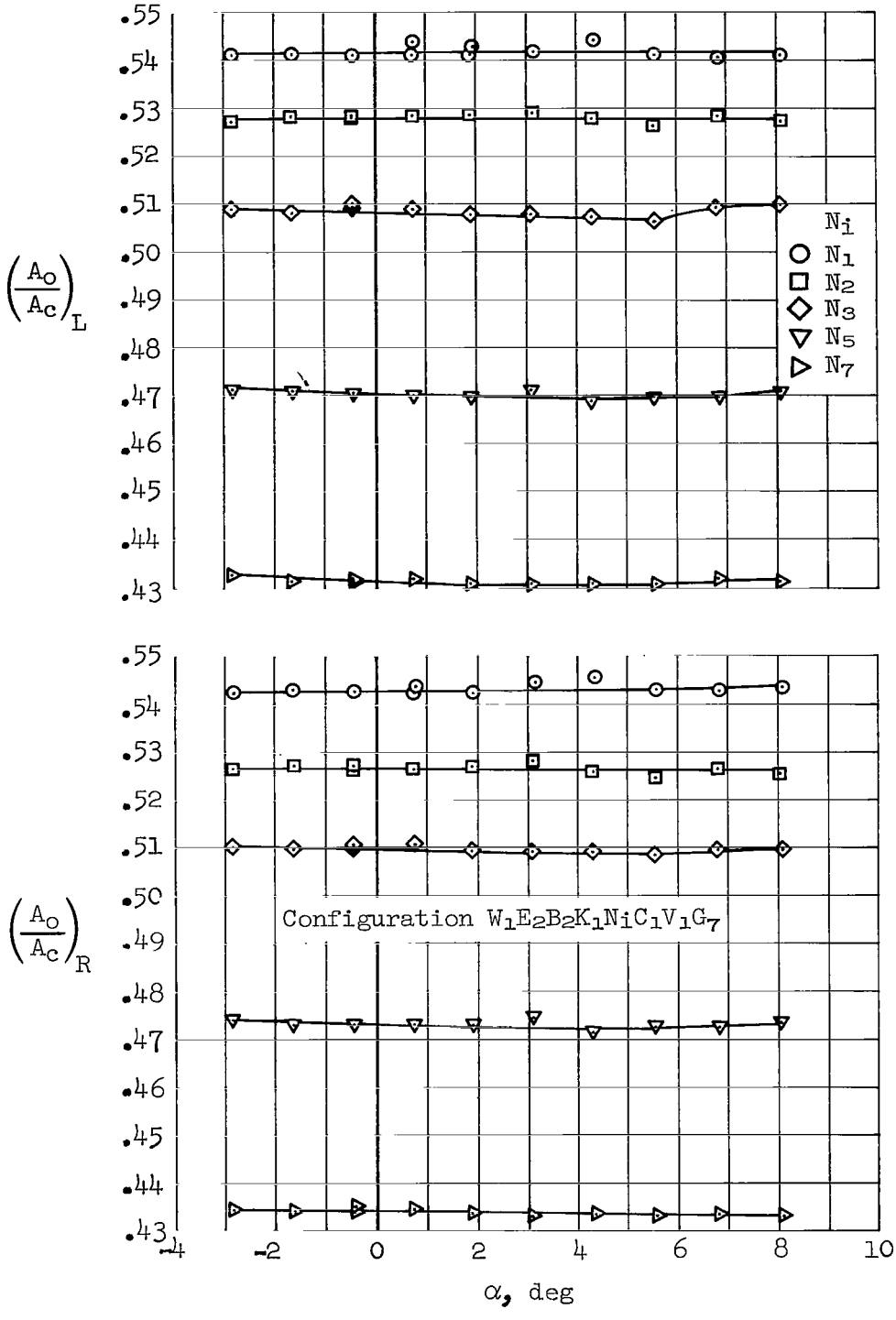

(f) M = 0.75, δ_y = 25°

Figure 35.- Continued.

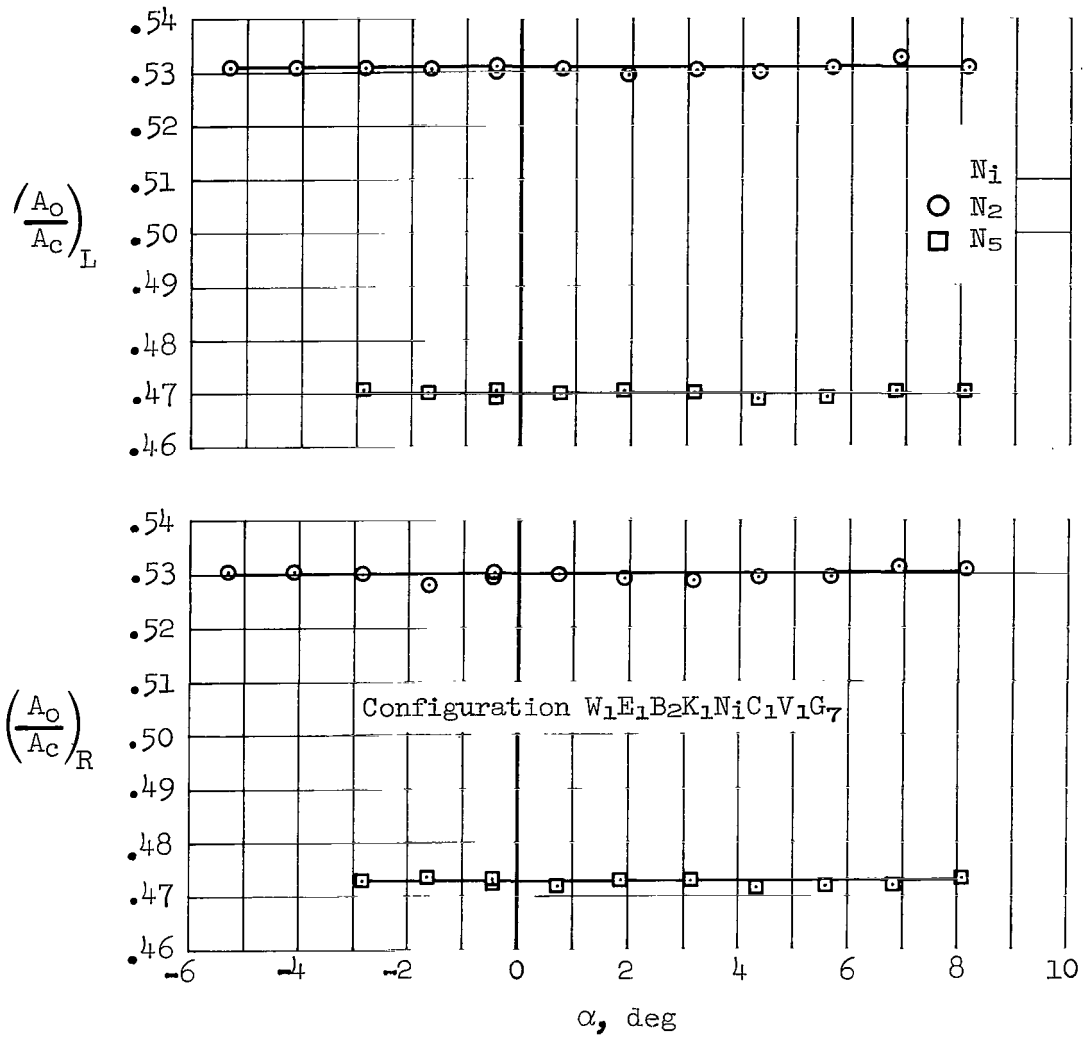

(g) M = 0.75, δ_y = 0°

Figure 35.- Concluded.

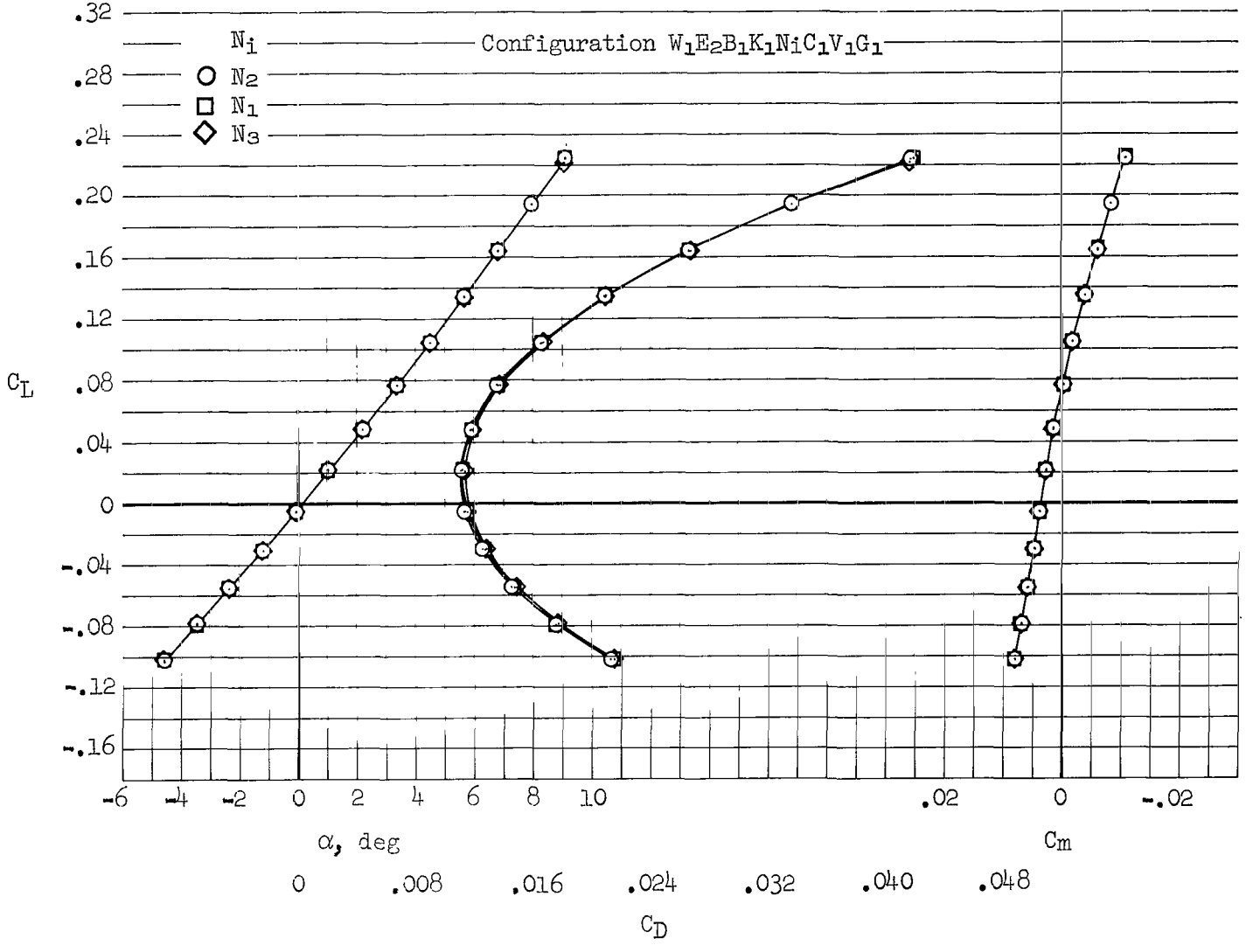

(a) M = 2.53, δ_y = 65°

Figure 36.- Effects of various nozzle configurations on longitudinal characteristics.

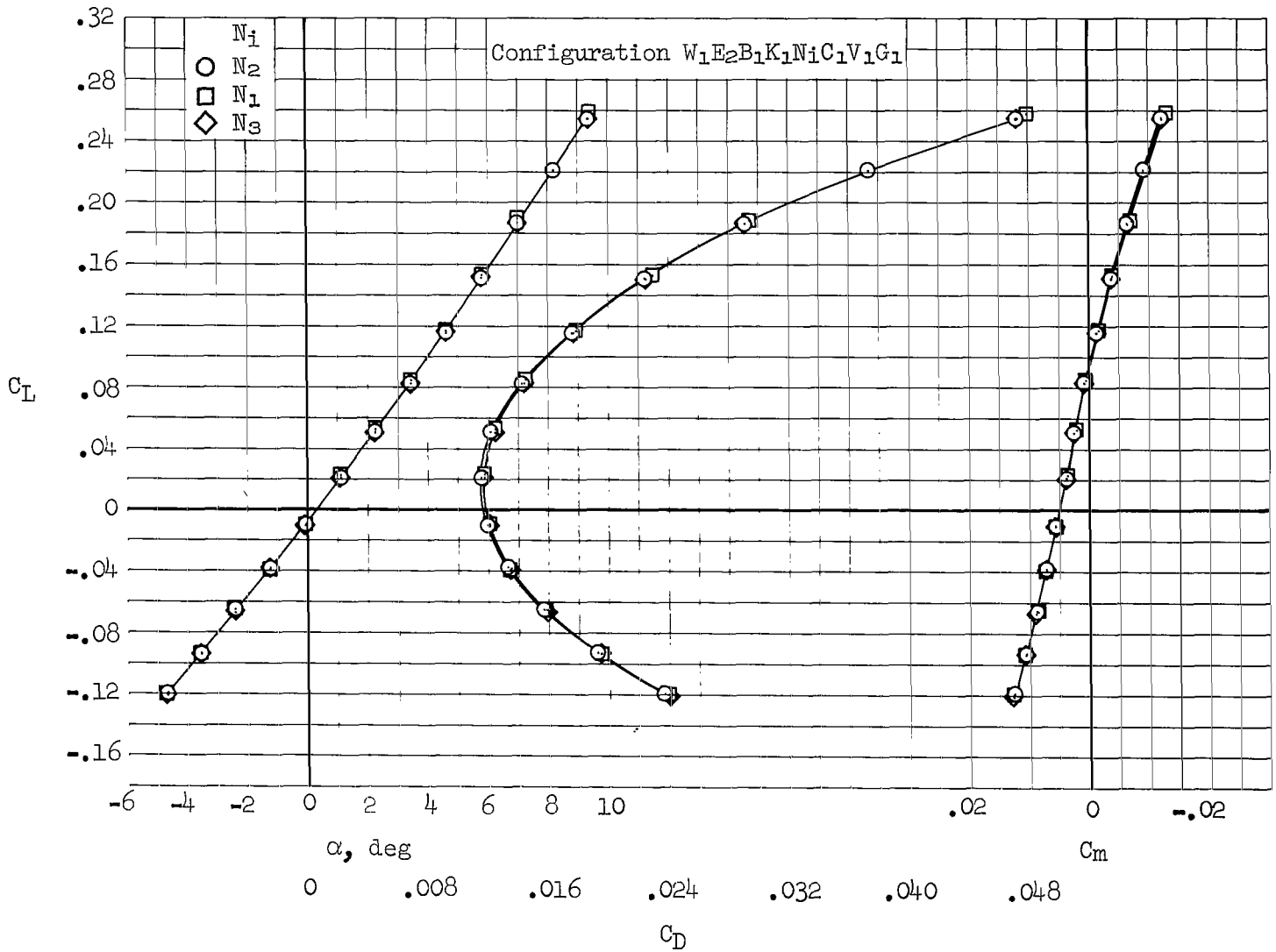

(b) M = 2.10, δ_y = 65°

Figure 36.- Continued.

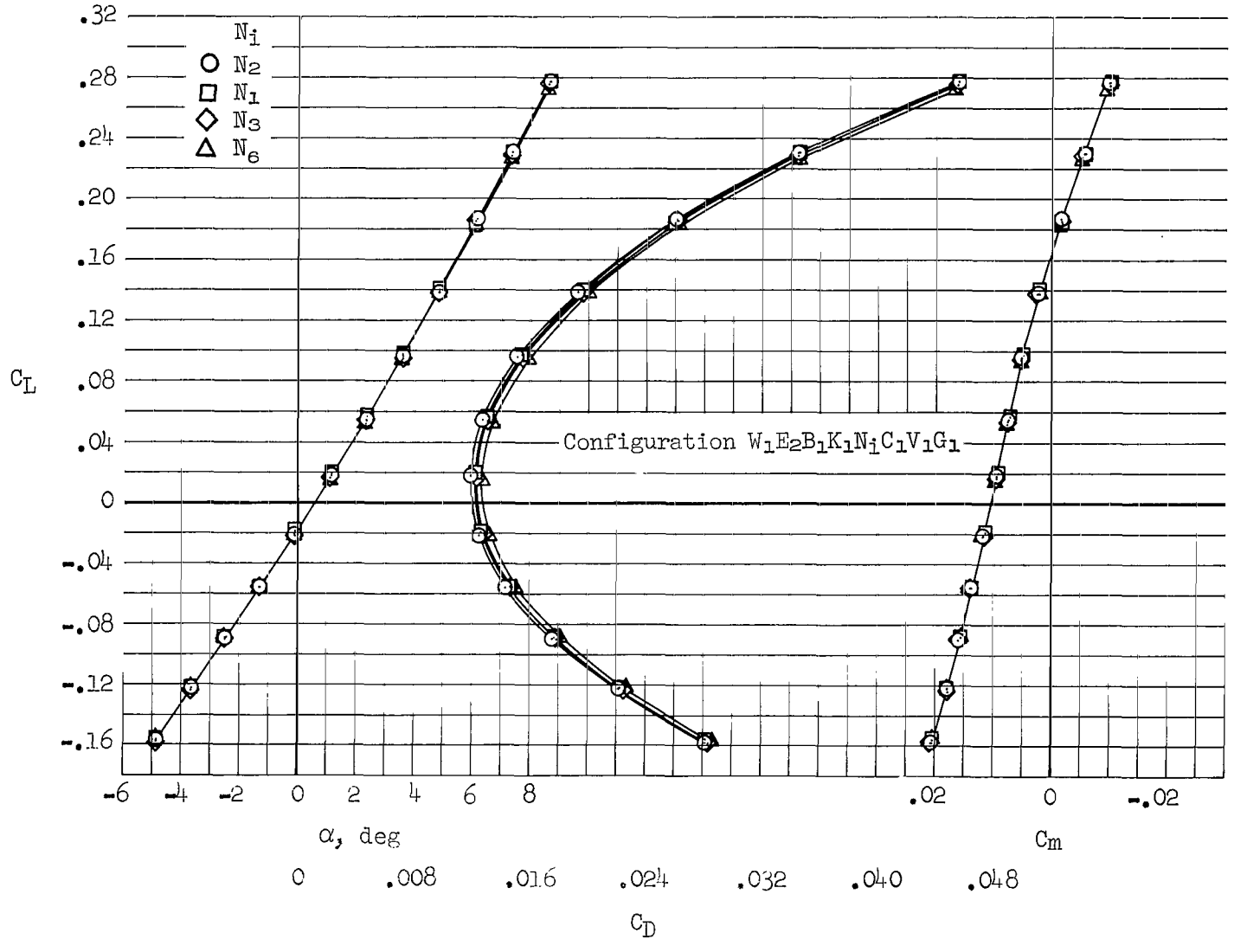

(c) M = 1.60, δ_y = 65°

Figure 36.- Continued.

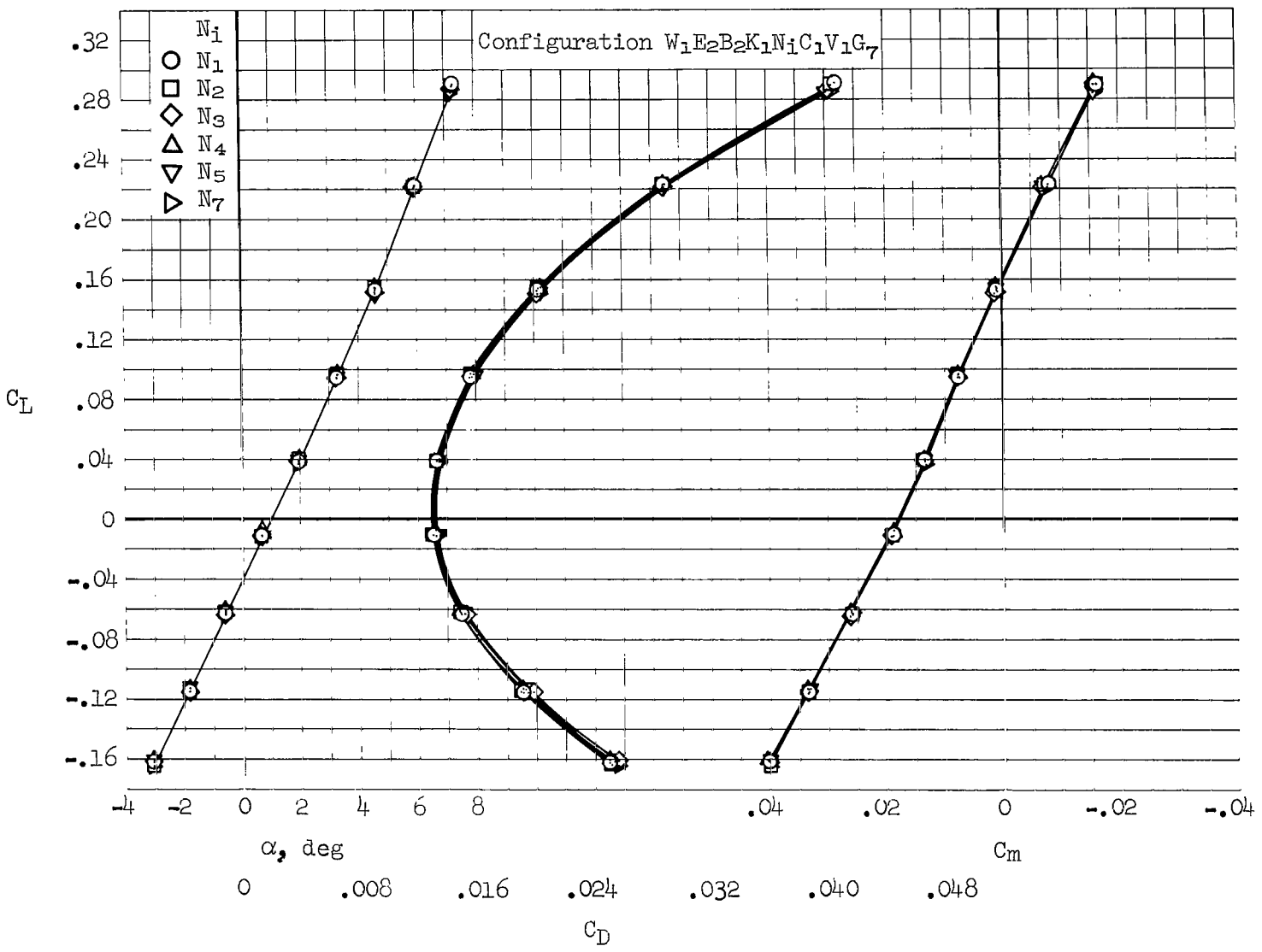

(d) M = 1.20, δ_y = 25°

Figure 36.- Continued.

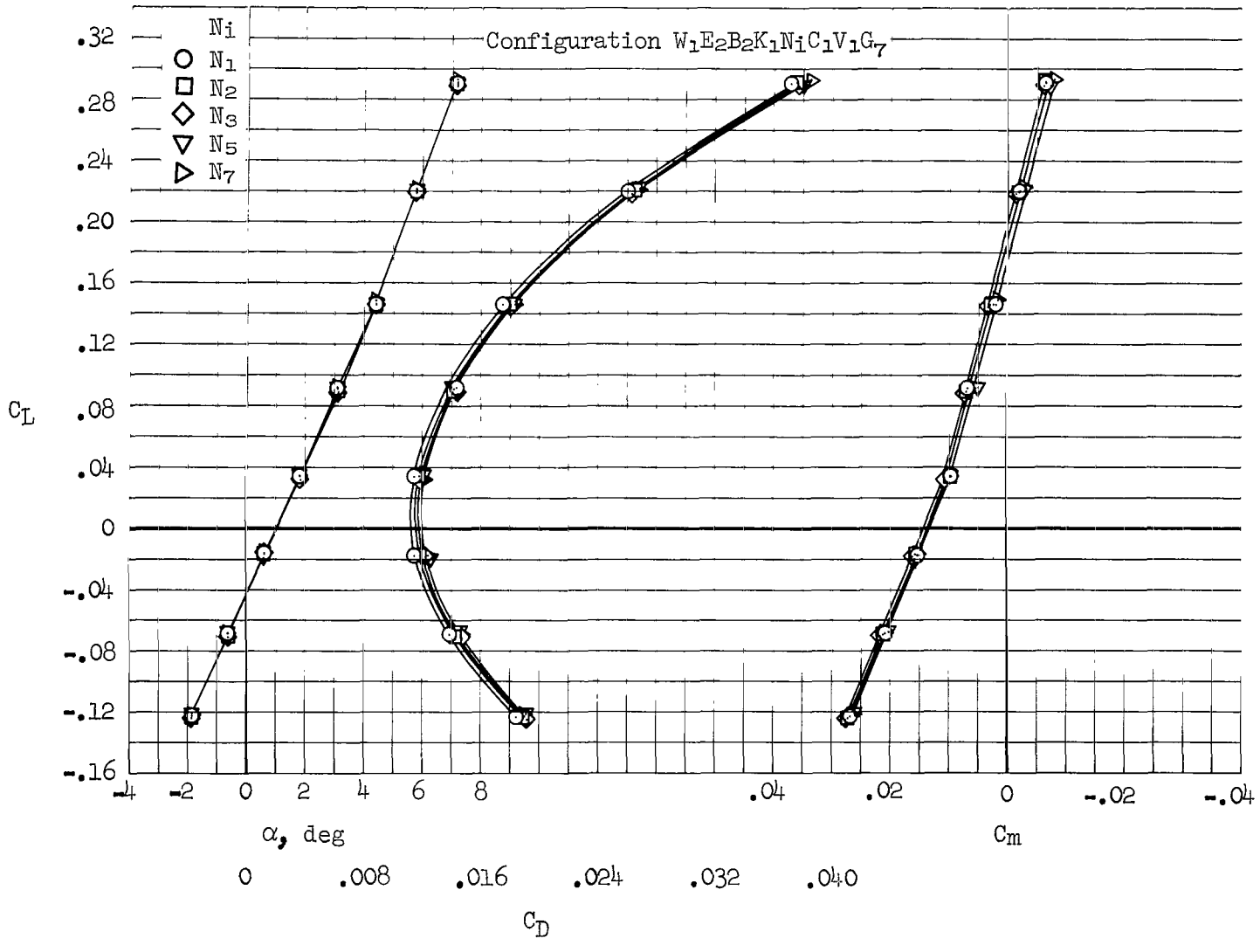

(e) M = 0.95, δ_y = 25°

Figure 36.- Continued.

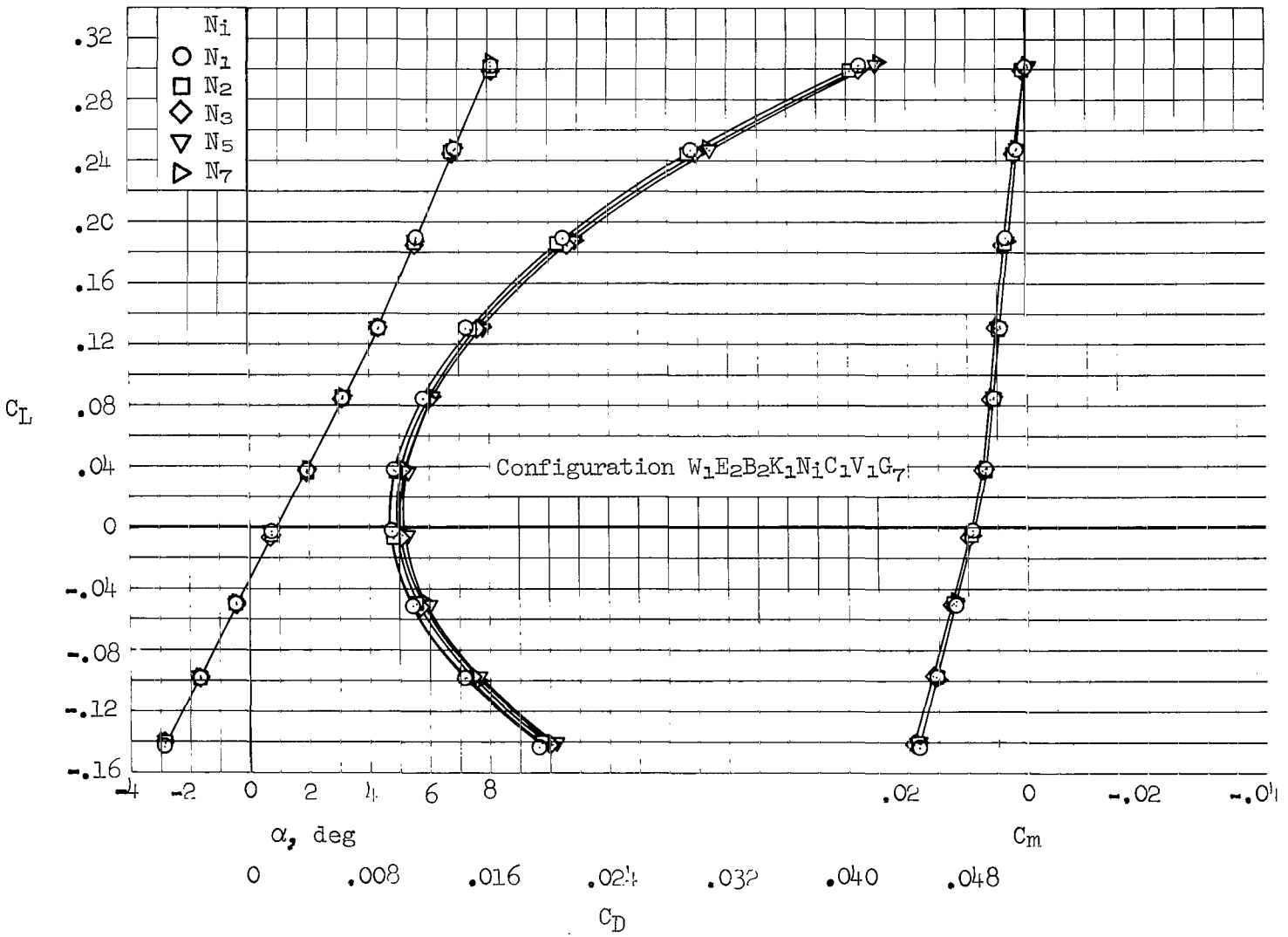

(f) M = 0.75, δ_y = 25°

Figure 36.- Continued.

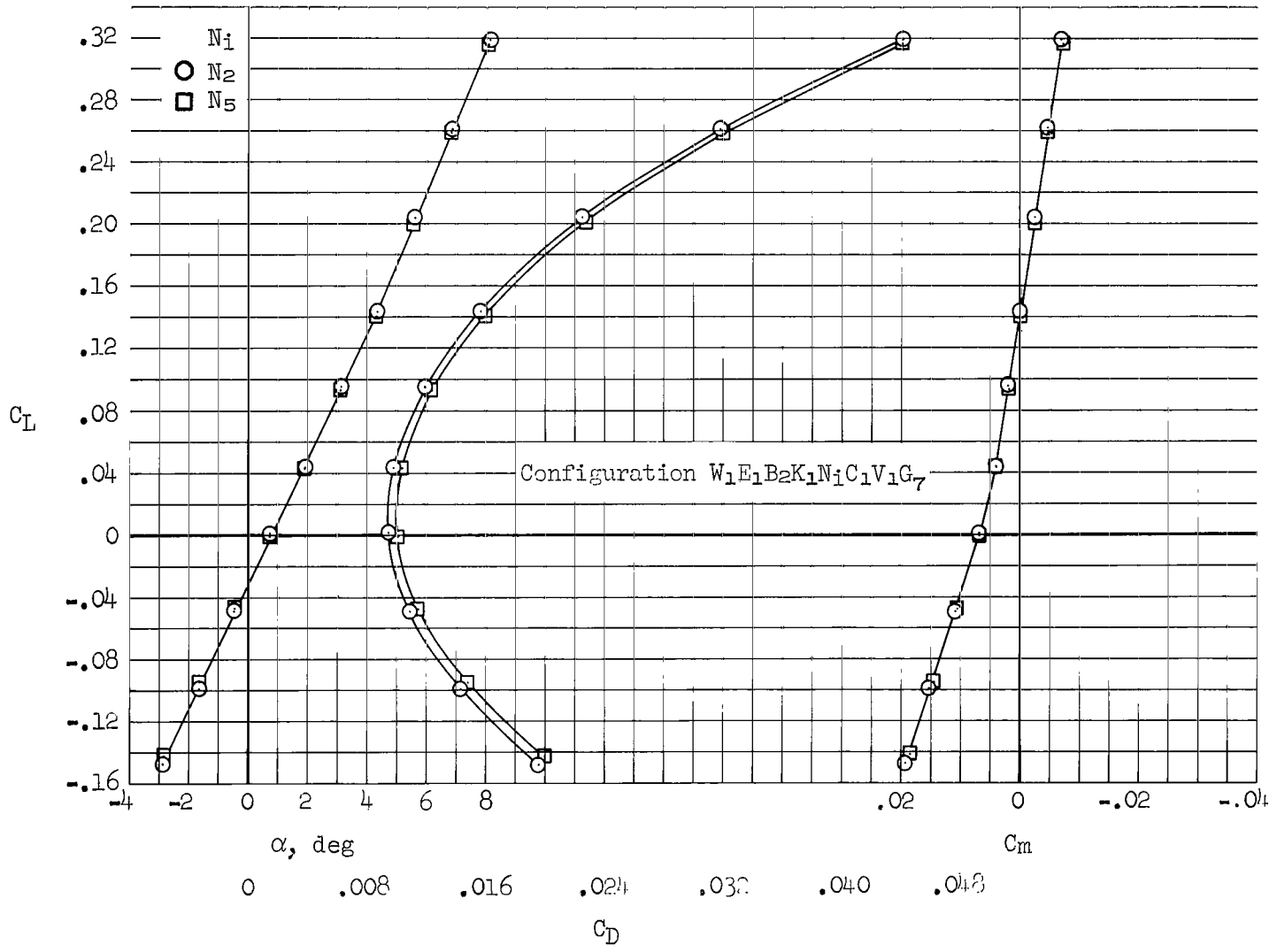

(g) M = 0.75, δ_y = 0°

Figure 36.- Concluded.

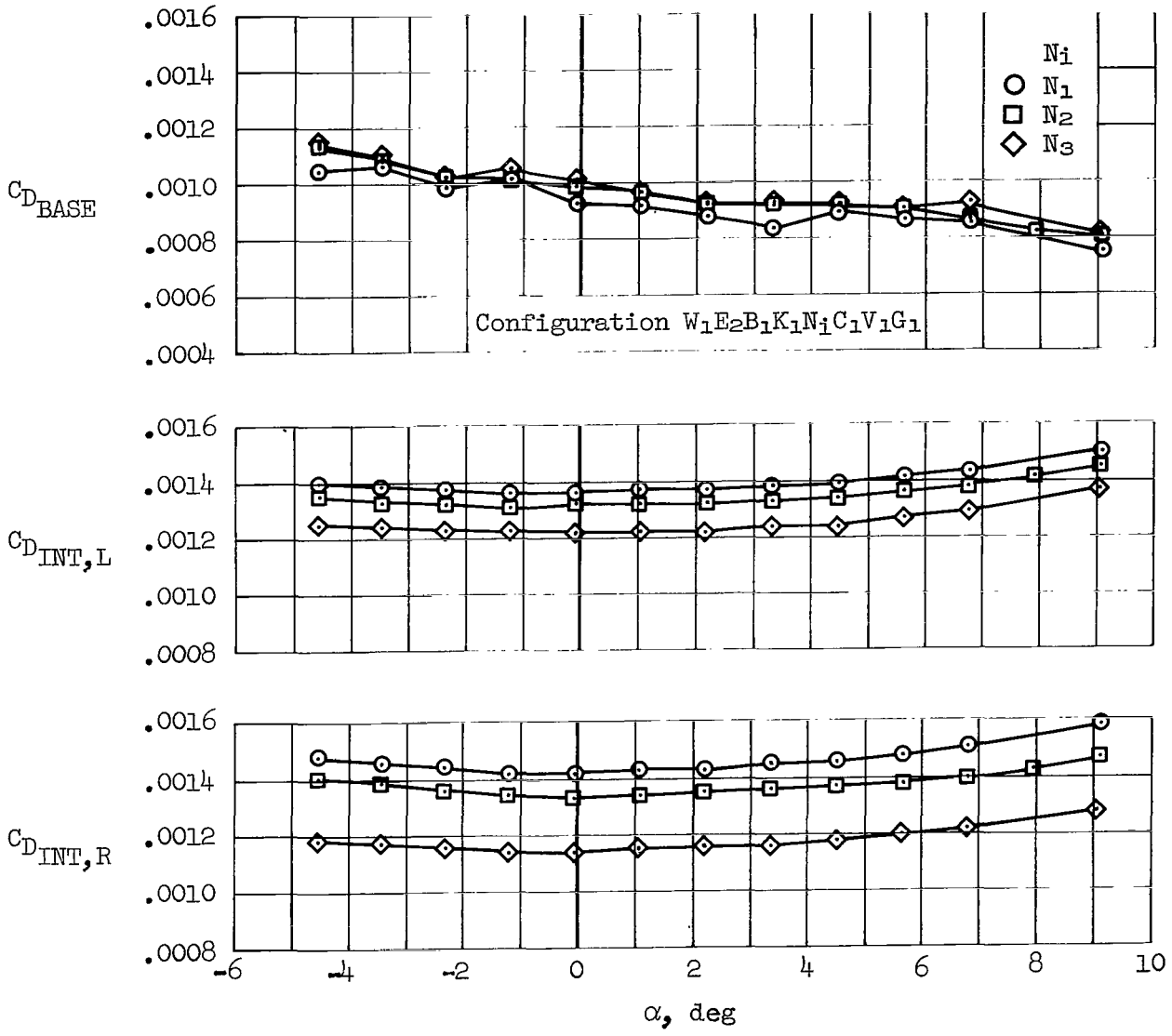

(a) M = 2.53, δ_y = 65°

Figure 37.- Effects of various nozzle configurations on base- and internal-drag coefficients.

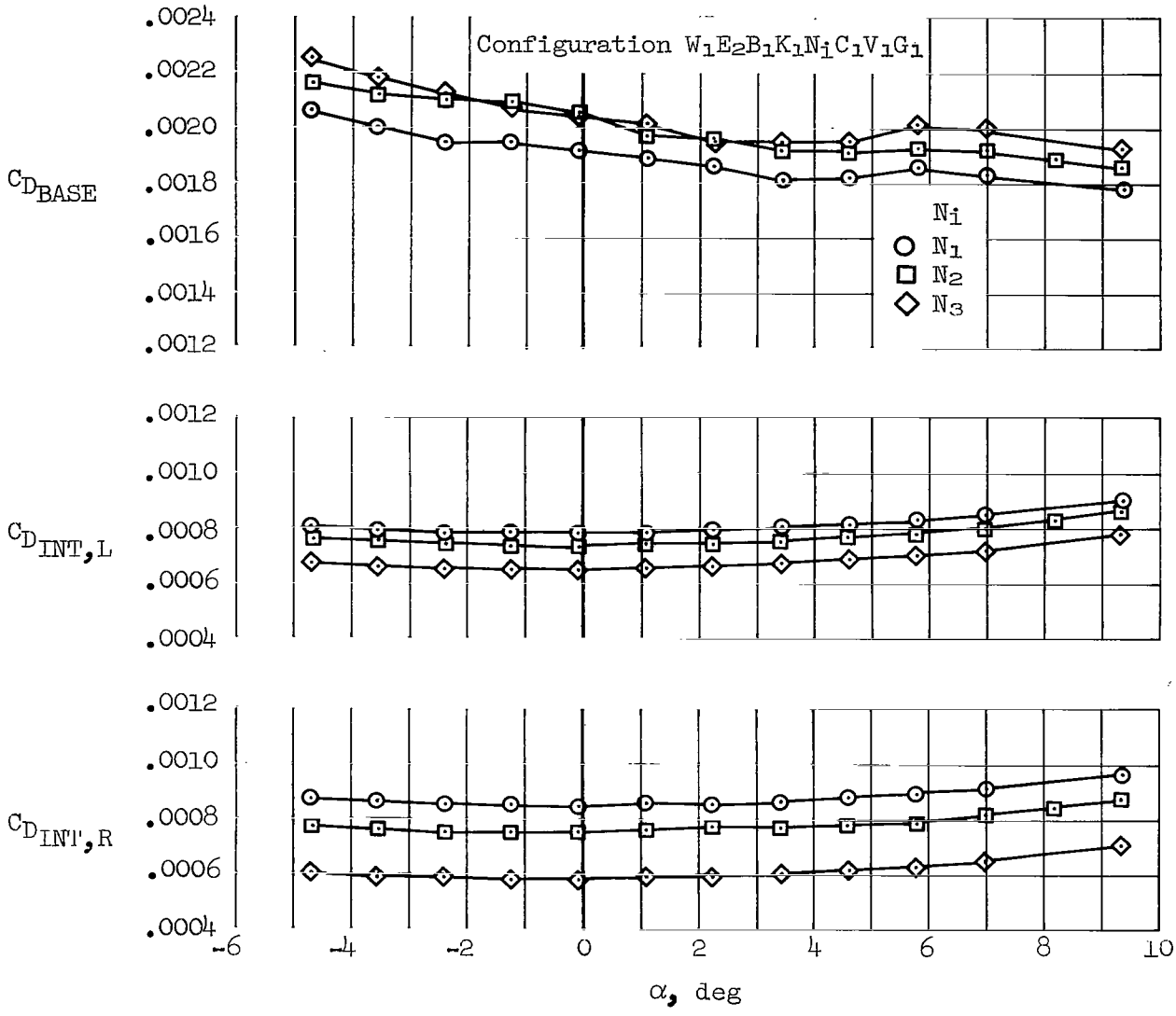

(b) M = 2.10, δ_y = 65°

Figure 37.- Continued.

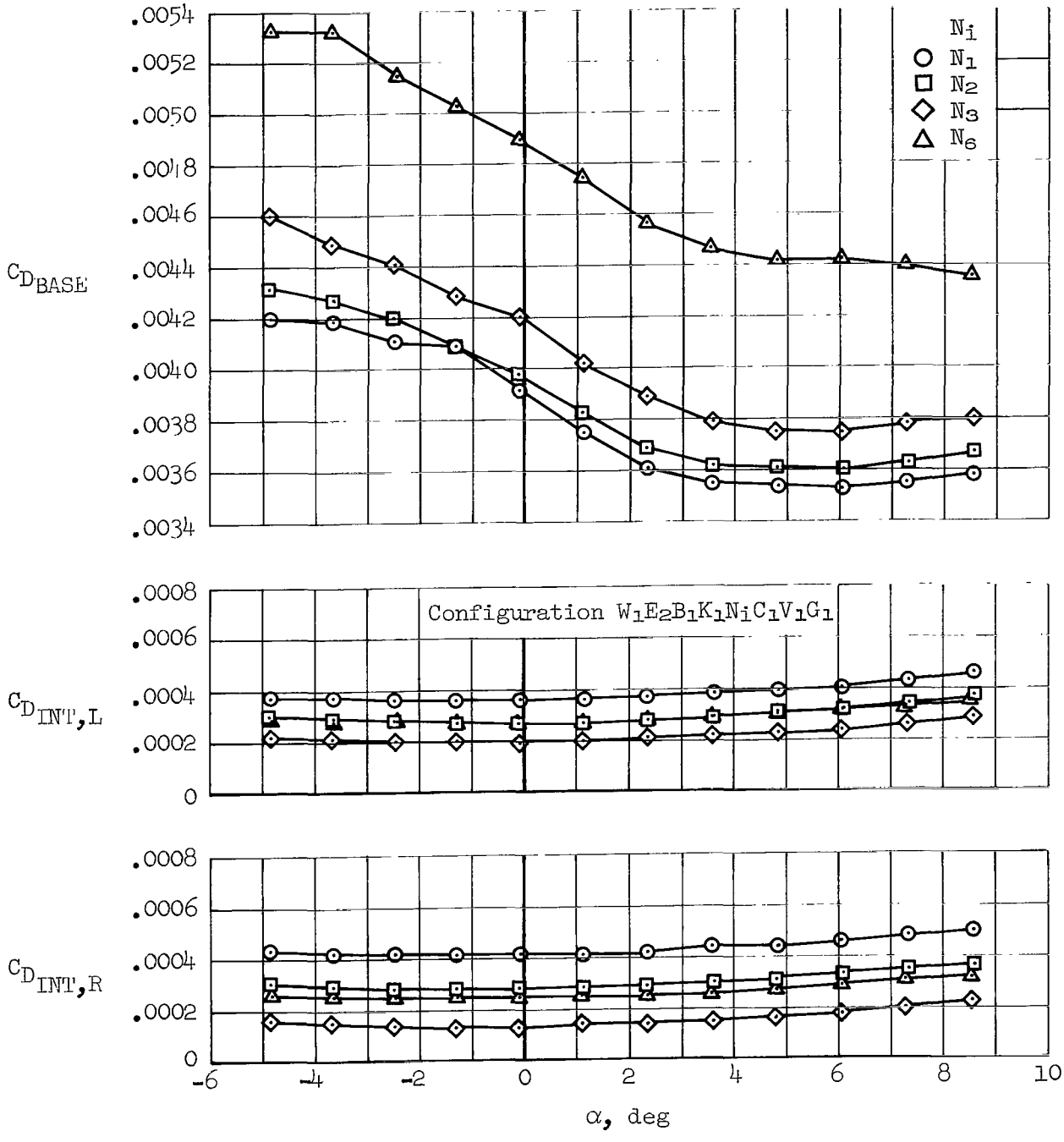

(c) M = 1.60, δ_y = 65°

Figure 37.- Continued.

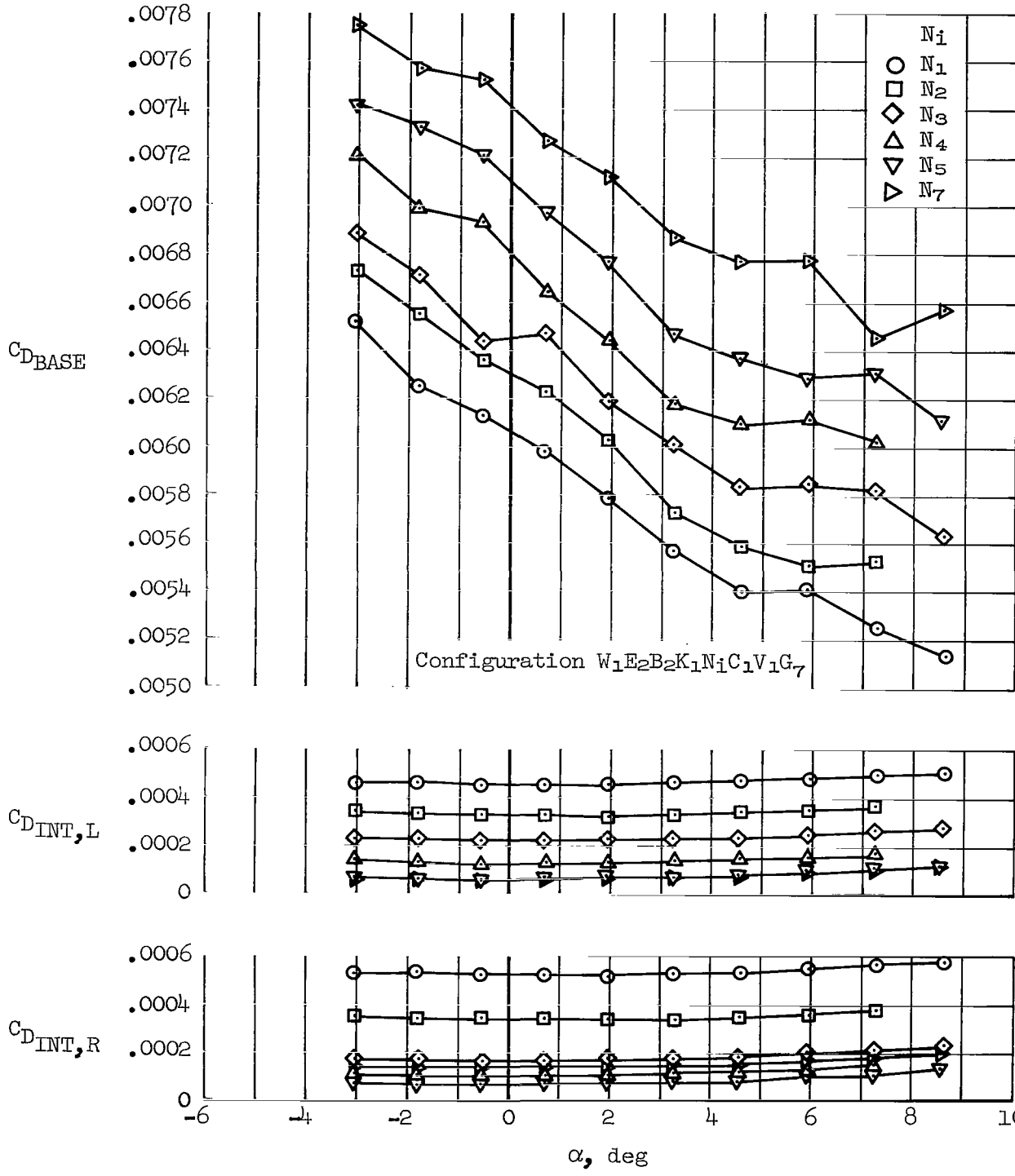

(d) M = 1.20, δ_y = 25°

Figure 37.- Continued.

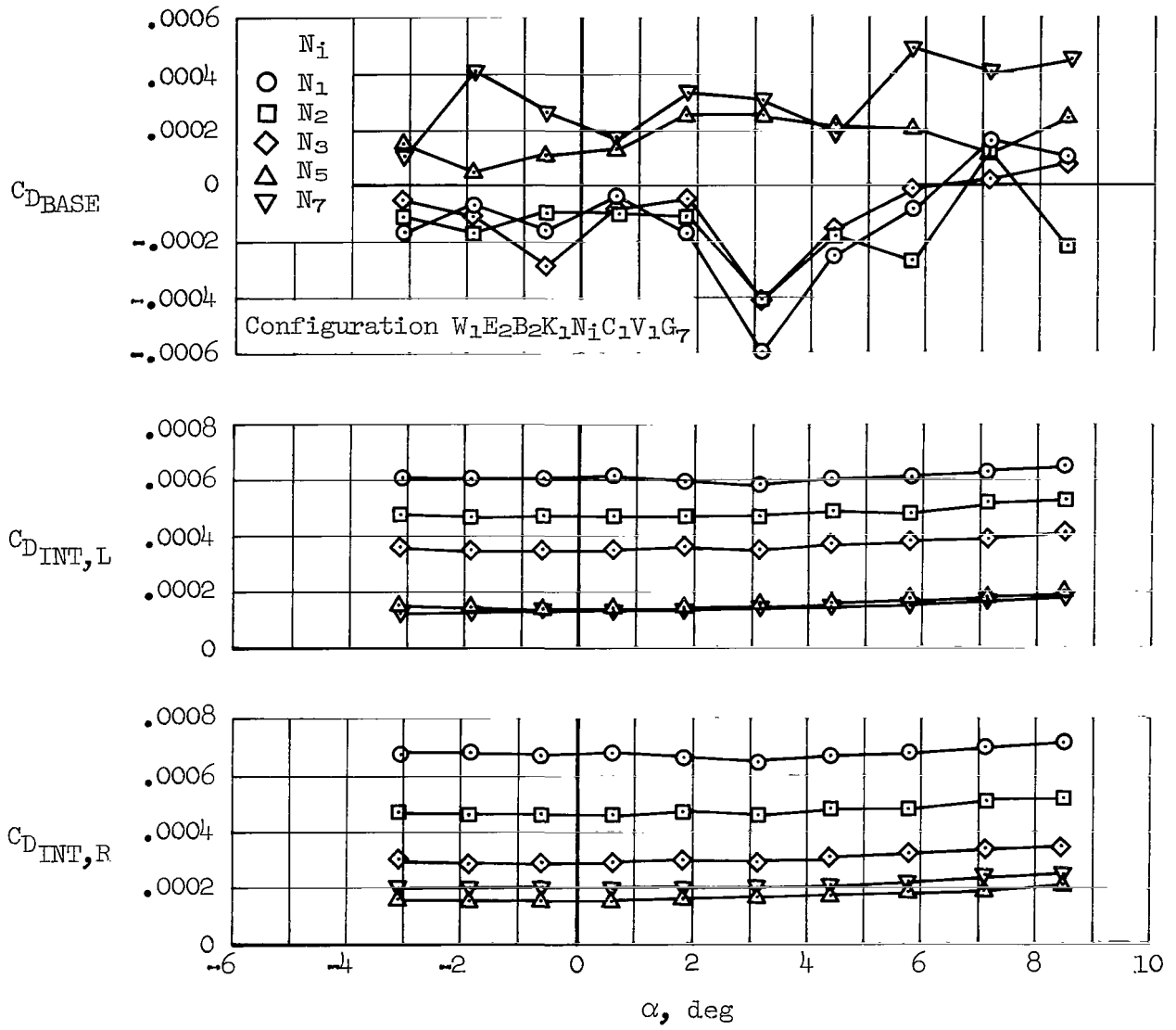

(e) M = 0.95, δ_y = 25°

Figure 37.- Continued.

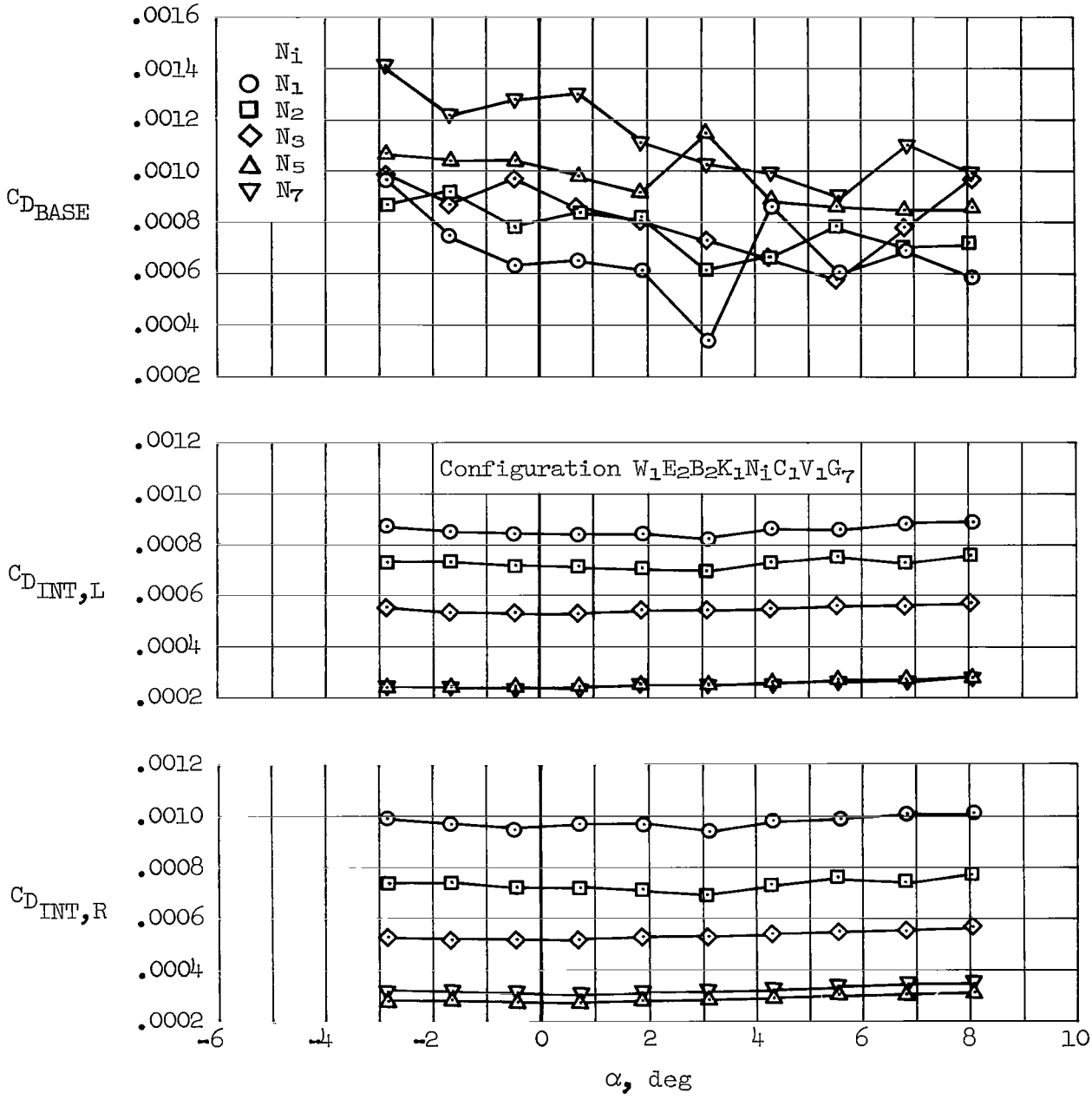

(f) M = 0.75, δ_y = 25°

Figure 37.- Continued.

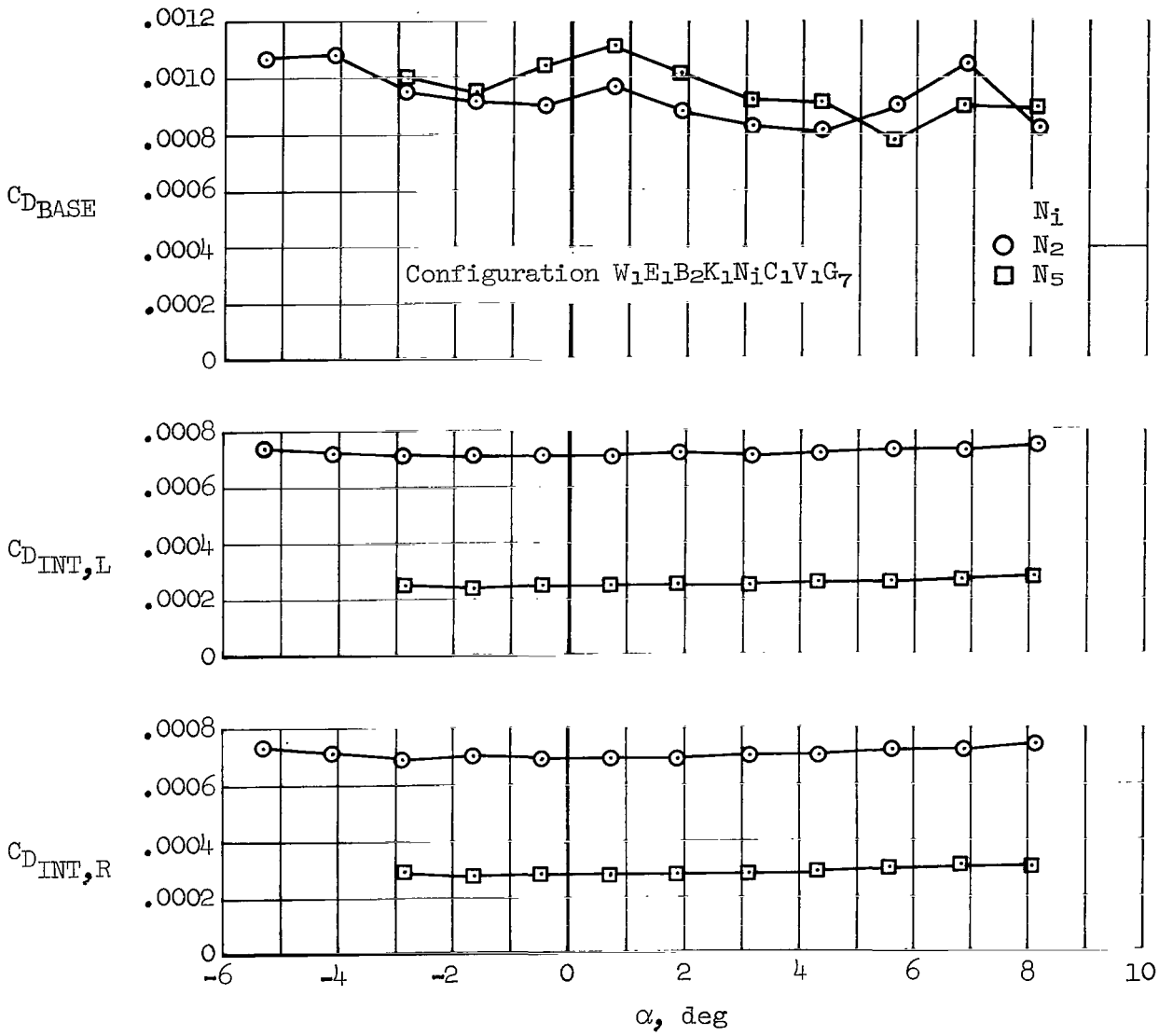

(g) M = 0.75, δ_y = 0°

Figure 37.- Concluded.

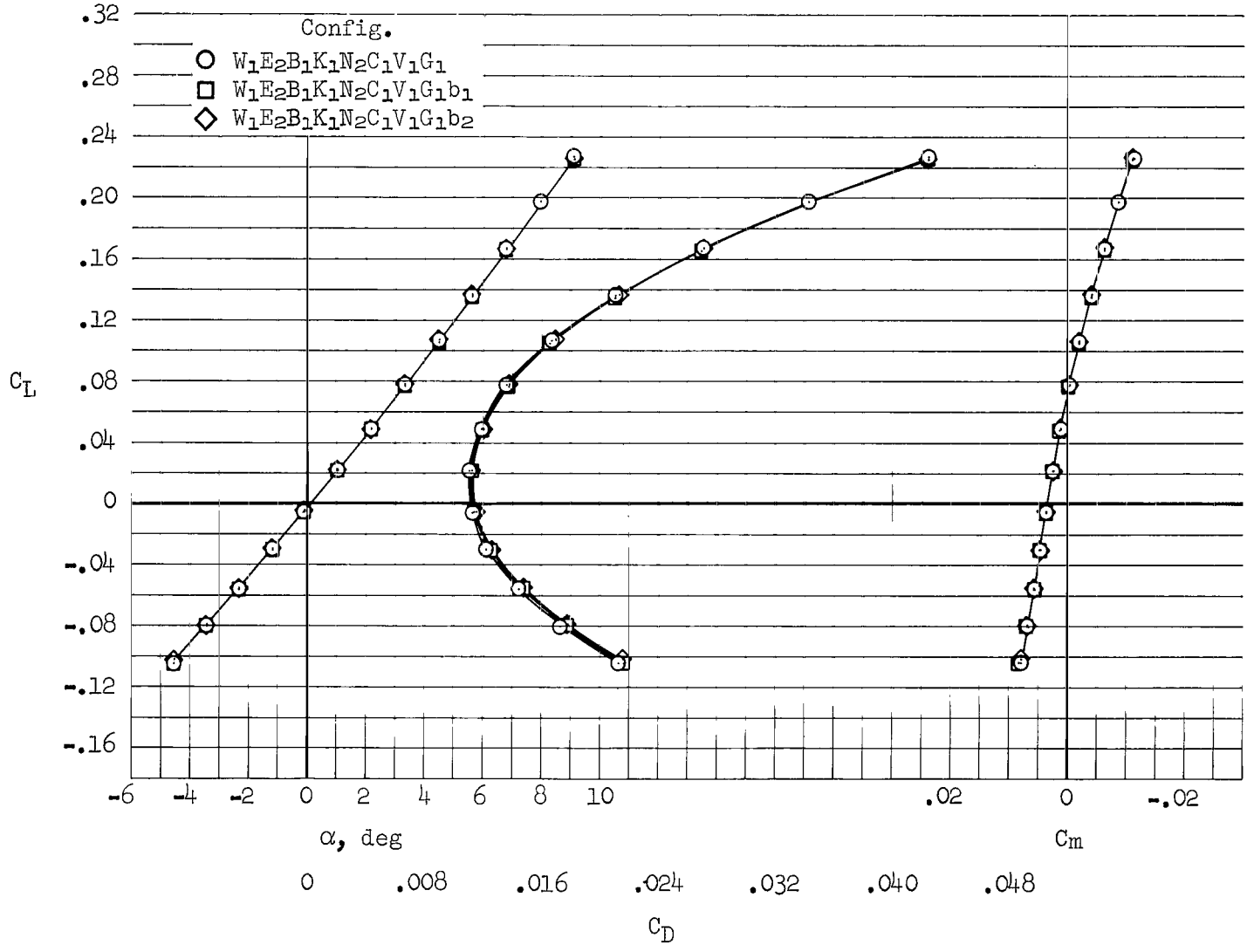

(a) M = 2.53, δ_y = 65°

Figure 38.- The effects of various bypass door configurations (door deflected, no airflow) on longitudinal characteristics.

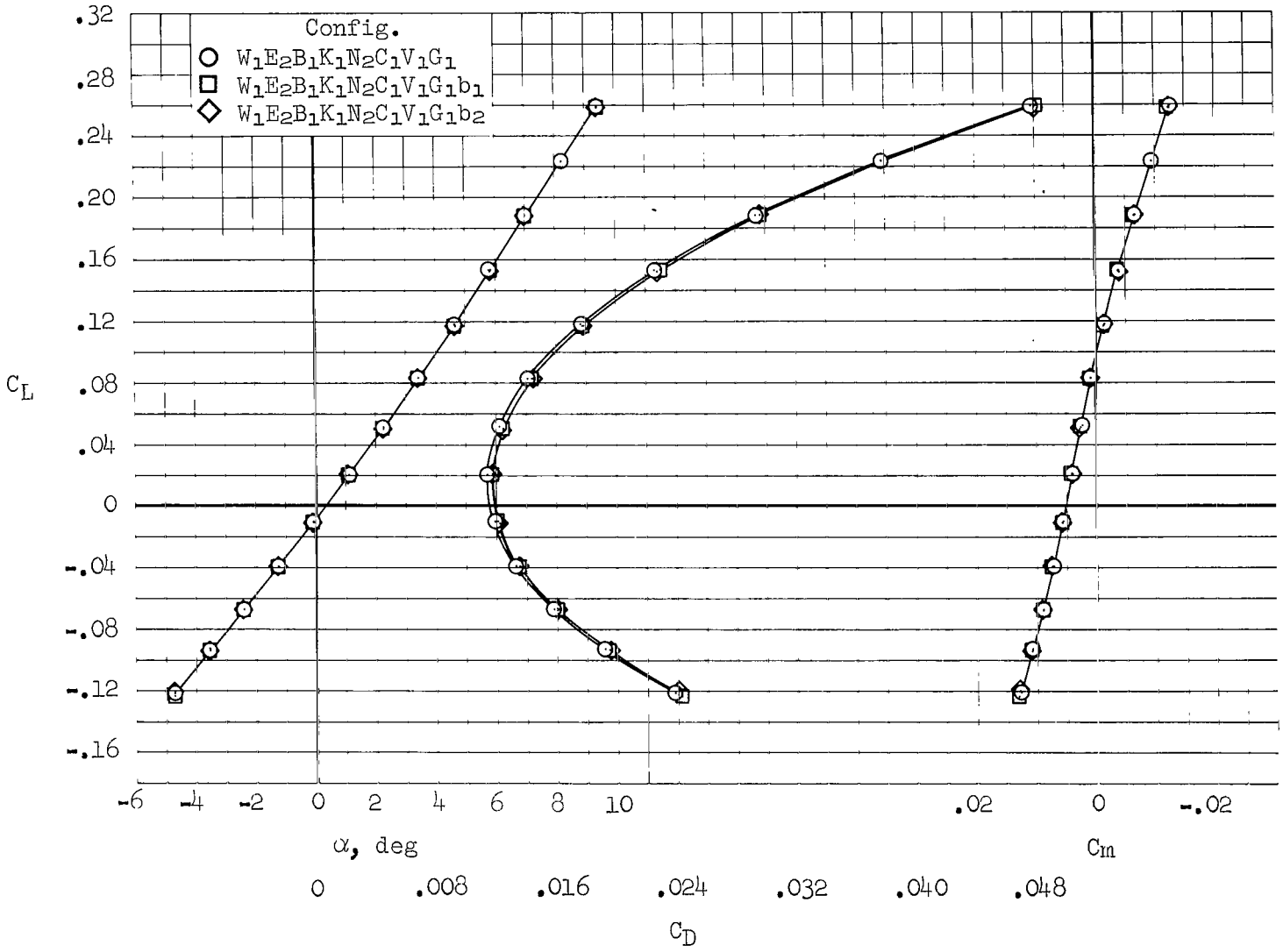

(b) M = 2.10, δ_y = 65°

Figure 38.- Continued.

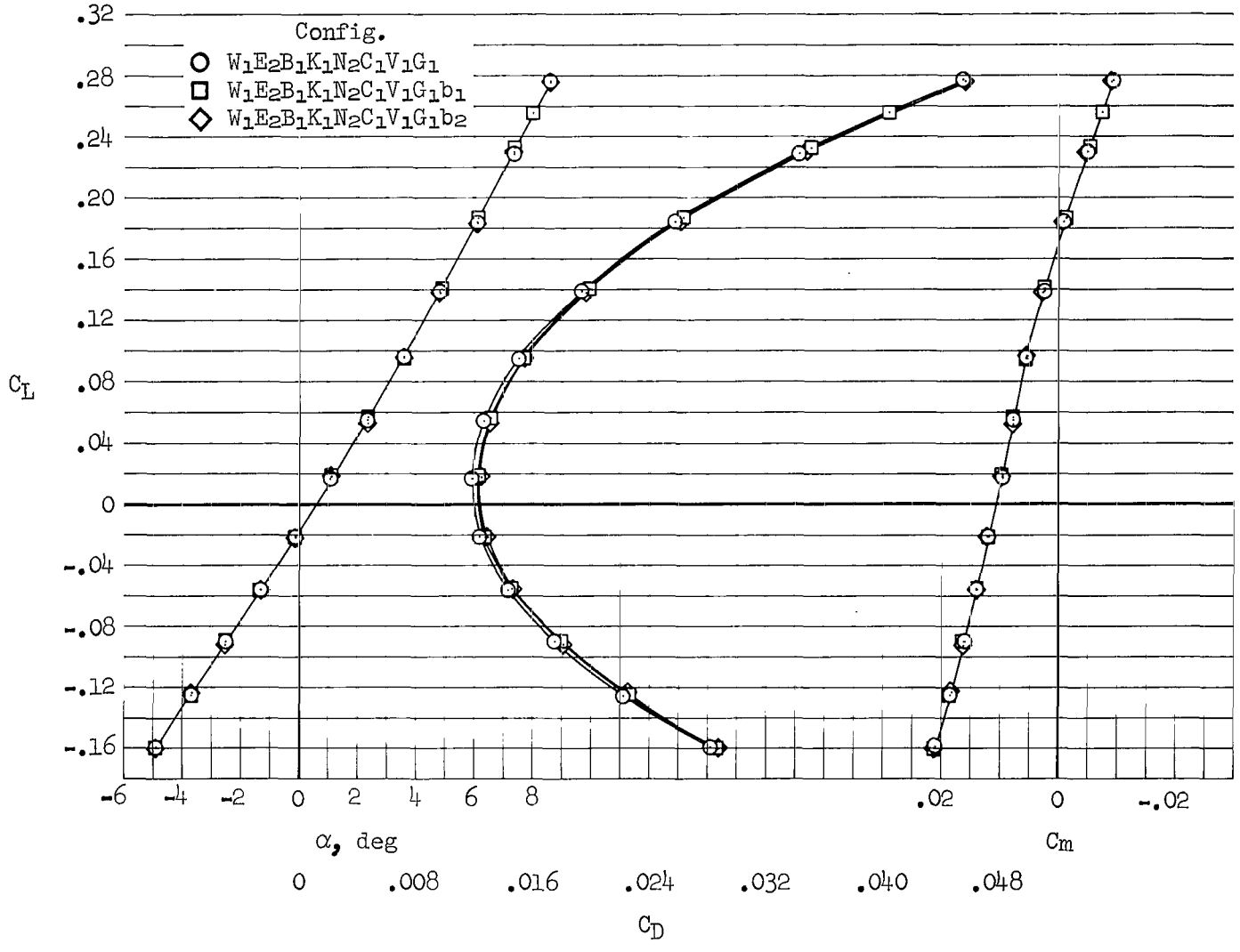

(c) M = 1.60, δ_y = 65°

Figure 38.- Continued.

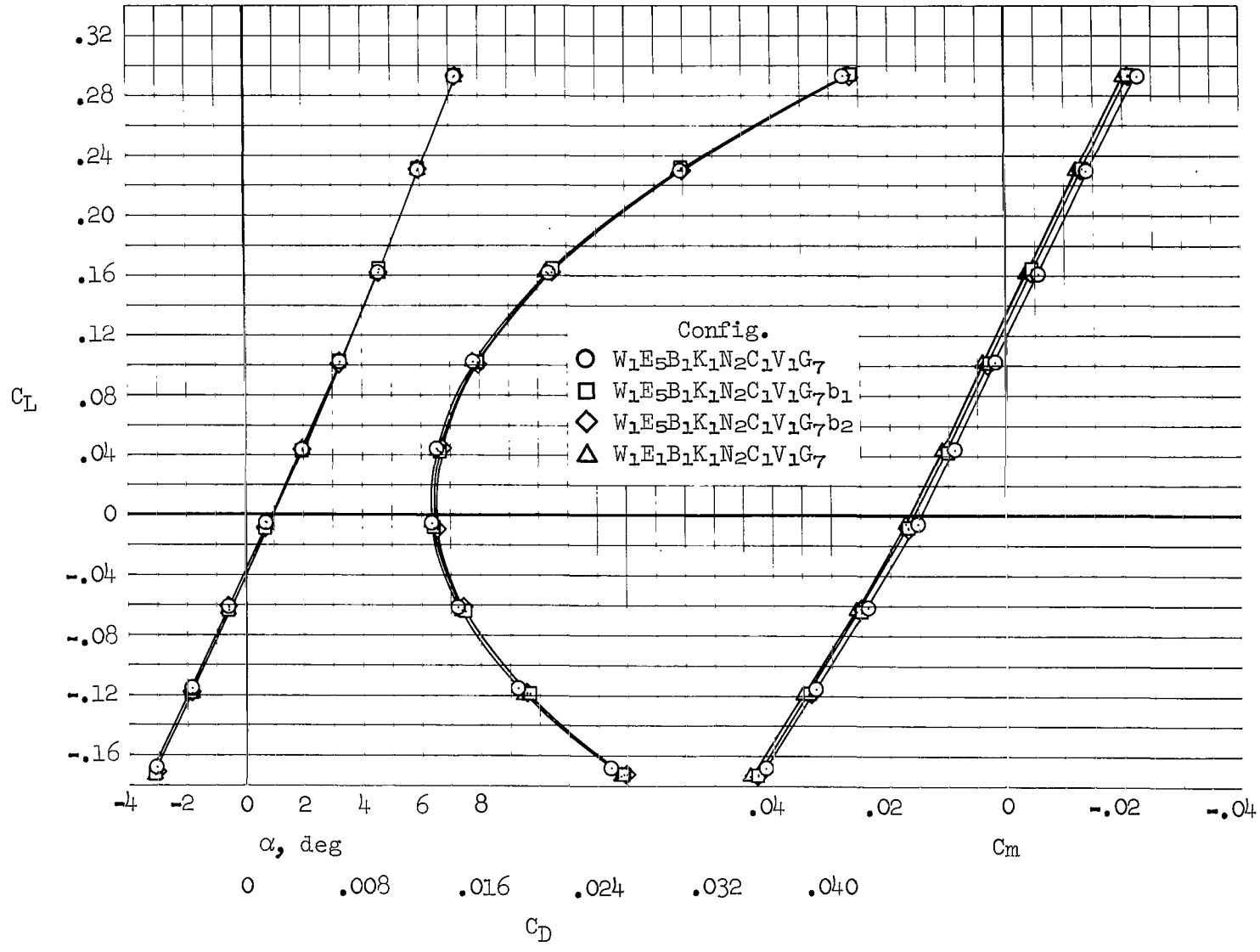

(d) M = 1.20, δ_y = 0°

Figure 38.- Concluded.

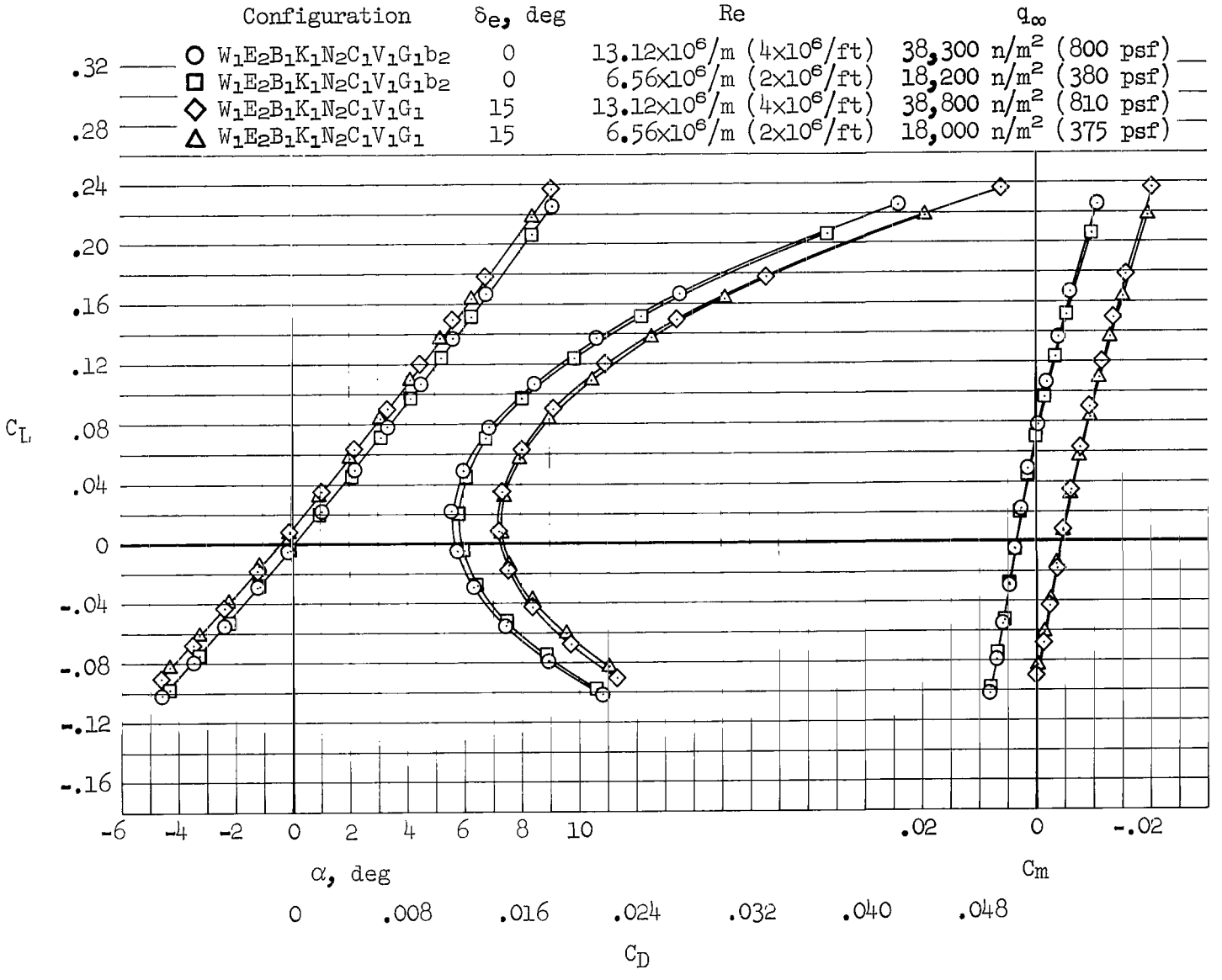

Figure 39.- Effects on longitudinal characteristics due to changes in unit Reynolds number and dynamic pressure, M = 2.53, δ_y = 65°.

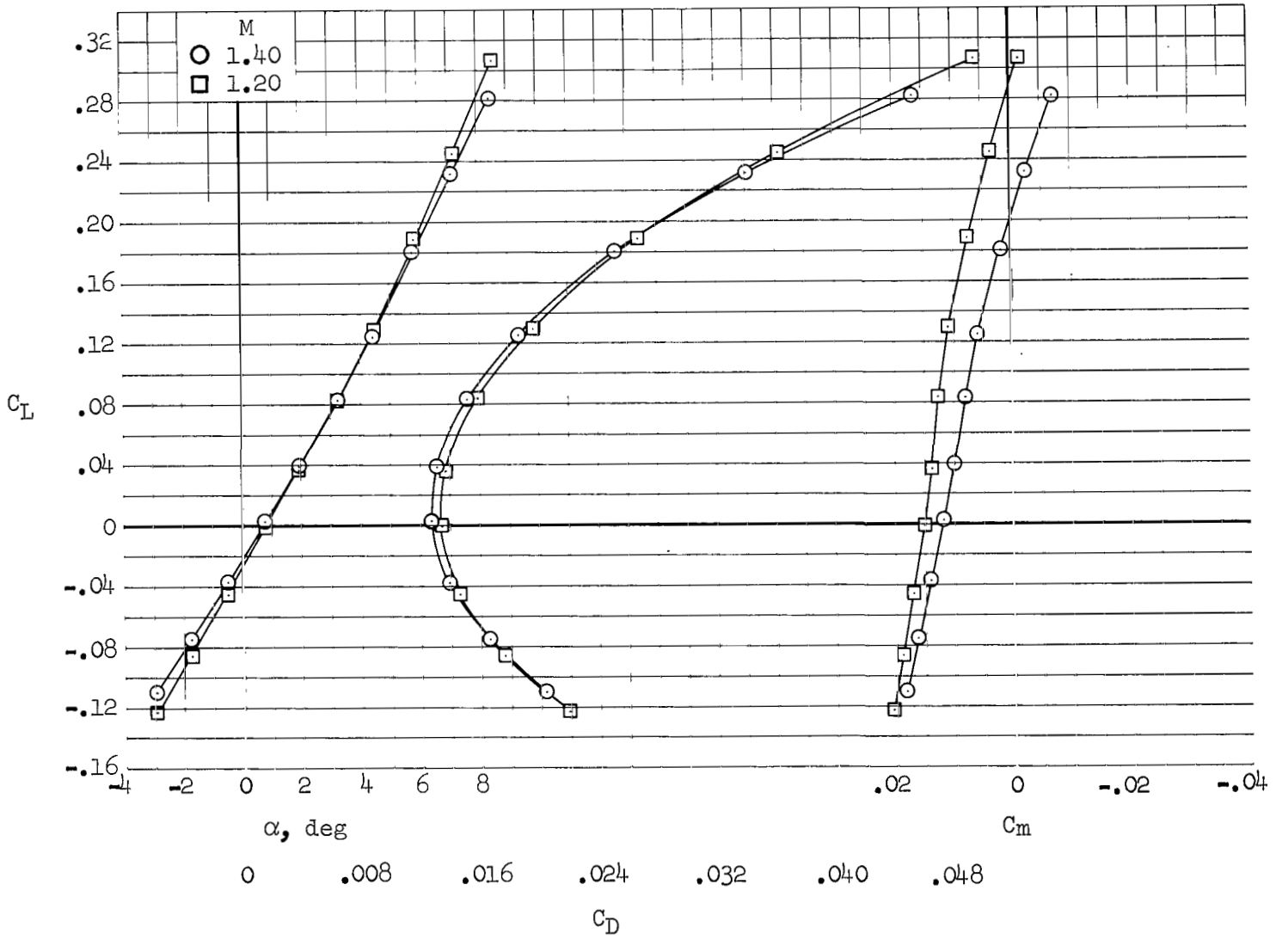

Figure 40.- Additional longitudinal data for configuration $W_1E_1B_1K_1N_2C_1V_1G_1$, δ_y = 65°.

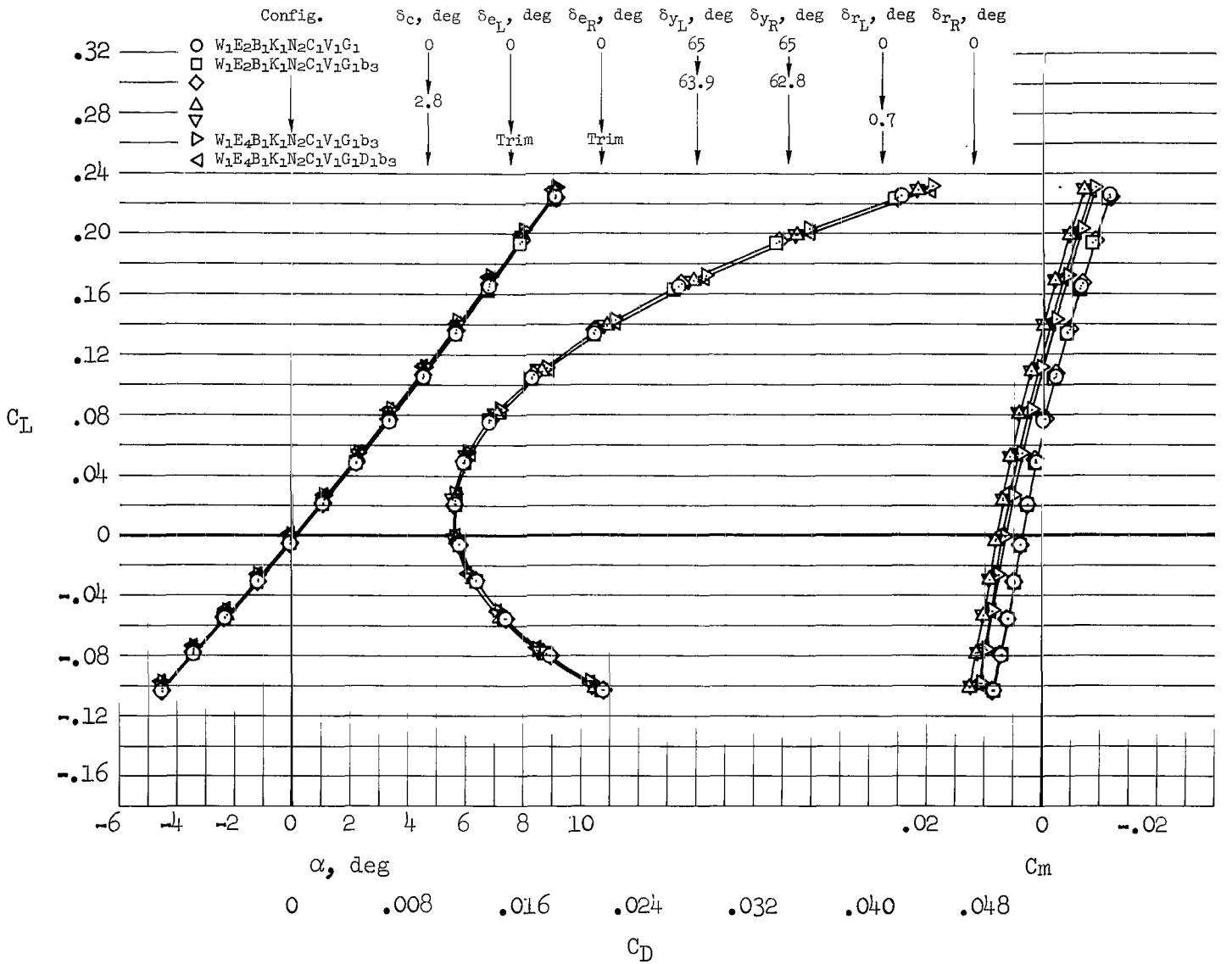

Figure 41.- Longitudinal characteristics for a systematic variation of surface-deflection angles from the basic supersonic-test configuration to a configuration representative of the design-point airplane; M = 2.53.

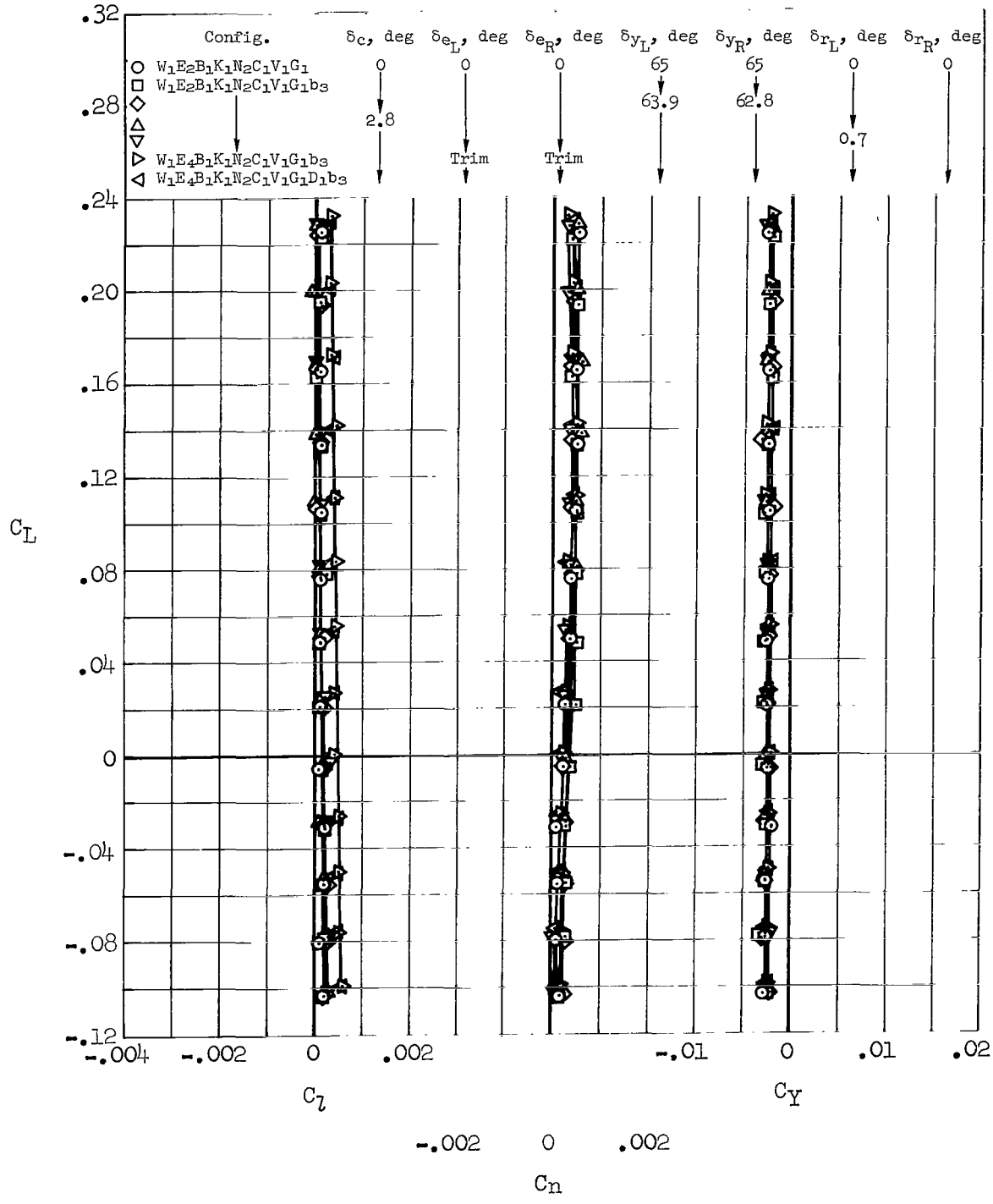

Figure 42.- Rolling-moment, yawing-moment, and side-force characteristics for a systematic variation of surface-deflection angles from the basic supersonic-test configuration to a configuration representative of the design-point airplane; M = 2.53.

1. Report No.	2. Government Accession No.	3. Recipient's Catalog No.
NASA TP-1514		

4. Title and Subtitle
WIND-TUNNEL/FLIGHT CORRELATION STUDY OF AERODYNAMIC CHARACTERISTICS OF A LARGE FLEXIBLE SUPERSONIC CRUISE AIRPLANE (XB-70-1)
I — WIND-TUNNEL TESTS OF A 0.03-SCALE MODEL AT MACH NUMBERS FROM 0.6 TO 2.53

5. Report Date: November 1979

6. Performing Organization Code:

7. Author(s)
James C. Daugherty

8. Performing Organization Report No.: A-7712

10. Work Unit No.: 517-51-021

9. Performing Organization Name and Address
Ames Research Center, NASA
Moffett Field, Calif. 94035

11. Contract or Grant No.:

13. Type of Report and Period Covered: Technical Paper

12. Sponsoring Agency Name and Address
National Aeronautics and Space Administration
Washington, D.C. 20546

14. Sponsoring Agency Code:

15. Supplementary Notes:

16. Abstract

Wind-tunnel studies were conducted on a 0.03-scale static-force model of the XB-70-1 airplane to provide data for the purpose of correlating flight predictions based on state-of-the-art wind-tunnel measurements, theoretical methods, and analytical procedures with results derived from flight tests. The model was designed and fabricated to be representative of the airplane at a specific speed-power-stabilized flight-test point. The longitudinal and lateral force and moment results reported herein were obtained at Mach numbers from 0.6 to 2.53 at a Reynolds number of 13.12×10^6/m (4×10^6/ft).

17. Key Words (Suggested by Author(s))
Aircraft design
Testing
Performance

18. Distribution Statement
Unlimited

STAR Category - 05

19. Security Classif. (of this report)	20. Security Classif. (of this page)	21. No. of Pages	22. Price*
Unclassified	Unclassified	222	$9.25

*For sale by the National Technical Information Service, Springfield, Virginia 22161

NASA-Langley, 1979